STUDY OF CHARGED-NEUTRAL FLUCTUATIONS AND CHARGE SEPARATION IN Pb-Pb COLLISIONS WITH ALICE AT THE LHC

A THESIS

Submitted to the

FACULTY OF SCIENCES

PANJAB UNIVERSITY, CHANDIGARH

for the degree of

DOCTOR OF PHILOSOPHY

2019

SONIA PARMAR

DEPARTMENT OF PHYSICS

(CENTRE OF ADVANCED STUDY IN PHYSICS)

PANJAB UNIVERSITY

CHANDIGARH-160014

DEPARTMENT OF PHYSICS
Centre of Advanced Study in Physics
PANJAB UNIVERSITY, CHANDIGARH-160 014 (INDIA)
Fax: ++91-172-2783336

Phone: ++91-172-2541741
EPABX: ++91-172-2534466, 2534446
Email: casphypu.ac.in

CORRECTION CERTIFICATE

It is certified that there were no specific corrections recommended by the examiner of **Ms. Sonia Parmar** in her Ph.D. thesis **"Study of Charged-Neutral Fluctuations and Charge Separation in Pb-Pb Collisions with ALICE at the LHC"**. The thesis submitted by **Ms. Sonia Parmar** in the present form, is acceptable.

Navdeep	MM Aggarwal	AK Bhati
(Prof. Navdeep Goyal)	(Prof. M.M. Aggarwal)	(Dr. A.K. Bhati)
Dept. of Physics,	Department of Physics	Department of Physics
P.U., Chandigarh	P.U., Chandigarh	P.U., Chandigarh
(Chairman)	**(Supervisor)**	**Supervisor)**

Chairperson
Department of Physics
Panjab University
Chandigarh-160014

PANJAB UNIVERSITY CHANDIGARH
STUDENT APPROVAL FORM FOR ELECTRONIC THESIS SUBMISSION

Thesis Title	STUDY OF CHARGED-NEUTRAL FLUCTUATIONS AND CHARGE SEPARATION IN Pb-Pb COLLISIONS WITH ALICE AT THE LHC
Name of the Research Scholar	SONIA PARMAR
Supervisor / Co-Supervisors	Dr. M.M. Aggarwal Dr. A.K. Bhati
Department/Centre	PHYSICS

STUDENT AGREEMENT

1. I represent that my thesis is my original work. Proper attribution has been given to all outside sources. I understand that I am solely responsible for obtaining any needed copyright permissions. I have obtained needed written permission statements(s) from the owner(s) of each third-party copyrighted matter to be included in my work, allowing electronic distribution (if such use is not permitted by the fair use doctrine) which will be submitted to Panjab University Chandigarh.
2. I hereby grant to the university and its agents the irrevocable, non-exclusive, and royalty-free license to archive and make accessible my work in whole or in part in all forms of media, now or hereafter known. I agree that the document mentioned above may be made available for worldwide access.

REVIEW, APPROVAL AND ACCEPTANCE

The thesis mentioned above has been reviewed and accepted by the student's advisor, on behalf of the program; I/We verify that this is the final, approved version of the student's thesis including all changes required.

It is certified that electronic copy of thesis is the same as submitted in print form and as per the Shodhganga format.

EMBARGO AGREEMENT (OPTIONAL)

Kindly tick the appropriate option:

- [x] No Embargo requested
- [ ] Embargo request for 6 months
- [ ] Embargo request for 1 Year
- [ ] Embargo request for 2 Year

Please specify the reasons for Embargo:

- The student is applying for a patent on an invention or procedure documented in the thesis and does not wish to make the contents public until the patent application has been filed.
- The thesis contains sensitive and/or classified information
- Immediate release of the thesis may impact an existing or potential publishing agreement.
- If any other, please specify:-

____

____

Note: *Research scholars are requested to please fill this form and get it signed from their supervisor/co-supervisors and HOD with proper stamp/seal and save the scanned copy of same in the CD (thesis).*

Sonia Parmar
Signature of the Research Scholar

MM Aggarwal
Supervisor
Name: M.M. Aggarwal

Co-Supervisor
Name: A.K. Bhati

Co-Supervisor
Name:

Chairperson
Department of Physics
Panjab University
Chandigarh-160014
Head of the Department

Acknowledgements

It gives me immense pleasure to express my sincere appreciation to the people who have contributed in one or another way towards the successfull accomplishment of my research work presented in this thesis.

Foremost, I take this opportunity to express my deep sense of gratitude to my Ph.D. thesis supervisor Dr. M.M. Aggarwal for his keen supervision, great enthusiasm, sincerity, and constant encouragement during my voyage in obtaining Ph.D. degree. His immense knowledge and valuable guidance always helped as well as insipred me. I am greatly indebted and heartfelt to my co-supervisor Dr. A.K. Bhati, for all time support, encouragement and valuable suggestions. I am thankful to them for providing me a good platform to work in an International Collaboration and for the extreemed exposure.

I would like to express my sincere thanks to Prof. Navdeep Goyal, Chairperson, Department of Physics, Panjab University Chandigarh, for facilitating all the requirements in the department which helped me in completing my thesis work. I am grateful to Dr. Lokesh Kumar for his everlasting support and useful physics discussions. My sincere thanks to Dr. Natasha Sharma and Dr. Navneet Kumar Pruthi for invaluable suggestions and help at every point. I sincerely acknowledge all the teachers I learnt from since my childhood.

I would like to express my deepest regards to ALICE-India Spokesperson, Dr. Subhasis Chattopadhyay for his encouragement and healthy discussions. I would also like to thank him for arranging regular ALICE-India Collaboration meetings where I learnt a lot from physics discussions with my colleagues and physicists from different institutes. I am also thankful to Dr. Tapan Nayak for his valuable guidance.

I would also like to thank ALICE Spokesperson, Dr. Federico Antinori. I am grateful to Dr. Jurgen Schukraft for useful discussions regarding the analysis. A vote of thanks to the ALICE collaboration for providing me several opportunities to interact with the experts of this vast sea of particle physics and especially conveners *of PWGCF and PAG-Flow group of ALICE.*

I am extremely thankful to the entire staff of library and purchase section, Department of Physics, Panjab University, for all time support and kind co-operation throughout my research work. I would like to thank Mr. Dinesh Kumar and Mr. Satish Kumar for their endless efforts for official work. Many thanks to G&P section at Admn. block Panjab University Chandigarh. I gratefully acknowledge the financial assistance received from UGC and DST.

I have special words of appreciation and praise for my best friends Dr. Meenu Thakur and Dr. Ankita Mehta for their endless support and love. I can never forget the memorable moments we have shared together during these years. Thanks to both of you for being a shoulder I can always depend upon. I am lucky enough to have best buddies like you. Thanks for your advices, friendship and truckloads of fun.

A sincere thanks to my seniors Dr. Bhanu Sharma and Dr. Deepika Rathee for their guidance and support in the beginning of my Ph.D. My profound appreciation to my fellow colleagues and friends at Panjab University, Anjali Attri, Anjali Sharma, Jagbir Singh, and Sandeep Dudi. I thank all of you for fruitful physics discussions from which I have learnt a lot. Thank you for making friendly environment in the lab. A special thanks to Prabhjot kaur, Dr. Amandeep Kaur kalsi, Dr. Ruchi Mahajan and Dr. Priya Sharma for wonderful time at Physics Department. Thank you Surbhi for being very nice to me. I would like to make a special mention for my friends, Ankita Sharma, Sonia Rajput, Bharti Naik, Dr. Pooja Pareek, Dr. Jitendra Nogia, Dr. Somnath Kar and Dr. Aditya Nath Mishra for their amazing company at CERN as well as during ALICE-India meetings in INDIA.

None of the words are adequate to express my sincere obligation towards my reverend parents whose blessings, limitless love, continuous encouragement and trust made me to come this far. A great compilation of heartfelt thanks to them for teaching me the lessons that books couldn't. There is no way to repay them for unconditional efforts they have made since childhood. I remember with deep affection the *love, care and support of my siblings Neha, Rajni and Sahil. I gratefully remember the endless support, countless blessings, and utmost moral support of my family without which it would not have been possible for me to complete much of what I have done. I love you all.*

Last but not the least, I take pride in acknowledging the Supremacy of God for giving me the strength, courage, good health and capability to accomplish this thesis work satisfactorily.

Date:

Place: Chandigarh **(Sonia Parmar)**

Abstract

At relativistic energies, the heavy-ion collisions provide a unique environment to study the properties of strongly interacting matter known as Quark Gluon Plasma (QGP) created just after the "Big-Bang". To explore the evolution of universe, A Large Ion Collider Experiment has been built at Large Hadron Collider (LHC) at CERN. ALICE is specially optimised for the study of heavy-ion collisions to characterize the properties of the QGP. The study of event-by-event fluctuations is the most effective way to address the properties of QGP matter. It helps to extract the dynamical fluctuations present in the system which might be weaken when studied as averaging over all events in an ensemble. The event-by-event study offers a chance to investigate each and every event, and extracts the rare physical events. The experiments at LHC and RHIC (Relativistic Heavy Ion Collider) provide a high multiplictiy environment to study the fluctuations in physical observables on event-by-event basis. A strong magnetic field created by the fast moving spectator protons induces the electric current that leads to the separation of positively and negatively charged particles along the magnetic field direction resulting in the phenomenon of Chiral Magnetic Effect (CME). The hunting for the existence of CME is possible via charge-dependent particle azimuthal correlation measurements. Several experiments at LHC and RHIC reported the charge separation measurement and the results are qualitatively in agreement with the CME expectations. For the charged-neutral correlation measurement, the STAR has studied the event-by-event fluctuations and found no significant deviation from the generic pion production.

In this thesis, the results on study of charged-neutral fluctuations and charge separation in Pb-Pb collisions at $\sqrt{s_{\rm NN}} = 2.76$ TeV using the ALICE detector at the LHC, are presented. An event-by-event fluctuations in charged-to-neutral particle multiplicities in nuclear-nuclear collisions might be the consequence of formation of DCC domains. The search for the DCC-type domains is performed using the Sliding Window Method (SWM) which locates the unusual charged-to-neutral particle

fraction in an event over the azimuthal plane. The fluctuations in charged neutral particle multiplicties are also measured via variable, $\nu_{dyn}^{\gamma,ch}$ and factorial moments $r_{m,1}$. The simulation study is also performed using the Monte Carlo event generators viz., HIJING and AMPT. Results obtained are compared with those of data and provide a hint for the existence of non-statistical fluctuations in data.

A new method of Sliding Dumbbell is developed to scan the full azimuthal plane to search event-by-event localised charge separation in $\eta - \phi$ phase space. The sum $Db_{\pm}$ of positive charge fraction on one side and negative charge fraction on other side of the dumbbell is computed and its maximum $Db_{\pm}^{max}$ value is obtained by sliding the dumbbell in steps of 1° over the whole azimuthal plane. The $Db_{\pm}^{max}$ distributions in each centrality are further divided into ten bins, where 0-10% corresponds to higher $Db_{\pm}^{max}$ values, while the 90-100% corresponds to lower $Db_{\pm}^{max}$ values. Furthermore, the two- and three- particle azimuthal correlations are investigated in terms of $Db_{\pm}^{max}$ bins to extract the events exhibitng large charge separation to have a sample enriched with CME-type events. The study of charge separation effect using different Monte Carlo event generators is also performed. The particle azimuthal correlations are measured for HIJING and AMPT as a function of centrality as well as for different $Db_{\pm}^{max}$ bins. In order to examine the effect of CME signal, the different percentages of CME signal are introduced in the standard string melting AMPT and performed the detailed study via particle azimuthal correlations. Reasonably very good results are obtained using Sliding Dumbbell Method (SDM) regarding the extraction of CME type signal. SDM is applied to Pb-Pb collision data at $\sqrt{s_{\mathrm{NN}}} = 2.76$ TeV to investigate the event-by-event charge separation. Thus, it is possible to get CME enriched sample events corresponding to top 10%, 20%, and 30% $Db_{\pm}^{max}$ values for 20-30%, 30-50%, and 50-70% collision centralities, respectively. The CME fraction (f_{CME}) is ∼35% in top 10%, 20%, and 30% $Db_{\pm}^{max}$ values in these centralities which corresponds to CME signal ∼ 5-10% in these collision centralities.

Contents

List of Figures

List of Tables

Chapter 1

Relativistic Heavy Ion Collisions

1.1 Introduction

The Standard Model (SM) is a well-tested theoretical framework which describes matter in terms of elementary particles (Fermions) and their interactions (Gauge Bosons) except gravitational one. The fermions are known as leptons and quarks whereas the force carriers of their interactions are the gauge bosons and a higgs boson. In SM, all elementary particles on the basis of their masses and stability, are categorized into three generations. The first generation holds most stable and the lightest particles whereas lesser stable and heavier particles are arranged into second and third generations [1].

Leptons: As stated above three generations or families of leptons are; electron (e), muon (μ) and tau (τ). In each generation, we also have associated neutrinos (ν_e, ν_μ, and ν_τ). In SM, each type of particle is associated to an anti-particle. The corresponding anti-leptons are also arranged into their respective particle generations. In total, we have 12 (6 particles + 6 anti-particles) leptons in SM.

Quarks: There are six types of quarks found in nature and are arranged into three generations: the first generation is made up of the up (u) and the down (d) quarks, the second generation includes the charm (c) and the strange (s) quarks and finally, the third generation contains the top (t) and the bottom (b) quarks.

Similar to leptons, each quark has corresponding anti-quark. Unlike the leptons, quarks come in three colours: Red (r), Blue (b) and Green (g) but physical states are colourless. In other words, only colourless combinations of quarks are stable and exists, for example, a combination of a quark and an anti-quark (known as mesons) or combination of three quarks (known as baryons) exists in nature.

Gauge Bosons: As described above, the force carriers are responsible for the interactions between fundamental particles. Each force has it's own force carrier (gauge boson). In SM, three out of four interactions viz., strong, weak and electromagnetic are included. The force carriers of the strong force, electromagnetic force, and weak force are known as gluon (g), photon (γ) and ($W^{\pm}$ and Z^{0}) bosons, respectively. The g and γ are massless, while $W^{\pm}$ and Z^{0} have masses $\sim 80.38\mathrm{Ge}V^{2}$ and $\sim 91.18\mathrm{Ge}V^{2}$, respectively.

Higgs Boson: The Higgs boson is known for providing mass to all the fundamental particles in SM [2]. The experimental observation of Higgs boson (~126 GeV) in ATLAS and CMS experiments validated the predictions of SM in July 2012 [3, 4].

1.1.1 Quantum Chromodynamics

The Quantum Chromodynamics (QCD) is a theory of strong interactions which explains the interaction between elementary particles [5]. The two important features of QCD are: Quark Confinement and Asymptotic Freedom.

Quark Confinement: It states that a single quark can never be found in an isolated form. When a bound quark pair (meson or baryon) is stretched at large distances, it does not break to multiple single quarks though the potential energy increases up to an extent that a new pair of a quark and an anti-quark forms instead. This therefore, concludes that free quarks do not exist in nature and always confined within the composite particles like mesons and baryons (also known as hadrons).

Asymptotic Freedom: When the partons (quarks and gluons) inside the hadrons come closer to each other at very short distances, the potential energy increases and the coupling strength becomes weaker. The increasing energy at short distance increases the temperature which allows the quarks to move freely inside hadrons and this phenomenon is known as asymptotic freedom [6]. At very high energy density, the QCD predicts the presence of a phase of coloured matter with deconfined quarks, known as Quark Gluon Plasma (QGP).

1.1.2 QCD phase diagram and Quark Gluon Plasma (QGP)

The universe popped out from an explosion named as "*Big-Bang*" which was ultra hot and superdense due to very high energy density and temperature. At that time the temperature was about 10^5 times the temperature in the core of the sun. Figure 1.1 shows the QCD phase diagram of nuclear matter as a function of baryo-chemical potential (μ) and temperature (T) [7]. A phase transition from normal nuclear matter to a deconfined state of quarks and gluons under high temperature and energy density leads to the formation of primordial matter known as Quark Gluon Plasma (QGP). The QGP undergoes an expansion with increasing time and cools down to form stable particles (hadrons).

In order to understand this superdense state of the early universe, powerful atom smasher machines, RHIC [8] and LHC [9] are built at BNL and CERN, respectively. In the laboratory, the transition from normal matter to a QGP state can be achieved through two different scenarios.

- In figure 1.1, a normal nuclear matter exists at $\mu_B \simeq 1$ GeV and $T = 0$. At low temperature ($T \sim 0$) and increasing baryon density (μ_B), the colliding two heavy nuclei at low energy $\sqrt{s_{NN}} \sim 15$ GeV lead to the formation of baryon rich smaller overlap region. The nucleon density increases in small overlap volume such that the nucleons start overlapping and concept of individual

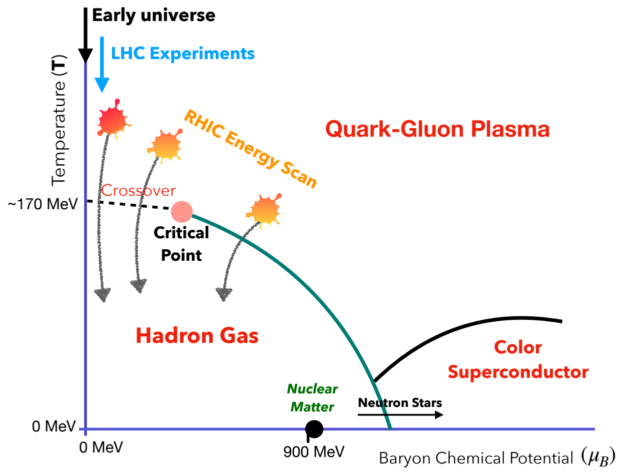

Figure 1.1: QCD phase diagram depicting the variation of Temperature (T) with the Baryon Chemical Potential (μ_B).

nucleons disappears. The quarks are now rushing hither and thither in a larger volume $\sim$ the size of a nucleus. At this stage, quarks do not belong to a particular nucleon and this phase is predicted to be equivalent to the core of neutron stars. The Condensed Baryonic Matter (CBM) experiment [10] at FAIR Germany aims to explore the physics of baryon rich region and the equation of state in this region.

- Another situation arises, if $\mu_B \simeq 0$ and the temperature of the system is increased more than the critical temperature ($T > T_c$), a deconfined state of quarks and gluons formed. The situation can be viewed by clashing two heavy nuclei at much higher energies in such a way that the colliding nucleons pass through each other and slow down the participants resulting in the energy loss that helps to create hot dense baryon free overlap region consisting of quarks and gluons. STAR [11], PHENIX [12], PHOBOS [13] and BRAHMS [14] experiments at Relativistic Heavy Ion Collider (RHIC) BNL and ATLAS [15], ALICE [16] and CMS [17] experiments at Large Hadron Collider (LHC) CERN are investigating the properties of the baryon free QGP matter in this phase of QCD.

1.2 Relativistic Heavy Ion Collisions

The heavy ion collisions provide a unique environment to explore the universe deeply to the level of micro seconds and allow to study the properties of hot dense soup of strongly interacting QGP [18]. The major role of relativistic heavy ion colliders is to recreate the "mini Big-Bang" in the laboratory by smashing highly accelerated (up to TeV energy) heavy nuclei. The two colliding nuclei, travelling at a velocity nearly equal to the speed of light, become Lorentz contracted along the direction of beam axis and can be represented by thin disks. During the collision, an overlap region of almond shape is formed. The nucleons lying in the overlap region are known as "participating nucleons" whereas those do not participate in a collision and lie outside the overlap region are known as "spectator nucleons". The size of the overlap region depends on the type of collision effectively the range of impact parameter (b; defined as the distance between the centres of two colliding nuclei). There are three main categories of collision which describe the type of overlap region. If r1 and r2 are the radii of incoming nuclei 1 and 2, then;

- **Central collision:** It is also known as head-on collision having nearly zero impact parameter $0 \leq b <\mid r1 - r2 \mid$.
- **Semi-central collision:** If impact parameter (b) ranges from $\mid r1-r2 \mid< b < (r1 + r2)$.
- **Peripheral collision:** When the colliding nuclei have minimum overlap or b nearly equals to the sum of radii of two colliding nuclei i.e., $b \simeq (r1 + r2)$.

An overlap region of almond shape is formed and a huge amount of energy is deposited in a relatively small volume for a very small duration of time, resulting in an enormous amount of energy density of the order of $\sim GeV/fm^3$ leads to the formation of QGP. Figure 1.2 depicts the different stages of heavy-ion collision.

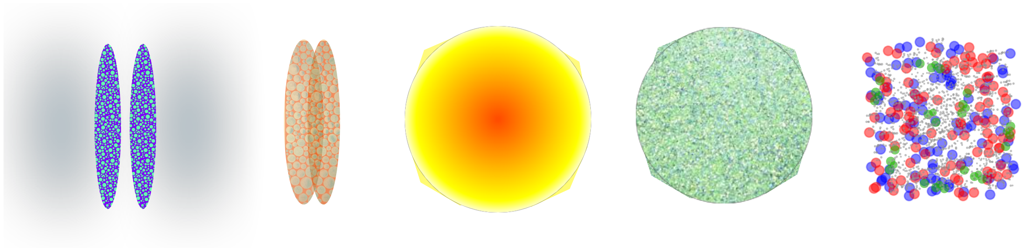

Figure 1.2: The colliding heavy ions depicting various stages of collision.

1.2.1 Space Time Evolution

The space time evolution of heavy-ion collisions is illustrated in figure 1.3. In the center of mass frame, the target nucleus (say A) coming from z = $+\infty$ and projectile nucleus (say B) from z = $-\infty$ with the speed of light collide at time t=0 and z=0 (collision point). After collision, the participating nucleons lose energy in the system and create baryon free overlap region. The large amount of energy is deposited by colliding nucleons. This is the initial stage of collision called "pre-equilibrium" phase which exists at about $< 1fm/c$. After this expansion begins and the system undergoes interactions within partons and a local thermal equilibrium state is achieved where the deconfined state of quarks and gluons (QGP) formed at the temperature 200-300 MeV. After the QGP formation, the system does not go to thermal equilibrium rapidly but a "mixed phase" of partons and hadrons exists.

As the system expands and cools down to the temperature below the critical temperature T_c, hadronization starts to take place. When the fireball further expands, all the inelastic scatterings stop and at this stage, the energy of the system is also not enough to create hadrons. This phase is known as "Chemical Freeze out". Further expansion stops the elastic interactions between hadrons, and system attains a "Kinetic Freeze out" phase. At this stage, the stable particles i.e., hadrons

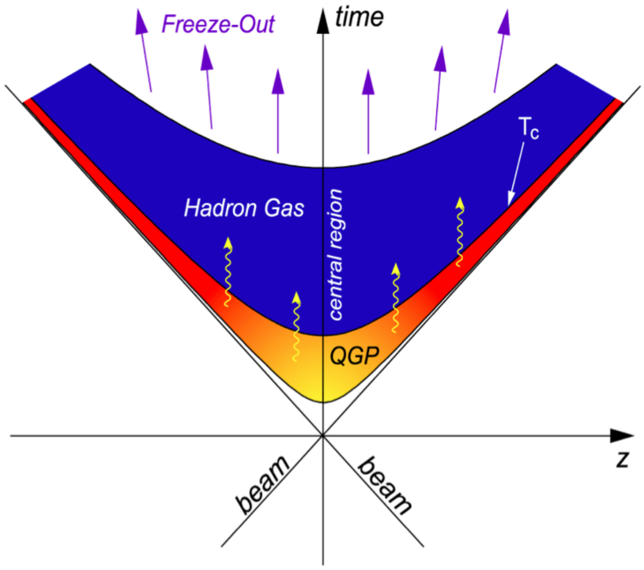

Figure 1.3: The space-time evolution of heavy ion collisions.

come into existence. These produced particles emerge from the fireball and finally hit the detector where they are measured experimentally and studied to probe the features of QGP and other properties of the system.

1.3 Signatures of QGP

Since the direct investigation of the QGP is not possible due to the confinement property of QCD vacuum [19], one needs to study the indirect measurements which could provide the evidence for the QGP formation in early stage of collision. There are various state of art which serve as probes to study the QGP properties.

1.3.1 Net Charge Fluctuations

The fluctuations in the conserved quantities such as, temperature, particle ratio, net-charge, etc., are expected to be sensitive signals for the formation of QGP and the phase transition. The net charge fluctuations depend on the squares of the charges of the system, therefore the fluctuations are smaller in QGP phase (fractional charge) than in hadronic phase (unit charge). Hence the fluctuations are strongly phase dependent. The net-charge fluctuations uses the particle ratio fluctuations ($R = N_+/N_-$) rather than particle fluctuations. This reduces the uncertainties arising from volume fluctuations. The parameter R defines the ratio of positively and negatively charged particles. The correlation between the charged particles is studied using the observable $\nu^{corr}_{+-,dyn}$ as a function of centrality. Furthermore, a key variable used to measure the net-charge fluctuations is the observable D, a measure of charged particle fluctuations per unit entropy, explained below.

$$D = \langle N_{ch} \rangle \langle \delta R^2 \rangle \simeq 4 \frac{\langle \delta Q^2 \rangle}{\langle N_{ch} \rangle} \tag{1.1}$$

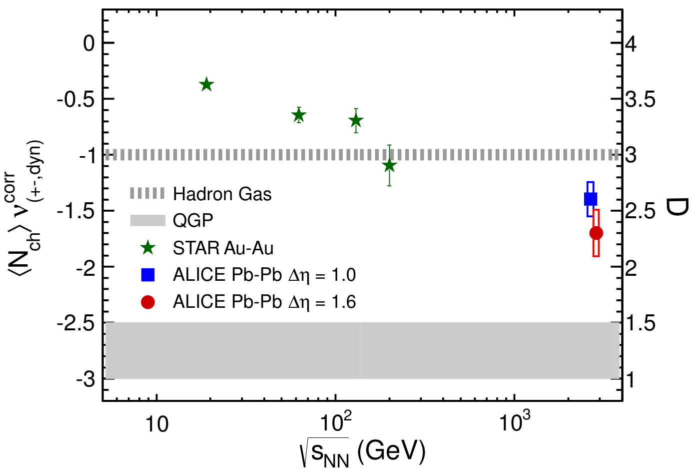

Figure 1.4: Beam energy dependence of net charge fluctuations measured in terms of $\langle N_{ch} \rangle \nu^{corr}_{(+-,dyn)}$ (left axis) and D-measure (right axis) for the most central Pb-Pb collisions.

For a simple case, if the quark-quark interaction is neglected then the value of D is estimated to be 4 times smaller for a QGP phase than HG (Hadron Gas) phase. The Lattice calculations on the other hand produce different estimation for QGP phase than HG because of the presence of quark-quark interactions but the value of D is still smaller than HG. For a particular case of pion gas, the value of D is 4 for uncorrelated pion gas and after including resonance yield, the value reduces to $\simeq 3$. The value of D has been calculated to be in between 1.0 and 1.5 for QGP phase. Thus, the D-measure can be used to differentiate the QGP and HG phase.

The variation of net charge fluctuations has been studied by STAR as a function of beam energy. The ALICE also measured the same for higher energy and compared the results with those of STAR for top central collisions as shown in figure 1.4. A monotonic decrease in dynamic net-charge fluctuations with increase in center of mass energy is observed [20]. The theoretical predictions for the QGP and HG phases are also indicated by bands in same figure 1.4.

1.3.2 Strangeness Enhancement

The study of baryons and anti-baryons production at ultra relativistic energies is another powerful tool to investigate the properties of strongly interacting matter created in heavy-ion collisions. The particle spectra of strange baryons reflects the information about kinetic freeze-out and collective flow. It is predicted that there is an enhancement in the production of strange particles per participant of colliding heavy nuclei than those in nucleon-nucleon collisions [21]. The strangeness enhancement feature can be characterized by factor "E" known as strangeness enhancement factor. It is defined as the ratio of strange particle yield in nuclear-nuclear collisions ($Yield^{AA}$) to the nucleon-nucleon collisions ($Yield^{NN}$) scaled by mean number of participating nucleons $\langle N_{Part}\rangle$.

$$E = \frac{Yield^{AA}/\langle N_{Part}^{AA}\rangle}{Yield^{NN}/\langle N_{Part}^{NN}\rangle} \tag{1.2}$$

where $\langle N_{Part}^{AA}\rangle$ and $\langle N_{Part}^{NN}\rangle$ represent the average number of participants in a nuclear-nuclear and hadronic collisions, respectively. Strangeness enhancement was measured by NA57 at SPS [22], STAR at RHIC [23] and ALICE at LHC [21]. Figure 1.5 presents the yields of strange particles Ξ and Ω as a function of $\langle N_{Part}\rangle$ in Pb-Pb collisions and p-p collisions. Results show that enhancement is larger than unity for all baryons and increases with increase in strange content of corresponding particle. It is also observed that the yields are larger at LHC than those measured at RHIC.

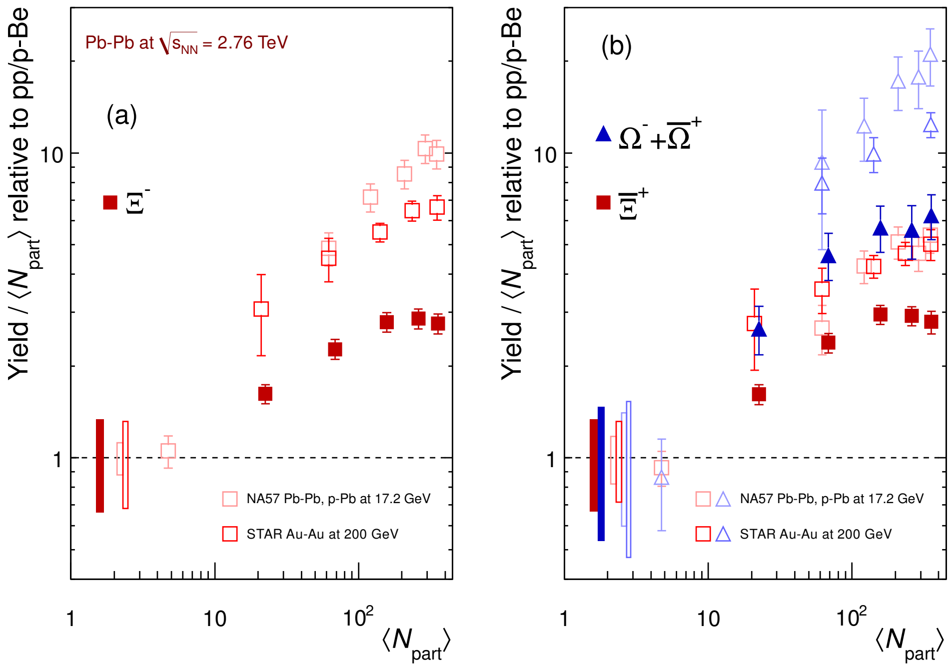

Figure 1.5: Enhancements in multi-strange baryon production in $| y |< 0.5$ for Pb-Pb collisions as a function of mean number of participating nucleons $\langle N_{part} \rangle$ in ALICE (full symbols), STAR and NA57 (open symbols).

1.3.3 Direct Photons

Prompt photon production is one of the direct signatures of the plasma phase created in ultra relativistic heavy-ion collisions. They arise from the colliding partons via hard scattering processes such as; quark, anti-quark pair annihilation ($q\overline{q} \rightarrow \gamma g$), quark(anti-quark)-gluon Compton scattering ($qg \rightarrow q\gamma$, $\overline{q}g \rightarrow \overline{q}\gamma$). Since photons lose energy via electromagnetic interactions only, so they do not interact with the surrounding particles and escape from the hot dense nuclear matter carrying detailed information about the evolution of the medium created after the collision. First attempt of direct photon measurement was performed by WA98 experiment at

CERN SPS in central Pb-Pb collisions at $\sqrt{s}_{\rm NN}$ = 17.3 GeV for transverse momentum range $1.5 < p_T < 4$ GeV/c [24]. The most central collisions (0-10%) exhibited a clear excess of direct photons for $p_T > 1.5$ GeV/c whereas no significant excess has been found in the peripheral collisions. The PHENIX [25] experiment at RHIC and ATLAS [26] and CMS [27] collaborations at LHC confirmed the direct photon production in heavy-ion collisions. ALICE collaboration at CERN also studied the invariant yield of direct photons for 0-20%, 20-40% and 40-50% centrality classes in p_T range $0.9 < p_T < 14$ GeV/c. Figure 1.6 shows the prompt photon spectra for all three centralities and follow the expectation of the pQCD calculations for high $p_T > 5$ GeV/c [28]. It provides no evidence for medium influence on direct photon spectra for $p_T > 5$ GeV/c. At $p_T < 2$ GeV/c, an excess has been found in central and semi-central collisions whereas no signal was observed in peripheral collisions.

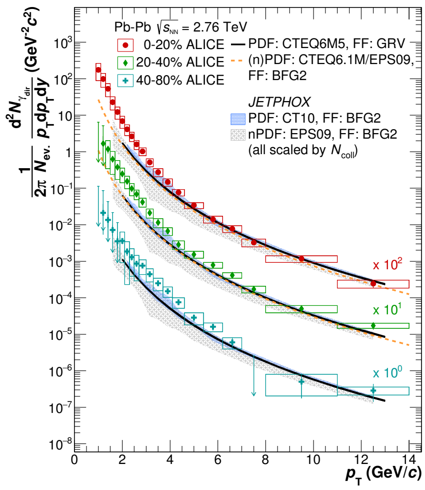

Figure 1.6: Direct photon production yield in Pb-Pb collisions for different centrality classes $0-20\%$, $20-40\%$, and $40-80\%$ and compared to the QCD predictions for pp collisions at $\sqrt{s}_{\rm NN}$ = 2.76 TeV.

1.3.4 Jet Quenching

Jet quenching is one of the important properties of QGP. Hard scattering of partons produces a highly energetic particles which lose their energy by radiating gluons in the hot dense matter created in heavy-ion collisions, resulting in the suppression of high transverse momentum particles. This phenomenon is known as jet quenching. This energy loss provides basic information on thermodynamical and transport properties of the medium [29]. The jet quenching is characterized by an observable known as Nuclear Modification Factor (R_{AA}) which is defined as ratio of high p_T hadronic yield in A-A collisions to the nucleon-nucleon (e.g. p-p) collisions scaled by number of elementary nucleon-nucleon collisions.

$$R_{AA} = \frac{d^2N^{AA}(dp_T d\eta)^{AA}}{T_{AA}d^2\sigma^{NN}(dp_T d\eta)^{NN}} \tag{1.3}$$

Here, $T_{AA} = \langle N_{bin}\rangle/\sigma_{inel}^{NN}$, the $\langle N_{bin}\rangle$ and the σ_{inel}^{NN} are the number of collisions and the inelastic cross-section, respectively.

The STAR [30] and PHENIX [31] experiments at RHIC reported the results on R_{AA} measurements in more central (0-5% and 0-10%) Au+Au collisions at $\sqrt{s}_{\mathrm{NN}}$ = 200 GeV and observed strong suppression of high p_T hadron yields. ALICE also measured the nuclear modification factor R_{AA} for charged hadrons in central Pb-Pb collisions at $\sqrt{s}_{\mathrm{NN}}$ = 2.76 TeV [32] and compared the results with those of STAR and PHENIX as shown in figure 1.7. Results indicate that R_{AA} is less than unity. At p_T = 6-7 GeV/c, a dip in the R_{AA} value is observed for ALICE which is smaller than that at RHIC. A strong suppression at LHC suggests a large energy loss at LHC as compared to RHIC. For high p_T ($> 7GeV/c$), a significant increase in R_{AA} is observed which indicates that the high p_T hadrons lose small amount of energy.

The dihadron angular correlation measurement is another tool to measure jet quenching in heavy-ion collisions. The first attempt to dihadron angular measurement was made at RHIC for Au+Au, d+Au and p+p collisions at $\sqrt{s}_{\mathrm{NN}}$ = 200 GeV. In figure 1.8, the upper plot shows jet azimuthal correlation distributions for central minimum bias d+Au collisions whereas bottom plot indicates the correlation for central Au+Au and minimum bias pp collisions. The away side correlations get

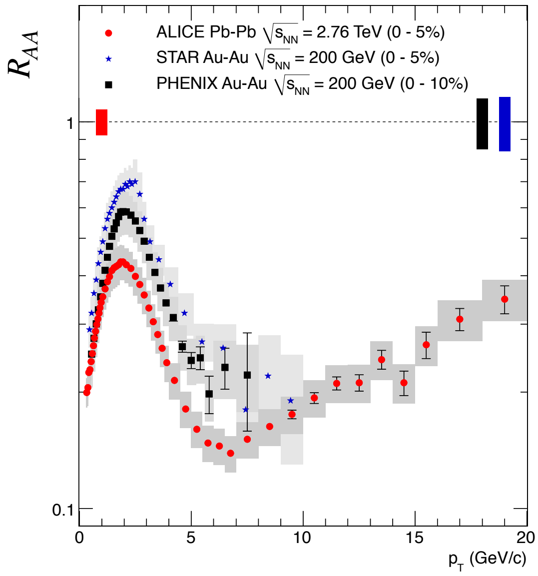

Figure 1.7: The R_{AA} yield for central Pb-Pb collisions at LHC at $\sqrt{s}_{\rm NN}$ = 2.76 TeV is compared to the same measurement at RHIC in Au+Au collisions at $\sqrt{s}_{\rm NN}$ = 200 GeV and observed a strong suppression at LHC energy.

quenched in Au+Au data indicating high suppression while no away side quenching effect has been found for d+Au and pp collision systems [33, 34].

1.3.5 Azimuthal Anisotropy

Azimuthal distribution of the produced particles in heavy-ion collisions is expected to provide information about the reaction dynamics and the equation of state (EOS) at extreme conditions of temperature and energy densities. In case of non-central collisions, because of the partial overlap of target and projectile nuclei, the almond shaped spatially asymmetric region is formed. The flow of particles is expected along transverse plane (x-y plane) due to the non-zero impact parameter and the beam (longitudinal) direction is considered along z-axis for the convention. The x-z plane is defined as a reaction plane, formed by impact parameter vector and the beam direction. The spatial asymmetry exhibits multiple collisions and due to larger pressure gradient along minor axis, the spatially asymmetric distribution

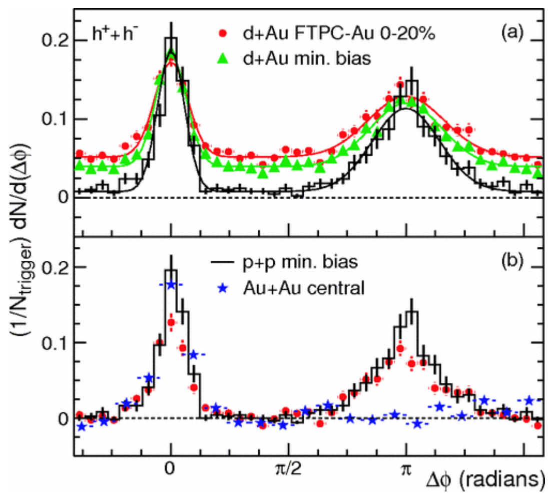

Figure 1.8: Dihadron azimuthal correlation distributions for central d+Au and minimum bias events are compared in plot (a) while in plot (b) a comparison of minimum bias pp collision events is shown with d+Au central events indicating the suppression of away side correlations peak.

transforms into momentum anisotropy. Figure 1.9 depicts the collision geometry in non-central heavy-ion collisions. The observation of anisotropic flow is the direct experimental evidence of flow coming from the particle momentum distributions w.r.t. the reaction plane.

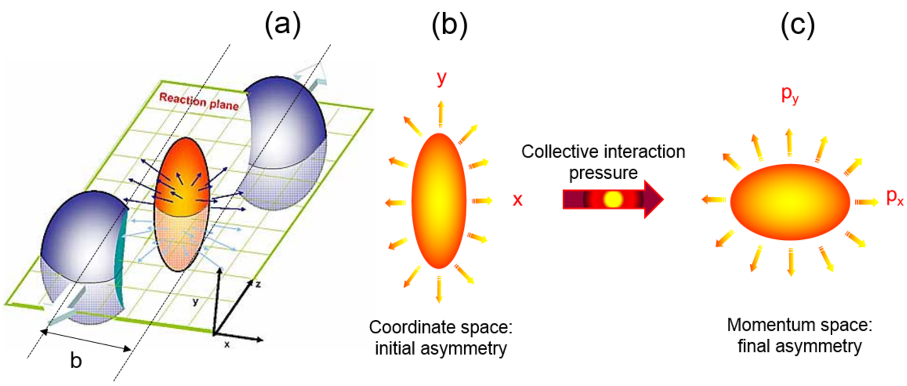

Figure 1.9: Collision geometry in non-central collisions depicting initial-state anisotrpoy converting into momentum anisotropy in the overlap zone.

In order to characterize various patterns of anisotropic flow, Fourier harmonics [35] have been used,

$$E\frac{d^3N}{d^3p} = \frac{1}{2\pi}\frac{d^2N}{p_t dp_t dy}(1 + 2\sum_{n=1}^{\infty} v_n cos[n(\phi - \Psi_{RP})]) \tag{1.4}$$

where E, p, p_t, ϕ, y, and Ψ_{RP} are the energy, momentum, transverse momentum, azimuthal angle, rapidity and the reaction plane angle, respectively. Above equation includes cosine term only because sine term vanishes due to the reflection symmetry w.r.t reaction plane. The flow coefficients can be written as,

$$v_n = \langle cos(n(\phi - \Psi_{RP}))\rangle \tag{1.5}$$

where, v_n is nth harmonic coefficient, ϕ is the azimuthal angle and Ψ_{RP} is the reaction plane angle of that event. The angular brackets represent an average over all the particles in an event followed by average over all events. The different harmonics of Fourier coefficients reflect different type of flow. First two harmonics, n=1 and 2 play an important role in anisotropic flow and are known as "Directed Flow" and "Elliptic Flow", respectively. Flow analysis sheds light on many aspects such as initial conditions, EOS, thermal equilibrium, evolution of the system, and freeze-out properties of the system.

1.3.5.1 Elliptic Flow

The second order harmonic, elliptic flow (v_2) measurements provide constraints on the equation of state and transport properties of QGP. The magnitude of v_2 depends on the properties of the medium as well as it is related to initial anisotropy in the geometry of colliding system. Since elliptic flow is expected to form at early time and survives till hadronization, so the measurement carries a detailed information of the partonic and hadronic level interactions.

RHIC and LHC measured v_2 and compared the results with various hydrodynamical models. The results of the measurement proved that the QGP has been formed in the early stages of the collision and behaves like an ideal fluid. The flow

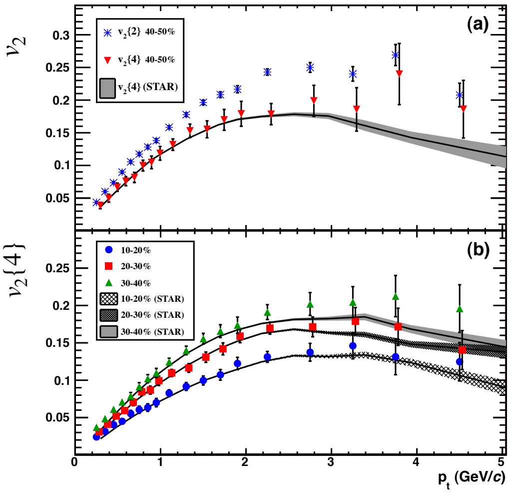

Figure 1.10: Transverse momentum p_T dependence of v_2 in Pb-Pb collisions at $\sqrt{s}_{\mathrm{NN}} = 2.76$ TeV for centrality $40-50\%$ (top) and $v_2\{4\}(p_T)$ for different centralities (bottom) are compared with the STAR v_2 measurements at $\sqrt{s}_{\mathrm{NN}} = 200$ GeV shown by shaded bands.

anisotropy provides information on the geometry of the initial density distributions via various symmetric (Cu+Cu, Au+Au, U+U) as well as asymmetric collisions (Cu+Au) at RHIC. Figure 1.10 represents the first measurement of elliptic flow reported by ALICE collaboration in Pb-Pb collisions at center of mass energy 2.76 TeV during the first run of heavy ions at LHC [36]. The p_t differential elliptic flow as a function of collision centrality has been estimated using 2- and 4- particle cumulant method [37]. Figure 1.10 (top) shows $v_2(p_t)$ for 40-50% centrality and the shaded area represents the STAR measurement for the same centrality in Au+Au collisions at $\sqrt{s}_{\mathrm{NN}} = 200$ GeV [38]. The $v_2(p_t)$ values do not change within uncertainties for both ALICE and STAR. Figure 1.10 (bottom) compares the $v_2\{4\}(p_t)$ obtained using cumulant method for three different centralities at LHC with those of STAR results at RHIC. A reasonably good agreement has been observed in both measurements.

The energy dependence of integrated v_2 has also been studied. The ideal hydrodynamic model calculations predicted an increase in v_2 with increase in beam energy.

The results from different experiments are combined to observe the behaviour of v_2 versus center of mass energy. Figure 1.11 shows a continuous increase in v_2 while going towards higher energies and an increase of ∼10-30% has been observed when energy goes from $\sqrt{s_{\mathrm{NN}}}$ = 200 GeV (at RHIC) to 2.76 TeV (at LHC). The reason for larger integrated v_2 at LHC is due to an increase in mean p_T ($\langle p_T \rangle$) of charged hadrons.

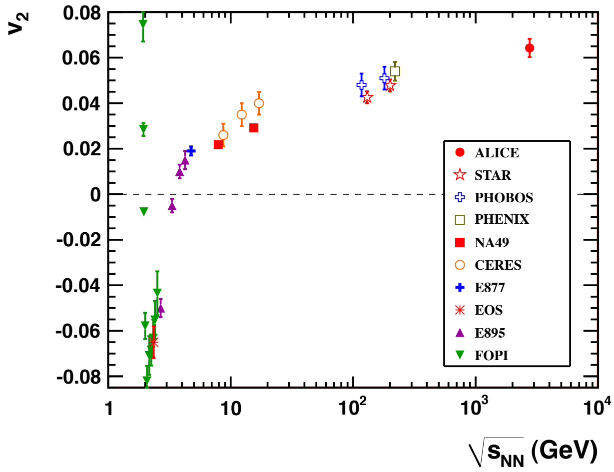

Figure 1.11: Energy dependence of integrated elliptic flow (v_2) in Pb-Pb at $\sqrt{s_{\mathrm{NN}}}$ = 2.76 TeV for central collision of $20 - 30\%$ is compared to the results for similar centrality from different experiments at lower energies.

1.4 Event-by-Event Physics

The origin of event-by-event fluctuations can be due to the deviation of mean value of an observable measured in an event instead of averaging the observable over all events in an ensemble. The study of event-by-event fluctuations helps to extract any kind of non-statistical fluctuations present in the system which might get diluted due to the averaging over all events. The dynamical fluctuations can provide the information about the collective phenomenon, such as the Quark Gluon Plasma formed in heavy ion collisions at relativistic energies. It is expected that the dynamical fluctuations may be formed in some events but not in others. Thus it is very important to study the experimental data on event-by-event basis to search for the non-statistical fluctuations [39]. Ultra relativistic heavy ion collisions at RHIC and LHC produce large number of particles per event which provides a remarkable opportunity to extract new physics by studying the fluctuations in physical observables on an event-by-event basis. For this thesis work, we are studying the event-by-event charge separation effect in heavy ion collisions to identify the non-statistical fluctuations via charge-dependent multi particle azimuthal correlations.

1.4.1 Chiral Magnetic Effect

During the collision, a fireball is formed by participating nucleons leaving the spectator nucleons aside. The spectator nucleons generate a strong magnetic field which induces the electric current that causes the separation of positively and negatively charged particles along the direction of magnetic field and parallel to system's orbital angular momentum direction as shown in figure 1.12. This phenomenon is known as "Chiral Magnetic Effect (CME)" [40, 41]. The two main ingredients needed for the CME in heavy-ion collisions are: an external magnetic field and a localized non-zero axial charge density. In heavy ion collision of two nuclei, the moving spectators produce highly strong magnetic field ($B = 10^{15}T$). Another requirement is a non-vanishing axial charge density in a localized region that can also be created in the interaction zone. The CME also depends upon the strength and duration of magnetic field [42]. It is argued in ref. [43] that the strength of CME signal decreases gradually at higher energies due to the fact that magnetic field develops and decays in very shot interval of time. Voloshin estimated the CME signal from measurements relative to the participants and spectator flow planes [44]. Thus the event-by-event study of multi-particle correlations is the possible way to estimate the CME signal [45]. In this thesis, the two- and three- particle azimuthal correlations have been studied to observe the charge separation effect.

The charge-dependent two particle azimuthal correlator $\delta_{\alpha,\beta}$ is defined as,

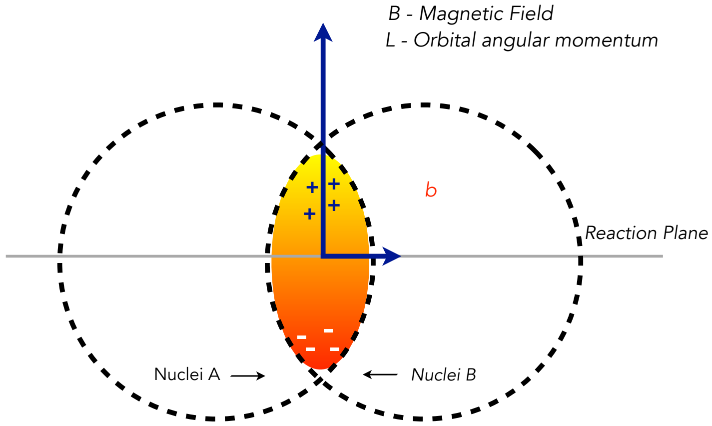

Figure 1.12: Non-central heavy-ion collisions depicting the emission of positively and negatively charged particles perpendicular to the reaction plane.

$$\delta_{\alpha\beta} = \langle cos(\phi_\alpha - \phi_\beta)\rangle = \langle cos(\Delta\phi_\alpha)cos(\Delta\phi_\beta)\rangle + \langle sin(\Delta\phi_\alpha)sin(\Delta\phi_\beta)\rangle \tag{1.6}$$

where $\Delta\phi = \phi - \Psi_{RP}$, is the azimuthal angle and Ψ_{RP} is the reaction plane angle spanned by the beam axis and the impact parameter vector of the collision. A schematic diagram of collision geometry for non-central collisions is shown in figure 1.13. The azimuthal angles and reaction plane are also represented in the same. The computation of reaction plane angle (Ψ_{RP}) is not possible. Thus the event plane angle is measured which is the estimation of reaction plane angle. The two particle correlator is not a good choice to study the CME because it includes strong contribution from "non-flow" effects along with the signal contribution. These non-flow correlations are not related to the azimuthal asymmetry in the initial geometry but come from the resonance decays and jet-correlations.

In order to quantify the CME contribution, the three particle correlator related to reaction plane is used [46] and is expressed as,

$$\gamma_{\alpha\beta} = \langle cos(\phi_\alpha + \phi_\beta - 2\Psi_{RP})\rangle = \langle cos(\Delta\phi_\alpha)cos(\Delta\phi_\beta)\rangle - \langle sin(\Delta\phi_\alpha)sin(\Delta\phi_\beta)\rangle \tag{1.7}$$

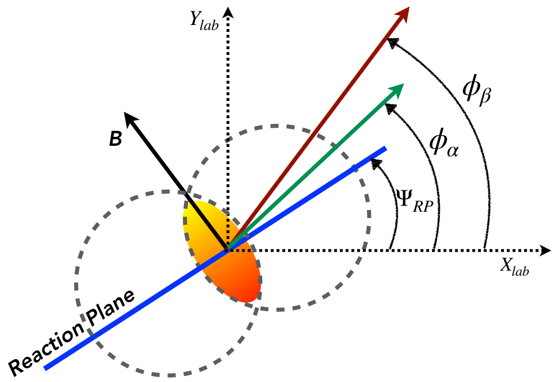

Figure 1.13: Schematic view of collision geometry of non-central nuclear collisions showing the azimuthal angles of produced particles in the transverse plane.

The three particle correlator $\gamma_{\alpha\beta}$ is the difference between in-plane (correlation projected onto the reaction plane) and out-of-plane correlations (parallel to the reaction plane) as shown in Eq. 1.7.

Instead of obtaining the reaction plane angle, the Eq. 1.7 can be alternatively evaluated using three particle correlator and is written as,

$$\gamma_{\alpha\beta} = \langle cos(\phi_\alpha + \phi_\beta - 2\Psi_{RP})\rangle = \frac{\langle cos(\phi_\alpha + \phi_\beta - 2\phi_\gamma)\rangle}{v_{2,\gamma}} \tag{1.8}$$

where $v_{2,\gamma}$ represents the elliptic flow of third particle i.e., γ. The observation of the CME includes a large part of observed correlations as a background correlations due to the background sources, such as statistical fluctuations, flow, transverse momentum conservation [47], resonance decays [48], etc. These sources can produce the effect similar to the charge separation w.r.t the reaction plane. In order to gain access to the CME signal one has to suppress the background correlations which are independent from the reaction plane orientation while the source of CME signal are strongly coupled to the orientation of reaction plane. Thus the reaction plane dependent charged-pair correlations are sensitive observables for the estimation of CME signal.

1.4.1.1 Results on Charge-dependent Azimuthal Correlations

The charge-dependent azimuthal correlations have been analyzed for the search of different chiral effects in different centrality intervals. The differential measurement of charge dependent azimuthal correlations as a function of transverse momentum (p_T), and pseudorapidity (η) are also studied by several major collaborations, including STAR, PHENIX, ALICE and CMS to understand the charge separation effect in heavy-ion collisions.

- **Centrality dependence:** STAR collaboration at RHIC performed the first measurement on azimuthal correlations of charged-pairs and found qualitative agreement with the expectations for the CME. Results from STAR data on charge dependent correlator at $\sqrt{s_{\mathrm{NN}}}$ = 200 GeV in Au+Au and at 62.4 GeV in Cu+Cu collisions for different centralities exhibit negative values for same sign (SS) charge pairs and mildly positive for opposite sign (OS) charge pairs shown in figure 1.14 (left) [49, 50]. Since the OS pairs are expected to move away from each other resulting in a weak correlation between them as they traverse the entire overlap region while the SS pairs going in same direction exhibit strong correlation among themselves. Thus the STAR data show a first evidence for the CME-type effect. ALICE collaboration also reported the estimation of charge dependent azimuthal correlation functions at $\sqrt{s_{\mathrm{NN}}}$ = 2.76 TeV in Pb-Pb collisions. ALICE measured the three particle charge dependent correlation $\gamma_{\alpha\beta}$ as a function of collision centrality and exhibit the similar trend for SS and OS charge pairs shown in figure 1.14 (right) [51]. The results agree with the STAR measurement for both SS and OS charge pairs.

  The CMS experiment at LHC also studied the charge-dependent azimuthal correlations in p-Pb and Pb-Pb collision systems for the search of CME signal [52]. Figure 1.15 presents the centrality dependence of SS and OS charge pairs for Pb-Pb collisions at $\sqrt{s_{\mathrm{NN}}}$ = 5.02 TeV. The ALICE and STAR data

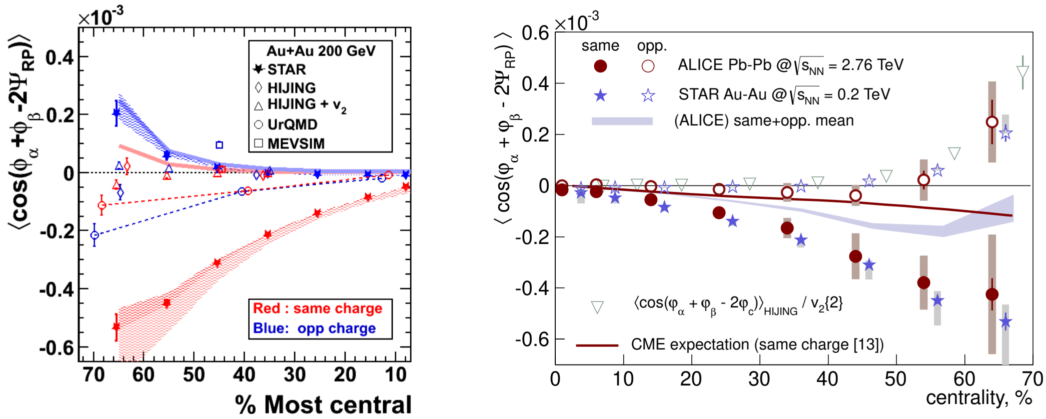

Figure 1.14: Centrality dependence of γ- correlator ($\langle cos(\phi_a + \phi_b - 2\Psi_{RP})\rangle$) for Cu+Cu and Au+Au collisions in STAR at RHIC for different charge combinations (++, - -, + -) at $\sqrt{s}_{\mathrm{NN}}$ = 200 GeV (left) and for Pb-Pb collisions in ALICE at $\sqrt{s}_{\mathrm{NN}}$ = 2.76 TeV (right). Also γ values are compared with those of STAR measurements.

points at center of mass energies 2.76 TeV and 200 GeV, respectively are also presented in figure 1.15 for comparison. No significant collision energy dependence is observed in going from top RHIC to LHC energies. The large difference in the γ-values for CMS results compared to other experiments, in peripheral collisions, is due to the different pseudorapidity acceptance of concerned particles.

- **Beam Energy dependence:** The STAR experiment reported the beam energy dependence of three particle correlator (γ) for different charge combinations (++, - -, + -) as a function of collision centrality in Au+Au collision data, at different center of mass energies $\sqrt{s}_{\mathrm{NN}}$ = 7.7 GeV, 11.5 GeV, 19.6 GeV, 27 GeV, 39 GeV, 62.4 GeV and 200 GeV as shown in figure 1.16 [53]. At lower collision energies, the difference between OS and SS γ-correlator seems to vanish whereas as going towards higher beam energies, a significant difference has been observed manifesting charge separation fluctuations. ALICE results for three particle correlator relative to reaction plane in Pb-Pb collisions at $\sqrt{s}_{\mathrm{NN}}$ = 2.76 TeV is added to the STAR measurement for complete scan of

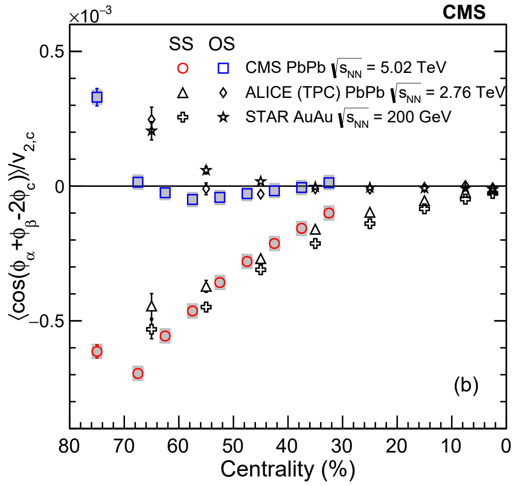

Figure 1.15: Centrality dependence of γ- correlator ($\langle cos(\phi_a + \phi_b - 2\phi_c)\rangle/v_{2,c}$) for Pb+Pb collisions in CMS at $\sqrt{s_{\rm NN}}$ = 5.02 TeV. ALICE and STAR data are also displayed for comparison.

energy dependence.

- **Confidence Limit on CME fraction:** The Event Shape Engineering technique has been adopted by ALICE collaboration to analyze the two- and three- particle azimuthal correlations in Pb-Pb collisions at $\sqrt{s_{\rm NN}}$ = 2.76 TeV. The selection of event shape classes is based on the second order reduced flow vector q_2 and the selection criteria has been discussed in ref. [54]. The centrality dependence of charge dependent azimuthal correlations for different event shape classes has been performed in the p_T range $0.2 < p_T < 5.0$ GeV/c and η range $-0.8 < \eta < 0.8$ for $0 - 60\%$ centrality interval. It is observed that the two particle correlator ($\delta_{\alpha\beta}$) is independent of v_2 within the centrality whereas the three particle correlator ($\gamma_{\alpha\beta}$) for different charge combinations (- -, ++, and + -) scales linearly with v_2 in each centrality. The three particle correlator is considered as the evidence for CME but the v_2 dependence of measured three particle correlator indicates large background effects i.e., non-CME contribution to the estimated correlator. An upper limit to the CME fraction is reported to be $26-33\%$ at the 95% confidence level in the centrality

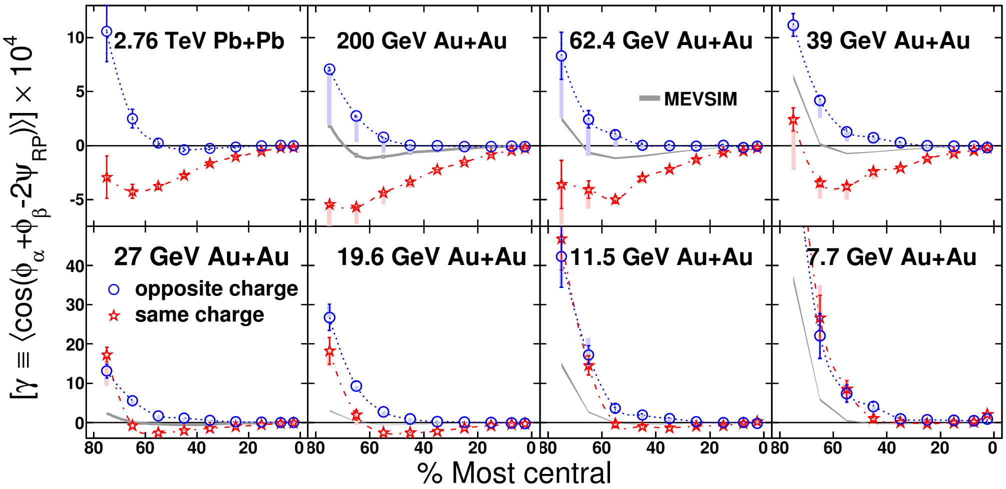

Figure 1.16: Beam energy dependence of γ- correlator as a function of collision centrality for OS (+ -) and SS (++, - -) charge pairs for Au+Au collisions at RHIC energies 7.7-200 GeV and for Pb+Pb collisions at LHC energy 2.76 TeV.

range $10 - 50\%$ [54].

1.4.2 Charged-to-Neutral Fluctuations

A large fluctuations in charged hadron versus neutral photon production in central heavy-ion collisions have been predicted as one of the consequences of chiral symmetry restoration. It has been expected that the hot dense matter created at relativistic energy may provide the physical conditions necessary for the formation of DCC (Disoriented Chiral Condensate) domains. As the temperature decreases the chiral condensate gets aligned and starts emitting coherent pions. The distribution of neutral to charged pion ratio is very different from the general pion distribution which are emitted incoherently [55]. The events with large fluctuations in charged and neutral particles were first observed by JACEE Collaboration [56] and found the exotic events with large neutral to charged particle ratio. The WA98 experiment at CERN studied the relative production of charged and neutral particle multiplicities in high-energy nuclear collisions [57]. The D0 [58], CDF [59], and MINIMAX [60] collaborations in hadronic collisions at Tevatron and NA49 [61] at CERN SPS also

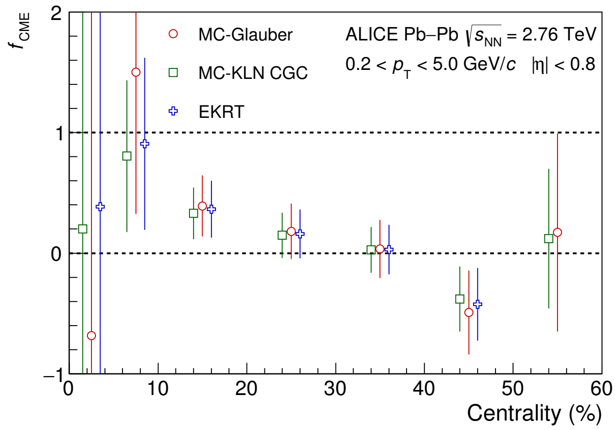

Figure 1.17: Centrality dependence of the fraction contribution to CME signal for Pb-Pb data at 2.76 TeV extracted from fit to data and different models. The upper limit for CME fraction found to be 26-33% at 95% CL for $10-50\%$ centrality.

searched for the unusual events of DCC type in nucleus-nucleus collisions.

1.4.2.1 Results on Charged-Neutral Fluctuations

The dynamical fluctuations in neutral charged particles have been measured by STAR collaboration using the observable ν_{dyn} [62] and bivariate factorial moment method $r_{m,1}$ [60] as a measure of correlation.

- **Global Event Analysis:** The STAR experiment estimated the charged-to-neutral fluctuations using ν_{dyn} as a function of average multiplicity at $\sqrt{s_{\mathrm{NN}}}$ = 200 GeV Au+Au collisions. The observable ν_{dyn} is defined as,

$$\nu_{dyn} = \frac{\langle N_\gamma(N_\gamma-1)\rangle}{\langle N_\gamma\rangle^2} + \frac{\langle N_{ch}(N_{ch}-1)\rangle}{\langle N_{ch}\rangle^2} - 2\frac{\langle N_\gamma N_{ch}\rangle}{\langle N_\gamma\rangle\langle N_{ch}\rangle} \quad (1.9)$$

  where the first two terms correspond to charged particle (N_{ch}) and photon number (N_γ) fluctuations and the third term is the correlation between charged and neutral particles. The angle brackets $\langle ... \rangle$ represent the average over all the events. The ν_{dyn} exhibits scaling behaviour as $\sim 1/\sqrt{\langle N_{ch} N_\gamma \rangle}$, for STAR data and matches with the Central Limit Theorem (CLT) expectation [63]. The results from data are compared with Mixed Events as well as with simulations obtained using HIJING and HIJING+GEANT. The non-statistical fluctuations have been observed in significant amount in data compared to others. Factorial Moments $r_{m,1}$ have also been measured for the $\gamma - ch$ correlation and its deviation from the regular pion production mechanism. The STAR $r_{m,1}$ results as a function of higher moments m exhibit different trend for data when compared to Mixed Events and simulations (HIJING, HIJING+GEANT) as shown in figure 1.18 (right). The multiplicity dependence of $r_{m,1}$ in most central collisions exhibit lower values than those observed by models indicating deviation from the generic pion production in real data [64].

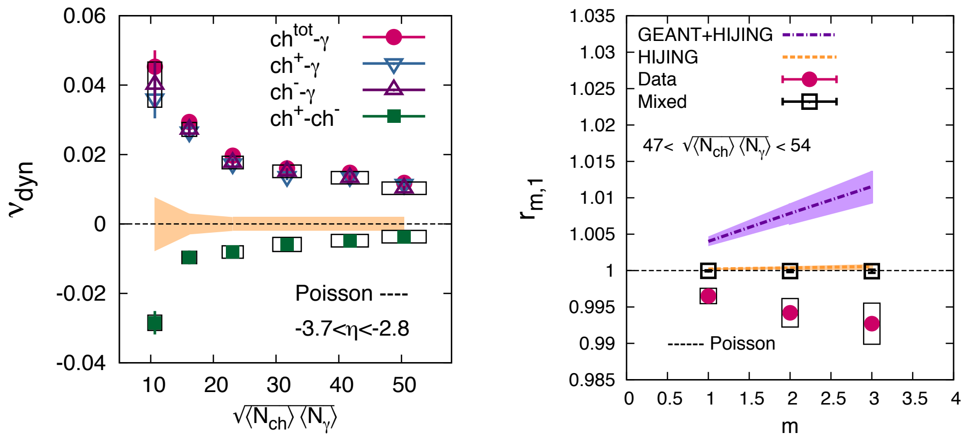

Figure 1.18: *Left:* Average multiplicity $\sqrt{\langle N_{ch} N_\gamma}$ dependence of observable $\nu_{dyn}^{\gamma-ch}$ for data and mixed event showing strong dependence on centrality. *Right:* $r_{m,1}^{\gamma-ch}$ variation with m for data and mixed events is shown where data points (pink markers) are below 1 and exhibit decreasing trend for higher moments. The dashed line for Poisson limit is shown in both plots.

- **Localized Analysis method:** For the first time JACEE Cosmic ray experiment searched a large fluctuations in charged to neutral particle production in a localized region of azimuthal plane [56]. The experiment observed a large number of neutral particles compared to charged particles and the ratio was around 36:1 i.e., 36 neutral and only 1 charged particle in a localized phase-space region. Events with excess of charged particles ($N_{ch} >> N_{\gamma}$) are named as "Centauro events" and if the density of photon like particles is more ($N_{\gamma} >> N_{ch}$) then the events are known as "Anti-centauro events". The DCC-like fluctuations have also been studied by WA98 collaboration in Pb+Pb collisions at 158A GeV at CERN SPS using the Discrete Wavelet Transform (DWT) technique [65]. The analysis results were compared with several mixed event techniques and no correlation was observed between charged and neutral particles. An upper limit has been set for the existence of non-statistical DCC-like fluctuations in different $\Delta\phi$ windows. The value for the upper limit is 10^{-2} for $\Delta\phi = 45-90^{\circ}$ and 3×10^{-3} for $90-135^{\circ}$. The variation of neutral pion fraction f ($= N_{\pi^{\circ}}/N_{\pi^{\circ}} + N_{\pi^{\pm}}$) has been estimated in common ($\eta - \phi$) phase space using a Sliding Window Method (SWM) [66]. This method scans the whole azimuthal plane to locate all the regions with large and small values of neutral pion fraction. The results obtained are compared with mixed events to check the sensitivity of the SWM. The f distribution is shown in figure 1.19 (top) for the 5% most central Pb+Pb collision data. A mixed event distribution is also shown in the same figure (represented by solid line) and fitted using a Gaussian function. The data and mixed events have asymmetric distributions and go toward higher $f-$values as shown in figure 1.19 (top). The ratio plot in figure 1.19 (bottom) observed that the distributions are broader in real data than mixed events indicating frequent occurrence of small and large fraction (f) values [67]. These small and large $f-$values represent the *"charge-excess"* and *"photon-excess"* events.

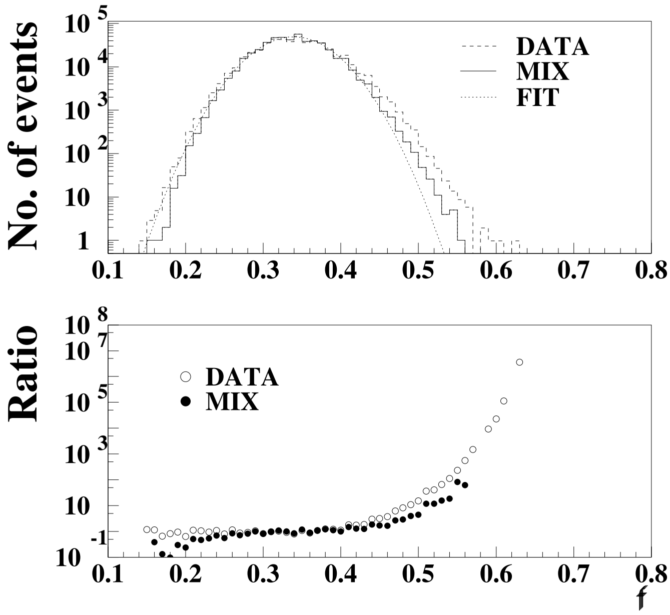

Figure 1.19: *Top:* The fraction (f) distributions in most central Pb-Pb collisions for data and mixed events exhibit different trend than a Gaussian fit function. *Bottom:* The ratio of data to fit function and mixed event to fit function for f distributions are studied and observed broader distributions in data.

1.5 Organization of thesis

This thesis presents the study of event-by-event charge separation and charge neutral fluctuations in ultra relativistic high energy heavy ion collisions. The results presented in this thesis are measured for Pb-Pb collision events recorded by ALICE experiment at $\sqrt{s_{\rm NN}}$ = 2.76 TeV. In total, there are 5 chapters in this thesis. Introduction of relativistic heavy-ion collisions and the experimental signatures of the QGP as well as the recent measurements performed by various experiments are given in chapter 1. The motivation to this thesis work is also reported at the end of the chapter. Sub-detectors of the ALICE experiment and a brief discussion about the sub-detectors used in current analysis are given in 2nd chapter. The detailed description of subsystems used in charge-neutral fluctuation analysis, methodology and the results obtained from data and Monte Carlo models are presented in chapter 3. Details of the analysis strategy and the simulation study of charge separation measurement using different Monte Carlo models (HIJING and AMPT) are described in chapter 4. Event-by-event charge separation results and its physics implications are presented in chapter 5.

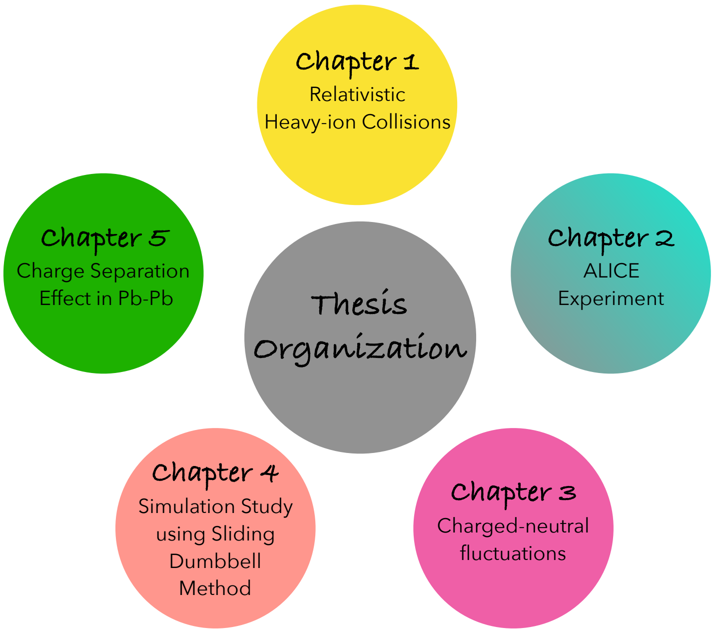

Figure 1.20: Pictorial view of thesis organization.

Bibliography

[1] W.N. Cottingham, and D.A. Greenwood, “An Introduction of the Standard Model of Particle Physics”, Cambridge University Press (2017).

[2] P.W. Higgs, “Broken Symmetries and the Masses of Gauge Bosons”, Phys. Rev. Lett. **13**, 508 (1964).

[3] ATLAS collaboration, G. Ad *et al.*, “Observation of a New Particle in the Search for the Standard Model Higgs Boson with the ATLAS detector at the LHC”, Phys. Lett. B **1**, 716 (2012).

[4] CMS collaboration, S. Chatrchyan *et al.*, “Observation of a New Boson at a Mass of 125 GeV with the CMS Experiment at the LHC”, Phys. Lett. B **30**, 716 (2012).

[5] M.G. Alford, “QCD at high density / temperature”, Nucl. Phys. Proc. Suppl. **117**, 65 (2003).

[6] H. Fritzsch, M. Gell-mann, and H. Leutwyler, “Advantages of the Color Octet Gluon Picture”, Phys. Lett. B **47**, 365 (1973).

[7] M. Cheng *et al.*, “The transition temperature in QCD”, Phys. Rev. D **74**, 054507 (2006).

[8] M. Harrison, T. Ludlam, and S. Ozaki, Nucl. Instr. Meth. A **499**, 235 (2003), http://www.bnl.gov/rhic/.

[9] O.S. Bruning *et al.*, “LHC Design Report”, CERN-2004-003-V-1 (2004).

[10] CBM collaboration, “Technical Design Report for the CBM”, (2013).

[11] STAR collaboration, “Conceptual Design Report for the solenoidal tracker at RHIC”, PUB-5347.

[12] PHENIX Collaboration, “PHENIX Experiment at RHIC - Preliminary Conceptual Design Report”, (1992).

[13] PHOBOS Collaboration, “The PHOBOS experiment at the RHIC and AGS”, Nucl. Phys. A **566**, 305 (1994).

[14] BRAHMS Collaboration, “Conceptual Design Report for the BRAHMS Experiment”, BNL-62018 (1995).

[15] ATLAS collaboration, “ATLAS Detector and Physics Performance”, Volume I and II, CERN/LHCC 99 (1999).

[16] ALICE collaboration, B. Alessandro et. al., “ALICE:Physics Performance Report, Volume II”, J. Phys. G **32**, 1295 (2006).

[17] CMS collaboration, “CMS Physics TDR”, Volume I CERN-LHCC-2006-001 (2006).

[18] G. Roland, K. Safarik, and P. Steinberg, “Heavy-ion collisions at the LHC”, Prog. in Part. and Nucl. Phys **77**, 70 (2014).

[19] H. Fritzsch, M. Gell-mann, and H. Leutwyler, “Advantages of the Color Octet Gluon Picture”, Phys. Lett. B **47**, 365 (1973).

[20] ALICE collaboration, B. Abelev *et al.*, “Net-charge fluctuations in Pb-Pb collisions at $\sqrt{s}_{\rm NN} = 2.76$ TeV”, Phys. Rev. Lett. **110**, 152301 (2013).

[21] ALICE collaboration, B. Abelev *et al.*, "Multi-strange baryon production at mid-rapidity in Pb-Pb collisions at $\sqrt{s}_{\mathrm{NN}} = 2.76$ TeV", Phys. Lett. B **728**, 216 (2014).

[22] NA57 collaboration, F. Antinori *et al.*, "Enhancement of hyperon production at central rapidity in 158 A GeV/c Pb-Pb collisions", J. Phys. G **32**, 427 (2006).

[23] STAR collaboration, B.I. Abelev *et al.*, "Enhanced strange baryon production in Au+Au collisions compared to p+p at $\sqrt{s}_{\mathrm{NN}} = 200$ GeV", Phys. Rev. C **77** 044908 (2008).

[24] WA98 Collaboration, M.M. Aggarwal *et al.*, "Observation of direct photons in central 158 A GeV Pb-Pb collisions", Phys. Rev. Lett. **85**, 3595 (200).

[25] PHENIX collaboration, S. Afanasiev *et al.*, "Measurement of direct photons in Au+Au collisions at $\sqrt{s}_{\mathrm{NN}} = 200$ GeV", Phys. Rev. Lett. **109**, 152302 (2012).

[26] ATLAS collaboration, "Centrality, rapidity and transverse momentum dependence of isolated photon production in lead-lead collisions at $\sqrt{s}_{\mathrm{NN}} = 2.76$ TeV measured with the ATLAS detector", Phys. Rev. C **93**, 034914 (2016).

[27] CMS collaboration, S. Chatrchyan *et al.*, "Measurement of isolated photon production in pp and Pb-Pb collisions", Phys. Lett. B **710**, 256 (2012).

[28] ALICE collaboration, J. Adam *et al.*, "Direct photon production in Pb-Pb collisions at $\sqrt{s}_{\mathrm{NN}} = 2.76$ TeV", Phys. Lett. B **754**, 235 (2016).

[29] I Edmond *et al.*, "Jet quenching parameter in an expanding QCD plasma",Phys. Lett. B **786**, 288 (2018).

[30] STAR collaboration, L. Adamczyk *et al.*, "Measurements of jet quenching with semi-inclusive hadron+jet distributions in Au+Au collisions at $\sqrt{s}_{\mathrm{NN}} = 200$ GeV", Phys. Rev. C **96**, 024905 (2017).

[31] PHENIX collaboration, S.S. Adler *et al.*, "High p_T charged hadron suppression in Au+Au collisions at $\sqrt{s}_{\rm NN}$ = 200 GeV", Phys. Rev. C **69**, 034910 (2004).

[32] ALICE collaboration, K. Aamodt *et al.*, "Suppression of Charged Particle Production at Large Transverse Momentum in Central Pb-Pb collisions at $\sqrt{s}_{\rm NN}$ = 2.76 TeV", Phys. Lett. B **696**, 30 (2011).

[33] STAR collaboration, J. Adams *et al.*, "Evidence from d+Au measurements for final state suppression of high p(T) hadrons in Au+Au collisions at RHIC", Phys. Rev. Lett. **91**, 072304 (2003).

[34] STAR collaboration, C. Adler *et al.*, "Disappearence of back-to-back high-pT correlations in central Au+Au collisions at $\sqrt{s}_{\rm NN}$ = 200 GeV", Phys. Rev. Lett **90**, 082302 (2003).

[35] R.S. Bhalerao, "Radial Flow, Anisotropic Flow and Relativistic Hydrodynamics for the Beginners", 3rd SERC School on Nuclear Physics (2009).

[36] ALICE collaboration, K. Aamodt *et al.*, "Elliptic flow of charged particles in Pb-Pb collisions at $\sqrt{s}_{\rm NN}$ = 2.76 TeV", Phys. Rev. Lett. **105**, 252302 (2010).

[37] A. Bilandzic, R. Snellings, and S. Voloshin, *et al.*, "Flow analysis with cumulants: direct calculations", Phys. Rev. C **83**, 044913 (2011).

[38] STAR collaboration, K.H. Ackerman *et al.*, "Elliptic flow of charged particles in Au+Au collisions at 130 GeV", Phys. Rev. Lett. **86**, 402 (2001).

[39] H. Heiselberg, "Event-by-event physics in relativistic heavy-ion collisions", arXiv:nucl-th/0003046v5, 3 May (2001).

[40] STAR collaboration, B.I. Abelev *et al.*, "Azimuthal Charged-Particle Correlations and Possible Local Strong Parity Violation", Phys. Rev. Lett. **103**, 251601 (2009).

[41] D.E. Kharzeev, "Parity violation in hot QCD: Why it can happen, and how to look for it", Phys. Lett. B **633**, 260 (2006).

[42] K. Fukushima, D.E. Kharzeev, and H.J. Warringa, "The Chiral Magnetic Effect", Phys. Rev. D **78**, 074033 (2008).

[43] D.E. Kharzeev *et al.*, "Chiral Magnetic and Vortical Effects in High Energy Nuclear Collisions - A Status Report", Prog. Part. Nucl. Phys. **88**, 1 (2016).

[44] S.A. Voloshin, "Estimate of the CME signal in heavy-ion collisions from measurements relative to the participant and spectator flow planes", Phys. Rev. C **98**, 054911 (2018).

[45] S.A. Voloshin, "Parity violation in hot QCD: How to detect it," Phys. Rev. C **70**, 057901 (2004).

[46] A. Bzdak, Volker Koch, and Jinfeng Liao, "Charge-Dependent Correlations in Relativistic Heavy Ion Collisions and the Chiral Magnetic Effect", arXiv:1207.7327v1 [nucl-th] (2012).

[47] S. Pratt, S. Schlitchting, and S. Gavin, "Effects of momentum conservation and flow on angular correlations observed in experiments at the BNL Relativistic Heavy Ion Collider", Phys. Rev. C **84**, 024909 (2011).

[48] F. Wang, "Effects of cluster particle correlations on local parity violation observables", Phys. Rev. C **81**, 064902 (2010).

[49] STAR collaboration, L. Adamczyk *et al.*, "Fluctuations of charge separation perpendicular to the event plane and local parity violation in $\sqrt{s_{\rm NN}} = 200$ GeV Au+Au collisions at the BNL Relativistic Heavy Ion Collider", Phys. Rev. C **88**, 064911 (2013).

[50] STAR collaboration, B.I. Abelev *et al.*, "Observation of charge-dependent azimuthal correlations and possible local parity violation in heavy-ion collisions", Phys. Rev. C **81**, 054908 (2010).

[51] ALICE collaboration, B. Abelev. *et al.*, "Charge separation relative to the reaction plane in Pb-Pb collisions at $\sqrt{s}_{\rm NN} = 2.76$ TeV", Phys. Rev. Lett. **110**, 012301 (2013).

[52] CMS collaboration, V. Khachatryan *et al.*, "Observation of charge dependent azimuthal correlations in pPb collisions and its implication for the search for the chiral magnetic effect", Phys. Rev. Lett. **118**, 122301 (2017).

[53] STAR collaboration, L. Adamczyk *et al.*, "Beam energy dependence of Charge Separation along the Magnetic Field in Au+Au Collisions at RHIC", Phys. Rev. Lett. **113**, 052302 (2014).

[54] ALICE collaboration, S. Acharya, *et al.*, "Constraining the magnitude of the Chiral Magnetic Effect with Event Shape Engineering in Pb-Pb collisions at $\sqrt{s}_{\rm NN} = 2.76$ TeV", Phys. Lett. B **777**, 151 (2018).

[55] J.P. Blaizot, and A. Krzywicki, "Soft pion emission in high-energy heavy ion collisions", Phys. Rev. D **46**, 246 (1992).

[56] JACEE Collaboration, C.M.G. Lattes *et al.*, "Hadronic Interaction of High-Energy Cosmic Ray Observed by Emulsion Chambers", Phys. Rep. **65**, 151 (1980).

[57] WA98 Collaboration, M.M. Aggarwal *et al.*, "Search For Disoriented Chiral Condensates In 158 AGeV Pb+Pb Collisions", Czech. J. Phys. **50**, Suppl. 2 126 (2000).

[58] D0 Collaboration, M.V.S. Rao *et al.*, "Search for Centauro events in the D0 detector at Fermilab Collider", Fermilab-CONF-94-343-E, Sept. (1994).

[59] CDF Collaboration, P.L. Melese *et al.*, "Search for Centauro Events at CDF",Fermilab-CONF-96-205-E July (1996).

[60] MiniMax Collaboration, T.C. Brooks *et al.*, "A Search for disoriented chiral condensate at the Fermilab Tevatron", Phys. Rev. D **61**, 032003 (2000).

[61] NA49 Collaboration, H. Appelshauser, *et al.*, "Event-by-event fluctuations of average transverse momentum in central Pb+Pb collisions at 158-GeV per nucleon", Phys. Lett. B **459**, 679 (1999).

[62] C. Pruneau, S. Gavin, and S. Voloshin, "Methods for the study of particle production fluctuations", Phys. Rev. C **66**, 044904 (2002).

[63] X.F. Luo, B. Mohanty, H.G. Ritter, and N. Xu, "Energy Dependence of Higher Moments for Net-proton Distributions", J. Phys. G **37**, 094061 (2010).

[64] STAR Collaboration, L. Adamczyk *et al.*, "Charged-to-neutral correlation at forward rapidity in Au+Au collisions at $\sqrt{s}_{\rm NN}$ = 200 GeV", Phys. Rev. C **91**, 034905 (2015).

[65] WA98 collaboration, M.M. Aggarwal *et al.*, "Localised charged-neutral fluctuations in 158A GeV Pb+Pb collisions", Phys. Rev. C **64** 011901(R) (2001).

[66] M.M. Aggarwal, G. Sood, and Y.P. Viyogi, "Event-by-event study of DCC-like fluctuation in ultra-relativistic nuclear collisions", Phys. Lett. B **638**, 39 (2006).

[67] WA98 Collaboration, M.M. Aggarwal *et al.*, "Event-by-event charged-neutral fluctuations in Pb+Pb collisions at 158 A GeV", Phys. Lett. B **701**, 300 (2011).

Chapter 2

A Large Ion Collider Experiment

2.1 Large Hadron Collider

Relativistic heavy ion collisions open a way to go back in time when the universe was of the age of few micro seconds and a deconfined state of quarks and gluons occured at that time. To recreate the QGP (Quark Gluon Plasma) state in the laboratory, one needs a state of art technology to provide the high energy, luminosity and excellent detector systems of high resolution. In order to explore the mysteries of the universe and to study its properties, the Large Hadron Collider (LHC) was built at CERN (European Council for Nuclear Research) [1]. The LHC, world's largest and most powerful particle accelerator, spanned over the border between France and Switzerland. It is enclosed in a circular tunnel of circumference ∼27 km at the depth ranging from 50 to 175 meters. LHC tunnel consists of two circular separate beam pipes containing large number of superconducting magnets (mainly dipoles and quadrupoles) with accelerating structures used to boost the beam to higher energies. The role of superconducting magnets is to focus the beam for maximizing a chance of head-on collision for which the LHC is designed. It is capable of colliding proton-proton (upto the maximum center of mass energy $\sqrt{s} = 13$ TeV), proton-lead (upto $\sqrt{s}_{\rm NN} = 8.16$ TeV), and lead-lead (upto $\sqrt{s}_{\rm NN} = 5.02$ TeV). In addition to p-p, p-Pb and Pb-Pb, Xe-Xe collision has also been done at the LHC at $\sqrt{s}_{\rm NN} =$

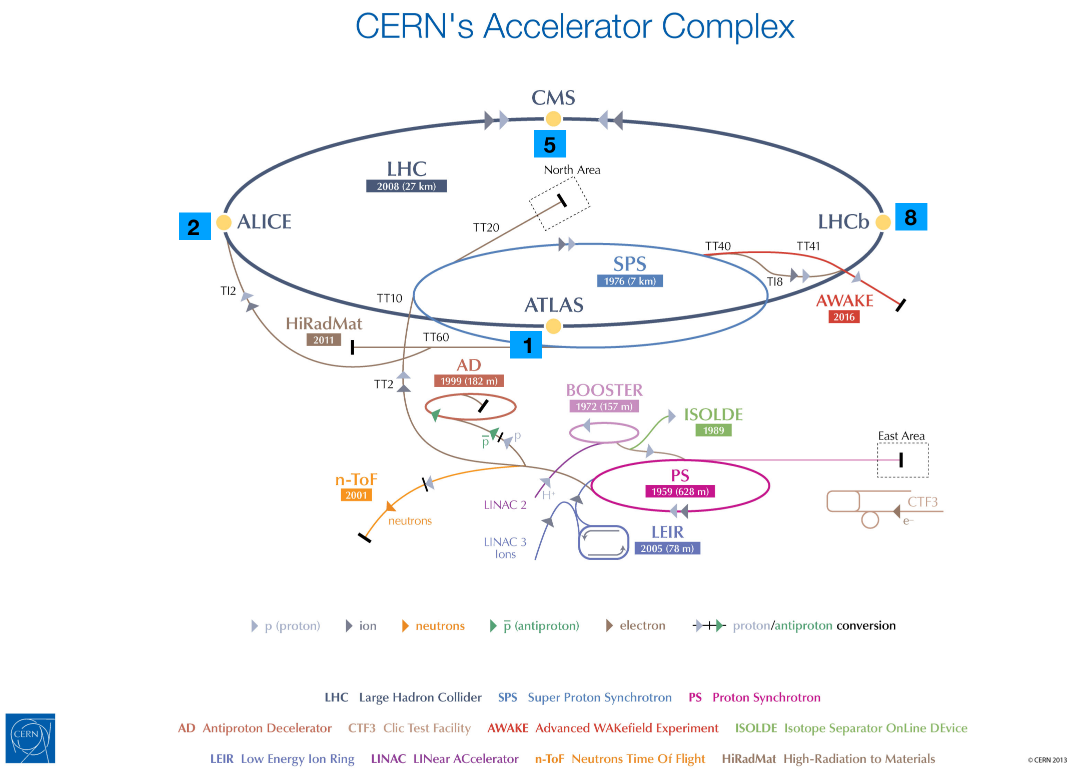

Figure 2.1: Schematic diagram of the CERN's complex accelerator system as a succession of machines with increasing energies: LINAC3, LIER, PS, SPS, LHC along with the energy boosters [2].

5.44 TeV. The layout of LHC accelerator complex is illustrated in figure 2.1 [2] and its important parameters are summarized in table 2.1 [3].

The CERN's complex accelerator system is a combination of numerous accelerators capable of operating at different beam energies. The output from the lower energy accelerator is fed to the next higher energy accelerator system to reach the maximum designed energy. The different collision systems pass through various steps to reach the main LHC ring.

Lead ion beam preparation: A sample of lead is heated to produce "Lead ions".

Quality	Number
Circumference	26659 m
Dipole operating temperature	1.9 K ($-271.3^{\circ}C$)
Number of magnets	9593
Number of main dipoles	1232
Number of main quadrupoles	392
Number of RF cavities	8 per beam
Nominal energy, protons	6.5 TeV
Nominal energy, ions	2.76 TeV/nucleon
No. of bunches per proton beam	2808
No. of protons per bunch (at start)	1.2×10^{11}
Number of turns per second	11245
Number of collisions per second	1 billion

Table 2.1: Description of the LHC parameters [3].

The lead ions of different charge states with a maximum of Pb^{29+} are produced by the Electron Cyclotron Resonance (ECR) source. The Pb^{29+} ions are fed to the LINAC 3 for acceleration upto maximum of 4.2 MeV per nucleon and passed through a carbon foil to strip most of them to Pb^{54+}. A beam of Pb^{54+} is now sent to the Low Energy Ion Ring (LEIR) for the acceleration up to 72 MeV per nucleon, which transfers it to the Proton Synchrotron (PS) and accelerates to 5900 MeV (5.9 GeV) per nucleon. Now the beam of Pb^{54+} is passed through a second carbon foil to strip out the remaining electron charges to form Pb^{82+} beam and sent to the Super Proton Synchrotron (SPS) where it is accelerated to 177 GeV per nucleon. After the SPS, a beam of Pb^{82+} is transferred to the LHC and accelerated to 2.76 TeV per nucleon.

Proton beam preparation: The proton beam is produced by stripping off electrons from the hydrogen atoms at LINAC 2 and sent to the Proton Synchrotron Booster (PSB) for the acceleration from 50 MeV to 1400 MeV (1.4 GeV). In next step, beam is injected to the PS where it is accelerated to 25 GeV and sent to the SPS to acquire higher energy upto 450 GeV. Finally the beam is transferred to the LHC ring and accelerated to maximum energy of 6.5 TeV.

Collision: After acquiring a sufficient amount of energy, protons or lead ions are injected to the two beam pipes where they are circulating in opposite directions at a speed close to the speed of light and are made to collide head-on to produce large number of new particles. A strong magnetic field is applied to the beams to move them in circular orbits and are kept in an ultra-high vacuum. The counter rotating beams collide at four different points of the LHC ring. These four points (1, 2, 5 and 8) correspond to four major experimental systems (ATLAS, CMS, ALICE and LHCb) shown in figure 2.1.

LHC data: The LHC has recorded the Pb-Pb collision data for two center of mass energies $\sqrt{s}_{\rm NN}$ = 2.76 TeV and 5.02 TeV. For proton-proton collisions, LHC has taken the data for many center of mass energies $\sqrt{s}_{\rm NN}$ = 0.9, 2.76, 5, 7, 8 and 13 TeV. Apart from *p*-*p* and Pb-Pb collisions, p-Pb collisions are also studied for two center of mass energies $\sqrt{s}_{\rm NN}$ = 5.02 and 8.16 TeV at the LHC. For the proton-lead collisions, the proton and lead ion beams are produced using the same procedure discussed above.

2.2 Experiments at the LHC

A **T**oroidal **L**HC **A**pparatu**S** (ATLAS) [4] and the **C**ompact **M**uon **S**olenoid (CMS) [5] are the two general purpose experiments built exactly opposite to each other at points 1 and 5, respectively, of the LHC ring. They are designed to cover the physics which includes the Higgs boson measurements, Standard Model predictions, physics beyond Standard Model (BSM) such as SUperSYmmetry (SUSY), dark energy etc. The discovery of Higgs boson in July 2012 completed one of the main physics goals of these two experiments [6], [7]. Though the ATLAS and the

CMS mainly focus on the study of *p*-*p* collisions, they also participate in the proton-lead and lead-lead collisions to study the heavy-ion physics. The third experiment, **LHCb**eauty (LHCb) [8] is an asymmetric detector mainly focuses on the study of CP violation and matter anti-matter asymmetry. It is located at point 8. The fourth experiment, **A** **L**arge **I**on **C**ollider **E**xperiment (ALICE) [9] situated at point 2, is specially optimized for the study of heavy-ion physics by colliding Pb ions to search for the signatures of Quark Gluon Plasma (QGP) - a deconfined state of quarks and gluons. In addition to Pb-Pb data, ALICE also records the proton-proton and proton-lead data to perform baseline study for Pb-Pb analysis and serve as complementary analysis for ALICE unlike other LHC experiments.

2.3 A Large Ion Collider Experiment

ALICE is a dedicated heavy-ion detector at LHC designed primarily to focus on the study of the behaviour of strongly interacting matter at very high temperature and energy densities in nearly zero baryochemical potential region. The experiment also aims to probe the different aspects of QCD such as presence of QGP phase transition, color confinement and chiral-symmetry restoration. Out of various physics topics, the study of quarkonia production, azimuthal anisotropy of heavy quarks, charm and beauty measurements, multi-particle correlation and fluctuation measurements, thermal photon production, low-mass dileptons and the jet measurements are some of the physics programmes going on in ALICE. The ALICE detector, of the $16 \times 16 \times 26\ m^3$ size and the $10,000$ *tonnes* weight, is located at Point-2 on the France side of the LHC ring. A pictorial view of the ALICE detector is shown in figure 2.2. It consists of three major components: *Central Barrel detectors*, *Forward detectors* and *Muon spectrometer* [10]. ALICE uses fine granularity detectors those are able to handle the enormous particle multiplicity ∼8000 charged particles per unit rapidity. The sub-detector, Time Projection Chamber (TPC) is the main tracking detector which in conjunction with the TOF (Time Of Flight)

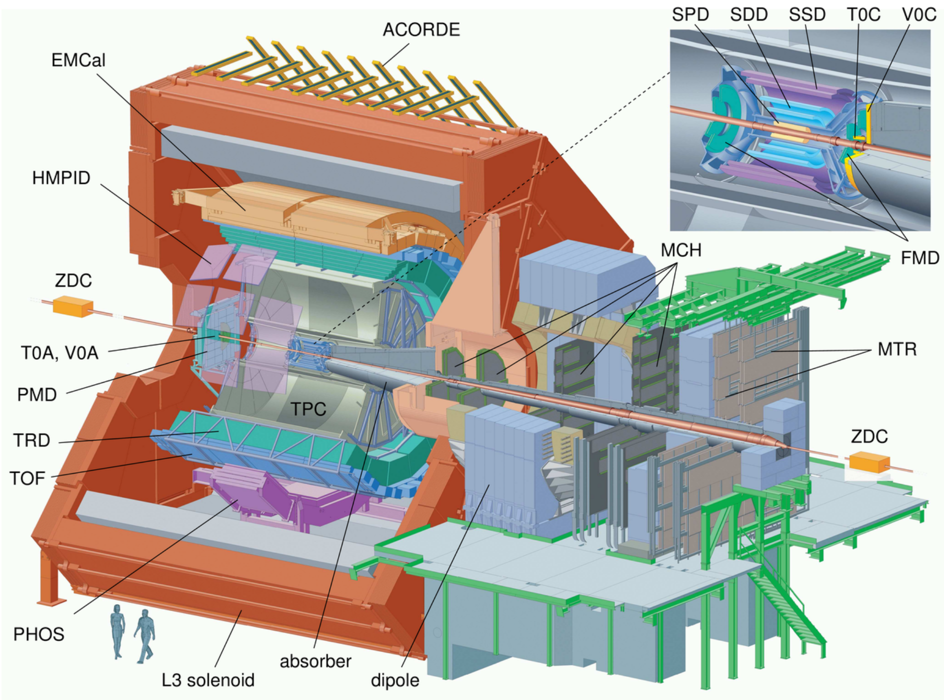

Figure 2.2: Perspective view of the ALICE detector set up with its subsystems.

and the ITS (Inner Tracking System) provides an excellent tracking capability from low transverse momentum (p_T) $\sim$150 MeV/c to high p_T $\sim$10 GeV/c. The excellent charged particle identification is also provided by TPC and ITS based on ionization energy loss mechanism (dE/dx) and TOF using time-of-flight information. The detailed description of each sub-detector is given in next section.

2.3.1 Central Barrel Detectors

The central barrel detectors are positioned around the collision point of ALICE covering a pseudorapidity range $-0.9 < \eta < 0.9$ over full azimuth. The detectors under this region have the main task of tracking and particle identification of charged particles and photons, in such high multiplicity environment. They are enclosed in the large L3 solenoid magnet which provides a uniform magnetic field $\sim$0.5 T to all the central barrel detectors. The sub-systems of the central barrel are placed in accordance with their increasing radii like the Inner Tracking System (ITS), the Time

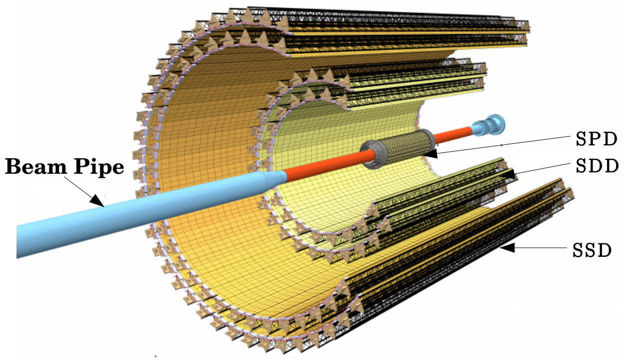

Figure 2.3: Pictorial view of the Inner Tracking System of ALICE

Projection Chamber (TPC), the Transition Radiation Detector (TRD), and the Time Of Flight (TOF) in full $\eta - \phi$ region. The PHOton Spectrometer (PHOS), the ElectroMagnetic Calorimeter (EMCal), the High Momentum Particle Identification Detector (HMPID), and the ALICE COsmic Ray DEtector (ACORDE) also lie in the central barrel region but with partial η and ϕ coverage. A brief description of these sub-systems is given below.

- **Inner Tracking System (ITS):** ITS is the innermost detector of ALICE, placed closest to the interaction point (IP) [11]. It is mainly used for improvement of impact parameter, primary vertex determination with a momentum resolution better than 100 μm. The ITS also provides secondary vertex reconstruction of hyperon decays, particle identification and track reconstruction of low-momentum particles below 100 MeV/c. ITS consists of six-layer cylindrical silicon vertex detector with two layers of Silicon Pixel Detector (SPD), Silicon Drift Detector (SDD) and Silicon Strip Detector (SSD) each as shown in figure 2.3. The innermost layer (of SPD) is located at radial distance of 3.9 cm and outermost layer (of SSD) at 43.0 cm in the pseudorapidity interval $|\eta| < 0.9$.

Silicon Pixel Detector (SPD): The SPD constitutes two innermost layers of the ITS located at a distance of 3.9 cm and 7.6 cm from the beam axis. Its main aim is to determine the primary and secondary vertex as well as the measurement of impact parameter of secondary tracks. SPD operates in high track density environment around 50 cm^{-2}. SPD has hybrid silicon pixels of size 50 $\mu m(r\phi)$ $\times$ 425 $\mu m(r\phi)$ and contains 9.8×10^6 cells. The extended pseudorapidity coverage of $|\eta| < 1.98$ provides uniform track matching with the Forward Multiplicity Detector (FMD).

Silicon Drift Detector (SDD): These are the two intermediate layers of the ITS positioned at 15.0 cm and 23.9 cm from the beam axis. In this region the particle density reaches up to 7 cm^{-2}. SDDs have multi particle tracking capability and provide energy loss measurements for particle identification.

Silicon Strip Detector (SSD): SSDs are the outermost layers of ITS at a distance of 38.0 cm and 43.0 cm from the beam axis. Both layers are equipped with the double-sided Silicon Strip Detectors and cover the pseudorapidity range $|\eta| < 0.9$ (common to other layers of the ITS) with the full azimuthal coverage. The SSD connects the ITS tracks to the tracks in the TPC and also provides dE/dx information.

- **Time Projection Chamber (TPC):** ALICE TPC is the main tracking detector in central barrel region with full azimuth and covers η range of $-0.9 < \eta < 0.9$. The TPC provides charged-particle tracking similar to ITS, TRD, and TOF detectors. A large transverse momentum range with good resolution is covered by the TPC from low $p_T \sim 0.1$ GeV/c to high $p_T \sim 100$ GeV/c. The TPC also provides excellent charged particle identification via dE/dx measurements, for example, the TPC along with the TOF $\pi/K(K/p)$ separation upto 2.5(2) GeV/c [12]. It provides vertex measurements, charged particle momentum measurements with good two-track resolution, together with the other central barrel detectors. Since TPC is one of the most impor-

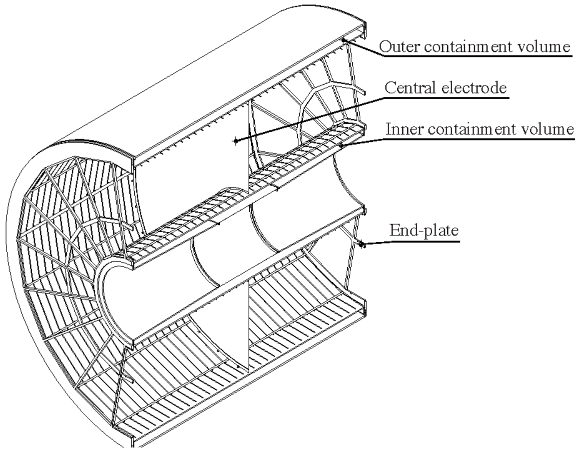

Figure 2.4: Layout of the field cage Time Projection Chamber of ALICE.

tant detectors of ALICE and is extensively used in the current analysis. The detailed description of the TPC is given below.

Layout of the TPC: The design of TPC detector is innovative in many aspects. It is a cylindrical detector having inner(outer) radius of about 85(250) *cm* and the length along the beam axis is 500 *cm*. The basic structure of the TPC is shown in figure 2.4. It has a cylindrical field cage structure with an active volume of 90 m^3 filled with gasses; Ne(90%), CO_2(10%), and N_2(5%) [13]. The field cage is operated at high drift field of 400 V/cm with a central high voltage electrode of 100 kV. The two opposite axial potential dividers are placed to provide uniform electrostatic field in the active volume of the TPC. The optimized gas mixture of $Ne/CO_2/N_2$ allows low multiple scatterings, low space-charge effect, drift time of about 90 μs and long term stability properties. The Multi Wire Proportional Counter (MWPC) is installed at the end plates of the cylinder. The total readout pads mounted on the endcaps are 550000 of three different sizes 4×7.5 mm^2 (inner chambers), 6×10 mm^2 and 6×15 mm^2 (outer chambers) providing low occupancy and better track resolution.

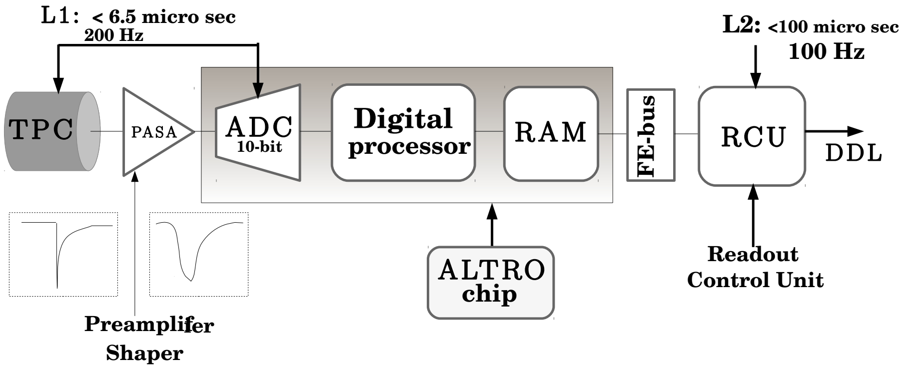

Figure 2.5: Block diagram of the TPC Front End Electronics readout.

Working Principle: When a charged particle emanates from the collision point, it passes through the active volume of the detector and gets ionized along its way by producing ions and electrons. The electrons drift towards end plates of the cylinder where they are detected by anode wires of the MWPC. The position of space point projected onto the endplate is measured as one coordinate and the other coordinate is taken from the induced signal on cathode pad along the anode wire. The third coordinate is given by the time taken (drift time) by ionized electrons to reach the anode wire. The TPC yields many three-dimensional points for each track which allows full track reconstruction [14]. The endcaps of the TPC are covered by eighteen trapezoidal shaped cathode readout chambers.

Front End Electronics: The charge collected on the TPC pads is further processed by Front End Electronic (FEE) boards mounted on the service support wheels independently supported by the TPC. The advantage of using support wheels is to avoid the loading of electronics weight on the TPC. A single readout channel consists of three basic parts: a charge sensitive amplifier, a 10-bit Analog to Digital converter (ADC) and a digital circuits with Multi-Event Buffer. A signal collected on the TPC pads has fast rise time (< 1 ns) along with the long tail due to the motion of positive ions. It gets amplified and integrated to a semi-Gaussian pulse by a low impedance amplifier based on the Charge Sensitive Amplifier (CSA) shaper. These functions are operated by a chip called Pre Amplifier Shaper (PASA). In the next step, an amplified analog signal is converted into digital signal by 10-bit low power ADC and the digitized signal passes through number of operations such as zero suppression, tail cancellation or baseline subtraction etc. The digital circuits, Multi-Event buffer, and the ADC, are contained in a single ALTRO (ALice Tpc ReadOut) chip. The readout process up to the ALTRO chip as shown in figure 2.5 is contained in the Front End Card (FEC), controlled by Readout Control Unit (RCU) which works as interface between FECs (on one side) and the trigger, the DAQ system, and the Detector Control System (DCS) (on the other side) via Detector Data Links (DDL).

- **Transition Radiation Detector (TRD):** TRD covers the pseudorapidity interval $-0.84 < \eta < 0.84$ with inner and outer radius of 2.90 m and 3.68 m, respectively. The main purpose of the TRD is to identify electrons inside the central barrel for momentum > 1 GeV/c and reject pions in central Pb-Pb collisions at 100% rejection capability [15]. TRD enhances the signal-to-background ratio for J/Ψ production measurements and due to excellent impact parameter resolution of ITS, the TRD is capable of reconstructing charm quark in semi leptonic decays. It provides level 1 trigger (L1) for charged hadrons.

- **Time Of Flight (TOF):** It is a large gaseous detector spanned in the pseudorapidity region $|\eta| < 0.9$. The Multi-gap Resistive Plate Chambers (MRPCs) are the best choice for the TOF detector [16]. It provides Particle IDentification (PID) with better resolution $> 3\sigma$ for π/K and K/p in the intermediate p_T range $2.0 - 2.5$ GeV/c for pions and kaons, while up to 4 GeV/c for protons [17]. The TOF in conjunction with the ITS and TPC allows the track and vertex reconstruction, dE/dx measurements in p_T range up to 1 GeV/c which further provides identification of large samples of pions, kaons, and protons.

- **ElectroMagnetic CALorimeter (EMCal):** EMCal is a cylindrical calorimeter, made of Pb-scintillators, situated adjacent to the ALICE solenoid magnet at a distance of ∼4.5 m from the beam axis covering $|\eta| \leq 0.7$ and azimuth angle $\Delta\phi = 107^{\circ}$. It measures the neutral pion yield via decay photon measurements. The main objective of ALICE EMCal is to study the energetic partonic interactions with the highly dense matter (physics of jet quenching) in such high energy heavy-ion collision environment. In combination with the TPC and the ALICE magnetic field strength, EMCal provides good resolution for jet reconstruction [18]. The structure of EMCal is designed to perform high p_T physics measurements. It also provides trigger (L0, L1) for photons, electrons and hard jets.

- **PHOton Spectrometer (PHOS):** The PHOton Spectrometer is a highly segmented high resolution electromagnetic calorimeter and provides meson identification with better position resolution due to the large distance (∼ 460 cm) from the IP. It covers pseudorapidity range $-0.12 < \eta < 0.12$ with the limited azimuthal acceptance ($220^{\circ} < \phi < 320^{\circ}$). The main task of PHOS is to detect and identify thermal photons and study the thermal properties of initial hot dense matter produced in the collision via low p_T direct photon measurements in a wide transverse momentum (p_T) range from 5 MeV to 100 GeV [19]. It measures the neutral pions (π°) up to the p_T range of 1-10 GeV/c which provides information about the initial and final state particle production. Due to the different sensitivity of di-photons and di-leptons to the various phases of collision, these measurements allow to explore the spectrum of different stages in heavy-ion collision. The PHOS consists of PHOS (Electromagnetic Calorimeter) and CPV (Charged Particle Veto) units, where the CPV rejects the charged particles for better resolution of photon measurements. In conjunction with the other charged particle detectors, PHOS is capable of providing the information about the domains of DCC (Disoriented Chiral Condensate) formation by studying the charged to neutral particle multiplicity fluctuations on an event-by-event basis.

- **High Momentum Particle Identification Detector (HMPID):** It is specifically optimized for particle identification at higher $p_T > 1$ GeV/c beyond the momentum range covered by the ITS, TPC (via energy loss measurements) and the TOF (via Time Of Flight measurements). It covers central pseudorapidity range ($|\eta| < 0.6$) with partial azimuthal coverage ($1.2^\circ < \phi < 58.8^\circ$). HMPID allows the track-by-track separation of π/K and K/p up to p_T range of 3 GeV/c and 5 GeV/c, respectively. The hadron identification mechanism in HMPID is based on the Ring Imaging CHerenkov (RICH) counters [20].

- **ALICE Cosmic Ray Detector (ACORDE):** ACORDE plays two important roles in ALICE: it provides a L0 trigger for the commissioning, calibration purpose, and secondly it detects the atmospheric muons in combination with the TPC, TRD and TOF to study high energy (0.1-2 TeV) cosmic rays. ACORDE constitutes two scintillator counters placed on top of L3 magnet at a distance of 8.5 m from the beam axis [21].

2.3.2 Forward Detectors

The sub-detectors of this category are located in the forward pseudorapidity region. They are mainly focused to provide the fast trigger signals for both the central barrel detectors and the ALICE main trigger system i.e., the Central Trigger Processor (CTP). In addition to trigger signal, the forward detectors: ZDC, PMD, FMD, T0, and V0 provide important physics results in *p*-*p*, *p*-*Pb*, and *Pb*-*Pb* data analysis.

- **Zero Degree Calorimeter (ZDC):** It is a quartz fibre sampling calorimeter consists of two hadronic calorimeters (ZDC) located at 116 m on either side of the IP [22]. Each ZDC comprises two distinct detectors namely, ZN and ZP, for the detection of spectator neutrons and protons, respectively. To complement the ZDC, two electromagnetic calorimeters (ZEM) are used to measure the energy of particles in the forward region. ZEM is placed at 7 m from the IP opposite to the muon arm. ZDC measures the energy deposited by non-interacting particles ($N_{spectators}$) to estimate the collision centrality and the number of participating nucleons. ZDC is situated at 0° relative to the beam axis whereas ZEM is placed at an angle of 45° w.r.t. beam axis.

- **Photon Multiplicity Detector (PMD):** PMD is a gaseous detector with honeycomb structure working in a proportional counter region located at 364 cm from the IP with η coverage of $2.3 < \eta < 3.7$ over the full azimuthal angle [23]. The main physics goals of the PMD are, photon multiplicity measurements [24], event plane estimation and transverse electromagnetic energy calculation. PMD is capable of providing information about the DCC domains by studying the event-by-event multiplicity fluctuations [25].

- **Forward Multiplicity Detector (FMD):** FMD has highly segmented radial structure with five rings made of silicon detectors located at different η positions ($-3.4 < \eta < -1.7$ and $1.7 < \eta < 5.0$) in the forward region with 2π azimuth. The main tasks of the FMD are: charged particle multiplicity measurements, event plane estimation, flow analysis, and the study of multiplicity fluctuations [26].

- **VZERO Detector (V0):** It consists of two arrays of plastic scintillator detectors named as V0A and V0C, installed on either side of the IP [26]. The V0 covers pseudorapidity ranges $2.8 < \eta < 5.1$ (V0A at a distance of 340 cm from the IP in a direction opposite to the muon arm) and $-3.7 < \eta < -1.7$

(V0C at a distance of 90 cm from the IP). It provides three types of trigger systems: Minimum Bias trigger, multiplicity trigger and semi central trigger in proton-proton and lead-lead collisions. Apart from the trigger information, it also measures luminosity, particle multiplicity, and centrality. The V0 detector serves as centrality estimator (V0M) for heavy-ion collisions by taking the sum of amplitude of multiplicity distributions from both detectors V0A and V0C.

- **TZERO Detector (T0):** T0 also consists of two arrays of Cherenkov detectors, T0-A ($4.61 < \eta < 4.92$) at a distance of 375 cm and T0-C ($-3.28 < \eta < -2.97$) at 72.7 cm from the IP. It is located close to the beam pipe to increase the triggering efficiency in heavy-ion collisions ($\sim 100\%$). T0 is designed to generate a start time (T0) signal for the TOF detector with a good time resolution of about 50 ps and "wake-up" signal for the TRD before L0 trigger [26]. T0 signal corresponds to real time of the collision. It provides vertex position measurements, multiplicity triggers and also a minimum bias trigger.

2.3.3 Muon Spectrometer

Muon spectrometer is positioned in the forward rapidity region ($-4.0 < \eta < -2.5$) of ALICE detector. It is designed for the study of heavy-quark vector mesons ($J/\Psi, \Psi', \Upsilon, \Upsilon', \Upsilon''$) and for ϕ meson productions from the decay products of $\mu^+\mu^-$ channel. This measurement allows one to analyze and compare the yields of all quarkonia species as a function of p_T in different collision centrality. The open heavy flavour production measurements are possible to analyze in the limited η range by detecting e and μ from the TRD and muon spectrometer, respectively. Muon spectrometer has a complex arrangement of many components, such as absorber which absorbs charged hadrons and photons coming from the interaction vertex, tracking system of 10 detection planes with high granularity and trigger chambers.

Muon spectrometer provides a dimuon trigger system along with the high granularity readout unit [27].

2.4 ALICE Data Processing

2.4.1 ALICE-online data processing systems

The Pb-Pb collisions provide enormous amount of particle multiplicity and the handling of such high multiplicity data is a big challenge for ALICE experiment. To perform this task efficiently, the data processing is divided into sub-systems named as: Central Trigger Processor System (CTP), Data Acquisition System (DAQ), High Level Trigger (HLT), Detector Control System (DCS) and Experiment Control System (ECS).

Central Trigger Processor System (CTP): The ALICE CTP is a hardware trigger which controls and synchronizes the trigger signals from all ALICE trigger detectors. CTP is optimized to select the rare physics events produced during the high multiplicity Pb-Pb collisions at the LHC. The trigger selection is performed for different colliding systems: pp, $p - Pb$, and $Pb - Pb$. The tracking detector's (e.g. TPC) design is optimized in such a way that they are capable to cope with the high multiplicity collisions. The trigger inputs in ALICE are divided into three parts: L0, L1, and L2. A level 0 (L0) signal reaches the detector after 1.2 μs and level 1 (L1) trigger reaches at 6.5 μs, after the collision. The CTP also takes care of the final trigger, a level 2 (L2), and waits for the past-future protection, which means that CTP restricts the superposition of large number of events known as pile-up events. The time interval for this process is about 88 μs. After collecting the information from all trigger signals, the CTP decides the selection and rejection of events and transfers the output signal to the trigger detectors using LTU (Local Trigger Units) and also a decision copy to the DAQ system.

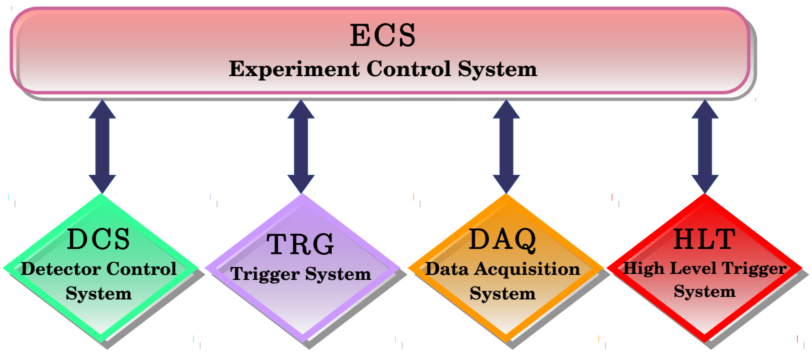

Figure 2.6: ALICE online data processing systems.

Data Acquisition System (DAQ): The DAQ combines the event information recorded by all sub-detectors to form a complete event [28]. The Detector Data Links (DDL) are used as interface between sub-detectors and the DAQ system. They transfer the event information to Local Data Concentrators (LDCs) where the information is collected from all the sub-detectors in the form of sub-events. Further, the sub-events are sent to Global Data Concentrators (GDCs) for the formation of full event and is stored in Transient Data Storage (TDS). The CTP trigger reduces the events by selecting the interesting physics events and maximize the performance of ALICE DAQ by minimizing the bandwidth consumption of the DAQ system. The task of event selection is shared by both the trigger and the DAQ systems and the selected events are sent to the High Level Trigger (HLT) for further selection in order to store the processed data at permanent data storage.

High Level Trigger (HLT): The ALICE High Level Trigger is a software trigger used to reduce the data volume in order to fit the data rate in available bandwidth [28]. In order to select the good physics events without loosing its physics content, the data passes through multiple steps, firstly the events from the detector are accepeted or rejected on the basis of online selection analysis, by selecting a region of interest (ROI) within the event. ROI corresponds to the selection of interesting $\eta - \phi$ phase space. HLT decides the selection of event and can also modify the data without losing the physics information.

Detector Control System (DCS): The main aim of DCS is to keep track of the ongoing processes to ensure the safety and correct operation of the ALICE, by monitoring all the sub-detectors and their corresponding Front End Electronics (FEE). It has a remote control to all the sub-systems and technical equipments. The DCS provides information about the detector conditions and parameters for the offline data reconstruction.

Experiment Control System (ECS): The ECS supervises and controls all the processes involve in the data processing (CTP, HLT, DCS and DAQ). It is the main part of ALICE control system.

2.4.2 ALICE-offline data processing systems

The raw data collected from all the sub-detectors is processed through ALICE offline framework known as AliROOT (mainly C++ and ROOT based) which performs number of tasks on the data after online data processing. The main tasks are: calibration, simulation, alignment, reconstruction, and data analysis etc.

Event Generation and Simulation: The simulation studies were performed to design the detector in order to make full use of the detector to extract interesting physics information from the data. The ALICE framework enables the access to different event generators such as HIJING [29], PYTHIA [30, 31], and AMPT [32] etc. The primary particles produced by these event generators contain full kinematic level information such as momentum, charge, mass and PID number of each produced particle for particle identification. The transport packages: GEANT3 [33], GEANT4 [34], and FLUKA [35], contain detailed information about the response of the detector when particle crosses the active volume after collision. The generated particles are passed through transport packages to create the environment of particle interactions similar to real experimental collision. The hit information stored in the detector is digitized by the corresponding electronics and the data are stored in binary form based on ROOT which is the object oriented data analysis framework.

Analysis: The reconstruction process is same for the experimental and simulated data. First of all, the data is stored in the form of Event Summary Data (ESD) after reconstruction of raw data. ESD includes whole information of an occured event e.g., primary and secondary vertex position, reconstruction parameters of all produced particles, particle identification information etc. The AOD (Analysis Object Data) is the reduced version of ESD obtained by applying some standard physics cuts to remove the unnecessary information for the physics analysis. Most of the physics analysis are performed on the AODs. ALICE analysis framework reads each event only once and different algorithms can be applied to it according to the need of the ALICE user [36].

ALICE Grid Facility: To process the ALICE data, a lot of computing power is required and for that the data processing is distributed over the GRID systems located worldwide to analyze the large amount of data in a reasonable time. The user interacts with the GRID systems via ALICE Environment (AliEn) User Interface (UI) [36, 37] and can analyze the data in different ways: (1) on local system of the user, (2) interactive mode or (3) on group of machines by submitting an alien batch job to the AliEn system which is independent of the local user system and is distributed to several computing systems (shown in figure 2.7) according to the availability.

AliROOT Framework: ALICE offline framework (AliROOT) is based on the Object Oriented programmes. The ROOT framework is a basic need of AliRoot and serves as supporting framework [38]. The whole framework is written in C++ computing language along with some external programs in FORTRAN language.

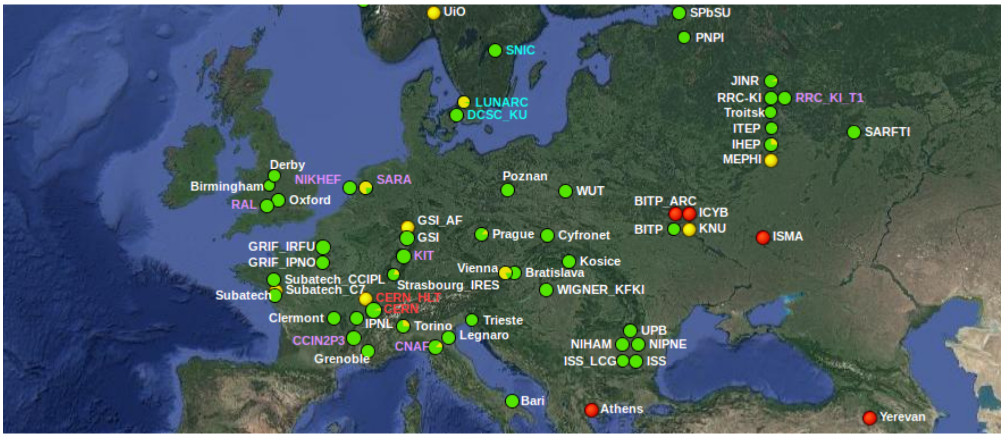

Figure 2.7: Snapshot of the ALICE-Grid computing systems located worldwide.

Bibliography

[1] O.S. Bruning *et al.*, "LHC Design Report Volume I: The LHC Main Ring" CERN-2004-003-V1 (2004).

[2] CERN database webpage: https://cds.cern.ch/record/1621583.

[3] "CERN LHC faq the guide", CERN database webpage: https://cds.cern.ch/record/2255762/files/CERN-Brochure-2017-002-Eng.pdf.

[4] ATLAS Collaboration, G. Aad *et al.*, "The ATLAS Experiment at the CERN Large Hadron Collider", JINST **3**, S08003 (2008).

[5] CMS Collaboration, S. Chatrchyan *et al.*, "The CMS Experiment at the CERN LHC", JINST **3**, S08004 (2008).

[6] ATLAS Collaboration, G. Aad *et al.*, "Observation of a new particle in the search for the Standard Model Higgs Boson with the ATLAS Detector at the LHC", Phys. Lett. B **1**, 716 (2012).

[7] CMS Collaboration, S. Chatrchyan *et al.*, "Observation of a new boson at a mass of 125 GeV with the CMS Experiment at the LHC", Phys. Lett. B **30**, 71 (2012).

[8] LHCb Collaboration, A. Augusto Alves, Jr. *et al.*, "The LHCb Detector at the LHC", JINST **3** S08005 (2008).

[9] ALICE Collaboration, B. Alessandro *et al.*, "ALICE: Physics Performance Report, Volume II", J. Phys. G **32**, 1295 (2006).

[10] ALICE Collaboration, K. Aamodt *et al.*, "The ALICE experiment at the CERN LHC", JINST **3**, S08002 (2010).

[11] ALICE Collaboration, "Technical Design Report of Inner Tracking System (ITS)", CERN-LHCC-99-012 (1999).

[12] ALICE Collaboration, "ALICE Technical Design Report of Time Projection Chamber", https://edms.cern.ch/file/398930/1/ALICE-DOC-2003-011.pdf.

[13] J. Alme *et al.*, "The ALICE TPC, a large 3-dimensional tracking device with fast readout for ultra-high multiplicity events", Nucl. Inst. Meth. A **622**, 316 (2010).

[14] W.R. Leo, "Techniques for Nuclear and Particle Physics Experiments", (1994).

[15] ALICE Collaboration, "A transition radiation detector for electron identification within the ALICE central detector - an addendum to the Technical Proposal", CERN-LHCC-99-013 (1999).

[16] ALICE Collaboration, "Construction and tests of the MRPC detectors for TOF in ALICE", Nucl. Inst. Meth. Phys. Res. A **602**, 658 (2009).

[17] ALICE Collaboration, "Technical Design Report of Time-Of-Flight system", CERN-LHCC-2000-012 (2000).

[18] ALICE Collaboration, "ALICE Electromagnetic Calorimeter Technical Design Report", CERN-LHCC-2008-014 (2008).

[19] ALICE Collaboration, "Technical Design Report of Photon Spectrometer (PHOS)", CERN-LHCC-99-004 (1991).

[20] ALICE Collaboration, S. Beole *et al.*, "ALICE technical design report: Detector for high momentum PID", CERN-LHCC-98-19 (1998).

[21] ALICE Collaboration, A. Fernandez, S. Kartal, and C. Pagliarone, "ACORDE a Cosmic Ray Detector for ALICE", ACORDE/PUB/2006/02 (2006).

[22] ALICE Collaboration, "Technical Design Report of the Zero Degree Calorimeter (ZDC)", CERN-LHCC-99-5 (1999).

[23] ALICE Collaboration, "Addendum to the Technical Design Report of the Photon Multiplicity Detector (PMD)", CERN/LHCC 2003-038 (2003).

[24] ALICE Collaboration, B.B. Abelev *et al.*, "Inclusive photon production at forward rapidities in proton-proton collisions at $\sqrt{s} = 0.9$, 2.76 and 7 TeV", Eur. Phys. J. C **75**, 146 (2015).

[25] WA98 Collaboration, M.M. Aggarwal *et al.*, "Centrality dependence of charged-neutral particle fluctuations in 158A GeV Pb-Pb collisions", Phys. Rev. C **67**, 044901 (2003).

[26] ALICE Collaboration, "Technical Design Report on Forward detectors: FMD, V0 and T0", CERN-LHCC-2004-02 (2004).

[27] ALICE Collaboration, "ALICE Technical Design Report of Muon Forward Tracker", CERN-LHCC-2015-001 (2015).

[28] ALICE Collaboration, "ALICE Technical Design Report of the Trigger, Data Acquisition, High Level Trigger and Control System", CERN-LHCC-2003-062, (2003).

[29] Miklos Gyulassy, and Xin-Nian Wang, "HIJING 1.0: A Monte Carlo Program for Parton and Particle Production in High Energy Hadronic and Nuclear Collisions", LBL-34246 (1997).

[30] Torbjrn Sjöstrand, “High-energy-physics event generation with PYTHIA 5.7 and JETSET 7.4”, Comp. Phys. Coun **82**, (1994).

[31] “PYTHIA 6.4, Physics and Manual”, FERMILAB-PUB-06-052-CD-T, hep-ph/0603175, Lu TP 06-13, FERMILAB-PUB-06-052-CD-T (2006).

[32] B. Zhang, C.M. Ko, Bao-An Li, and Ziwei Lin, “A Multi-Phase Transport Model for Relativistic Nuclear Collisions”, Phys. Rev. C **61**, 067901 (2000).

[33] R. Brun, F. Bruyant, Carminati, S. Giani, M. Maire, A. McPherson, G. Patric, and L. rban, “GEANT Detector Description and Simulation Tool”, CERN-W5013 (1994).

[34] GEANT4 Collaboration, S. Agostinelli *et al.*, “GEANT4: A Simulation toolkit”, Nucl. Inst. Meth. A **506**, 250 (2003).

[35] A. Fasso *et al.*, “FLUKA: present status and future developments”, Proceedings of the IV International Conference on Calorimeters and their Applications, World Scientific, Singapore (1994).

[36] ALICE Collaboration, “ALICE Technical Design Report of the Computing”, CERN-LHCC-2005-018 (2005).

[37] P. Saiz *et al.*, “AliEn: ALICE environment on the GRID”, Nucl. Inst. Meth. Phys. Res. A **502**, 437 (2003).

[38] R. Brun, and F. Rademakers, “ROOT - An object oriented data analysis framework”, Nucl. Inst. Meth. Phys. Res. A **389**, 81 (1997).

Chapter 3

Charged-Neutral Fluctuations in Pb-Pb collisions at $\sqrt{s_{\mathrm{NN}}} = 2.76$ TeV

3.1 Introduction

It is believed that at very high temperature and energy density, the matter produced may undergo chiral phase transition. In heavy ion collisions, the collision debris are produced and move outward from the collision zone for a distance of about few fermi at the speed of light leaving behind relatively colder interior whose vacuum has chiral orientation different from the true vacuum. The misalignment of the vacuum direction is called as Disoriented Chiral Condensate (DCC) [1]. As the temperature of the system drops, the chiral field starts oscillating toward the direction of true vacuum emitting pions coherently. It is expected that the distribution of these coherently radiated pions is very different from those emitted incoherently.

The detection and study of the DCC provides valuable information about the nature of chiral phase transition. The most important signal to investigate the DCC domains is the distribution of neutral pion fraction. Thus, in practice one has to look into the ratio of neutral to charged pions multiplicity. Several experiments have made many attempts to search for the DCC signal. JACEE collaboration detected some events with large number of neutral particles compared to charged particles in the localized pseudorapidity-azimuth ($\eta - \phi$) phase space [2]. The different techniques have been already used for the search of DCC viz., normalised factorial moments and Discrete Wavelet Transform analysis (DWT) [3]. The normalised factorial moment technique was adopted by the Minimax collaboration for the DCC study in p-$\bar{p}$ collisions at center-of-mass energy 1.8 TeV. They have introduced a robust observable which is insensitive to detector efficiency and gives very different values for generic pion events and DCC type events though they found no evidence for the existence of DCC domains [4]. Huang *et al.* [5] suggested the Discrete Wavelet Transform (DWT) method for the DCC study. WA98 collaboration used this method to measure charged-neutral fluctuations which is considered as a possible signature for the DCC. The analysis was performed on Pb-Pb collisions data at 158 A GeV at CERN SPS facility. The measurements proved the absence of correlated DCC type fluctuations in charged to neutral particles and put an upper limit on the localized non-statistical DCC-like fluctuations of 10^{-2} for azimuthal window ($\Delta\phi$) = $45^\circ - 90^\circ$ and 3×10^{-2} for $\Delta\phi = 90^\circ - 135^\circ$ with 90% confidence level [3]. The Sliding Window Method (SWM) was also used by WA98 collaboration for the charged-neutral fluctuation measurements which helps to scan each $\eta - \phi$ region microscopically, for the presence of non-statistical DCC fluctuations [6].

STAR collaboration at RHIC studied the event-by-event charged neutral correlation at forward rapidity in Au+Au collisions at $\sqrt{s}_{\rm NN} = 200$ GeV. The observables used for the measurements are ν_{dyn} and $r_{m,1}$ and are studied as a function of centrality [7]. The results obtained exhibited a very small deviation ($< 1\%$) from the generic pion production.

For this analysis, the Pb-Pb data recorded by the ALICE detector at $\sqrt{s}_{\rm NN} = 2.76$ TeV is used to study the non-statistical charged-neutral fluctuations on event-by-event basis. The photon multiplicity is measured with the Photon Multiplicity Detector (PMD) and the charged particles with the Forward Multiplicity Detector (FMD). A brief overview of the PMD and FMD is given in the next sections.

3.2 Photon Multiplicity Detector

The Photon Multiplicity Detector (PMD), a highly-segmented pre-shower detector, allows to study an event-by-event measurement of photon multiplicity and its spatial distributions ($\eta - \phi$) in forward rapidity region. It is a purely Indian detector, including the design, fabrication and testing of the detector. For the first time, PMD was installed in WA93 experiment [8] at CERN SPS and was also used in WA98 experiment [9] at CERN SPS. Later on, PMD design was upgraded with latest electronics and readout techniques to handle the high multiplicity heavy-ion collisions and installed in the STAR experiment [10] at RHIC BNL and in the ALICE experiment [11] at LHC CERN.

3.2.1 Photon Multiplicity Detector in ALICE

ALICE PMD is a high granularity gas detector designed to measure photon multiplicity at TeV energies and works in the proportional counter region [12]. It consisted of two parallel planes: the Preshower plane (PRE) and the Charged Particle Veto (CPV) plane sandwiched by a lead converter of thickness 1.5 cm equals three radiation length ($3X_0$). PMD was located at a distance of 367.2 cm from the interaction point (IP) and covered a full azimuthal acceptance ($0^\circ < \phi < 360^\circ$) with pseudorapidity range of $2.3 < \eta < 3.9$.

3.2.1.1 Design and Fabrication

The two types of modules were fabricated for the PMD viz., the Long type and the Short type. The long type module consisted of 96 rows and 48 columns whereas the short type module had 48 rows and 96 columns. Each of the PMD plane contained four super modules (SM) and each super module had six unit modules resulting in total of 48 modules for PMD (24 unit modules for each CPV and PRE). A

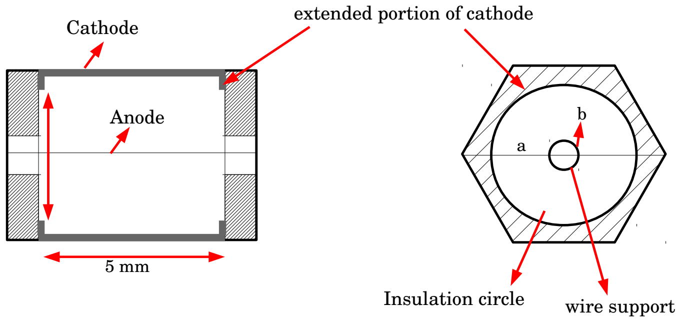

Figure 3.1: Schematic view of ALICE PMD unit cell.

rectangular shaped honeycomb arrangement had 96×48 or 48×96 unit cells. In order to control high multiplicity environment created in Pb-Pb collisions at LHC, the dimension of a cell was kept smaller for ALICE PMD than that of STAR PMD which led to a high granularity detector. Figure 3.1 shows the schematic view of hexagonal shaped unit cell having cross section area of 0.23 cm^2 and depth 0.5 cm [13]. The honeycomb chamber made of thin copper sheet was placed between two gold plated Printed Circuit Boards (PCB). A gold plated tungsten wire of diameter 20 μm was passed through the centre of each cell and a proper tension was applied to the wire while soldering. A continuous flow of gas mixture of Ar and CO_2 (70:30) was used as an active medium. The Pb converter plates placed between the CPV and PRE planes were also of two types depending upon the size of the module. The long plate had dimensions 49.05 cm × 21.7 cm and a short one had 42.5 cm × 25.15 cm. Also a support of 5 mm stainless steel (SS) plate was given to the lead converter plate and the module. The whole PMD was divided into two halves so as to install it easily around the beam pipe and each half had its own electronic accessories, gas supply and cooling systems.

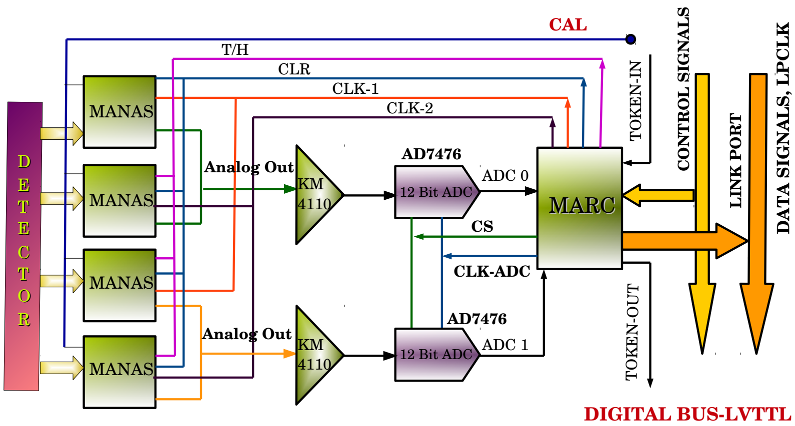

Figure 3.2: A circuit diagram of PMD FEE board.

3.2.1.2 Front End Electronics Readout

The honeycomb array had common cathode and gold plated anode wire readout. The Front End Electronic (FEE) board consisted of Multi Chip Module (MCM) and were used to collect the signal from anode wires at ground potential using the flexible kapton cables. The collected signals were processed, digitized and transferred to the Translator Board (TB). Further, TB forwarded the signal to Cluster Read Out Concentrator Unit System (CROCUS) through Patch Bus (PB) cables. The PMD Data Acquisition System (DAQ) received the signal from CROCUS via Detector Data Link (DDL) connected directly to ALICE DAQ system. The various PMD readout components are discussed below.

Front End Electronic Board: The FEE board comprised of four 16 input channel Multiplexed ANAlog Signal Processor (MANAS) chips, two inverting buffer amplifiers, a Muon Arm Readout Chip (MARC) and two serial 12 bit Analog to Digital Converters (AD7476). The schematic layout of the PMD FEE board is shown in figure 3.2.

MANAS chip is the basic component of FEE board. It is based on the GAS-

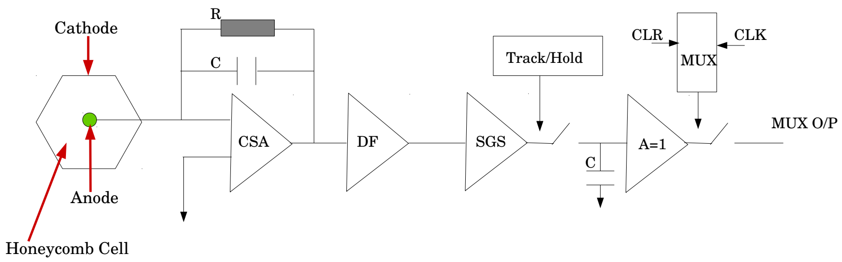

Figure 3.3: A circuit diagram of MANAS Chip.

SIPLEX with modified capacitor used for calibration and high voltage isolation for each channel. All the components of MANAS chip are depicted in figure 3.3. The design and fabrication of MANAS chip was done by the Indian members of ALICE-INDIA Collaboration. MANAS chip consisted of Charge Sensitive Amplifier (CSA), Semi Gaussian Shaper (SGS), Deconvolution Filter (DF), Track/Hold device and an analog multiplexer (MUX). The signal information from anode wire was collected by the CSA and integrated using feedback capacitor placed over the CSA. A long hyperbolic tail of integrated signal was removed by the DF and ensured the base line restoration. The SGS worked as pulse shape amplifier used to shape the signal pulse to Semi Gaussian and suppressed the signal pile up resulting in an increase in the signal-to-noise ratio. The MANAS chips were coupled to a single output channel where output signal was collected. The clock (CLK) pulse manages all the 16 input channels of MANAS chip.

An inverting buffer amplifier was another important component of PMD FEE board. Since ADCs operate on positive signals only, the inverting amplifiers were used to invert the collected negative signal into positive signal. The analog output signal received from the MANAS chip was converted to digital signal using 12-bit serial ADCs. Further, the digitized output was transferred to MARC which controls all the four MANAS chips and two ADCs.

CROCUS: The main task of Cluster Read Out Concentrator Unit System (CROCUS) was to collect and concentrate the signal from FEE board and send it to the PMD DAQ system which further transfers it to the ALICE DAQ system. The CROCUS had three parts: the CROCUS Back board, the CROCUS Front board (FRT) and the CROCUS Concentrator board (CRT). Each CROCUS consisted of five FRTs and one CRT board. In total there were four CROCUSs in the PMD connected to the two halves of the PRE and CPV planes.

Translator Board (TB): The output of the FEE board is Low Voltage Transistor Transistor Logic (LVTTL) signal whereas the output from the CROCUS is Low Voltage Differential Signal (LVDS). The TB converts all the LVTTL signals to LVDS before transferring it to the CROCUS and also translates the LVDS signals to LVTTL signals.

Patch Bus Cable: The main function of flexible and flat PATCH BUS cable was to transfer the LVDS signals from TB to CROCUS and vice-versa. The PMD patch bus cable was around 8.5 m long and 200 such cables were used for the readout in PMD.

3.2.1.3 Working Principle

PMD consisted of two identical planes: Preshower plane (PRE) and Charge Particle Veto (CPV) plane, and a lead converter plate was placed in between the planes. When a photon hits the plane facing the IP i.e., CPV plane and passes through the lead converter, an electromagnetic shower is produced, which produces equivalent signals in PRE plane as shown in figure 3.4. These showers produce signals in various cells of the active volume of PRE plane. When a charged particle hits the CPV, no electromagnetic shower is created by lead converter and therefore affects only single cell resembling those of Minimum Ionizing Particles (MIPs). The thickness of

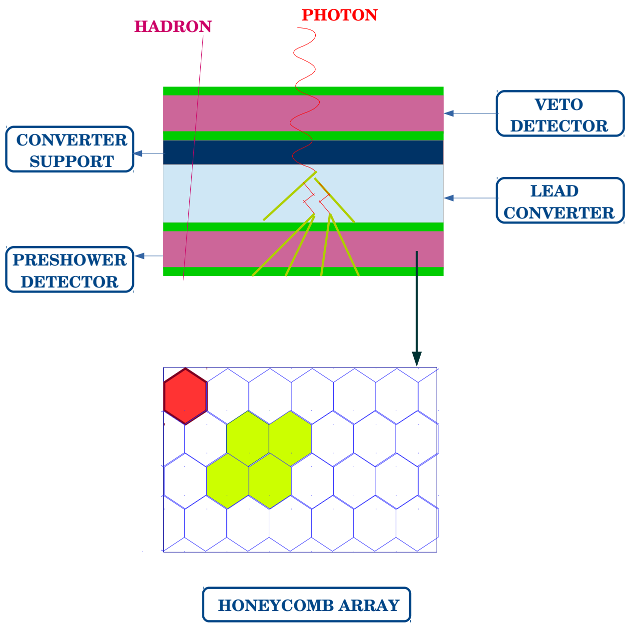

Figure 3.4: Schematic view of the working principle of PMD.

the lead converter is optimized in such a way that there should be large conversion of photons to electromagnetic showers and less transverse shower spread so as to prevent the shower overlap in high multiplicity heavy-ion collisions. In summary, the photons do not hit the CPV plane but deposit energy in the PRE plane whereas the charged particles produce hits in both planes. This information helps to reject the charged particles in obtaining the photon multiplicity as well as many event-by-event measurements sensitive to fluctuations analysis. A pictorial representation of the ALICE PMD is shown in figure 3.5.

3.2.1.4 Photon Reconstruction

The raw data collected from the ALICE PMD is further passed through various steps such as, zero suppression, pedestal subtraction, removal of hot/noisy cells of PMD, gain correction, etc. After applying all these corrections to the PMD data,

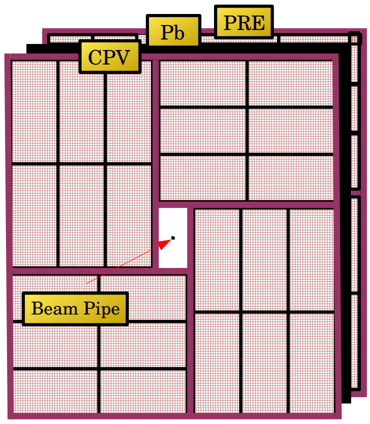

Figure 3.5: Pictorial view of ALICE PMD depicting two parallel planes CPV and PRE and a lead converter placed between the planes.

the photon reconstruction is performed which involves two steps: Clustering and Photon-hadron discrimination.

Clustering: A group of adjacent cells with non-zero ADC values are termed as clusters. The two clusters are separated from each other by a cell with zero ADC. For the clustering of cells, a clustering algorithm is used on raw data [14]. This algorithm is used in p+p collision data which involves low multiplicity events and is known as "*crude clustering*". The clusters are identified as the particles falling on the PMD. In case of Pb-Pb collisions, the particle density is very high and a cluster might merge into the other cluster resulting into the formation of a supercluster containing large number of cells. Thus, for the better identification of particles (clusters), one needs to divide the supercluster into smaller clusters which is named as *refined clusters* and the process is called "*refine clustering*". The photon and the charged particle both make clusters in preshower plane of PMD. In order to differentiate between the charged particles and the photons, photon-hadron discrimination is performed.

Photon-hadron discrimination: There are two ways to discriminate hadrons from photons in the data sample. The first one is based on the cluster size and ADC value. When an incident photon creates an electromagnetic shower in the PRE plane, it hits the number of cells rather than a single cell. The adjacent fired cells collectively make one cluster which is large and has higher ADC value compared to any incident hadron having small cluster size and lower ADC value. In order to reject the charged hadrons, an optimized cut on the cluster size (number of cells) and the cluster ADC is applied. At this stage, most of the charged particles are rejected and the data sample is dominated by photons. Another method to enhance the photon-to-hadron ratio is based on the hit information from the CPV plane. The CPV records a single hit for the hadrons and no hit for the photons. The CPV and PRE planes have one to one cell matching which is very useful in the discrimination procedure. A single hit for the hadron in CPV plane also produces a single hit in PRE plane in the same cell whereas photon passes through CPV with no hit information produces a shower of particles in the PRE plane by hitting more than one cell. This information leads to the identification of photons and charged particles. However, the data set used in the present analysis have very limited coverage for CPV and this method is not suitable to use.

3.3 Forward Multiplicity Detector

The Forward Multiplicity Detector (FMD) is a silicon pixel detector used to measure the charged particle multiplicity, pseudorapidity densities, the study of flow effects via azimuthal multiplicity dependence of charged particles on event-by-event basis and the thermodynamical properties of the deconfined state produced in heavy ion collisions.

Ring	z (cm)	Radial coverage (cm)	no. of Azimuthal sectors	no. of Radial strips	Eta (η) coverage
FMD1I	320	4.2-17.2	20	512	$3.68 < \eta < 5.0$
FMD2I	83.4	4.2-17.2	20	512	$2.28 < \eta < 3.68$
FMD2O	75.2	15.4-28.4	40	256	$1.70 < \eta < 2.29$
FMD3I	-62.8	4.2-17.2	20	512	$-3.40 < \eta < -2.01$
FMD3O	-75.2	15.4-28.4	40	256	$-2.29 < \eta < -1.70$

Table 3.1: FMD segmentation, radial coverage, distance from the IP and the pseudorapidity coverage for the FMD rings.

3.3.1 Layout of the FMD

FMD consists of three subdetectors: FMD1, FMD2 and FMD3. It has five rings separately placed around the beam pipe as shown in figure 3.6. Out of the five rings of FMD the two outer rings are named as: FMD2O and FMD3O, and the inner rings are called FMD1I, FMD2I, and FMD3I. The FMD2 and FMD3 covers the same η region on either side of the IP whereas FMD1 is positioned at larger distance compared to FMD2 and FMD3 from the IP and lies in the forward η region. The silicon sensor detector of thickness 300 μm is used for FMD [15]. These sensors are mounted on thin ceramic spacers and fixed onto the hybrid PC board containing preamplifier electronics. The silicon module containing silicon sensors is mounted on the honeycomb support structure and forms a complete FMD ring. Table 3.1 summarizes the z-position, segmentation, radial and pseudorapidity coverage of each ring. The radial overlap between the inner and outer rings reflects the overlap in the pseudorapidity coverage.

The present analysis needs the multiplicity of neutral and charged particles in the common η coverage. Out of the three FMDs, FMD1 and FMD2 lie on the same side where PMD is located while the FMD3 is positioned on the opposite side. The pseudorapidity range of FMD2I ($2.28 < \eta < 3.68$) overlaps with the PMD range ($2.3 < \eta < 3.9$). Thus FMD2I is used for the analysis.

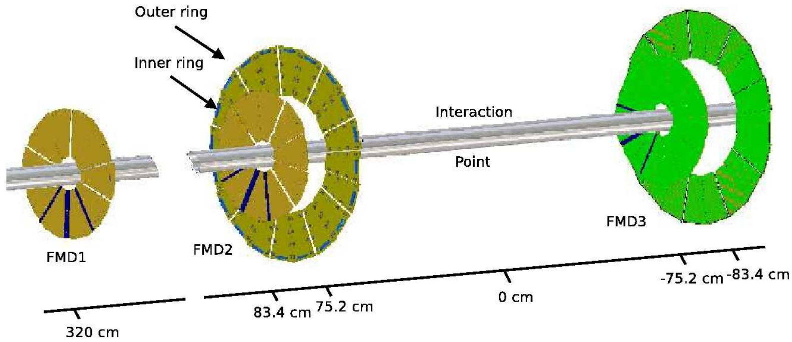

Figure 3.6: Conceptual layout of the FMD showing five rings mounted around the beam pipe. The FMD comprises three sub-detectors FMD1 (left), FMD2 (middle) and FMD3 (right).

3.3.2 Readout Electronics of the FMD

A complete FMD readout system of FMD is shown in figure 3.7. The silicon sensor and hybrid card contain VA1_ALICE Pre-Amplifier-Shaper integrated chips attached directly to the FMD modules via pitch adaptors in order to amplify the weak signal collected from the silicon strips. An amplified analog signal is digitized in the ALTRO Analog-to-Digital Converter and the digital information is stored in multi-event buffers before transferring it to DAQ. The Readout Control Unit (RCU) is used to send the data into another multi event buffer and transfers to the ALICE DAQ system via optical DDL link. RCU connects the FMD digitizer cards to the DAQ system, the Detector Control System (DCS) and the Timing and Trigger System (TTC). The RCU module also handles the data acquisition, trigger systems and detector control via indicated links.

3.4 Monte Carlo Models

At relativistic energies, heavy-ion collision is a possible choice to investigate the transition from normal nuclear matter to the deconfined state of quarks and gluons. Several experimental facilities at SPS, RHIC, and LHC, provide the opportunity to study the properties of highly dense matter and measured many observables, such as

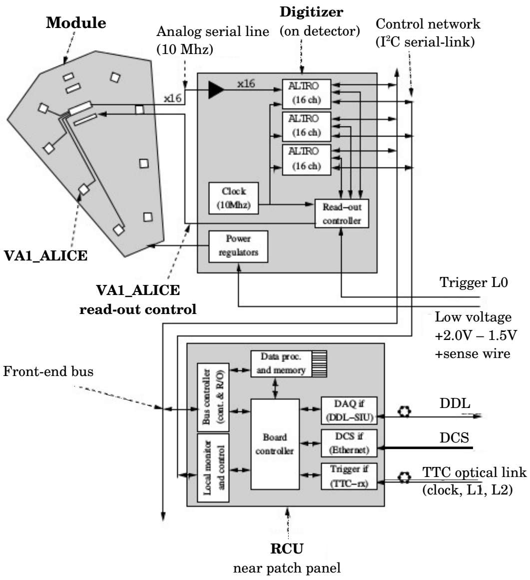

Figure 3.7: Architecture of the FMD readout electronics system.

transverse momentum spectra, pseudorapidity densities, elliptic flow, and particle azimuthal correlations etc. To understand the results from different measurements, many Monte Carlo models have been developed. The Heavy Ion Jet INteraction Generator (HIJING) and A Multi Phase Transport (AMPT) models are used to study the non-statistical fluctuations in charged neutral particle multiplicities.

HIJING: Heavy Ion Jet INteraction Generator (HIJING) is a FORTRAN based event generator which includes two processes, viz., jet production and jet fragmentation [16]. First includes the pQCD model and the jet fragmentation is carried by the Lund JETSET fragmentation model which hadronizes the partons. HIJING is mainly designed to explore the range of initial conditions possible in relativistic heavy ion collisions, multijet production, nuclear effects, jet quenching, and particle production for pp, $p\bar{p}$, pA, and AA collision systems over a wide energy range.

AMPT: A Multi Phase Transport (AMPT) is s dynamical transport model which includes various stages of heavy-ion collisions [17]. AMPT is capable of generating events for wide range of energies from 5 GeV to 5500 GeV for different collision systems viz., pp, pA, and AA. AMPT consists of four main components: the initial conditions, partonic interactions, transition from partonic to hadronic matter, and the final hadronic interactions. The spatial and momentum distributions of minijets are the part of initial conditions described by the HIJING model. Scatterings among partons are described by ZHang's Parton Cascade (ZPC), which includes two-body scatterings only [18]. The hadronic interactions are described by A Relativistic Transport (ART) model [19]. The AMPT model is characterized into two different parts based on the processes involved in it.

- **AMPT Default:** In default AMPT version [20], after successive collisions partons recombine to their parent strings and resulting in hadron production using the Lund string fragmentation model [21]. The particle production after the collision of two Woods Saxon shaped nuclei is described by hard and soft components. Hard processes involve higher energy transfer and produce energetic jets described by PYTHIA whereas the soft component includes JETSET fragmentation model.

- **AMPT String Melting:** In this AMPT model [22], the partons undergo a transition to the hadronic matter via quark coalescence mechanism, which converts a pair of quark and anti-quark ($q\bar{q}$) into mesons and three quarks (qqq) into baryons. So besides the recombination to their parent strings like in Default AMPT, the transition from partonic to hadronic state is achieved by the Quark Coalescence Model [23]. In the absence of partonic and hadronic interactions, the AMPT model with string melting configuration reduces to HIJING.

For the current study, the official Monte Carlo samples of HIJING and AMPT

Collision system	Pb–Pb
Collision energy	2.76 TeV
HIJING	LHC11a10a_bis, $\sim$ 3M
AMPT (String Melting ON Rescattering OFF)	LHC13f3a, $\sim$ 39M
AMPT (String Melting OFF Rescattering ON)	LHC13f3b, $\sim$ 53M
AMPT (String Melting ON Rescattering ON)	LHC13f3c, $\sim$ 39M

Table 3.2: Details of the data sets used for the analysis.

included in the ALICE AliRoot framework are used and a detailed description of data sets is listed in Table 3.2.

3.5 Analysis Strategy

The heavy-ion collision data collected by ALICE contain millions of events which are good and bad according to the run conditions. In order to select the highly efficient heavy-ion runs one has to select good run numbers and the events which are different from the beam-gas or machine induced interactions.

3.5.1 Event Selection

A nearly uniform detector acceptance can be achieved by applying different selection cuts over good events. In ALICE framework, this task is performed by a class named *AliPhysicsSelection* which selects the real physical events by rejecting the background rich events. There are different types of trigger classes on the basis of which *AliPhysicsSelection* class works. For this thesis work, a minimum bias collision events are analyzed. The Minimum Bias (MB) trigger rejects the events produced by beam-gas interactions or from other possible backgrounds. It is configured by a hit in the VZERO-A or VZERO-C detector or in any of the first two layers of the ITS i.e., SPD detector.

- **Centrality Selection:** In ALICE analysis, the centrality selection is done by an official centrality task i.e., *AliCentrality*, using the multiplicity distri-

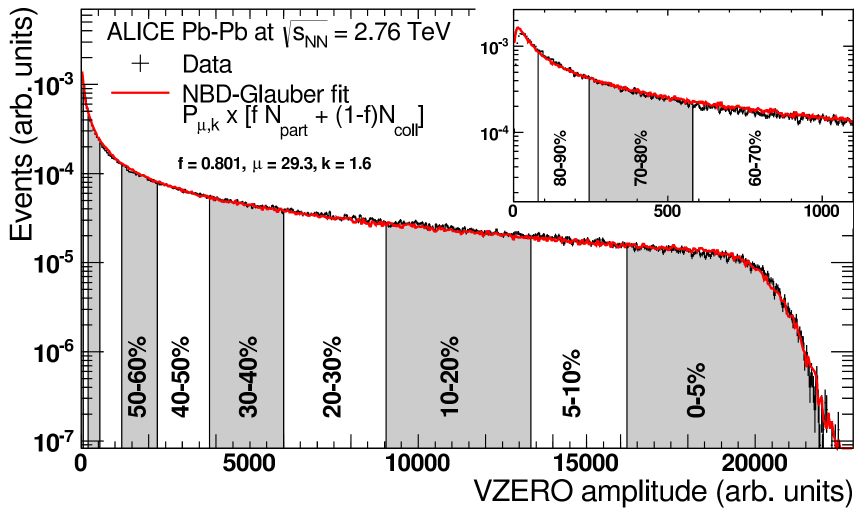

Figure 3.8: The centrality distribution obtained by summing the VZERO amplitude distributions and fitted with the Glauber NBD fit (represented by red line). Different centrality bins shown by vertical lines are used in the analysis of Pb-Pb collisions at $\sqrt{s}_{\mathrm{NN}} = 2.76$ TeV.

butions from various detectors meant for this measurement, such as VZERO, ZDC, SPD, and TPC. In particular, the centrality using VZERO detectors is obtained from the sum of the signal amplitude distributions in the VZERO detectors. On the basis of this centrality calculation, analysis task in ALICE framework assigns a value for each centrality by dividing it into different classes from 0 to 90% illustrated in figure 3.8. The ZDC estimates the collision centrality by measuring the energy deposited by non-interacting particles ($N_{spectators}$) in ZDC. In this analysis, the VZERO detector is used as the centrality estimator.

- **Vertex Selection:** The vertex cut ($| v_z |$) of ± 10 cm at longitudinal vertex position from the nominal interaction point is applied on MB selected events and the distribution is shown in figure 3.9. The vertex cut ensures a uniform acceptance region.

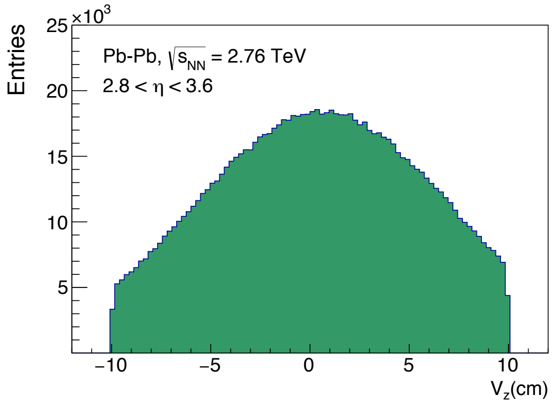

Figure 3.9: Z-vertex distribution for Pb-Pb collisions at $\sqrt{s}_{\mathrm{NN}}$ = 2.76 TeV.

Event and track cuts	Value
Physics selection	AliEvent::kMB
Vertex	$\mid V_z \mid < 10cm$
Centrality Estimator	V0M
Pseudorapidity (η)	$2.8 < \eta < 3.6$
N_{ch} hits	$0.3 < E_{dep}/E_{MIP} < 1$ taken as one particle $E_{dep}/E_{MIP} > 1$ taken as two particles
$N_{\gamma-like}$ hits	> 432 (6∗MIP)
Number of cells (N_{cell}) fired in PMD	> 1

Table 3.3: Event and track cuts used for the analysis.

3.5.2 Track Selection

After the event selection, the next step is to select good tracks by rejecting the fake tracks (tracks which fail during the reconstruction process). For the present analysis, the neutral particles are reconstructed in the PMD and the charged tracks are taken from the FMD. The analysis is performed on Event Summary Data (ESD) due to the absence of Analysis Object Data (AOD) for PMD. As discussed earlier in section 3.3.1, the FMD2I ring is selected due to the common pseudorapidity coverage ($2.28 < \eta < 3.68$) with the PMD ($2.3 < \eta < 3.9$). Table 3.3 lists the detailed description of event and track cuts used in the analysis.

Since FMD is not an isolated detector and is surrounded by other ALICE detectors. The primary particles produced during the collision pass through various

ALICE detectors before reaching the FMD. Thus the scattering of primary particles on the detector material leads to the production of secondary particles which also deposit energy in the FMD. Figure 3.10 shows the energy deposited by secondary particles in each FMD ring and the SPD [24]. It is clear from the figure that the main source of secondary particles is from the material interactions. FMD2I ring has comparatively lesser energy deposition from the secondary particles as compared to the other FMD rings. Thus, the FMD2I ring with η coverage $2.8 < \eta < 3.6$ is selected for the analysis.

The FMD2I ring consists of twenty sectors and 512 strips covering the full azimuthal plane. Each sector of FMD2I ring has four pre-amplification chips (VA) named as VA0, VA1, VA2, and VA3. Figure 3.11 depicts the energy loss distributions per VA chip for the sector 16 and 17. It is observed that there are issues with the two VA chips of sector 16 and 17. The MIP peak is shifted down in four out of eight VA chips which consequently affect the azimuthal distribution and the analysis. The dashed line in each plot is marked to compare the distributions of eight VA chips. Thus, out of 20 the two sectors 16 and 17 are excluded from the analysis [24].

3.5.3 Methodology

WA98 experiment searched the charged-neutral fluctuations in nuclear collisions at CERN SPS using the SWM with magnetic field off operation at 158 A GeV [3]. STAR experiment at RHIC also performed the same analysis at $\sqrt{s_{\rm NN}} = 200$ GeV using the observables $\nu_{dyn}^{ch-\gamma}$ and $r_{m,1}$ [7]. The study of charged to neutral particle fluctuations in heavy-ion collisions is performed using the PMD and FMD with overlapping geometric acceptance in the forward pseudorapidity region ($2.28 < \eta < 3.68$). Due to the absence of some modules or the non-working cells of PMD, and as well as less energy deposition by secondary particles in $2.8 < \eta < 3.6$ region of FMD2I, a reduced common η coverage of both detectors is used for the analysis. The

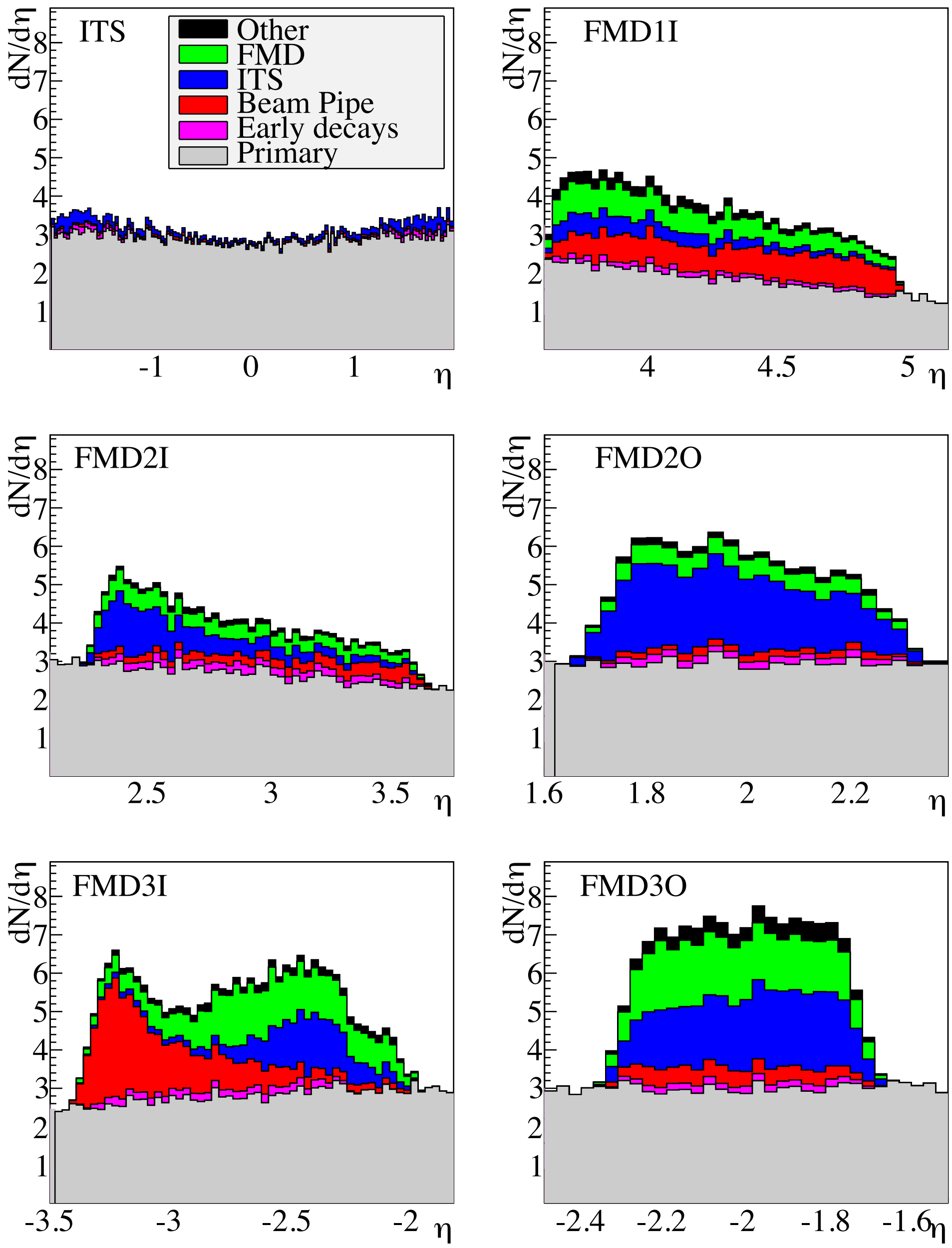

Figure 3.10: Detailed view of energy deposition by secondary particles in the SPD and each FMD ring.

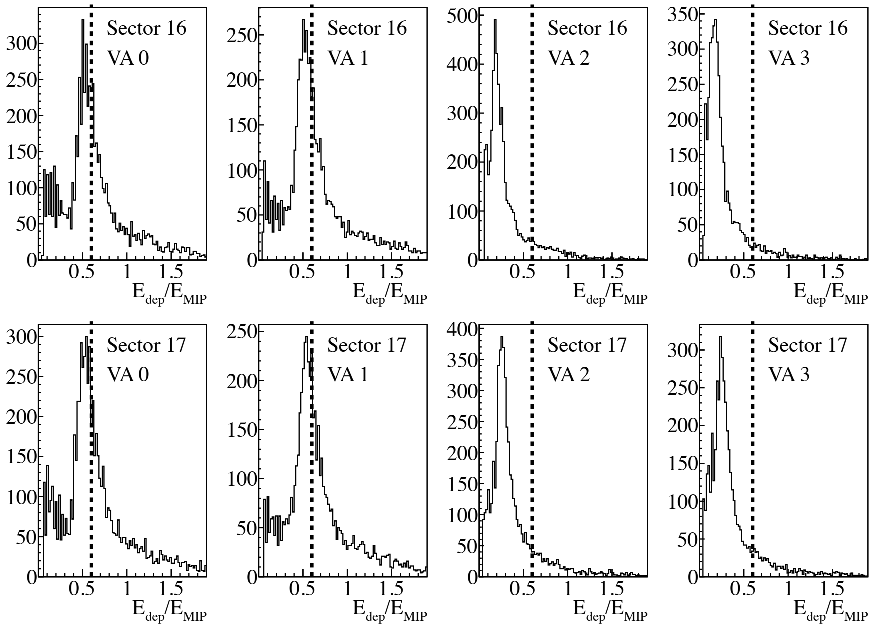

Figure 3.11: Energy distributions per VA chip in sectors 16 and 17 of the FMD2I ring. Each distribution shows the energy loss in FMD strips of a single VA chip.

measurement of dynamical fluctuations is performed using two different methods which are discussed below.

- Localized Event Analysis
- Global Event Analysis

3.5.3.1 Localized Event Analysis

The localized event analysis method scans each available $\eta - \phi$ region at microscopic level and search for the unusual events present in the data sample.

Sliding Window Method: The localized charged neutral fluctuations are studied using the Sliding Window Method (SWM) [25] which was previously used in WA98 experiment at CERN SPS. This method allows to investigate all regions with unusually small or large fractional values of f defined as,

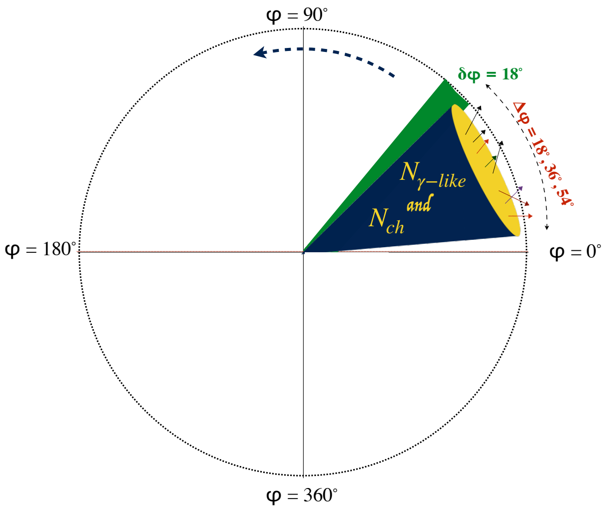

Figure 3.12: A pictorial view of the Sliding Window Method (SWM).

$$f = \frac{N_{\gamma-like}}{N_{ch}} \tag{3.1}$$

where, $N_{\gamma-like}$ and N_{ch}, are the number of gamma-like particles and charged particles, respectively. The fraction is measured for the most central (10%) events, determined by the V0M centrality estimator. The whole azimuthal plane is scanned by sliding $\Delta\Phi$ window of chosen step size $\delta\phi = 18^{\circ}$ over the full $\eta - \phi$ plane as depicted in figure 3.12. The choice of step size $\delta\phi = 18^{\circ}$ is limited by FMD resolution in the azimuthal plane. The fraction f is calculated in each event for different window sizes $\Delta\Phi = 18^{\circ}$, 36°, and 54°, using Eq. 3.1. The maximum and minimum values of fraction f obtained in each event correspond to "*gamma excess*" and "*charge excess*", respectively.

3.5.3.2 Global Event Analysis Methods

This method includes the analysis of the observables averaged over all the events for a given centrality.

$\boldsymbol{\nu_{dyn}^{ch-\gamma}}$ **for Charged Neutral Fluctuations:** The deconfined phase transition is associated with enhanced fluctuations in conserved quantities such as strangeness, net-charge, and baryon number etc. The formation and decay of DCC domains could lead to distinct distributions of neutral to pion ratio than the generic pion production. If this process survives the final state interactions, it will appear as anti-correlation between the yields of neutral and charged pions. The charged particle multiplicity is represented as charged pions (ch) and photons (γ) as neutral pions. In case of generic production, the neutral and charged particles would be produced in equal abundances due to the isospin symmetry. The formation of pions of particular isospin causes large deviation in the $\gamma - ch$ correlation from the generic expectation. To understand the relation between neutral and charged pions, the observable needs to be sensitive to $\gamma - ch$ correlation. Thus, a robust variable $\nu_{dyn}^{ch-\gamma}$ is introduced which involves lowest order factorial moments that helps to reduce the statistical uncertainties and is defined as,

$$\nu_{dyn}^{ch-\gamma} = \frac{\left\langle N_\gamma(N_\gamma - 1)\right\rangle}{\left\langle N_\gamma\right\rangle^2} + \frac{\langle N_{ch}(N_{ch} - 1)\rangle}{\langle N_{ch}\rangle^2} - 2\frac{\left\langle N_\gamma N_{ch}\right\rangle}{\left\langle N_\gamma\right\rangle\langle N_{ch}\rangle} \tag{3.2}$$

$$= \omega_\gamma + \omega_{ch} - 2 \times corr_{ch-\gamma} \tag{3.3}$$

The first two terms are the measures of photon number fluctuations (ω_γ) and charged particle multiplicity fluctuations (ω_{ch}) and the third term corresponds to $ch - \gamma$ correlation ($corr_{ch-\gamma}$). The $\langle ... \rangle$ represents an average over all events. In case of high multiplicity environment, i.e., a purely statistical fluctuations, the individual terms in Eq. 3.2 would become unity whereas for low multiplicity events, the three individual terms may deviate from unity even in the absence of dynamical fluctuations. In view of this, it is difficult to decide on the basis of individual terms whether the fluctuations are dynamical or statistical. To overcome this individual term problem, the observable $\nu_{dyn}^{ch-\gamma}$ is constructed by adding the three terms defined in Eq. 3.2 [26]. Thus, the $\nu_{dyn}^{ch-\gamma}$ term becomes non-zero in case of dynamical fluctuations and zero for purely statistical fluctuations.

The observable $\nu_{dyn}^{ch-\gamma}$ is strongly dependent on the average multiplicity of photons ($\langle N_\gamma \rangle$) and charged particles ($\langle N_{ch} \rangle$). The scaled average multiplicity dependence of $\nu_{dyn}^{ch-\gamma}$ is studied and the results are compared with those of Monte Carlo event generators viz., HIJING and AMPT.

Factorial Moments: The dynamical fluctuations in charged-to-neutral particles were also studied by the Minimax collaboration at the Tevatron, Fermilab by using factorial moments method [4]. The expression for the normalized factorial moment analysis can be written as,

$$F_m \equiv \frac{\langle N(N-1).....(N-m+1) \rangle}{\langle N \rangle^m} \tag{3.4}$$

To search for the DCC domains, a usual multiparticle formalism (F_m) is extended to bivariate distributions with variables N_γ and N_{ch},

$$F_{m,n} = \frac{\left\langle N_{ch}(N_{ch}-1).....(N_{ch}-m+1)\ N_\gamma(N_\gamma-1).....(N_\gamma-n+1) \right\rangle}{\langle N_{ch} \rangle^m \left\langle N_\gamma \right\rangle^n} \tag{3.5}$$

The ratio of normalized factorial moments introduces a robust observable,

$$r_{m,1} = \frac{F_{m,1}}{F_{m+1,0}} \tag{3.6}$$

putting the values from Eq. 3.5 in Eq. 3.6, the $r_{m,1}$ becomes,

$$r_{m,1} = \frac{\left\langle N_{ch}(N_{ch}-1)...(N_{ch}-m+1)\ N_\gamma \right\rangle \langle N_{ch} \rangle}{\langle N_{ch}(N_{ch}-1)...(N_{ch}-m) \rangle\ \ \left\langle N_\gamma \right\rangle} \tag{3.7}$$

For the pion production under isospin symmetry case i.e., the generic case of

Poisson distribution, $r_{m,1} = 1$ while for the pure DCC case, $r_{m,1}$ deviates from unity. The advantage of using this variable is that it is independent of inclusive particle multiplicities and insensitive to detector inefficiencies.

$$r^{gen}_{m,1} = 1, \qquad (Poisson\ limit/generic\ pion\ case) \tag{3.8}$$

$$r^{DCC}_{m,1} = \frac{1}{m+1} \qquad (DCC) \tag{3.9}$$

The variation of $r_{m,1}$ is studied as a function of average multiplicity for data and different Monte Carlo models. The $r_{m,1}$ dependence on higher moments for top central collisions is also studied. In order to minimize the contamination effects, the tight selections are applied on the photon-hadron discrimination procedure and the results obtained from the data are compared with the HIJING and AMPT models.

3.6 Statistical Error Estimation

For an event-by-event fluctuations analysis, the statistical errors are estimated using two methods explained in this section.

- **Analytic Method:** The uncertainty in the $\nu^{ch-\gamma}_{dyn}$ is estimated using analytic method. The detailed description of this method can be found in ref. [27] and the expression for the analytic method is written below.

$$
\begin{aligned}
V[\nu_{dyn}] = \frac{1}{N}\frac{1}{\langle m\rangle^6\langle n\rangle^6} \times \Big\{ & 6\left\langle n^2m^2\right\rangle\langle n\rangle^4\langle m\rangle^4 - 4\left\langle n^3m\right\rangle\langle n\rangle^3\langle m\rangle^5 \\
& -4\left\langle nm^3\right\rangle\langle n\rangle^5\langle m\rangle^3 + 8\left\langle n^2m\right\rangle\left\langle n^2\right\rangle\langle n\rangle^2\langle m\rangle^5 + 8\left\langle nm^2\right\rangle\left\langle m^2\right\rangle\langle n\rangle^5\langle m\rangle^2 \\
& -4\left\langle n^2m\right\rangle\langle nm\rangle\left\langle n^3\right\rangle\left\langle m^4\right\rangle - 4\left\langle nm^2\right\rangle\langle nm\rangle\langle n\rangle^4\left\langle m^3\right\rangle - 4\left\langle n^2m\right\rangle\left\langle m^2\right\rangle\langle n\rangle^4\langle m\rangle^3 \\
& -4\left\langle nm^2\right\rangle\left\langle n^2\right\rangle\langle n\rangle^3\langle m\rangle^4 + 8\langle nm\rangle^3\langle n\rangle^3\langle m\rangle^3 - 4\langle nm\rangle^2\left\langle n^2\right\rangle\langle n\rangle^2\langle m\rangle^4 \\
& -4\langle nm\rangle^2\left\langle m^2\right\rangle\langle n\rangle^4\langle m\rangle^2 - 4\langle nm\rangle^2\langle n\rangle^4\langle m\rangle^4 + 4\langle nm\rangle\left\langle n^3\right\rangle\langle n\rangle^2\langle m\rangle^5 \\
& +4\langle nm\rangle\left\langle m^3\right\rangle\langle n\rangle^5\langle m\rangle^2 - 8\langle nm\rangle\left\langle n^2\right\rangle^2\langle n\rangle\langle m\rangle^5 - 8\langle nm\rangle\left\langle m^2\right\rangle^2\langle n\rangle^5\langle m\rangle \\
& +8\langle nm\rangle\left\langle n^2\right\rangle\left\langle m^2\right\rangle\langle n\rangle^3\langle m\rangle^3 + 4\langle nm\rangle\left\langle n^2\right\rangle\langle n\rangle^3\langle m\rangle^5 + 4\langle nm\rangle\left\langle m^2\right\rangle\langle n\rangle^5\langle m\rangle^3 \\
& +\langle n\rangle^4\langle n\rangle^2\langle m\rangle^6 + \left\langle m^4\right\rangle\langle n\rangle^6\langle m\rangle^2 - 4\left\langle n^3\right\rangle\left\langle n^2\right\rangle\langle n\rangle\langle m\rangle^6 - 4\left\langle m^3\right\rangle\left\langle m^2\right\rangle\langle n\rangle^6\langle m\rangle \\
& +4\left\langle n^2\right\rangle^3\langle m\rangle^6 + 4\left\langle m^2\right\rangle^3\langle n\rangle^6 - \left\langle n^2\right\rangle^2\langle n\rangle^2\langle m\rangle^6 - \left\langle m^2\right\rangle^2\langle n\rangle^6\langle m\rangle^2 \\
& -2\left\langle n^2\right\rangle\left\langle m^2\right\rangle\langle n\rangle^4\langle m\rangle^4 + 2\left\langle n^2m\right\rangle\langle n\rangle^4\langle m\rangle^4 + 2\left\langle nm^2\right\rangle\langle n\rangle^4\langle m\rangle^4 \\
& -4\left\langle n^2m\right\rangle\langle n\rangle^3\langle m\rangle^5 - 4\left\langle nm^2\right\rangle\langle n\rangle^5\langle m\rangle^4 + 4\langle nm\rangle^2\langle n\rangle^4\langle m\rangle^3 + 4\langle nm\rangle^2\langle n\rangle^3\langle m\rangle^4 \\
& -4\langle nm\rangle\left\langle n^2\right\rangle\langle n\rangle^3\langle m\rangle^4 - 4\langle nm\rangle\left\langle m^2\right\rangle\langle n\rangle^4\langle m\rangle^3 + 4\langle nm\rangle\left\langle n^2\right\rangle\langle n\rangle^2\langle m\rangle^5 \\
& +4\langle nm\rangle\left\langle m^2\right\rangle\langle n\rangle^5\langle m\rangle^2 - 4\langle nm\rangle\langle n\rangle^5\langle m\rangle^4 - 4\langle nm\rangle\langle n\rangle^4\langle m\rangle^5 + 2\left\langle n^3\right\rangle\langle m\rangle^6 \\
& +2\left\langle m^3\right\rangle\langle n\rangle^6\langle m\rangle^2 - 4\left\langle n^2\right\rangle^2\langle n\rangle\langle m\rangle^6 - 4\left\langle m^2\right\rangle^2\langle n\rangle^6\langle m\rangle + 2\left\langle n^2\right\rangle\langle n\rangle^4\langle m\rangle^5 \\
& +2\left\langle m^2\right\rangle\langle n\rangle^5\langle m\rangle^4 + 2\left\langle n^2\right\rangle\langle n\rangle^3\langle m\rangle^6 + 2\left\langle m^2\right\rangle\langle n\rangle^6\langle m\rangle^3 + 2\langle nm\rangle\langle n\rangle^4\langle m\rangle^4 \\
& +\left\langle n^2\right\rangle\langle n\rangle^2\langle m\rangle^6 + \left\langle m^2\right\rangle\langle n\rangle^6\langle m\rangle^2 - \langle n\rangle^6\langle m\rangle^4 - \langle n\rangle^4\langle m\rangle^6 \\
& -2\langle n\rangle^5\langle m\rangle^5 + O(\frac{1}{N^2})\Big\}
\end{aligned}
\tag{3.10}
$$

here N is the total number of events, m and n are photon number and charged particle multiplicity, respectively.

- **Sub-sampling Method:** In this method, the total number of events in data are divided into "k" sub-samples by randomly choosing the almost equal number of events in each sub-sample. The observable x is calculated for each sub sample and the final error in x is also estimated by taking the standard deviation (σ) of those calculated values (x_k) in each sub-sample from the average value ($\langle x \rangle$). The statistical error in the mean value of x is defined as,

$$\sigma_{\langle x \rangle} = \frac{\sigma}{\sqrt{N}} \tag{3.11}$$

where

$$\sigma = \sqrt{\frac{\sum (x_k - \langle x \rangle)^2}{N-1}} \tag{3.12}$$

$$and \qquad \mu = \langle x \rangle = \frac{1}{N} \sum_{k=1}^{N} x_k \tag{3.13}$$

here μ is the mean value of observable x. For this analysis, ten such sub-samples are taken to estimate the statistical uncertainties for data as well as for Monte Carlo models.

3.7 Analysis Results

The results obtained for charged-neutral fluctuations measurement in Pb-Pb collisions at $\sqrt{s_{\mathrm{NN}}} = 2.76$ TeV are discussed in this section.

3.7.1 Data Quality Assurance Checks

To check the uniform acceptance of the detector, the data quality assurance plots are studied such as azimuthal angle (ϕ) and pseudorapidity (η) distributions. In the data quality checks, the azimuthal angle distributions for both detectors FMD and PMD are studied in the selected common pseudorapidity coverage $2.8 < \eta < 3.6$ and are shown in figure 3.13 (left) and (right), respectively. In case of FMD, ϕ

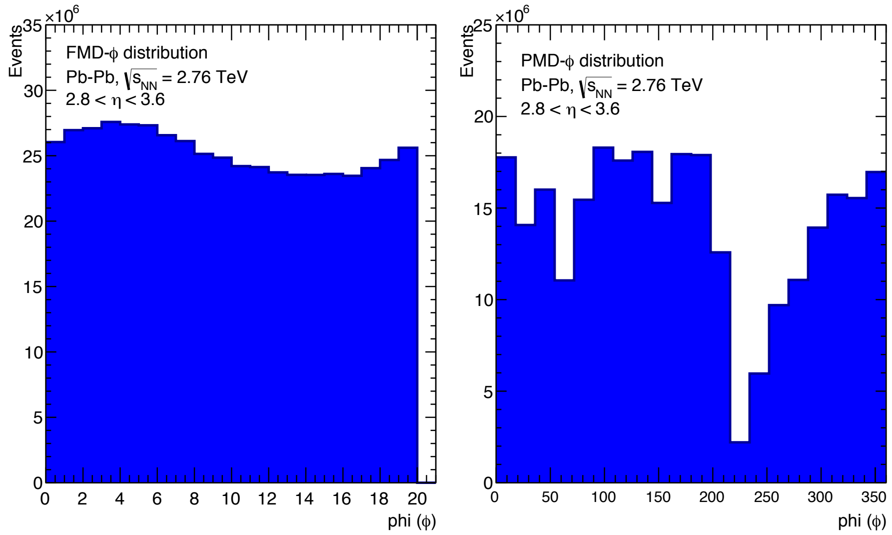

Figure 3.13: Azimuthal angle distributions for FMD (left) and PMD (right) in a common pseudorapidity region $2.8 < \eta < 3.6$ selected for the analysis.

is close to uniform distribution whereas for PMD, the variation is much more. In PMD, some of the sectors have very low multiplicity with respect to neighbouring sectors. This large variation is due to the non-working modules of PMD shown by blank areas in figure 3.14. Due to the large variation, the PMD azimuthal coverage $216^\circ < \phi < 334^\circ$ corresponding to sectors 13, 14, 15, 16, 17 and 18 is rejected and the analysis is performed for the sectors $1-12$ ($0^\circ < \phi < 216^\circ$) and for 19, 20 ($334^\circ < \phi < 360^\circ$).

Figure 3.14 shows the X and Y positions of hits on the preshower plane of PMD and plotted as a function of η. Each ring corresponds to different η range and is represented by different colour. Figure 3.14 presents the full η coverage of PMD (left) and the hit distribution for the selected η region (right). The rectangular shaped boxes represent the PMD modules and the blank area in the figure with no hits corresponds to uninstalled modules or the non-functional area of the PMD.

Figure 3.15 shows the correlation between $N_{\gamma-like}$ and FMD2I N_{ch} in a common

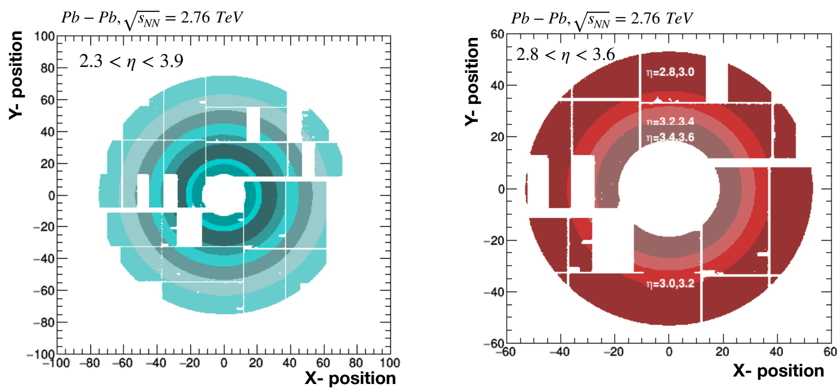

Figure 3.14: X-Y display of hits on the preshower plane of PMD in full η coverage $2.3 < \eta < 3.9$ (left) and for $2.8 < \eta < 3.6$ selected for the analysis (right) in Pb-Pb collisions at $\sqrt{s}_{\mathrm{NN}} = 2.76$ TeV. The coloured rings indicate different η regions.

η coverage of $2.8 < \eta < 3.6$. It is observed that N_{ch} increases linearly with $N_{\gamma-like}$.

3.7.2 Charged-to-Neutral Fluctuations using SWM

An event-by-event charged-to-neutral fluctuations are analyzed for Pb-Pb collisions at $\sqrt{s}_{\mathrm{NN}} = 2.76$ TeV for the most central events (0-10%) in the chosen window $\Delta\Phi = 18^\circ, 36^\circ$, and 54° over the azimuthal plane. The fraction f is calculated for each $\Delta\Phi$ using Eq. 3.1 and the distributions are shown in figures 3.16, 3.17, and 3.18. The scatter plots for $N_{\gamma-like}$ versus N_{ch} are also displayed in these figures.

For Azimuth Window Size $\Delta\Phi = 18^\circ$: In figure 3.16, the top left and right panels show the scatter plots of $N_{\gamma-like}$ versus N_{ch} for gamma excess ($\gamma-$excess) and charge excess ($ch-$excess), respectively. From the upper plots it is clearly seen that the correlation between $N_{\gamma-like}$ and N_{ch} is not symmetric around the line $N_{\gamma-like} = N_{ch}$. In the top left plot, one can see more number of photons than charged particles in some events. The similar behaviour is observed in the top right plot, where more number of N_{ch} are observed compared to $N_{\gamma-like}$. Such events with an excess of one particular type of particles lead to the dynamical fluctuations. The distributions of fractions are displayed in bottom left and right

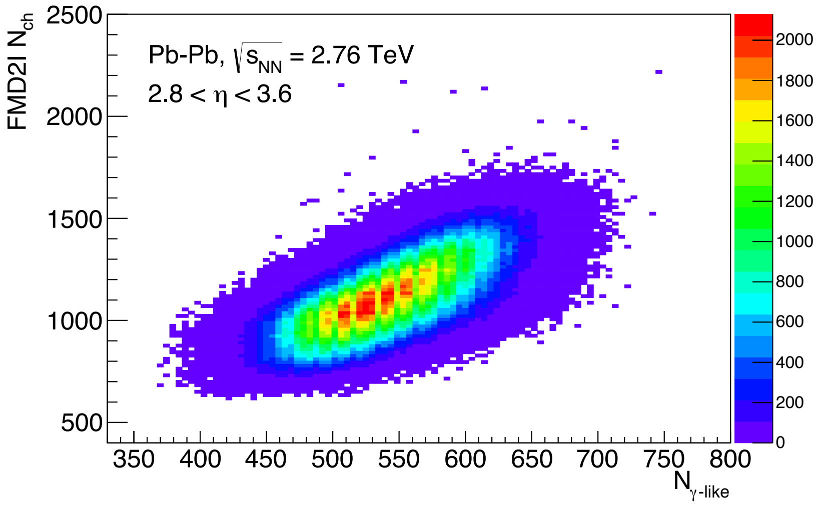

Figure 3.15: Distributions of $N_{\gamma-like}$ vs N_{ch} for PMD and FMD2I ring in pseudo-rapidity region $2.8 < \eta < 3.6$.

panels for $\gamma-$excess and $ch-$excess, respectively. The one-dimensional plots describe that the distributions are not Gaussian which is the case for statistical fluctuations, but have an extra tail for higher fraction values of f ($\gamma-$excess) and $1/f$ ($ch-$excess) indicating the presence of localized charged-neutral fluctuations.

For Azimuth Window Size $\Delta\Phi = 36^\circ$ and 54°: A similar distributions showing the correlation between $N_{\gamma-like}$ versus N_{ch} for gamma excess and charge excess, and their respective 1-dimensional projections are studied for $\Delta\Phi = 36^\circ$ and 54° in figures 3.17 and 3.18, respectively. If we compare the three azimuth windows, it is seen that the $\gamma-$excess and $ch-$excess decreases with increase in window size from 18° to 36° and further to 54°.

3.7.2.1 Event Characterization for $\Delta\Phi = 18^\circ$, 36° and 54°

From 1-dimensional distributions of $\gamma-$excess and $ch-$excess, the events from the tail of the distributions are filtered out by applying cut on higher f and $1/f$ values, respectively, for $\Delta\Phi = 18^\circ$, 36°, and 54°. Again the ratios f $(= N_{\gamma-like}/N_{ch})$ and

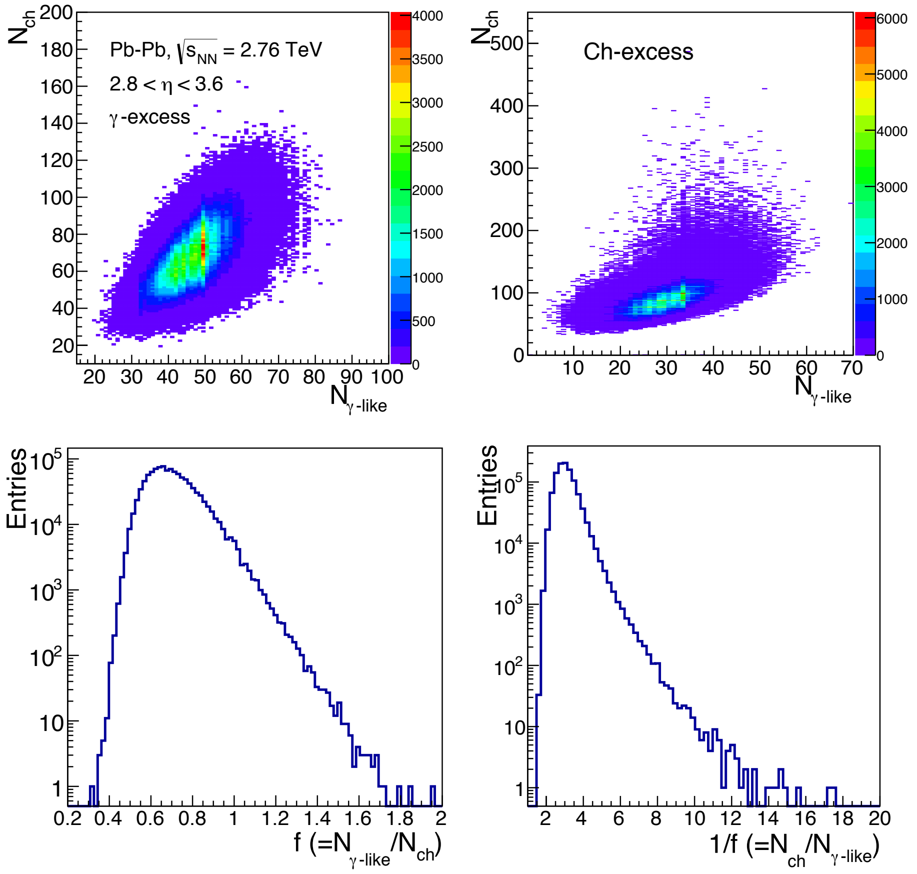

Figure 3.16: For $\Delta\Phi = 18^{\circ}$: the scatter plots between $N_{\gamma-like}$ versus N_{ch} (upper panels) and fraction (f), ($1/f$) distributions for $\gamma-$excess and $ch-$excess (bottom panels), respectively.

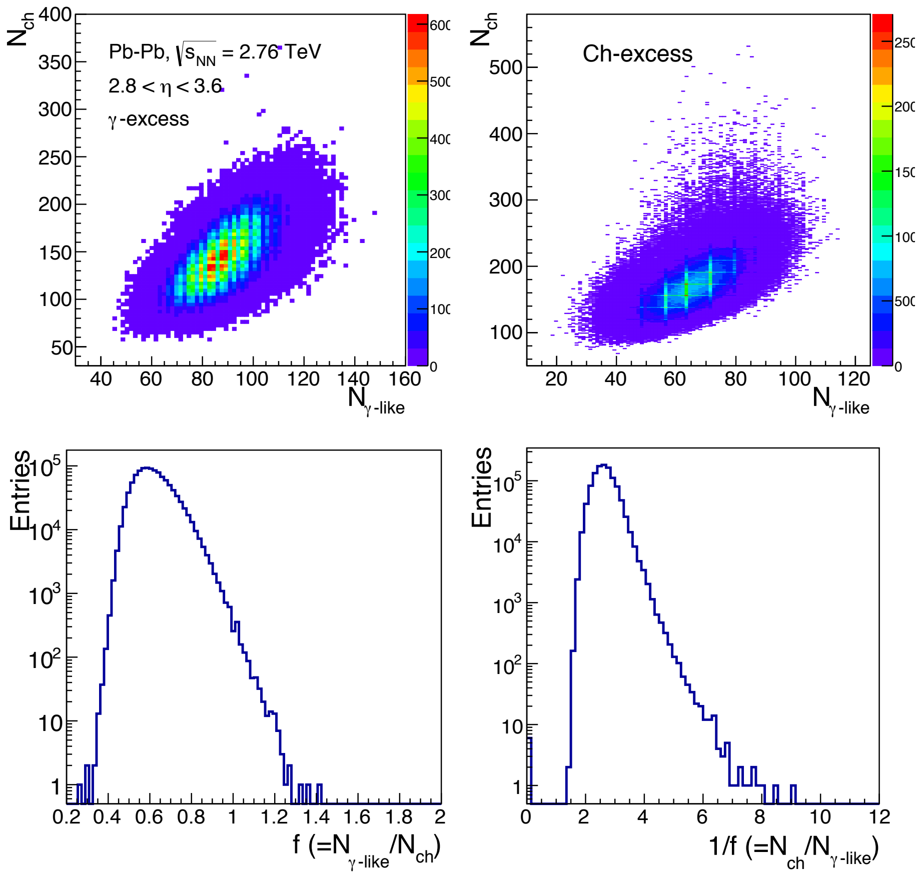

Figure 3.17: For $\Delta\Phi = 36^{\circ}$: the scatter plots between $N_{\gamma-like}$ and N_{ch} (upper panels) and fraction (f), ($1/f$) distributions for $\gamma-$excess and $ch-$excess (bottom panels), respectively.

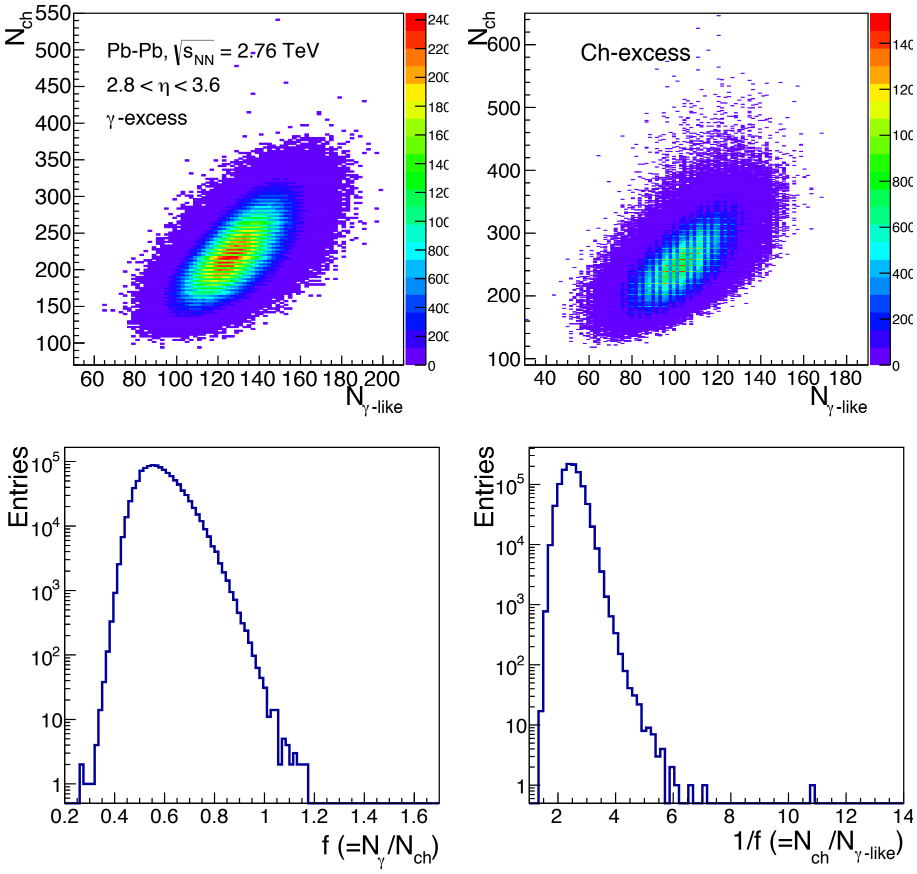

Figure 3.18: For $\Delta\Phi = 54^{\circ}$: the scatter plots between $N_{\gamma-like}$ and N_{ch} (upper panels) and fraction (f), ($1/f$) distributions for $\gamma-$excess and $ch-$excess (bottom panels), respectively.

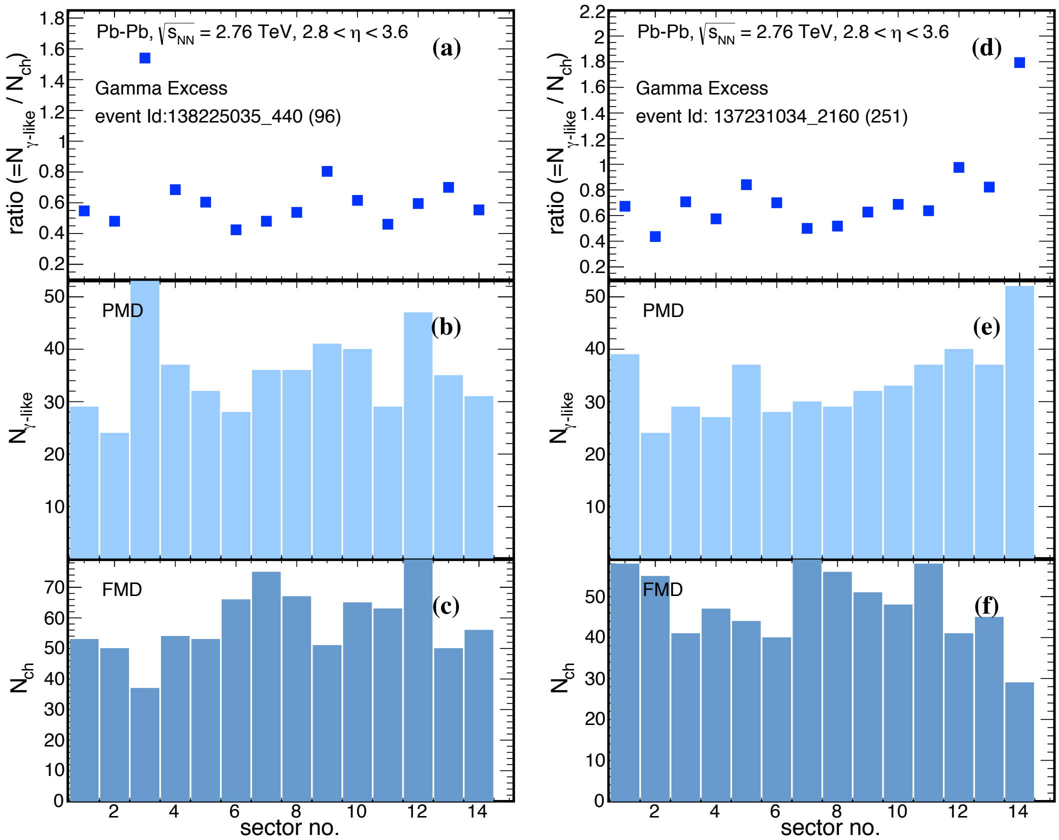

Figure 3.19: $\gamma-$excess for $\Delta\phi = 18^{\circ}$: the ratio plot of $N_{\gamma-like}/N_{ch}$ in (a), $N_{\gamma-like}$ hit distribution in (b), and N_{ch} hits in (c) w.r.t sectors covering the azimuthal angle selected for the analysis. Another example event is also shown in right side column figure.

$1/f$ are obtained for each filtered event and the distributions of $N_{\gamma-like}$ and N_{ch} are also studied as a function of ϕ (bin width $\delta\phi = 18^{\circ}$) shown in figure 3.19. Some of the example plots for different events showing $\gamma-$excess and $ch-$excess in $\Delta\Phi = 18^{\circ}$, 36°, and 54° are discussed. A particular event is identified by its run number, event number, and file number written inside each figure.

- *Gamma excess:* Figure 3.19(a) shows plot for the fraction $N_{\gamma-like}/N_{ch}(= f)$ for different azimuthal sectors of $\Delta\Phi = 18^{\circ}$. Apart from all the sectors, only the sector number 3 has larger fraction value out of the selected events in tail of f distributions implies that the concentration of photons is more than the charged particles in that particular sector. The middle and bottom plots are the distributions of $N_{\gamma-like}$ and N_{ch} w.r.t sector number. A rise in sector number 3 of figure 3.19(b) shows large number of $N_{\gamma-like}$ hits in PMD and dip in the corresponding sector of figure 3.19(c) shows less number of charged particle hits in FMD. Similar plots for one more event are shown in figures 3.19(d), (e), and (f). In order to understand the event Id written in figure 3.19(a), the number "138225035_440 (96)" indicates run number (138225), file number (138225035_440), and event number (96). Similarly, figures 3.21(a), (b), and (c) illustrate the gamma excess plots for $\Delta\Phi = 36^{\circ}$. In the upper plot, the fraction values are much higher for two sectors 2 and 3 relative to other sectors and corresponding rise in number of photons ($N_{\gamma-like}$) is reflected in figure 3.21(b) and the bottom plot displays the dip for N_{ch} in those two sectors in comparison to other sectors. Figure 3.22(a) presents the f distribution showing higher values in three adjacent sectors (11, 12 and 13) for γ-excess in the window size $\Delta\Phi = 54^{\circ}$. The same sectors got large number of $N_{\gamma-like}$ hits in PMD and dip in FMD, when compared to other sectors.

- *Charge excess:* In figures 3.20(a), (b), and (c), the fraction distributions ($N_{ch}/N_{\gamma-like}$), and the hits of particles in PMD and FMD in each sector are displayed for a particular event exhibiting $ch-$excess for $\Delta\phi = 18^{\circ}$. The middle plot shows a dip in PMD sector corresponding to highest fraction value whereas a peak is observed in the FMD shown in figure 3.20(c). It is observed that the fraction values in all other sectors except for the sector number 1 are within statistical uncertainty. Another event of charge excess for $\Delta\phi = 18^{\circ}$ is also shown in figures 3.20(d), (e), and (f). The charge excess plots are also studied for $\Delta\phi = 36^{\circ}$ and 54°. For 36°, the highest fraction ($1/f$) values in two of the sectors and corresponding dip and rise in same sectors is observed for PMD and FMD in figures 3.21(e) and (f), respectively. A similar behaviour

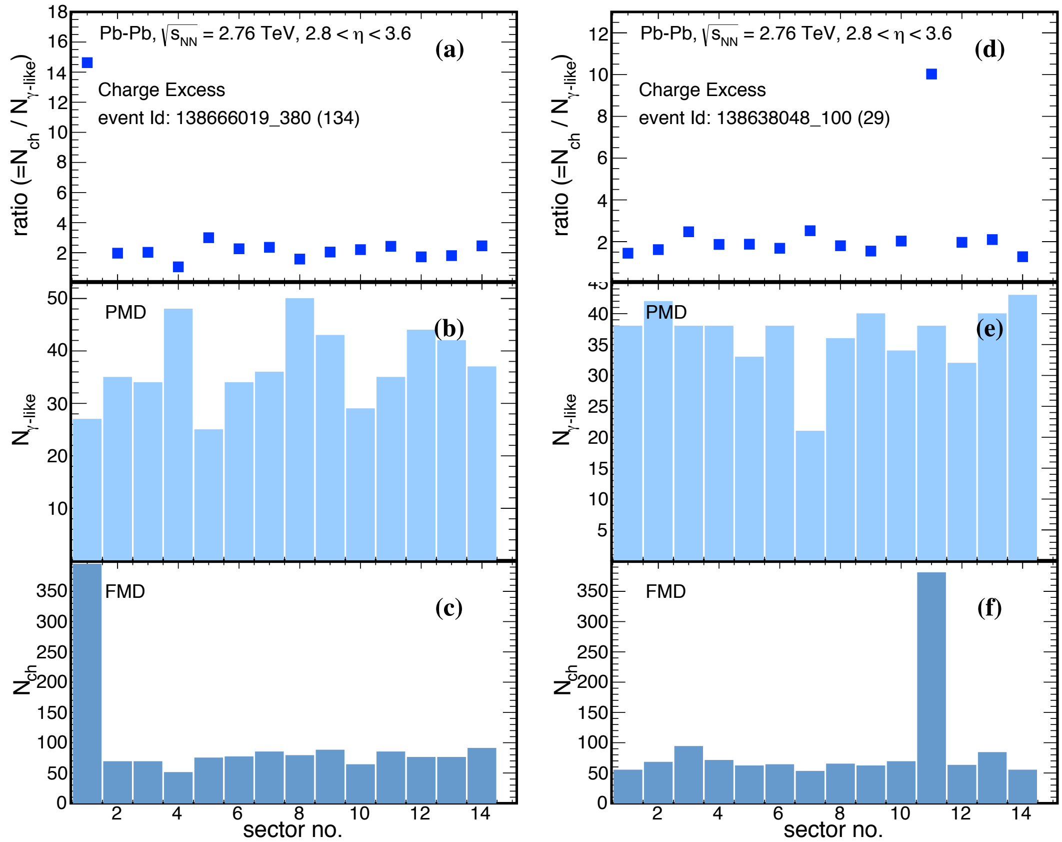

Figure 3.20: $ch-$excess for $\Delta\phi = 18^{\circ}$: the ratio plot of $N_{ch}/N_{\gamma-like}$ in (a), $N_{\gamma-like}$ hit distribution in (b), and N_{ch} hits in (c) w.r.t sectors covering the azimuthal angle selected for the analysis. Another example event is also shown in right side column figure.

is observed in figures 3.22(d), (e), and (f) showing relatively larger fraction values in three adjacent sectors exhibiting less $N_{\gamma-like}$ and more N_{ch} in the corresponding sectors for $\Delta\phi = 54^{\circ}$.

3.7.3 Charged-to-Neutral Fluctuations using $\nu_{dyn}^{\gamma-ch}$

The fluctuations in the relative production of charged and neutral particles are studied in Pb-Pb collisions via $\nu_{dyn}^{\gamma-ch}$. The neutral and charged particle multiplicity used for the estimation of $\nu_{dyn}^{\gamma-ch}$ is obtained from the PMD and FMD in a common

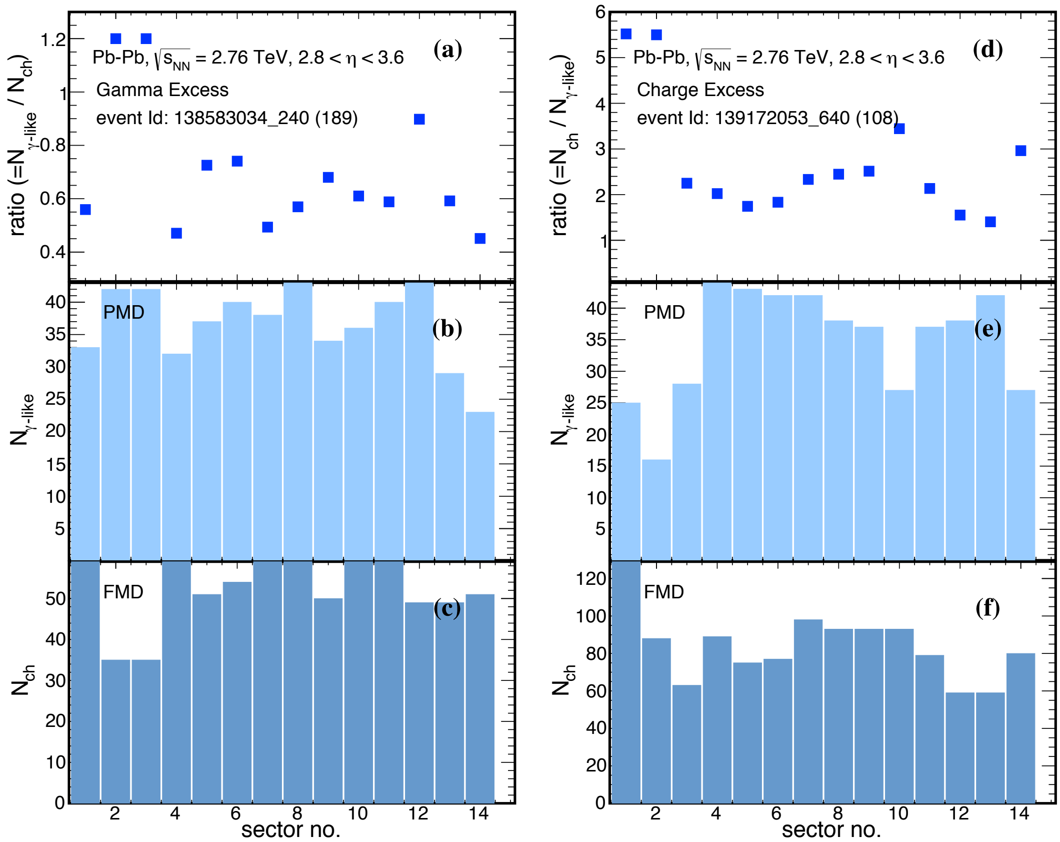

Figure 3.21: For $\Delta\phi = 36^{\circ}$: the ratio plot of $N_{\gamma-like}/N_{ch}$ in (a), $N_{\gamma-like}$ hit distribution in (b), and N_{ch} hits in (c) for $\gamma-$excess w.r.t sectors covering the azimuthal angle selected for the analysis. Right side column figure represents the $ch-$excess plots showing ratio for $N_{ch}/N_{\gamma-like}$ in (d), $N_{\gamma-like}$ hit distribution in (e), and N_{ch} hits in (f).

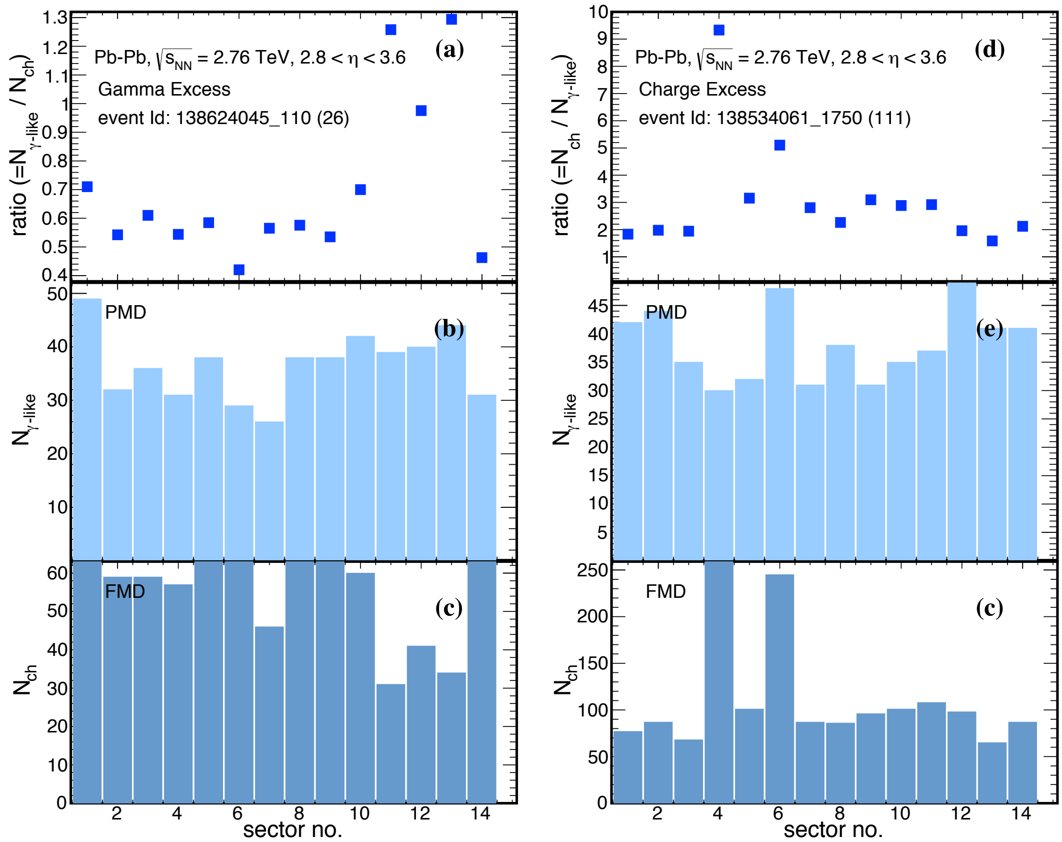

Figure 3.22: For $\Delta\phi = 54^\circ$: the ratio plot of $N_{\gamma-like}/N_{ch}$ in (a), $N_{\gamma-like}$ hit distribution in (b), and N_{ch} hits in (c) for $\gamma-$excess w.r.t sectors covering the azimuthal angle selected for the analysis. Right side column figure represents the $ch-$excess plots showing ratio for $N_{ch}/N_{\gamma-like}$ in (d), $N_{\gamma-like}$ hit distribution in (e), and N_{ch} hits in (f).

pseudorapidity range $2.8 < \eta < 3.6$ for azimuthal angle $0^{\circ} < \phi < 216^{\circ}$ and $334^{\circ} < \phi < 360^{\circ}$ due to the non-uniform acceptance of PMD and FMD.

3.7.3.1 Variation of individual terms in $\nu_{dyn}^{\gamma-ch}$

Eq. 3.2 can also be expressed as a linear combination of three terms,

$$\nu_{dyn}^{\gamma-ch} = w_{\gamma\gamma} + w_{ch\ ch} - 2 \times w_{ch-\gamma} \tag{3.14}$$

where $w_{\gamma\gamma}$, $w_{ch\ ch}$, and $w_{ch-\gamma}$ are defined as

$$w_{\gamma\gamma} = \frac{\langle N_{\gamma}(N_{\gamma}-1)\rangle}{\langle N_{\gamma}\rangle^{2}}, \tag{3.15}$$

$$w_{ch\ ch} = \frac{\langle N_{ch}(N_{ch}-1)\rangle}{\langle N_{ch}\rangle^{2}}, \tag{3.16}$$

and

$$w_{ch-\gamma} = 2 \times \frac{\langle N_{\gamma}N_{ch}\rangle}{\langle N_{\gamma}\rangle\langle N_{ch}\rangle} \tag{3.17}$$

The variation of these individual terms in $\nu_{dyn}^{\gamma-ch}$ are studied as a function of collision centrality and average multiplicity in the acceptance region. The three possibilities for the observable $\nu_{dyn}^{\gamma-ch}$ can be $+, -$ or $= 0$.

- $\nu_{dyn}^{\gamma-ch} > 0$: This is the case when $w_{ch-\gamma} < (w_{\gamma\gamma} + w_{ch\ ch})$ which implies the dominance of self-correlation terms ($\gamma\gamma$ and $ch - ch$).
- $\nu_{dyn}^{\gamma-ch} < 0$: In this case, the third term involving cross correlation ($w_{ch-\gamma}$) dominates resulting in $w_{ch-\gamma} > (w_{\gamma\gamma} + w_{ch\ ch})$. The negative correlation tells that the photons and charged particles are strongly correlated rather than the self correlations among photons and charged particles.

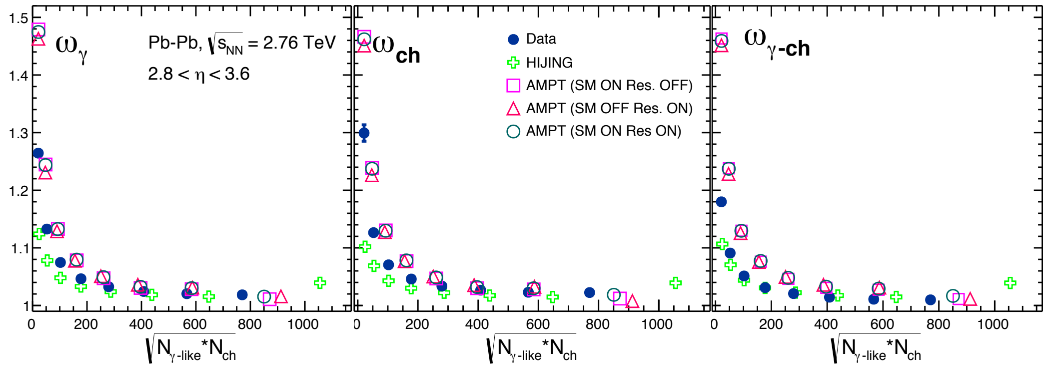

Figure 3.23: The average multiplicity dependence of three individual terms in $\nu_{dyn}^{\gamma-ch}$ for data and different event generators: HIJING and AMPT (SM On/Off).

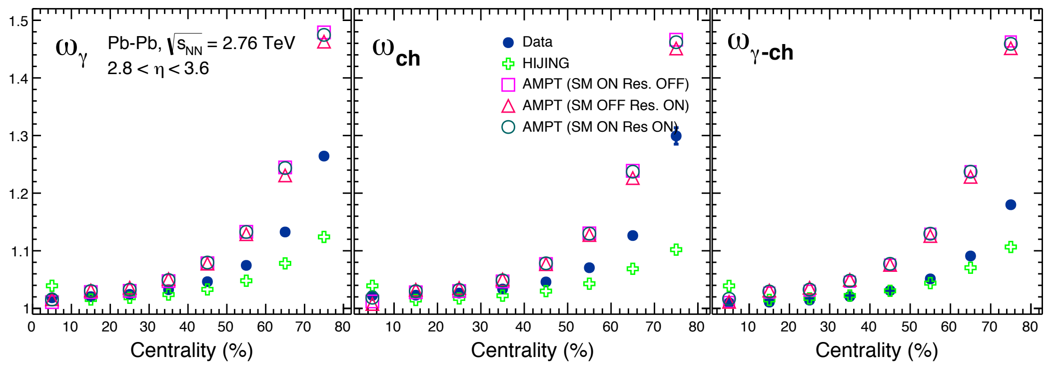

Figure 3.24: Centrality dependence of three individual terms in $\nu_{dyn}^{\gamma-ch}$ for data and different event generators: HIJING and AMPT (SM On/Off).

- $\nu_{dyn}^{\gamma-ch} = 0$: A Poisson distribution expects the zero value for $\nu_{dyn}^{\gamma-ch}$.

The multiplicity dependence ($\sqrt{N_{\gamma-like} * N_{ch}}$) of three independent terms $w_{\gamma\gamma}$, w_{chch}, and $w_{\gamma-ch}$ is shown in figures 3.23(a), (b), and (c), respectively. It is observed that the three terms decreases as one moves from lower multiplicity towards higher multiplicity. For all three plots, the data have lower values than AMPTs of different configurations viz., String Melting (SM) ON rescattering ON/Off, and SM Off rescattering ON, but higher than HIJING. All the three terms decreases gradually for higher multiplicity and approaches unity which is the Poisson limit for each term.

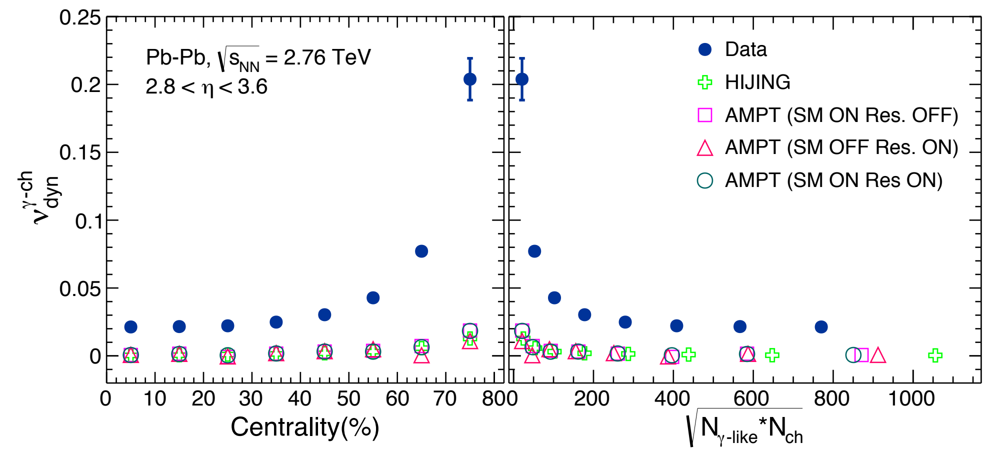

Figure 3.25: Non-statistical fluctuations of $\nu_{dyn}^{\gamma-ch}$ as a function of collision centrality (left) and average multiplicity (right) at $\sqrt{s_{\rm NN}}$ = 2.76 TeV for data and different Monte Carlo models: HIJING and AMPT (SM On/Off).

Figure 3.23 can also be expressed in another form as a variation of collision centrality for the individual terms shown in figure 3.24. The trend is same in both figures 3.23 and 3.24, because the centrality of an event reflects the average multiplicity. The values for individual terms are positive and the experimental data lies in between the AMPT and HIJING data points in each centrality class.

3.7.3.2 Centrality and Average Multiplicity Dependence of $\nu_{dyn}^{\gamma-ch}$

The non-statistical fluctuations in charged-neutral particles are measured for Pb-Pb collision data at $\sqrt{s_{\rm NN}}$ = 2.76 TeV as a function of average multiplicity and collision centrality for common pseudorapidity interval $2.8 < \eta < 3.6$ of PMD and FMD.

Figure 3.25 (left) shows the centrality dependence of robust observable $\nu_{dyn}^{\gamma-ch}$ for experimental data. The results obtained from data are compared with the AMPT and HIJING event generators. The data points represented by solid blue markers show an increasing trend as one moves from more central collisions toward peripheral collisions. The average multiplicity ($\sqrt{N_{\gamma-like} * N_{ch}}$) dependence of $\nu_{dyn}^{\gamma-ch}$ is also

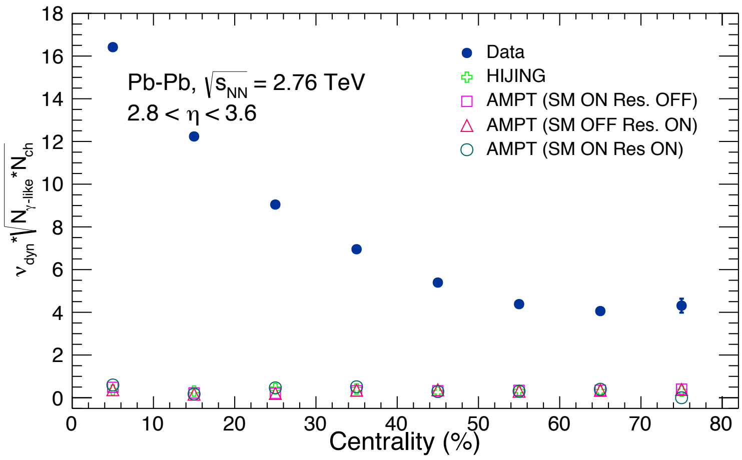

Figure 3.26: Centrality dependence of scaled $\nu_{dyn}^{\gamma-ch}$ at $\sqrt{s}_{\mathrm{NN}} = 2.76$ TeV for data and different Monte Carlo models: HIJING and AMPT (SM On/Off).

studied and shown in figure 3.25 (right). It is seen that the Monte Carlo models are consistent in all centralities as expected for Poisson distribution and shows slight deviation for low multiplicity events. The non-zero positive values for data represent the presence of non-statistical fluctuations in all centrality bins.

3.7.4 Scaled multiplicity dependence of $\nu_{dyn}^{\gamma-ch}$

Figure 3.26 presents the $\nu_{dyn}^{\gamma-ch}$ values scaled by the average multiplicity ($\nu_{dyn} * \sqrt{N_{\gamma-like}N_{ch}}$) for different centrality classes from 0 to 80%. The AMPT and HIJING show that the scaled $\nu_{dyn}^{\gamma-ch}$ values are constant in each centrality and have flat structure exhibiting no centrality dependence. The data have completely different trend as compared to different Monte Carlo event generators.

3.7.5 Robust Variables

The Minimax collaboration introduced a robust observable $r_{m,1}$ to explore further the charged-neutral $(ch-\gamma)$ correlation strength. The multiplicity dependence of $r_{1,1}$

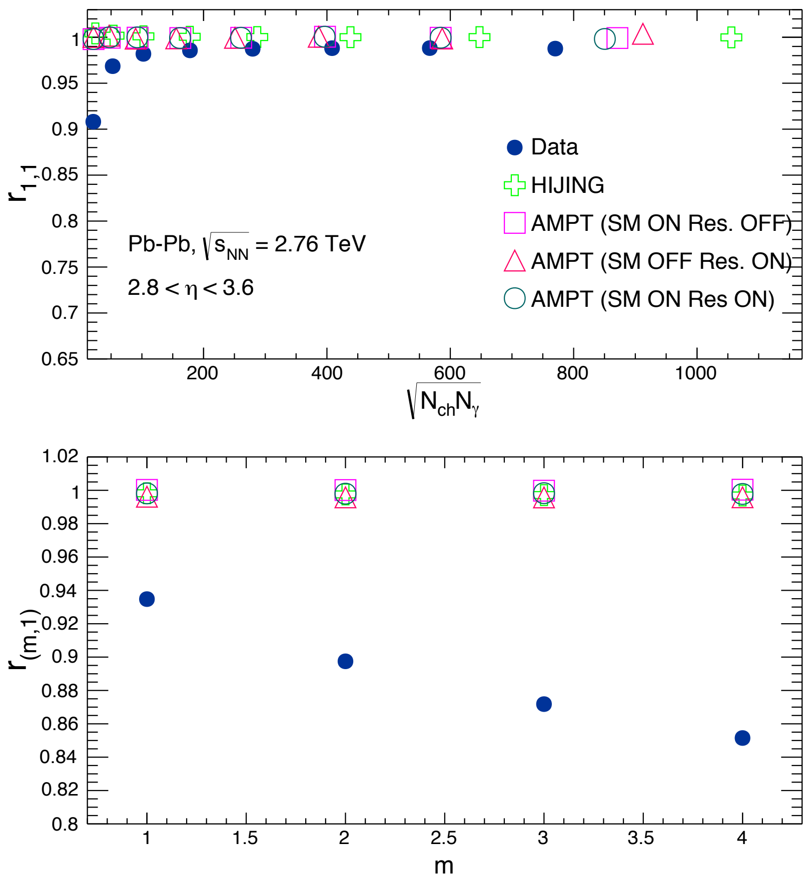

Figure 3.27: Variation of robust observable $r_{1,1}$ as a function of average multiplicity (upper panel) and $r_{1,1}$ dependence on higher order moments (bottom panel), in Pb-Pb collisions at $\sqrt{s}_{\rm NN}$ = 2.76 TeV for data and different Monte Carlo models: HIJING and AMPT (SM On/Off).

is shown in upper plot of figure 3.27 for data and HIJING events. The comparison is also performed with AMPT model of three different configurations. The data points follow an increasing trend with increase in $\sqrt{N_{\gamma-like} * N_{ch}}$ as one moves from more peripheral collisions towards semi-central collisions and saturates for more central high multiplicity collisions. The results show that $r_{1,1}$ values for HIJING and AMPTs are constant and almost equal to unity indicates the generic pion production scenario.

The bottom plot in figure 3.27 presents the $r_{m,1}$ dependence on its higher order moments (m) for most central collisions ($0-10\%$). The HIJING and AMPTs lie on the Poisson value ($\sim$1) for higher moments too whereas the $r_{m,1}$ decreases with increasing m for data.

3.8 Summary

An event-by-event charged-neutral multiplicity fluctuations are measured in the common azimuthal coverage of the PMD and the FMD in pseudorapidity range $2.8 < \eta < 3.6$ for Pb-Pb collisions at $\sqrt{s}_{\mathrm{NN}} = 2.76$ TeV. The three different observables f, $\nu_{dyn}^{\gamma-ch}$ and $r_{m,1}$ are used for the estimation of $\gamma - ch$ fluctuations as a function of multiplicity and centrality. The fraction f is measured for experimental data in a localized phase-space region and an excess of events are separated from the whole sample which show either $\gamma-$excess or $ch-$excess. For the present analysis, the non-statistical fluctuations are observed in $\nu_{dyn}^{\gamma-ch}$ for the data whereas the model studies show very small deviations from the Poisson value. The variation of $\nu_{dyn}^{\gamma-ch} * \sqrt{\langle N_{\gamma-like} * N_{ch}\rangle}$ with respect to centrality exhibits $\sim 1/\sqrt{\langle N_{\gamma-like} * N_{ch}\rangle}$ dependence in data, whereas the HIJING and AMPT are compatible with zero. To explore further the correlation between γ and ch particles, the factorial moments $r_{m,1}$ is also studied as a function of m. For more central events, the $r_{m,1}$ exhibits decreasing trend with increasing m in data, whereas HIJING and AMPT exhibit no dependence. The PMD Pb-Pb data used for this analysis had some problems viz., the hot cell removal, gain calibration corrections, etc. The results presented are not explained by any Monte Carlo models used for this analysis.

Bibliography

[1] A.A. Anselm *et al.*, "Production of classical pion field in heavy ion high energy collisions", Phys. Lett. B **266**, 482 (1991).

[2] JACEE Collaboration, C.M.G. Lattes *et al.*, "Hadronic Interaction of High-Energy Cosmic Ray Observed by Emulsion Chambers", Phys. Rep. **65**, 151 (1980).

[3] WA98 Collaboration, M.M. Aggarwal *et al.*, "Localized charged-neutral fluctuations 158A GeV Pb+Pb collisions", Phys. Rev. C **64**, 011901(R) (2001).

[4] MiniMax Collaboration, T.C. Brooks *et al.*, "A Search for disoriented chiral condensate at the Fermilab Tevatron", Phys. Rev. D **61**, 032003 (2000).

[5] A. Graps, "An Introduction to wavelets", IEEE Computational Sciences and Engineering, **2**, 50 (1995).

[6] M.M. Aggarwal, G. Sood, and Y.P. Viyogi, "Event-by-event study of DCC-like fluctuation in ultra-relativistic nuclear collisions", Phys. Lett. B **638**, 39 (2006).

[7] STAR Collaboration, L. Adamczyk *et al.*, "Charged-to-neutral correlation at forward rapidity in Au + Au collisions at $\sqrt{s}_{\mathrm{NN}} = 200$ GeV", Phys. Rev. C **91**, 034905 (2015).

[8] WA93 Collaboration, M.M. Aggarwal *et al.*, "A preshower photon multiplicity detector for the WA93 experiment", Nucl. Inst. and Meth in Phys. Res. Sec A: **372**, 143 (1996).

[9] H.H. Gutbrod *et al.*, "Proposal for a large acceptance hadron and photon spectrometer", CERN-SPSLC-91-17, CERN-P260, 87 (1991).

[10] STAR Collaboration, K.H. Ackermann *et al.*, "STAR Detector Overview", Nucl. Instr. Meth. A 499, 624 (2003).

[11] Alice Collaboration, Alice Technical Design Report, JINST, vol-3 (2008), p.S08002, http://iopscience.iop.org/1748-0221/3/08/S08002.

[12] W.R. Leo, "Techniques for Nuclear and Particle Physics Experiments", November (1993).

[13] ALICE Collaboration, "Technical Design Report of Photon Multiplicity Detector (PMD)", CERN-LHCC-99-032 (1999).

[14] S.C. Phatak, "Clustering Algorithm For PMD Data", http://www.iopb.res.in/phatak/cluster/clusters.html.

[15] ALICE Collaboration, "ALICE Technical Design Report on Forward Detectors: FMD, T0 and V0", CERN-LHCC-2004-025 ALICE-TDR-011 (2004).

[16] X.N. Wang and M. Gyulassy, "HIJING: A Monte Carlo model for multiple jet production in pp, pA and AA collisions", Phys. Rev. D **44**, 3501 (1991).

[17] Z.w. Lin, C.M. Ko, B.A. Li, and S. Pal, "A Multi-phase transport model for relativistic heavy ion collisions", Phys. Rev. C **72**, 064901 (2005).

[18] B. Zhang, "ZPC 1.0.1: A Parton cascade for ultrarelativistic heavy ion collisions", Comput. Phys. Commun. **109**, 193 (1998).

[19] B.A. Li, and C.M. Ko, "Formation of superdense hadronic matter in high-energy heavy ion collisions", Phy. Rev. C **52**, 2037 (1995).

[20] Z.w. Lin, and C.M. Ko, “Deutron nucleus collisions in a multiphase transport model”, Phys. Rev. C **68**, 054904 (2003).

[21] B. Andersson, G. Gustafson, and B. Soderberg, “A General Model for Jet Fragmentation”, Z. Phys. C **20**, 317 (1983).

[22] Z.w. Lin, and C.M. Ko, “Kaon interferometry at RHIC from AMPT model”, J. Phys. G **30**, S263 (2004).

[23] L.W. Chen, and C.M. Ko, “System size dependence of elliptic flows in relativistic heavy-ion collisions”, Phys. Lett. B **634**, 205 (2006).

[24] H.H. Dalsgaard, “Pseudorapidity Densities in p+p and Pb+Pb collisions at LHC measured with the ALICE experiment”, Ph.D. thesis, (2012).

[25] WA98 Collaboration, M.M. Aggarwal *et al.*, “Event-by-event charged-neutral fluctuations in Pb+Pb collisions at 158 A$\sim$ GeV”, Phys. Lett. B **701**, 300 (2011).

[26] C. Pruneau, S. Gavin, and S. Voloshin, “Methods for the study of particle production fluctuations”, Phys. Rev. C **66**, 044904 (2002).

[27] P. Christiansen, E. Haslum, and E. Stenlund, “Number-ratio fluctuations in high energy particle production”, Phys. Rev. C **80**, 034903 (2009).

Chapter 4

Event-by-event charge separation using Sliding Dumbbell Method

4.1 Introduction

At relativistic energies, the colliding heavy ions produce an overlap region leaving the spectator nucleons aside [1, 2]. These spectator nucleons create a strong magnetic field and induces the electric current that causes the separation of oppositely charged particles along the system's orbital angular momentum direction resulting in the Chiral Magnetic Effect (CME) [3–5]. So far, charge separation effect study has been reported by STAR [6, 7] at RHIC in Au+Au collisions, ALICE [8, 9] in Pb-Pb collisions and CMS [10] collaboration in p-Pb and Pb-Pb collisions data. No strong evidence has been reported yet for the presence of CME though the studies are still going. The aim of the thesis is another attempt to study possible correlations between the charged particles with ALICE Pb-Pb collisions using the two- and three-particle correlators proposed by Voloshin [11] as well as using a new method named as "Sliding Dumbbell Method" (SDM) developed to search for the localized charge separation. The particle azimuthal correlations are studied in terms of different centrality intervals and in each centrality, different event shape classes to isolate the events showing charge separation effect classified using SDM method.

The HIJING (Heavy Ion Jet Interaction generator) and the AMPT (A Multi

Phase Transport) event generators are used for simulation study. HIJING does not include elliptic flow thus one should not expect any flow-induced background correlations, whereas the AMPT has elliptic flow which can contribute to background correlations for the two- and three- particle correlations. To observe the effects of CME signal on the particle correlations in AMPT, the CME signal is injected in the standard String Melting AMPT. The standard AMPT and signal injected AMPT results are compared for two- and three- particle azimuthal correlations.

4.2 Monte Carlo models

The HIJING and the AMPT generated events are used for the particle azimuthal correlation measurements in Pb-Pb collisions at $\sqrt{s_{\rm NN}} = 2.76$ TeV. The charged particle track in the transverse momentum range $0.2 < p_T < 5.0$ GeV/c and pseudorapidity interval $-0.8 < \eta < 0.8$ are selected for the analysis. The full azimuthal coverage ($0^\circ < \phi < 360^\circ$) is used for the analysis.

4.3 Analysis Strategy

In previous measurements, the CME has been measured via multi-particle correlator averaged over a collection of events and hence there is a possibility that the effect might get diluted. We have studied the event-by-event localized charge separation using Sliding Dumbbell Method (SDM) similar to the Sliding Window Method (SWM) [12] used by the WA98 collaboration at the CERN SPS [13, 14]. The advantage of using SDM is one can separate the events exhibiting CME type effects. The particle azimuthal correlations measured using Q-cumulant method [15] are studied for different categories of charge separation events using SDM and for each centrality bin.

4.3.1 Sliding Dumbbell Method

In this method, a full azimuthal plane is scanned by sliding the dumbbell of $\Delta\phi = 90^\circ$ (shown in Figure 4.1) in steps of $\delta\phi = 1^\circ$ while calculating the value of $Db_\pm$ everytime which is defined as,

$$Db_\pm = Db_+^{forw} + Db_-^{back} \tag{4.1}$$

$$Db_\pm = \frac{N_+^{forw}}{(N_+^{forw} + N_-^{forw})} + \frac{N_-^{back}}{(N_+^{back} + N_-^{back})} \tag{4.2}$$

where N_+^{forw} and N_-^{forw} are the number of positively and negatively charged particles in the forward side of the dumbbell, respectively, whereas N_+^{back} and N_-^{back} are the number of positively and negatively charged particles in the backward side of the dumbbell, respectively. A pictorial view of the Sliding Dumbbell Method (SDM) is depicted in figure 4.1. $Db_\pm$ is basically the sum of positive charge fraction (Db_+^{forw}) on one side of the dumbbell and the negative charge fraction (Db_-^{back}) on the other side of the dumbbell. If the charged particles are uniformly distributed over the full azimuthal plane then the value of each fraction in Eq. 4.2 will be equal to 0.5 and the sum will be $Db_\pm^{max} = 1$ but if the charged particles are not uniformly distributed then the $Db_\pm^{max}$ value will exceed unity and the maximum value can be equal to 2.

After calculating the $Db_\pm$ value in each step of sliding the dumbbell, an asymmetry Db_{asy} also calculated which is defined as,

$$Db_{asy} = \frac{(Pos_{ex}^{forw} - Neg_{ex}^{back})}{(Pos_{ex}^{forw} + Neg_{ex}^{back})} \tag{4.3}$$

where $Pos_{ex}^{forw} = N_+^{forw} - N_-^{forw}$ is the positive charge excess on the forward side of the dumbbell and $Neg_{ex}^{back} = N_-^{back} - N_+^{back}$ is the negative charge excess on

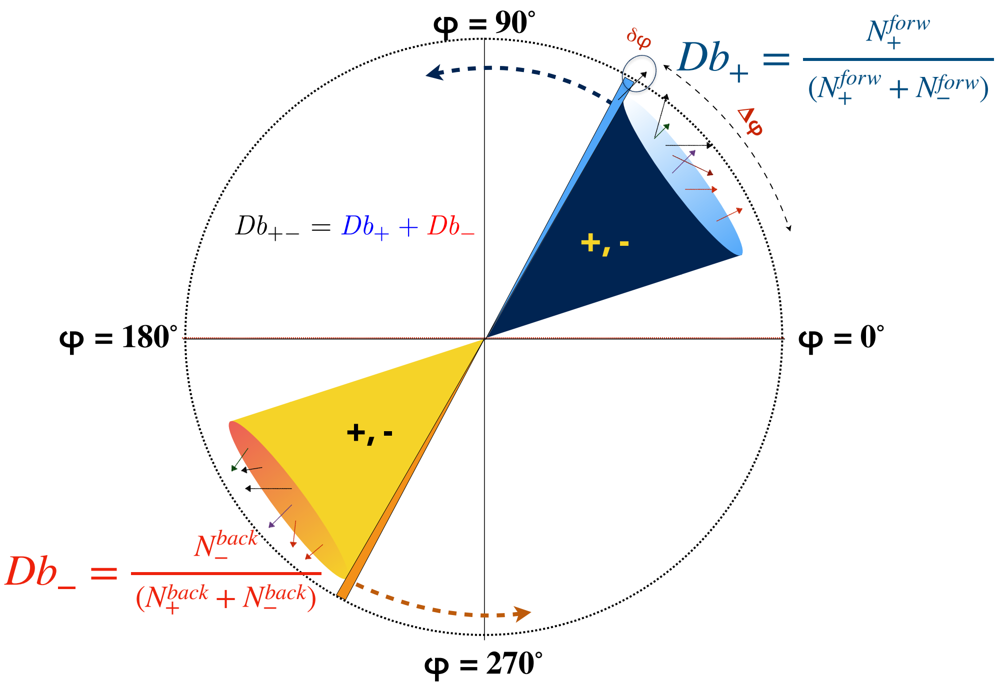

Figure 4.1: A pictorial view of the Sliding Dumbbell Method.

the backward side of the dumbbell. An asymmetry cut (Db_{asy}) rejects the events with large asymmetry in the positive and negative charge particle excess on either side of the dumbbell within an event. Figure 4.2 (A) presents an ideal case of CME event and figures 4.2 (B), (C), and (D) display three examples showing different Db_{asy} values. The $\mid Db_{asy} \mid = 0.1$ shown in figure 4.2 (B) contains almost similar number of positive charge excess (Pos_{ex}^{forw}) and negative charge excess (Neg_{ex}^{back}) on the forward and backward side of the dumbbell, respectively. Such type of events are selected for the analysis exhibiting CME-type behaviour. Figure 4.2 (C) indicates an event with $\mid Db_{asy} \mid < 0.25$ is also selected for further analysis. In figure 4.2 (D), asymmetry value becomes 0.5 due to the large positive charge excess on forward side but no negative charge excess on the backward side of the dumbbell. Such type of events are rejected by applying the Db_{asy} cut. In each event $Db_{\pm}^{max}$ with the condition $\mid Db_{asy} \mid < 0.25$ is obtained by sliding the dumbbell in steps of 1° over the whole azimuthal plane.

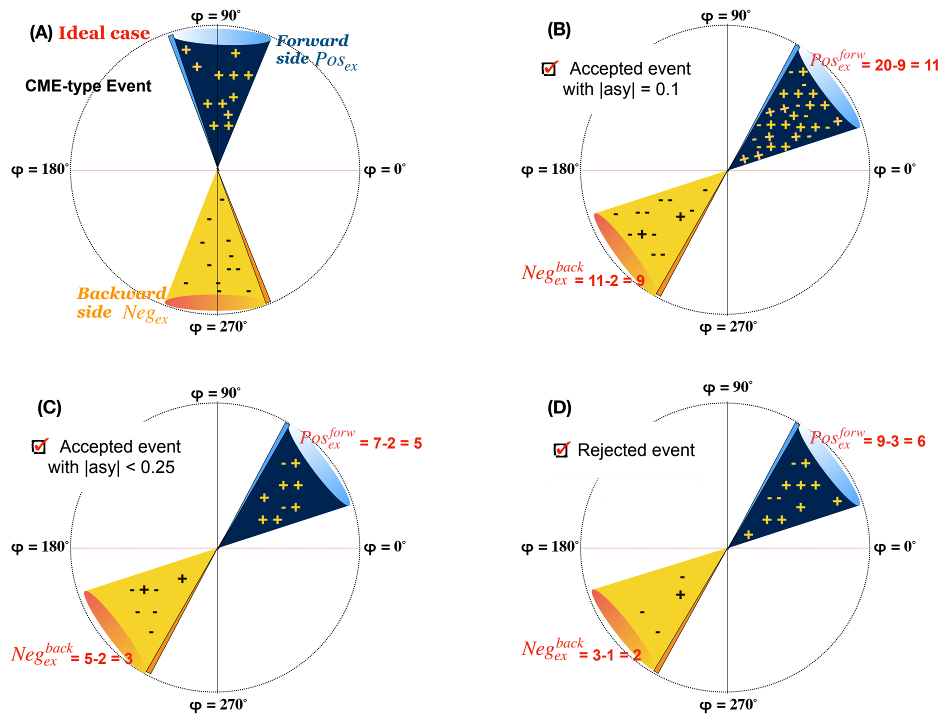

Figure 4.2: (A) is ideal case of CME-type event and (B), (C), and (D) show different example events exhibiting different asymmetry values in an event.

To understand the usefulness of SDM in searching the CME-type effects, the obtained distributions of $Db_{\pm}^{max}$ in each centrality are further sliced into 10 bins where top 10% $Db_{\pm}^{max}$ corresponds to higher $Db_{\pm}^{max}$ values while 90-100% bin corresponds to lowest $Db_{\pm}^{max}$ values. The multi-particle correlators are investigated for different classes of charge separation based on $Db_{\pm}^{max}$.

4.3.2 Multi-particle Azimuthal Correlations

Aim of this thesis is to measure the three particle azimuthal correlations for the analysis of charge separation effect due to the CME. Voloshin [15] suggested the multi-particle correlator defined as,

$$\langle cos(n(\phi_i + \phi_j - 2\Psi_{RP}))\rangle = \langle cos(n(\phi_i + \phi_j - 2\phi_k))\rangle / v_{2,k} \tag{4.4}$$

where ϕ_i and ϕ_j are the azimuthal angles of i^{th} and j^{th} particle. The determination of reaction plane angle (Ψ_{RP}) (defined by the impact parameter and beam direction) is not possible experimentally. Thus for calculating the three particle correlator relative to reaction plane, one can use the third particle as an event plane and divide three particle correlator by the elliptic flow of third particle as written in Eq. 4.4. The three particle correlator ($\langle cos(\phi_i - \phi_j - 2\phi_k)\rangle$) and the $v_{2,k}$ are measured via Q-cumulants discussed in next section.

4.3.2.1 Q-cumulants

The calculation of multi-particle correlations need computing power to go over all possible particle multiplets. Moreover, the heavy-ion collision data contain high multiplicity events which will consequently take enormous time for the calculations. To avoid this problem, Voloshin [15] suggested to express cumulants in terms of flow vector, Q_n. The main advantage of using Q-cumulants is that it reduces the relative non-flow contributions.

The Q-vector ("flow-vector") for n harmonic is denoted by Q_n and defined as,

$$Q_n = \sum_{i=1}^{M} e^{in\phi_i} \tag{4.5}$$

where ϕ_i is the azimuthal angle of i^{th} particle and summation runs over all the particles in an event with multiplicity M.

The strategy used in measuring the multi-particle correlations via Q-cumulants involve some steps discussed below.

Step 1: The first step in calculating the particle correlations involves the decomposition of the expressions $\mid Q_n \mid^2$, $Q_n Q_n Q^*_{2n}$, and $\mid Q_n \mid^4$, in terms of $\langle 2\rangle_{n|n}$,

$\langle 3\rangle_{n,n|2n}$, and $\langle 4\rangle_{n,n|n,n}$, respectively, which are,

$$\langle 2\rangle_{n|n} \equiv \frac{1}{P(M,2)} \sum_{\substack{i,j=1\\(i\neq j)}}^{M} e^{in(\phi_i-\phi_j)}, \tag{4.6}$$

where $P(n,m)$ is $\frac{n!}{(n-m)!}$

$$\langle 3\rangle_{n,n|2n} \equiv \frac{1}{P(M,3)} \sum_{\substack{i,j,k=1\\(i\neq j\neq k)}}^{M} e^{in(\phi_i+\phi_j-2\phi_k)}, \tag{4.7}$$

$$\langle 4\rangle_{n,n|n,n} \equiv \frac{1}{P(M,4)} \sum_{\substack{i,j,k,l=1\\(i\neq j\neq k\neq l)}}^{M} e^{in(\phi_i+\phi_j-\phi_k-\phi_l)}. \tag{4.8}$$

Step 2: In second step, the system of coupled equations obtained in first step are solved for two-, three-, and four- particle azimuthal correlations and are expressed totally in terms of various combinations of Q-vectors.

Step 3: To obtain the final results for the multi-particle correlations, an average over all events is performed.

$$\langle\langle 2\rangle\rangle_{n|n} \equiv \frac{\sum_{i=1}^{N}(w_2)_i(\langle 2\rangle_{n|n})_i}{\sum_{i=1}^{N}(w_2)_i} \tag{4.9}$$

$$\langle\langle 3\rangle\rangle_{n,n|2n} \equiv \frac{\sum_{i=1}^{N}(w_3)_i(\langle 3\rangle_{n,n|2n})_i}{\sum_{i=1}^{N}(w_3)_i} \tag{4.10}$$

$$\langle\langle 4\rangle\rangle_{n,n|2n} \equiv \frac{\sum_{i=1}^{N}(w_4)_i(\langle 4\rangle_{n,n|n,n})_i}{\sum_{i=1}^{N}(w_4)_i} \tag{4.11}$$

where double brackets denote an average over all tracks and then over all N events. $w_2 = M(M-1)$, $w_3 = M(M-1)(M-2)$, and $w_4 = M(M-1)(M-2)(M-3)$, are event weights which make correlations free from multiplicity fluctuations.

- **Flow Estimation via Cumulants:** To estimate the three particle correlator defined in Eq. 4.4, the flow coefficient of 2^{nd} harmonic is measured using cumulants which are defined in terms of particle azimuthal correlations as,

$$c_2\{2\} = \langle\langle 2\rangle\rangle \tag{4.12}$$

$$c_2\{4\} = \langle\langle 4\rangle\rangle - 2 * \langle\langle 2\rangle\rangle^2 \tag{4.13}$$

In terms of flow harmonic, the cumulants can be written as,

$$v_2\{2\} = \sqrt(c_2\{2\}) \tag{4.14}$$

$$v_2\{4\} = (-c_2\{4\})^{1/4} \tag{4.15}$$

- **Three Particle Correlator:** The Q-vector is defined as,

$$Q_n Q_n Q_{2n}^* = \sum_{i,j,k=1}^{M} e^{in(\phi_i+\phi_j-2\phi_k)} \tag{4.16}$$

There are three different cases for the indices i, j, and k.

(1) When all the 3 indices are different i.e., $(i \neq j \neq k)$

$$\langle 3\rangle_{n,n|2n} * M(M-1)(M-2) \tag{4.17}$$

(2) When out of three, the two indices are different i.e., $(i \neq j = k)$ or $(i = j \neq k)$

$(\phi_i + \phi_j - 2\phi_k) = (\phi_i - \phi_k)$ for $(i \neq j = k)$

$(\phi_i + \phi_j - 2\phi_k) = (2\phi_i - 2\phi_k)$ for $(i = j \neq k)$

The corresponding coefficients and weight factors are,

$$\langle 2\rangle_{n|n} * M(M-1)2! \tag{4.18}$$

$$\langle 2\rangle_{2n|2n} * M(M-1) \tag{4.19}$$

(3) When all the three indices are same i.e., $(i = j = k)$

$$1 * M \tag{4.20}$$

After combining all the individual terms, the Eq. 4.16 becomes,

$$Q_nQ_nQ^*_{2n} = \langle 3\rangle_{n,n|2n}*M(M-1)(M-2)+\langle 2\rangle_{n|n}*M(M-1)2!+\langle 2\rangle_{2n|2n}*M(M-1)+M \tag{4.21}$$

$$\langle 3\rangle_{n,n|2n} = \frac{Q_nQ_nQ^*_{2n} - 2* \mid Q_n \mid^2 - \mid Q_{2n} \mid^2 +2 * M}{M(M-1)(M-2)} \tag{4.22}$$

The three particle correlator for ++ and - - combinations are obtained for a given sample using above mentioned method. The average of both terms is taken for the final three particle correlator for same sign.

Similarly, the three particle correlator is obtained for opposite sign (OS) charge pairs by restricting one type of particles as positive with multiplicity M and other type as negative with multiplicity m. The three particle correlator for OS charge pairs (+ -) can be written as,

$$\langle 3\rangle_{\underline{n},n|2n} = \frac{q_{\underline{n}}Q_nQ^*_{2n} - q_{\underline{n}}Q^*_n}{mM(M-1)} \tag{4.23}$$

where Q_n and $q_{\underline{n}}$ denote Q-vectors for positive and negative charged particles with multiplicity "m" and "M", respectively. The final three particle correlator is obtained using Eq. 4.10.

- **Two Particle Correlator:** The estimation of elliptic flow requires the measurement of two-particle correlator as indicated in Eq. 4.12. The two particle azimuthal correlations are obtained for different charge combinations i.e., SS and OS charge pairs. Consider the case of SS charge pairs and the Q-vector can be written as,

$$\mid Q_n \mid^2 = \sum_{i,j=1}^{M} e^{in(\phi_i - \phi_j)} \tag{4.24}$$

There are two cases:
(1) $(i \neq j)$ i.e., correlation between different types of particles. It gives,

$$\langle 2 \rangle_{n|n} * P_{M,2} \tag{4.25}$$

(2) $(i = j)$ represents the self correlation term which is given as,

$$1 * M \tag{4.26}$$

Thus, the decomposition contains two terms; 2- particle and 1- particle contributions. By combining the values from Eqs. 4.25 and 4.26, the Eq. 4.24 becomes,

$$\mid Q_n \mid^2 = \langle 2 \rangle_{n|n} * P_{M,2} + 1 * M \tag{4.27}$$

After rearranging the above equation, the two particle correlator for SS (+ +, - -) charge pairs becomes,

$$\langle 2 \rangle_{n|n} = \frac{\mid Q_n \mid^2 - M}{M(M-1)} \tag{4.28}$$

For the OS charge pairs, the two particle azimuthal correlations are obtained in a similar way and can be written as,

$$\langle 2\rangle_{\underline{n}|n} = \frac{q_{\underline{n}} Q_n^*}{m(M)} \tag{4.29}$$

The averaging over all events is performed using Eq. 4.9 and the resulting expression is used to estimate the second order cumulant defined in Eq. 4.12.

- **Four Particle Correlator:** To obtain the 4^{th} order cumulant, the Q-vector is written as,

$$\mid Q_n \mid^4 = \sum_{i,j,k,l=1}^{M} e^{in(\phi_i+\phi_j-\phi_k-\phi_l)} \tag{4.30}$$

For SS charge pair combination, the above equation can be decomposed into 4 cases on the basis of indices i, j, k, and l.

(1) When all the 4 indices are different i.e., $(i \neq j \neq k \neq l)$

The corresponding coefficient is four particle correlator and the associated weight factors can be written as,

$$\langle 4\rangle_{n,n|n,n} * M(M-1)(M-2)(M-3) \tag{4.31}$$

(2) When three of the four indices are different i.e., $(i = j \neq k \neq l)$ or $(i \neq j \neq k = l)$ or $(i \neq j = k \neq l)$,

$(\phi_i + \phi_i - \phi_k - \phi_l) = (2\phi_i + \phi_k - \phi_l)$ for $(i = j \neq k \neq l)$

$(\phi_i + \phi_j - \phi_k - \phi_k) = (\phi_i + \phi_j - 2\phi_k)$ for $(i \neq j \neq k = l)$

$(\phi_i + \phi_j - \phi_j - \phi_l) = (\phi_i - \phi_l)$ for $(i \neq j = k \neq l)$

The corresponding coefficients and weight factors are,

$$\langle 3\rangle_{2n|n,n} * M(M-1)(M-2) \tag{4.32}$$

$$\langle 3\rangle_{n,n|2n} * M(M-1)(M-2) \tag{4.33}$$

$$\langle 2\rangle_{n|n} * M(M-1)2!(M-2)2! \tag{4.34}$$

(3) When two indices are different i.e., $(i = j \neq k = l)$ or $(i = j = l \neq k)$

$(\phi_i + \phi_i - \phi_k - \phi_k) = (2\phi_i - 2\phi_k)$ for $(i = j \neq k = l)$

$(\phi_i + \phi_i - \phi_i - \phi_l) = (\phi_i - \phi_k)$ for $(i = j = l \neq k)$

The corresponding coefficients and weight factors are

$$\langle 2\rangle_{n|n} * M(M-1) * 2! * 2! \tag{4.35}$$

$$\langle 2\rangle_{2n|2n} * M(M-1) \tag{4.36}$$

$$1 * M(M-1) * 2 \tag{4.37}$$

(4) When all indices are same i.e., $(i = j = k = l)$, only the auto-correlation terms survive given as,

$$1 * M \tag{4.38}$$

In order to obtain the four particle correlation term, put all the calculated values in Eq. 4.30.

$$\begin{aligned} \mid Q_n \mid^4 = & \langle 4\rangle_{n,n|n,n} * M(M-1)(M-2)(M-3) \\ & +[\langle 3\rangle_{2n|n,n} + \langle 3\rangle_{n,n|2n}] * M(M-1)(M-2) \\ & + \langle 2\rangle_{n|n} * [(M(M-1)2!(M-2)2! + M(M-1)2! * 2!)] \\ & +\langle 2\rangle_{2n|2n} * M(M-1) + M(M-1)2 + M \end{aligned} \tag{4.39}$$

Rearranging the Eq. 4.39, the expression for four particle correlator becomes,

$$\begin{aligned} \langle 4\rangle_{n,n|n,n} = & \frac{(\mid Q_n \mid^4 + \mid Q_{2n} \mid^2 - 2 * R[Q_{2n}Q_n^* Q_n^*] - 4(M-2) \mid Q_n \mid^2)}{M(M-1)(M-2)(M-3)} \\ & + \frac{2}{(M-1)(M-2)} \end{aligned} \tag{4.40}$$

Final four particle correlator can be obtained by averaging over N events and is used to estimate the 4^{th} order cumulant.

Thus, we have estimated the both 2^{nd} and 4^{th} order cumulants and the three particle correlator. The three particle azimuthal correlations relative to reaction plane are measured by inserting the values from Eqs. 4.10, 4.12, and 4.13 in Eq. 4.4. The $v_{2,k}$ used in Eq. 4.4 is taken as the average of $v_2\{2\}$ and $v_2\{4\}$.

4.3.3 Event characterization using Sliding Dumbbell Method

The $Db_{\pm}^{max}$ distributions obtained using the Sliding Dumbbell Method are divided into 10 bins where 0-10% $Db_{\pm}^{max}$ bin contains higher $Db_{\pm}^{max}$ values and the lower values fall in the lowest $Db_{\pm}^{max}$ bin of 90-100%. In this way the events of same centrality are categorized into 10 different $Db_{\pm}^{max}$ bins exhibiting different charge separation. The correlator values are estimated for all charge combinations (+ +, - -, + -) for different $Db_{\pm}^{max}$ values for all centralities. The results obtained for the two- and three- particle azimuthal correlations are discussed in the next sections.

4.3.4 Background Estimation

Every experimental measurement of an observable contains physics correlations as well as some contribution from the background correlations which can induce similar effect as data. To extract the physics signal from the estimated quantity one has to eliminate or minimize the background. The two different techniques are used for the estimation of background correlations and compared with the data to quantify the signal contribution.

- **Charge Reshuffle:** In charge reshuffle technique, the charges of the particles are reshuffled randomly over the azimuthal plane keeping polar angle (θ) and azimuthal angle (ϕ) same. A new sample of reshuffled charge events is obtained It is named as "**ChrgR**".

- **Randomization of Azimuthal angle:** Another technique used to measure the background correlations is performed by randomizing the azimuthal angles (ϕ) of the particles in an event keeping the same number of positive and negative charged particles as that of data event. The advantage of using this technique is that it destroys all correlations amongst particles.

The analysis results obtained from the ChrgR and Random are compared with those of HIJING and AMPT event generators for the multi-particle azimuthal correlations.

4.4 Heavy Ion Jet Interaction Generator

HIJING is a Monte Carlo event generator developed to study jet and associated particle production in pp, $p\bar{p}$, pA, and AA collisions at ultra-relativistic energies [16]. It combines the QCD model for jet production with the Lund model for jet fragmentation. HIJING is designed to explore the wide range of initial conditions that may occur in heavy-ion collisions and covers a wide energy range from 50 GeV to few TeV. About 3 M official ALICE HIJING events of Pb-Pb collisions at $\sqrt{s}_{\rm NN}$ = 2.76 TeV are analyzed in this thesis work.

4.5 Simulation results from HIJING

The results on the study of charge separation effect using multi-particle correlators are obtained for HIJING event generator. The centrality dependence of $Db_{\pm}^{max}$ distributions and the variation of two- and three- particle azimuthal correlators for HIJING events are discussed in this section.

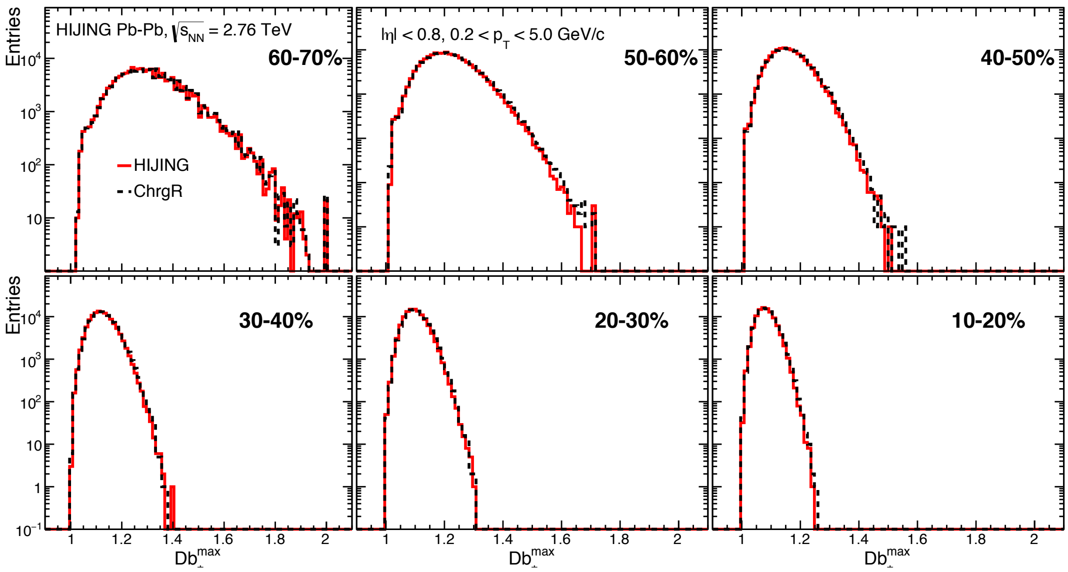

Figure 4.3: Centrality dependence of $Db_{\pm}^{max}$ distributions obtained using the sliding dumbbell method for HIJING events. The $Db_{\pm}^{max}$ distributions from ChrgR are also displayed.

4.5.1 $Db_{\pm}^{max}$ distributions using Sliding Dumbbell Method

The observable $Db_{\pm}^{max}$ is the sum of positive charge fraction on the forward side of the dumbbell and negative charge fraction on the backward side of the dumbbell, measured using the SDM. The centrality dependence of $Db_{\pm}^{max}$ distributions obtained from HIJING and ChrgR are shown in figure 4.3. Both the distributions exhibit similar behaviour in each centrality interval and shift towards higher $Db_{\pm}^{max}$ values as one moves from more central to semi-central collisions indicating events with large charge separation.

4.5.2 Multi-particle Azimuthal Correlations

The multi-particle correlations are used to investigate the charge separation effect relative to the reaction plane. The two- and three- particle correlators are measured using cumulant method and the results from HIJING are compared with those of

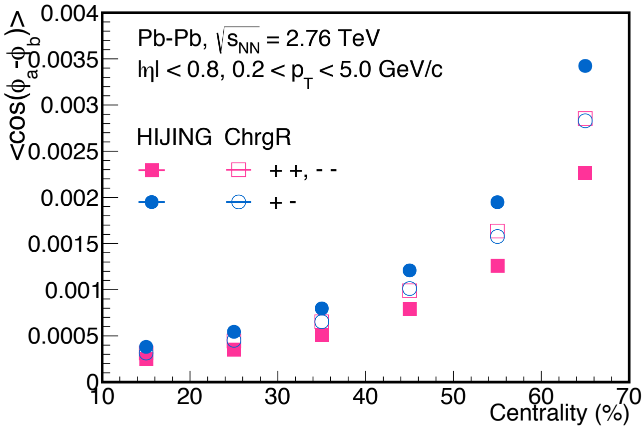

Figure 4.4: Centrality dependence of two particle correlator for opposite sign and same sign charge pairs for HIJING and ChrgR.

charge reshuffle to investigate the presence of non-statistical fluctuations.

4.5.2.1 Two Particle Azimuthal Correlations

Figure 4.4 presents the two particle correlations for the pairs of same sign (SS) and opposite sign (OS) charged particles in each centrality and exhibit similar trend for all charge combinations. The OS charge pairs have more positive values than those of SS pairs, whereas the charge reshuffle has similar magnitude for both OS and SS charge combinations.

4.5.2.2 $Db_{\pm}^{max}$ bin dependence of Two Particle Correlations

To further investigate the correlation between the particles of SS and OS, the two particle correlator ($\langle cos(\phi_a - \phi_b)\rangle$) is studied as a function of $Db_{\pm}^{max}$ bins. These bins are formed on the basis of lower and higher $Db_{\pm}^{max}$ values where the higher $Db_{\pm}^{max}$ values correspond to top 10% $Db_{\pm}^{max}$ bin while the lower $Db_{\pm}^{max}$ values belong to 90-100% $Db_{\pm}^{max}$ bin.

- **Opposite Sign:** Figure 4.5 (left) shows the two particle correlator as a func-

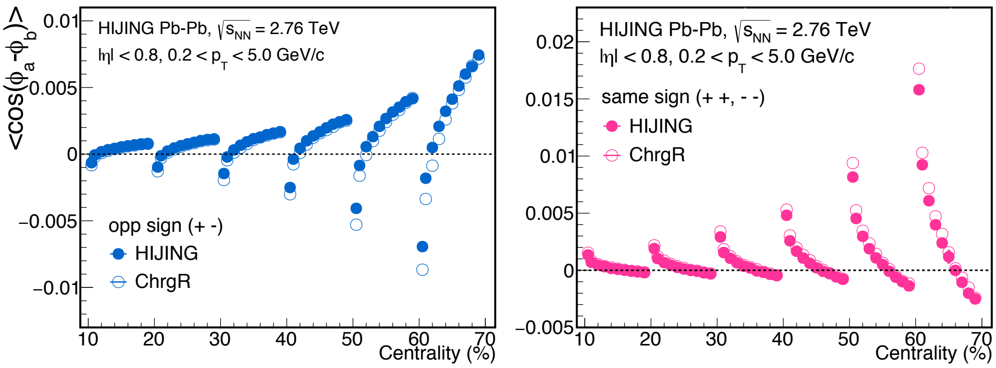

Figure 4.5: Centrality dependence of two particle correlator for opposite sign charge pairs (left) and same sign charge pairs (right) in different $Db_{\pm}^{max}$ bins for HIJING and ChrgR.

tion of $Db_{\pm}^{max}$ bin for OS pairs in different centrality classes. The first point in each centrality belongs to top 10% $Db_{\pm}^{max}$ bin and the last one belongs to 90-100% $Db_{\pm}^{max}$. HIJING exhibit negative values for higher $Db_{\pm}^{max}$ bins, whereas the correlation values become positive as one moves toward lower $Db_{\pm}^{max}$ bins in each centrality. Also the correlator values for HIJING matches well with ChrgR within statistical errors except for the top $Db_{\pm}^{max}$ bins of 50-70% centrality.

- **Same Sign:** Figure 4.5 (right) presents the two particle correlation for HIJING and ChrgR where it is observed that both follow similar trend. The higher $Db_{\pm}^{max}$ bins exhibit more positive values and the magnitude decreases gradually for lower $Db_{\pm}^{max}$ bins. The CME production also predicts the positive values for $\langle cos(\phi_a - \phi_b)\rangle$. Though the HIJING and ChrgR exhibit positive correlation but they matches with each other within statistical uncertainties except for top 10% $Db_{\pm}^{max}$ bin of peripheral events.

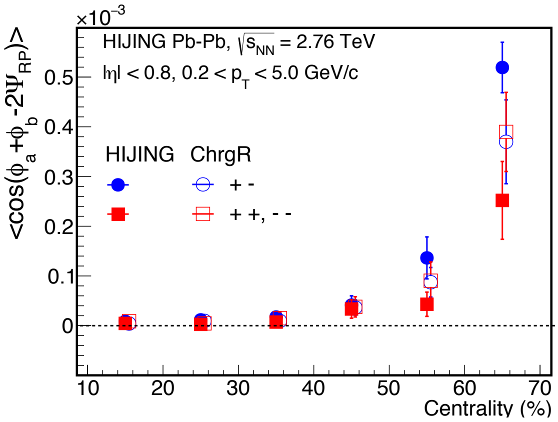

Figure 4.6: Centrality dependence of three particle correlator for opposite and same sign charge pairs for HIJING and ChrgR.

4.5.3 Three Particle Azimuthal Correlations

The centrality dependence of three particle correlator ($\gamma_{a,b}$) is measured for different charge combinations SS (+ +, - -) and OS (+ -) and is presented in figure 4.6 for the HIJING. The measurement of three particle correlator defined in Eq. 4.4 requires the elliptic flow of third particle c ($v_{2,c}$). Since HIJING does not include flow of the particles, thus the value of elliptic flow (v_2) is taken from the experimental data of Pb-Pb collisions at $\sqrt{s}_{\rm NN} = 2.76$ TeV. The estimated three particle correlator exhibit positive values for both OS and SS charge pairs in each centrality. The ChrgR shows no difference between the OS and SS charge pairs and correlation values matches with each other in all centrality intervals within the statistical errors.

4.5.3.1 $Db^{max}_{\pm}$ bin dependence of Three Particle Correlations

The three particle correlator is also studied in all $Db^{max}_{\pm}$ bins for different charge combination pairs.

- **Opposite Sign:** Figure 4.7 (left) shows the $Db^{max}_{\pm}$ dependence of three particle correlator for OS pairs (γ_{opp}) for HIJING and ChrgR. The positive values

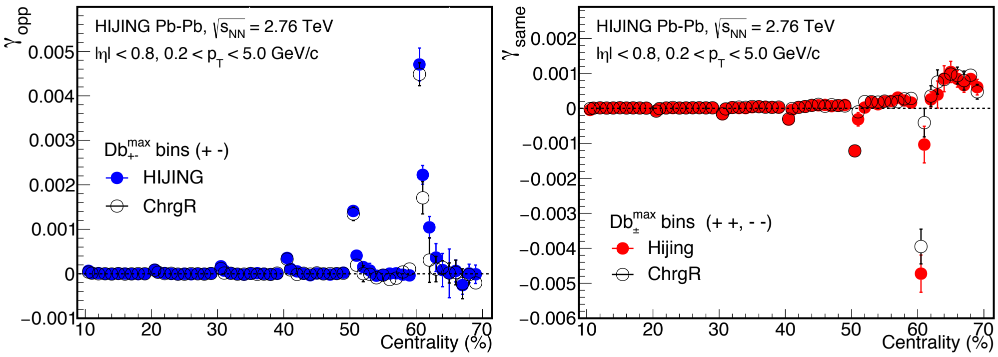

Figure 4.7: Centrality dependence of three particle correlator for opposite sign charge pairs (left) and same sign charge pairs (right) in different $Db^{max}_{\pm}$ bins for HIJING and ChrgR.

are observed in ten $Db^{max}_{\pm}$ bins showing no correlation between the oppositely charged particles. The first point in each centrality have larger positive value than the other $Db^{max}_{\pm}$ bins but it matches with the ChrgR within statistical errors showing that the observed correlations are originated from the statistical fluctuations only.

- **Same Sign:** The $Db^{max}_{\pm}$ bin dependence of γ_{same} for HIJING and ChrgR for SS charge pairs is presented in figure 4.7 (right). The γ_{same} exhibit negative values for higher $Db^{max}_{\pm}$ bins in 50-70% centrality and for the rest of the centrality intervals the values are compatible with zero and also matches well with ChrgR within error bars.

- **Opp-Same sign:** The difference between opposite and same sign three particle correlations ($\Delta\gamma = \gamma_{opp} - \gamma_{same}$) is also measured. The $\Delta\gamma$ values are positive for higher $Db^{max}_{\pm}$ bins whereas they become mildly negative for lower $Db^{max}_{\pm}$ bins in all centrality intervals as shown in figure 4.8. The HIJING and ChrgR exhibit similar values for $\Delta\gamma$ and matches with each other in all $Db^{max}_{\pm}$ bins within the statistical uncertainties.

The multi-particle correlator study observed the positive correlation for both

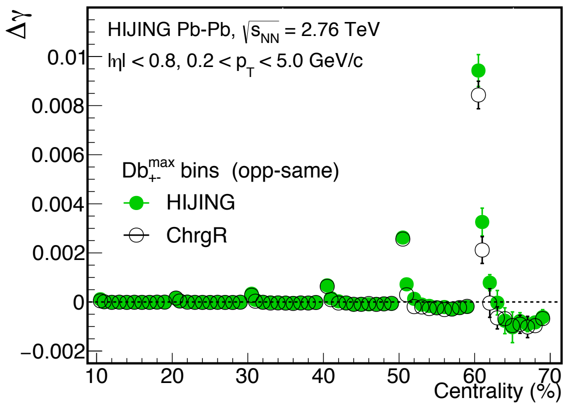

Figure 4.8: Centrality dependence of three particle correlator for the difference of opposite and same sign charge pairs in different $Db^{max}_{\pm}$ bins for HIJING and ChrgR.

two particle and three particle correlators for all charge combinations. The centrality dependence of two particle correlator exhibit the similar trend as is expected for the CME whereas the three particle correlator shows positive correlation for SS charge pairs which is exactly opposite to the CME predictions. Also the charge reshuffle do not differentiate between the pairs of particles of different charges and exhibit same magnitude for the correlation values. Thus the ChrgR can be used for the background estimation while analyzing the experimental data. Further, the particle correlations are discussed in terms of $Db^{max}_{\pm}$ bins where the measured three particle correlator shows positive values for the OS charge pairs and negative correlation values for SS charge pairs in higher $Db^{max}_{\pm}$ which is expected for the CME. Though the correlation values in higher $Db^{max}_{\pm}$ bins follow the CME expectations but they also matches with the background correlations measured using ChrgR. This suggests that no CME signal is present in HIJING and the observed correlations are the statistical fluctuations only.

4.6 A Multi Phase Transport model

AMPT is a dynamical model contains information about the transition from the partonic phase to hadronic matter. It includes information about the different phases of heavy-ion collisions and generate events for different collision systems, viz., *pp*, *pA*, and *AA* for wide energy range from few GeV to 5500 GeV [17–19]. AMPT has flow whereas HIJING does not have flow. As discussed in chapter 3, AMPT has two configurations named as, Default AMPT and String Melting AMPT (SM AMPT), which are different according to the mechanisms involved in these. For the CME study, about 1.6 M Pb-Pb events of AMPT with the SM ON configuration are generated to measure the charge-dependent particle azimuthal correlations. Similar to HIJING, the AMPT does not include CME signal.

In this section, the multi-particle azimuthal correlators are studied using the SM AMPT events. In order to understand the effect of the presence of CME signal, the different percentages of CME signal are introduced in the SM AMPT generated events and the particle azimuthal correlations are studied. The results obtained are compared with the standard SM AMPT events.

4.6.1 CME signal injection

The occurrence of CME predicts the emission of positively charged particles in one direction and the negatively charged particles in opposite direction perpendicular to the reaction plane (charge separation axis). To study the charge separation due to CME, the CME signal is injected by flipping the charges of the particles in the standard AMPT events. The different types of AMPT samples with different CME signal are generated as listed below:

- **0% CME signal:** It is the standard string melting AMPT sample and is denoted as "0% CME".

- **Fix_1 CME signal:** Charges of only one pair of charged particles are flipped perpendicular to the reaction plane in an event and a new sample of events is generated which is represented by "$Fix\_1\ CME$".

- **CME signal in 50% events:** The sample of AMPT events is created by taking the 50% of events from the standard AMPT of 0% CME and 50% from the sample of "Fix_1 CME" and is denoted as "50% $standard$−50% $Fix\_1\ CME$".

- **1% CME signal:** Charges of 1% of the total charged particles are flipped in an event to form a new sample of AMPT events. It is denoted by "1% CME".

4.7 Simulation results from AMPT

In order to observe the sensitivity of SDM and the effects of the presence of CME, the CME signal is injected in AMPT generated events. Results obtained are also compared with those of ChrgR and Random event samples generated for different samples of AMPT injected CME signals.

4.7.1 $Db_{\pm}^{max}$ distributions using Sliding Dumbbell Method

The observable $Db_{\pm}$ defined in Eq. 4.2 is measured and distributions of maxima are shown in figure 4.9 for standard AMPT events in each centrality. The $Db_{\pm}^{max}$ distributions of ChrgR and Random are also displayed. All the distributions seem similar in each centrality interval and shift toward higher $Db_{\pm}^{max}$ values as one moves toward peripheral collisions.

4.7.2 $Db_{\pm}^{max}$ distributions of CME injected AMPTs

Figure 4.10 shows the $Db_{\pm}^{max}$ distributions obtained for the signal injected AMPT events. The $Db_{\pm}^{max}$ distributions for AMPT with "Fix_1 CME" are compared with those of ChrgR and Random in each centrality interval. The distributions match

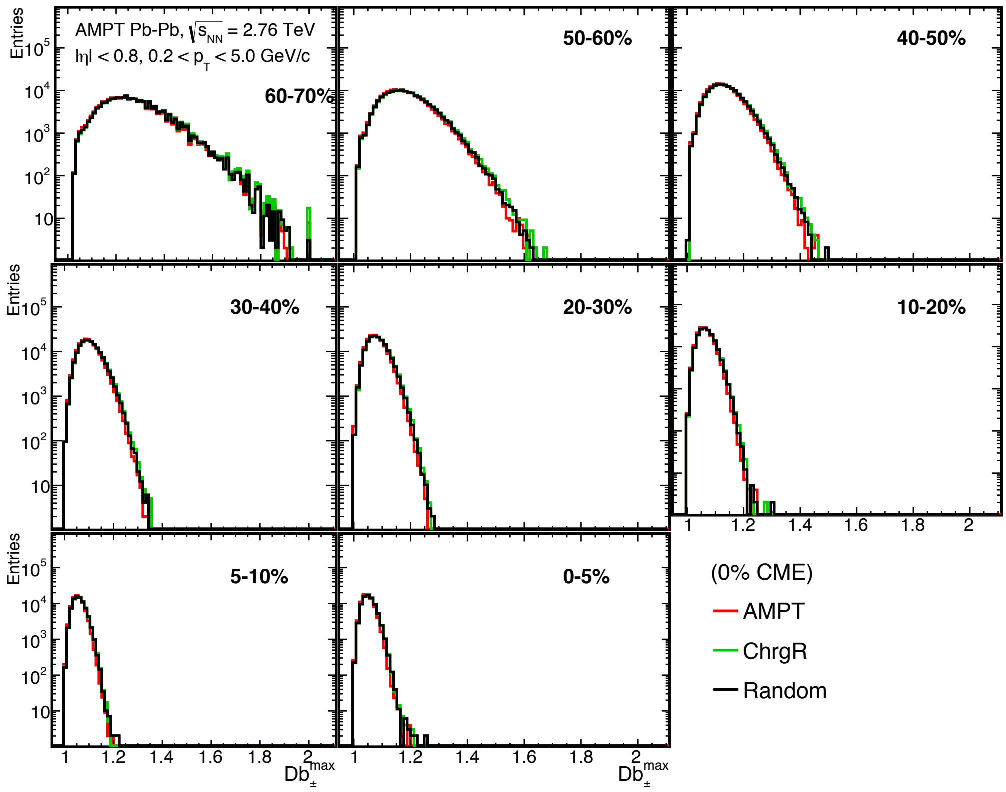

Figure 4.9: Centrality dependence of $Db_{\pm}^{max}$ distributions obtained using the sliding dumbbell method for AMPT events with 0% CME signal. The $Db_{\pm}^{max}$ distributions for ChrgR and Random are also displayed.

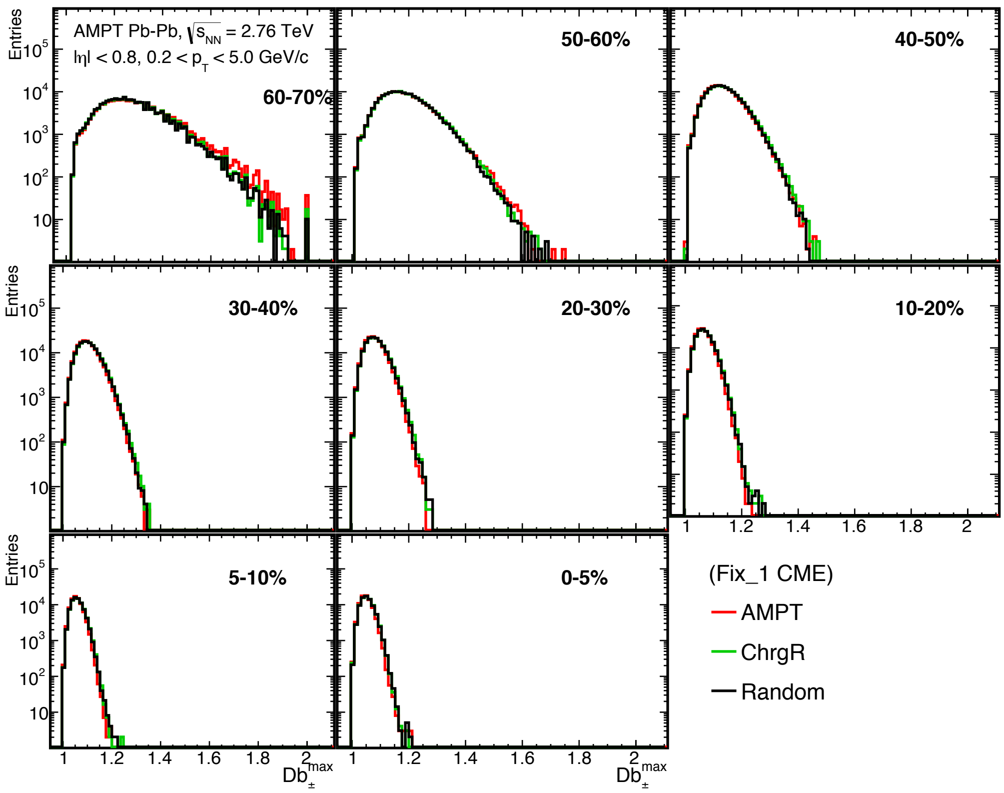

Figure 4.10: The comparison of $Db_{\pm}^{max}$ distributions obtained using the sliding dumbbell method for AMPT events with Fix_1 CME signal with the $Db_{\pm}^{max}$ distributions for ChrgR and Random.

with each other indicates that the flipping of charges of a pair of particles in an event does not lead to the large CME type contribution. Figure 4.11 displays the $Db_{\pm}^{max}$ distributions obtained from the AMPT sample formed by taking 50% events from standard AMPT and 50% events from the Fix_1 CME sample. The distributions for AMPT, ChrgR, and Random, seem similar in all centralities. Furthermore, if the CME signal is injected by flipping the charges of 1% of the particles in an event, the $Db_{\pm}^{max}$ distributions for AMPT shift towards higher $Db_{\pm}^{max}$ values whereas the ChrgR and Random distributions do not change much as shown in figure 4.12. The shift is more in central collisions rather than the peripheral events is due to the fact that the multiplicity is higher in more central collisions and hence the 1% CME signal leads to a large number of events with enhanced charge separation. Also the obtained azimuthal correlations for two- and three- particle correlators exhibit larger correlation values for 1% CME signal than those in data (calculated in next chapter). Thus we have restricted our study to 0% CME, Fix_1 CME, and 50% standard-50% Fix_1 CME signal injected AMPT events.

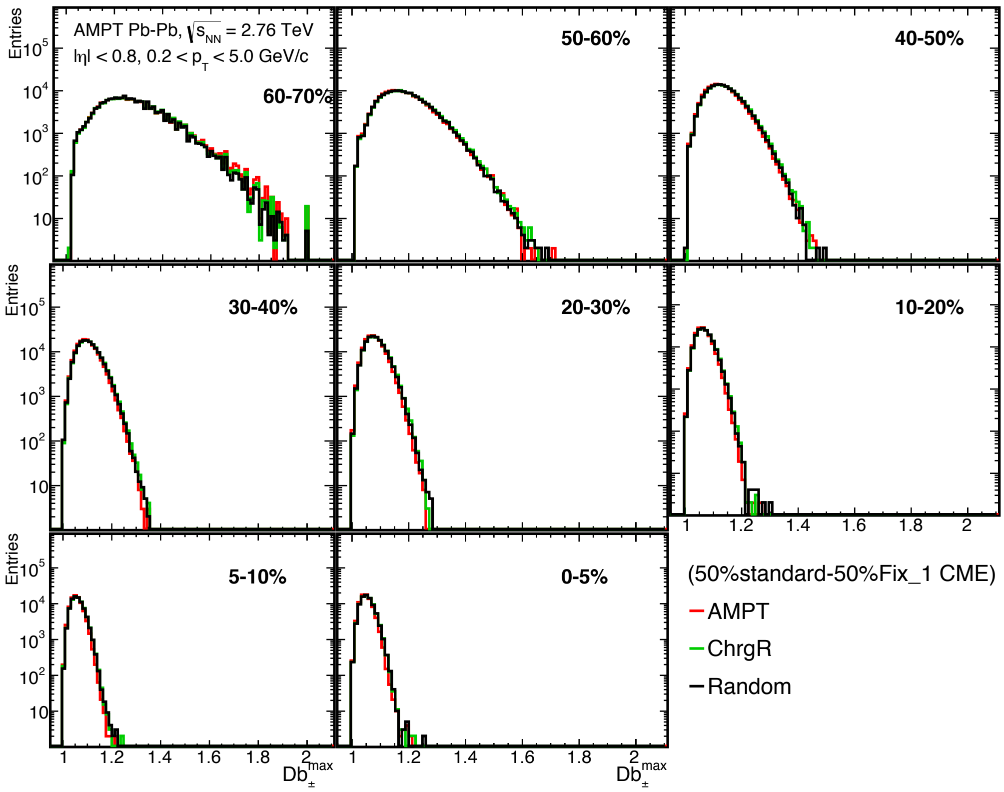

Figure 4.11: The comparison of $Db_{\pm}^{max}$ distributions obtained using the sliding dumbbell method for AMPT events containing 50% standard-50% Fix_1 CME signal with those for ChrgR and Random.

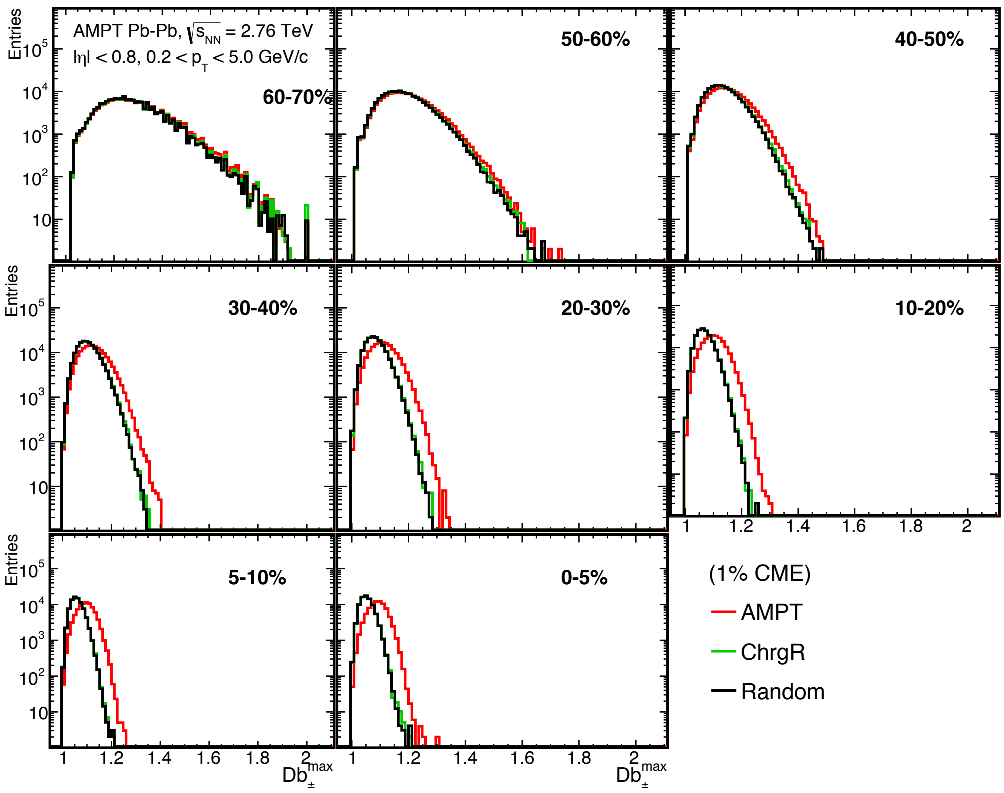

Figure 4.12: The comparison of $Db_{\pm}^{max}$ distributions obtained using the sliding dumbbell method for AMPT events containing 1% CME signal with those for ChrgR and Random.

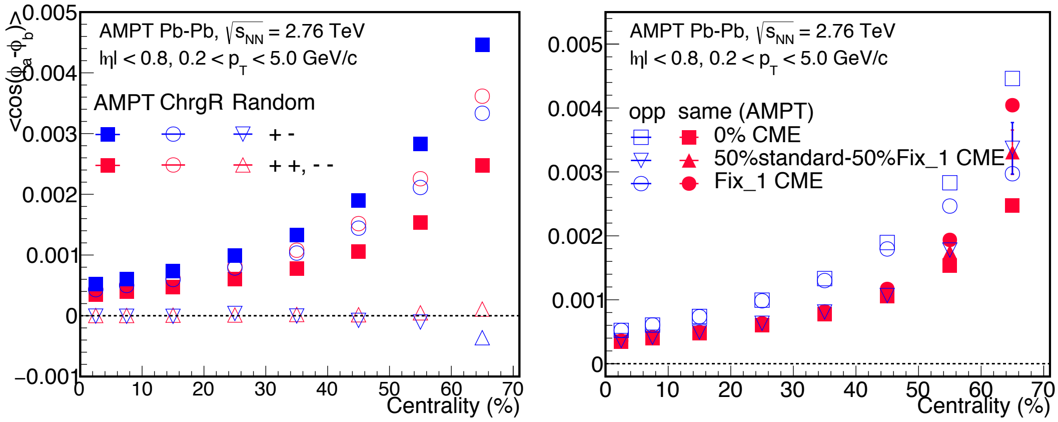

Figure 4.13: Centrality dependence of two particle correlator for opposite sign charge pairs of AMPT, ChrgR, and Random (left) and the comparison of signal injected AMPT events with the standard AMPT (right).

4.7.3 Two Particle Azimuthal Correlations

Figure 4.13 (left) presents the centrality dependence of two particle azimuthal correlator for different charge combinations and exhibit positive values for both OS and SS charge pairs in AMPT. The ChrgR and Random are also displayed in figure which show positive values for ChrgR whereas the Random is compatible with zero in all centrality bins. Also the ChrgR and Random do not differentiate between the charges of different combinations and show similar values.

The two particle correlator ($\langle cos(\phi_a - \phi_b)\rangle$) is also measured for AMPTs with different fractions of CME signal and compared with the standard AMPT. Figure 4.13 (right) shows the centrality dependence of different AMPTs and observed that the correlator values become more positive with increase in CME contribution for SS charge pairs whereas the values become smaller in magnitude for OS charge pairs. The difference in correlation values for different CME fractions is significant for 50-70% collision centrality.

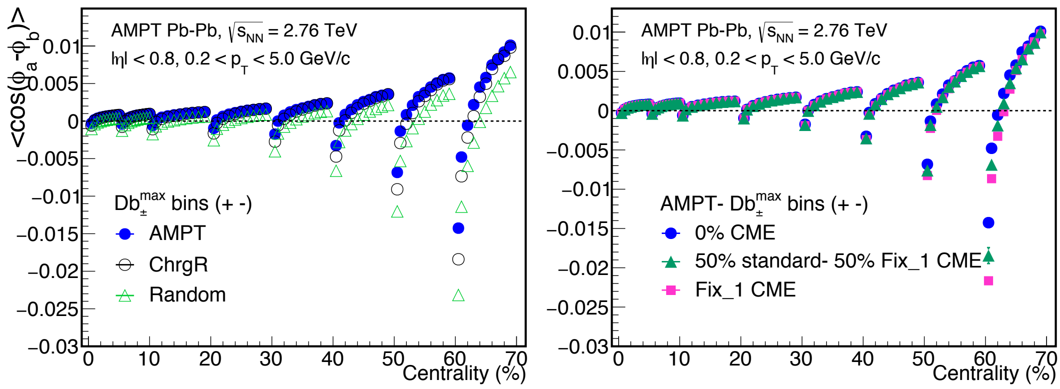

Figure 4.14: Centrality dependence of two particle correlator for opposite sign charge pairs in terms of $Db^{max}_{\pm}$ bins for AMPT, ChrgR, and Random (left) and the comparison of signal injected AMPT events with the standard AMPT (right).

4.7.3.1 $Db^{max}_{\pm}$ bin dependence of Two Particle Azimuthal Correlations

The average values for two particle correlator are positive for both OS and SS charge pairs in each centrality. The variation of $\langle cos(\phi_a - \phi_b)\rangle$ is studied in different $Db^{max}_{\pm}$ bins for AMPT, ChrgR, and Random. Also the comparison of standard AMPT is made with different fractions of injected CME signal.

- **Opposite Sign:** The two particle correlator measured in terms of $Db^{max}_{\pm}$ bins for OS charge pairs is presented in figure 4.14 (left). The higher $Db^{max}_{\pm}$ bins show negative correlation for AMPT, ChrgR, and Random, whereas in the lower $Db^{max}_{\pm}$ bins the AMPT matches with the ChrgR. The $\langle cos(\phi_a - \phi_b)\rangle$ is also estimated for signal injected AMPT events and compared with the standard AMPT shown in figure 4.14 (right). The correlation values become more negative with increase in signal contribution in the AMPT events.

- **Same Sign:** Figure 4.15 (left) presents the centrality dependence of $\langle cos(\phi_a - \phi_b)\rangle$ for SS charge pairs in terms of $Db^{max}_{\pm}$ bins. The higher $Db^{max}_{\pm}$ bins exhibit positive correlation values in AMPT, ChrgR, and Random as expected for the CME. Though the AMPT has positive values in higher $Db^{max}_{\pm}$ bins but they

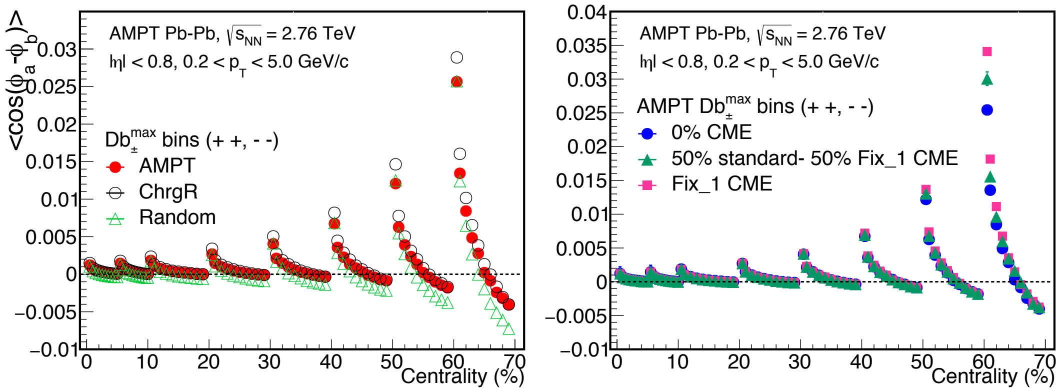

Figure 4.15: Centrality dependence of two particle correlator for same sign charge pairs in terms of $Db_{\pm}^{max}$ bins for AMPT, ChrgR, and Random (left) and the comparison of signal injected AMPT events with the standard AMPT (right).

matches with those obtained from Random showing the absence of any kinds of dynamical effects. The comparison of two particle correlator for different AMPTs is shown in figure 4.15 (right). The more the injected CME signal the larger are the correlation values for 40-70% collision centralities.

4.7.4 Three Particle Azimuthal Correlations

The three particle correlator (γ_{ab}) is sensitive to the CME-type effects in heavy-ion collisions. Figure 4.16 (left) displays the centrality dependence of γ_{ab} correlator for OS and SS charge pairs. Both the charge combinations exhibit negative values in AMPT. The correlation values for SS charged pairs are more negative than those of OS charged pairs showing strong correlation among themselves. The ChrgR exhibits negative values of same magnitude for both OS and SS charge pairs whereas the Random is compatible with zero irrespective of charges of the particles.

The comparison of signal injected AMPTs are also done in different centrality intervals and is displayed in figure 4.16 (right). As discussed in figure 4.16 (left), the OS and SS charge pairs exhibit negative values for standard AMPT, whereas for the AMPTs with CME signal injected, the correlation values rise up and become

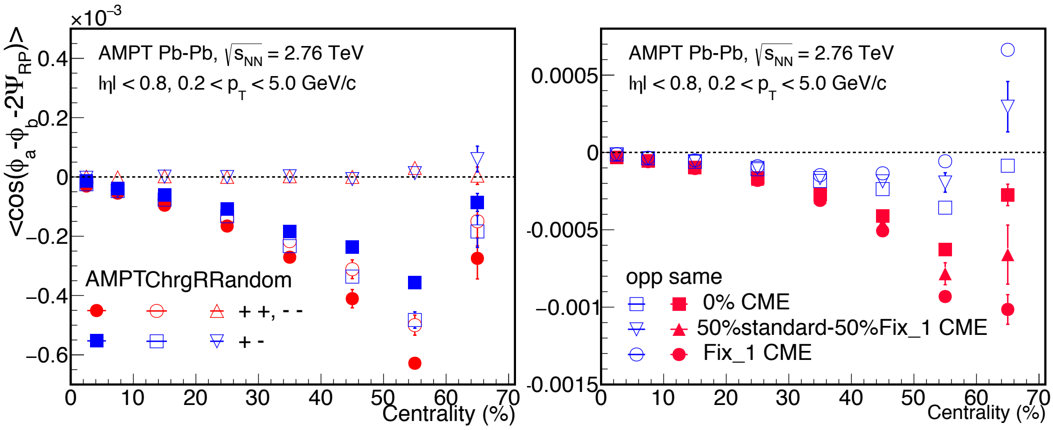

Figure 4.16: Centrality dependence of three particle correlator for different charge combinations for AMPT, ChrgR, and Random (left) and the comparison of signal injected AMPT events with the standard AMPT (right).

positive for OS charge pairs in semi-central collisions. For the SS charge pairs γ_{same} becomes more negative than those of standard AMPT in each centrality.

4.7.4.1 $Db_{\pm}^{max}$ bin dependence of Three Particle Azimuthal Correlations

The three particle correlator is estimated for OS, SS and the difference of OS and SS charge pairs as a function of $Db_{\pm}^{max}$ bins in each centrality.

- **Opposite Sign:** Figure 4.17 (left) shows the variation of γ_{opp} in terms of $Db_{\pm}^{max}$ bins for standard AMPT, ChrgR, and Random. The observed correlator values are positive in higher $Db_{\pm}^{max}$ bins and matches with each other within statistical uncertainties for all centrality intervals. Figure 4.17 (right) presents centrality dependence of γ_{opp} for signal injected AMPTs and observed that the correlation values become more positive with increase in injected CME signal.

- **Same Sign:** For the SS charge pairs, the $Db_{\pm}^{max}$ bin dependence of γ_{same} is presented in figure 4.18 (left). A large negative values are seen in higher $Db_{\pm}^{max}$ bins for each centrality indicating the presence of strong correlation between the particles of same sign. The more negative correlation values are

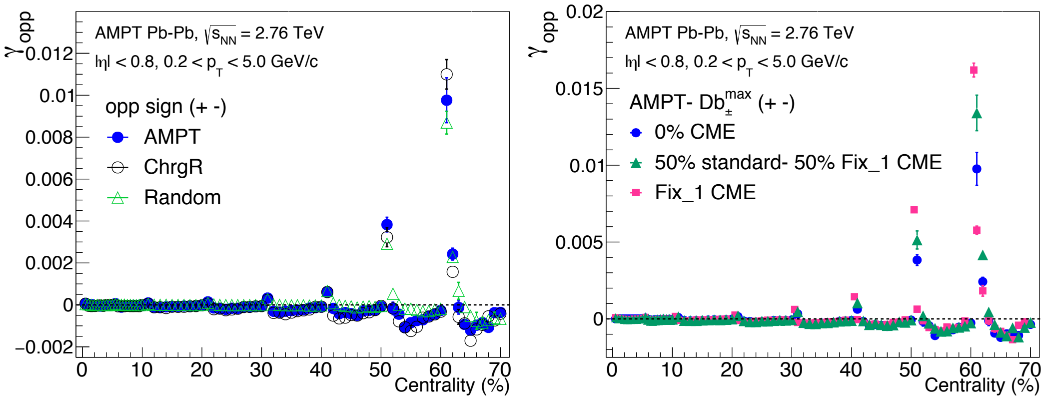

Figure 4.17: Centrality dependence of three particle correlator for opposite sign charge pairs in terms of $Db_{\pm}^{max}$ bins for AMPT, ChrgR, and Random (left) and the comparison of signal injected AMPT events with the standard AMPT (right).

seen for the injected CME signal samples. The ChrgR also behaves in a similar manner like AMPT whereas the Random exhibits relatively smaller values for the γ_{same} in higher $Db_{\pm}^{max}$ bins.

The γ_{same} values for AMPTs with different CME signal contributions are compared in each $Db_{\pm}^{max}$ bin. Figure 4.18 (right) shows the centrality dependence of γ_{same} for 0% CME, Fix_1 CME signal, and for 50%standard-50%Fix_1 CME signal. The correlation values become more and more negative as the signal contribution increases indicating the strong dependence of three particle correlator on the percentage of signal injected.

- **Opp-Same Sign:** Figure 4.19 (left) presents the difference of opposite and same sign three particle correlation ($\Delta\gamma$) as a function of centrality in each $Db_{\pm}^{max}$ bin. The values are positive in higher $Db_{\pm}^{max}$ bins and matches with those of ChrgR. The Random shows positive correlation but comparatively smaller in magnitude in each $Db_{\pm}^{max}$ bin. The Random is also compatible with zero except for the top 10-20% $Db_{\pm}^{max}$ bins.

  The centrality dependence for the signal injected AMPT events are also studied and compared with the standard AMPT as shown in figure 4.19 (right). The

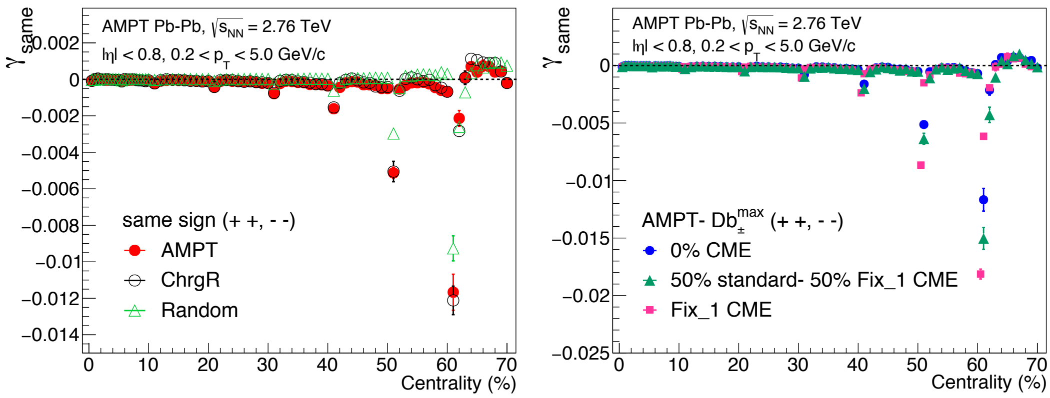

Figure 4.18: Centrality dependence of three particle correlator for same sign charge pairs in terms of $Db_{\pm}^{max}$ bins for AMPT, ChrgR, and Random (left) and the comparison of signal injected AMPT events with the standard AMPT (right).

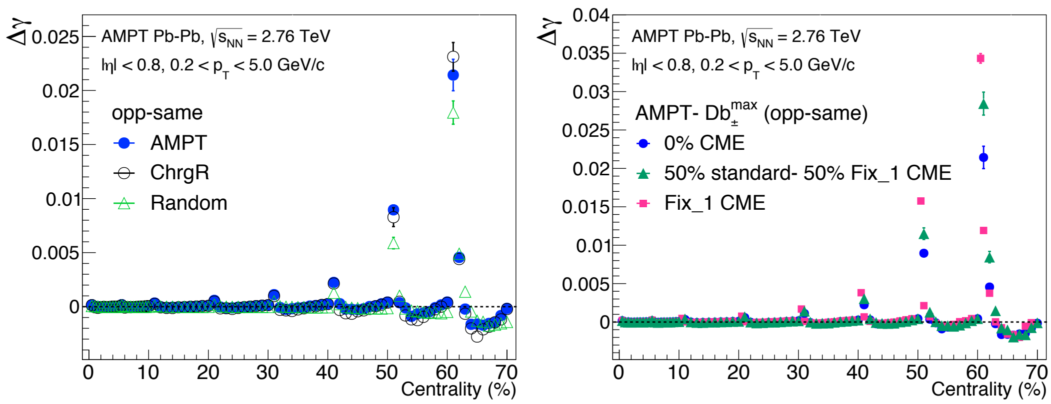

Figure 4.19: Centrality dependence of three particle correlator for the difference of opposite and same sign charge pairs in terms of $Db_{\pm}^{max}$ bins for AMPT, ChrgR, and Random (left) and the comparison of signal injected AMPT events with the standard AMPT (right).

higher correlation values are observed for the AMPT with large injected CME signal.

The classification of events in different categories on the basis of $Db_{\pm}^{max}$ bins offers a chance to study the particle azimuthal correlations on an advanced level rather than studying them by averaging over all events which can reduce the chances to observe rare physical events. The SDM helps to extract the events with large charge separation and to estimate the CME fraction in different AMPTs having different injected CME signal.

4.7.5 Fraction Estimation

In order to measure the CME contribution in the three particle correlator, the observable f_{CME} is calculated which is defined as,

$$f_{CME} = \frac{(\Delta\gamma_{AMPT} - \Delta\gamma_{Bkg})}{\Delta\gamma_{AMPT}} \tag{4.41}$$

where $\Delta\gamma_{AMPT}$ and $\Delta\gamma_{Bkg}$ are the difference of opposite sign and same sign three particle correlation for AMPT and background, respectively. For the estimation of $\Delta\gamma_{Bkg}$, the two techniques of charge reshuffle and randomization of azimuthal angles of particles in an event are used. Figure 4.19 (left) shows the large positive correlation values in higher $Db_{\pm}^{max}$ bins than those in lower $Db_{\pm}^{max}$ bins for each centrality. Also the different number of $Db_{\pm}^{max}$ bins in each centrality lead to the large correlation values for $\Delta\gamma$. We have also studied the particle correlations for signal injected AMPT events which are created by flipping the charges of the particles in an event. The $\Delta\gamma$ correlation values go higher and higher with increase in the injected CME signal as shown in figure 4.19 (right). From figure 4.19 (right), it is observed that for 50-70% centrality interval the $Db_{\pm}^{max}$ bins exhibiting large correlation values for different AMPTs are 2 in number and in 10-50% centrality only 1 $Db_{\pm}^{max}$ bin is contributing to large positive $\Delta\gamma$ values.

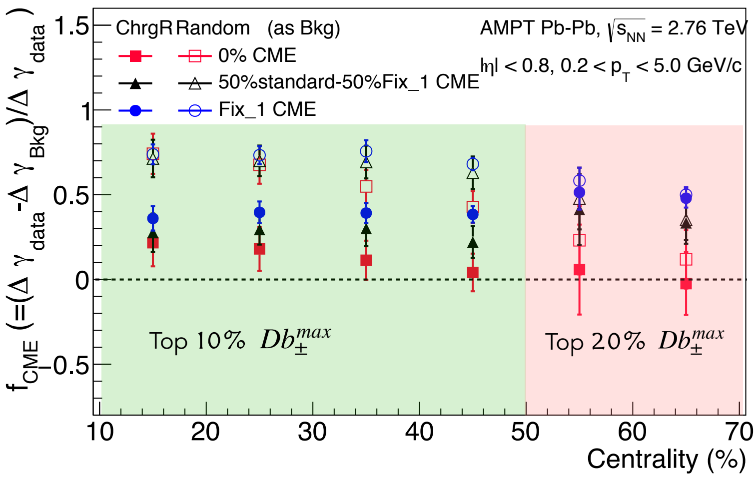

Figure 4.20: Centrality dependence of the CME fraction obtained from the higher $Db^{max}_{\pm}$ bins for AMPTs with different percentage of signal injected.

Figure 4.20 presents the estimated fraction defined in Eq. 4.41. Only top 0-10% $Db^{max}_{\pm}$ events exhibit CME type signal for 10-50% collision centrality, whereas for lower centralities of 50-70%, top 20% $Db^{max}_{\pm}$ events show CME type signal.

The more central collisions exhibit almost similar values for f_{CME} whereas a clear dependence on the injected signal contribution is seen for 30-70% collision centralities. The injected signal is not recovered in 10-20% centrality due to the large multiplicities in top centrality and the flipping of charges of a pair remain within the statistical fluctuations in these collisions. The larger fraction values are observed when Random is used as background. This is because of the absence of any type of particle correlations in randomizing azimuthal angles of particles.

4.8 Summary

An event-by-event charge separation effect is studied at $\sqrt{s_{\rm NN}}$ = 2.76 TeV using HIJING and AMPT event generators. The Sliding Dumbbell Method is used which scans the azimuthal plane to search for the events showing charge separation effect and the observable $Db_{\pm}^{max}$ is measured. The particle azimuthal correlations are studied in terms of $Db_{\pm}^{max}$ bins for different centrality intervals. The background is estimated by reshuffling the charges of the particles keeping θ and ϕ same in an event and by randomizing the azimuthal angles of the particles in an event. Results obtained are compared for the two particle (δ_{ab}) and three particle (γ_{ab}) correlators using Q-cumulant method. The HIJING and AMPT results on two particle correlator show positive correlation for both OS and SS charge pairs. The ChrgR exhibits positive values and do not differentiate between the charges of the particles, whereas the Random values are compatible with zero in each centrality class. The γ_{ab} correlator is also estimated for different charge combinations as a function of centrality and exhibit positive values for HIJING and negative values for AMPT events. The $Db_{\pm}^{max}$ distributions are also obtained using sliding dumbbell method for HIJING and AMPT event generators. The distributions seem similar in each centrality and shift towards higher $Db_{\pm}^{max}$ indicating the presence of events with large charge separation. For the better understanding of SDM, the $Db_{\pm}^{max}$ distributions are divided into 10 bins for each collision centrality and measured the γ_{ab} correlator in each $Db_{\pm}^{max}$ bin. The events lying in the top $Db_{\pm}^{max}$ bins exhibit larger values for $\Delta\gamma$ correlator as compared to the rest of events belonging to lower $Db_{\pm}^{max}$ bins. We have also studied the AMPT by injecting the CME signal of different percentages viz., the AMPT with 0% CME signal (standard), AMPT with Fix_1 CME signal, AMPT with 50% events from standard AMPT and 50% from the Fix_1 CME signal events. The CME fraction (f_{CME}) is extracted and found that it increases with increase in the injected CME signal for 20-70% collision centrality.

Bibliography

[1] K. Fukushima *et al.*, "The Chiral Magnetic Effect", Phys. Rev. D **78**, 074033 (2006).

[2] D.E. Kharzeev, "Parity violation in hot QCD: Why it can happen, and how to look for it", Phys. Lett. B **633**, 260 (2006).

[3] D.E. Kharzeev, and A. Zhitnitsky, "Charge separation induced by P-odd bubbles in QCD matter", Nucl. Phys. A **797**, 67 (2007).

[4] S.A. Voloshin, "Estimate of the CME signal in heavy-ion collisions from measurements relative to the participant and spectator flow planes", arXiv:1805.05300v1 [nucl-ex] (2018).

[5] K. Fukushima *et al.*, "The Chiral Magnetic Effect", Phys. Rev. D **78**, 074033 (2006).

[6] STAR collaboration, B. Abelev *et al.,* "Observation of charge-dependent azimuthal correlations and possible local parity violation in heavy-ion collisions", Phys. Rev. C **81**, 054908 (2010).

[7] STAR Collaboration, L. Adamczyk *et al.*, "Beam-Energy Dependence of Charge Separation along the Magnetic Field in Au + Au Collisions at RHIC", Phys. Rev. Lett. **113**, 052302 (2014).

[8] ALICE collaboration, B. Abelev *et al.,* "Charge separation relative to the reaction plane in Pb-Pb collisions at $\sqrt{s}_{\mathrm{NN}} = 2.76$ TeV", Phys. Rev. Lett. **110**, 012301 (2013).

[9] ALICE Collaboration, S. Acharya *et al.*, "Constraining the magnitude of the Chiral Magnetic Effect with Event Shape Engineering in Pb-Pb collisions at $\sqrt{s}_{\mathrm{NN}} = 2.76$ TeV", Phys. Lett. B **777**, 151 (2018).

[10] CMS collaboration, V. Khachatryan *et al.,* "Observation of charge dependent azimuthal correlations in pPb collisions and its implication for the search for the chiral magnetic effect", Phys. Rev. Lett. **118**, 122302 (2014).

[11] S.A. Voloshin, "Parity violation in hot QCD: How to detect it", Phys. Rev. C **70**, 057901 (2004).

[12] M.M. Aggarwal, G. Sood, and Y.P. Viyogi, "Event-by-event study of DCC-like fluctuation in ultra-relativistic nuclear collisions", Phys. Lett. B **638**, 39 (2006).

[13] WA98 Collaboration, M.M. Aggarwal *et al.*, "Event-by-event charged-neutral fluctuations in Pb+Pb collisions at 158 A GeV", Phys. Lett. B **701**, 300 (2011).

[14] A.A. Anselm *et al.*, "Production of classical pion field in heavy ion high energy collisions", Phys. Lett. B **266**, 482 (1991).

[15] A. Bilandzic, R. Snellings, and S. Voloshin, "Flow analysis with cumulants: direct calculations", Phys. Rev. C **83**, 044913 (2011).

[16] X.N. Wang and M. Gyulassy, "HIJING: A Monte Carlo model for multiple jet production in pp, pA and AA collisions", Phys. Rev. D **44**, 3501 (1991).

[17] Z.w. Lin, C.M. Ko, B.A. Li, and S. Pal, "A Multi-phase transport model for relativistic heavy ion collisions", Phys. Rev. C **72**, 064901 (2005).

[18] Z.w. Lin, and C.M. Ko, “Deutron nucleus collisions in a multiphase transport model”, Phys. Rev. C **68**, 054904 (2003).

[19] Z.w. Lin, and C.M. Ko, “Kaon interferometry at RHIC from AMPT model”, J. Phys. G **30**, S263 (2004).

Chapter 5

Charge Separation Effect in Pb-Pb collisions at $\sqrt{s_{\mathrm{NN}}} = 2.76$ TeV

5.1 Introduction

The strong magnetic field ($B \sim 10^{15}$ T) created by the highly energetic fast moving spectator protons in non-central heavy-ion collisions causes the separation of oppositely charged particles along the system's angular momentum direction and perpendicular to the reaction plane (spanned by the impact parameter and beam axis direction). The phenomenon is known as the Chiral Magnetic Effect (CME) [1–4]. The two conditions needed for the occurrence of CME are, strong magnetic field produced by the moving spectator protons having large positive charge, and the non-zero axial charge density created in high energy heavy-ion collisions [5, 6]. The CME formation depends on the strength of magnetic field and the duration for which the magnetic field survives without significant modifications [7]. Voloshin [8] suggested the multi-particle azimuthal correlator for the measurement of CME. The two-particle and three-particle azimuthal correlators are given by,

$$\gamma_{\alpha,\beta} = \langle cos(\phi_\alpha + \phi_\beta - 2\Psi_{RP}) \rangle \qquad and \qquad \delta_{\alpha,\beta} = \langle cos(\phi_\alpha - \phi_\beta) \rangle \tag{5.1}$$

where ϕ_α, ϕ_β and Ψ_{RP} denote the azimuthal angles of the produced particles (α and β) and reaction plane, respectively.

The expectations of the CME signal to the two particle and three particle azimuthal correlations for the pairs of same sign (SS) charged particles are,

$$\gamma_{++,--} < 0 \;\; and \;\; \delta_{++,--} > 0 \tag{5.2}$$

These correlators are expected to be equal in magnitude and opposite in sign [9]. The first measurement on the charge separation effect was reported by the STAR collaboration at RHIC BNL for Au+Au collisions at center-of-mass energy $\sqrt{s}_{\rm NN}$ = 200 GeV [10, 11]. Results obtained exhibited negative values for same sign (+ +, - -) (SS) and positive values for opposite sign (+ -) (OS) charge pairs and are qualitatively in good agreement with the CME expectations. Investigation of the charge separation effect was also performed by ALICE collaboration for Pb-Pb collisions at $\sqrt{s}_{\rm NN}$ = 2.76 TeV [12]. The ALICE results agree with the STAR measurements for three particle azimuthal correlator.

Further, STAR has also studied the reaction plane dependent three particle correlator with their Beam Energy Scan program for different center-of-mass energies ranging from 7.7 to 200 GeV in Au+Au collisions. The results show that the difference between the SS and OS charge pairs seems to vanish with decreasing beam energy, which is as expected for the CME [13].

STAR and ALICE collaborations measured the reaction plane independent two particle correlator ($\delta_{\alpha,\beta}$) for SS and OS charge pairs. Results from STAR data differ from those measured by ALICE. STAR exhibits positive correlation for OS and negative correlation for SS charge pairs showing the in-plane back-to-back correlations which is opposite to the expectations for the CME. On the other hand, ALICE data exhibit positive values for both OS and SS charge pairs showing similar behaviour as predicted by the CME.

The in-plane ($\langle cos(\phi_\alpha)cos(\phi_\beta)\rangle$) and out-of-plane ($\langle sin(\phi_\alpha)sin(\phi_\beta)\rangle$) correlation functions obtained from the decomposition of two-particle and three-particle correlators are also measured by ALICE. For the OS and SS charge pairs, the ALICE measurements show positive values for in-plane and out-of-plane correlations, whereas the STAR data have positive values for OS pairs similar to ALICE, but have negative values for SS charge pairs indicating in-plane back-to-back correlations. Thus the ALICE data qualitatively agree with the CME expectations while STAR shows some deviations.

The CMS collaboration also presented the results on charge-dependent azimuthal particle correlations in p-Pb and Pb-Pb collisions at $\sqrt{s}_{\mathrm{NN}} = 5.02$ TeV at CERN LHC [14]. The measurement has been performed for the SS and OS charged pairs as a function of multiplicity and pseudorapidity gap between two charged particles. The observed correlations have similar magnitude for both p-Pb and Pb-Pb collision systems at the same event multiplicities.

Recently, the ALICE collaboration reported the measurement on constraining the magnitude of the CME in heavy-ion collisions. The event shape engineering technique has been adopted to analyze the particle azimuthal correlations. The change in elliptic flow (v_2) reflects the initial geometry of the collision system and offers a chance to select the events with different initial geometry. This selection is based on the reduced flow vector (q_2) and is explained in detail in ref. [15]. The two particle azimuthal correlations observed the positive values for both SS and OS charge pairs. Also no v_2 dependence has been observed for two particle correlator. The three particle correlator exhibits negative values for SS and positive values for OS charge pairs in all event classes. A linear v_2 dependence is observed in each centrality interval indicating the presence of large part of background correlations in the three particle correlator. An upper limit of the CME signal contribution is reported to the three particle correlator and is found to be 26-33% at 95% confidence level [15].

In this thesis, we have investigated the event by event charge separation effect in Pb-Pb collisions at $\sqrt{s}_{\mathrm{NN}} = 2.76$ TeV. A new method named "Sliding Dumbbell Method" (SDM) is used to get event-by-event charge separation. The charge-dependent particle azimuthal correlations are measured using the Q-cumulant method [16] and studied in different centrality intervals as well as for different categories of charge separation to extract the CME-type enriched sample of events.

5.2 Data Analysis

The workflow chart shown in figure 5.1 illustrates the complete analysis procedure. The Pb-Pb collision data with good runs and events are used for the analysis. More details on data set, event selections and track selections are given below.

5.2.1 Data Set

The Pb-Pb collision data at center-of-mass energy 2.76 TeV, recorded by the ALICE detector during run-I is used in this analysis. The ALICE official name of this data set is LHC10h pass2. The list of cuts used for selecting good runs and events are listed in Table 5.1. The good runs selected from the Run Condition Table (RCT) [17] for the current analysis are listed below:

- 137161, 137232, 137235, 137431, 138192, 137162, 137231, 138275, 137236, 137243, 137430, 137440, 137441, 137443, 137530, 137531, 137539, 137541, 137544, 137549, 137595, 137608, 137638, 137639, 137685, 137686, 137691, 137692, 137693, 137704, 137718, 137722, 137724, 137751, 137752, 137844, 137848, 138190, 138197, 138201, 138225, 138364, 138396, 138438, 138439, 138442, 138469, 138534, 138578, 138579, 138582, 138583, 138621, 138624, 138638, 138652, 138653, 138662, 138666, 138730, 138732, 138837, 138870, 138871, 138872, 139028, 139029, 139036, 139037, 139038, 139105, 139107, 139173, 139309, 139310, 139314, 139328, 139329, 139360, 139437, 139438, 139465, 139503, 130505, 139507, 139510.

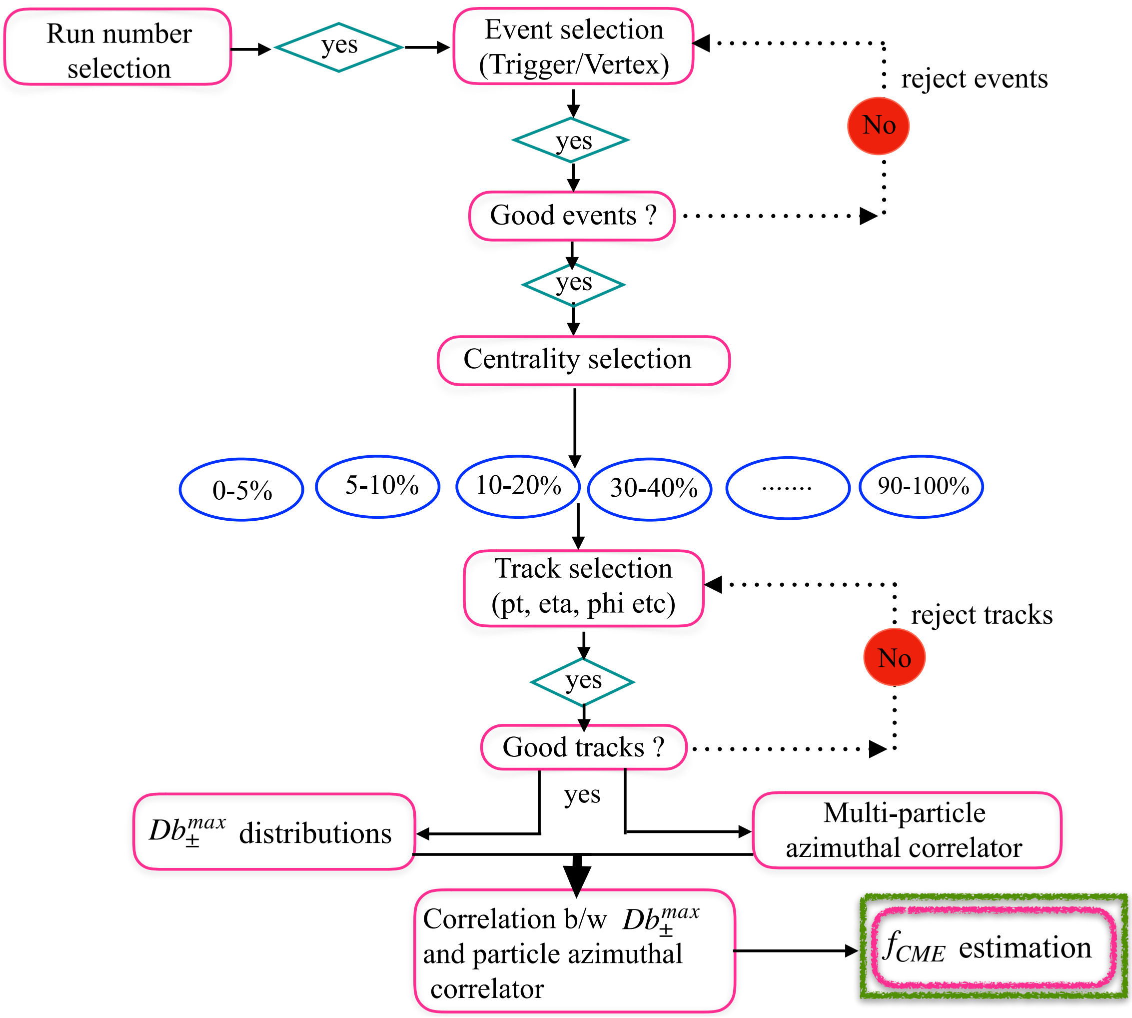

Figure 5.1: Flow chart followed for the analysis.

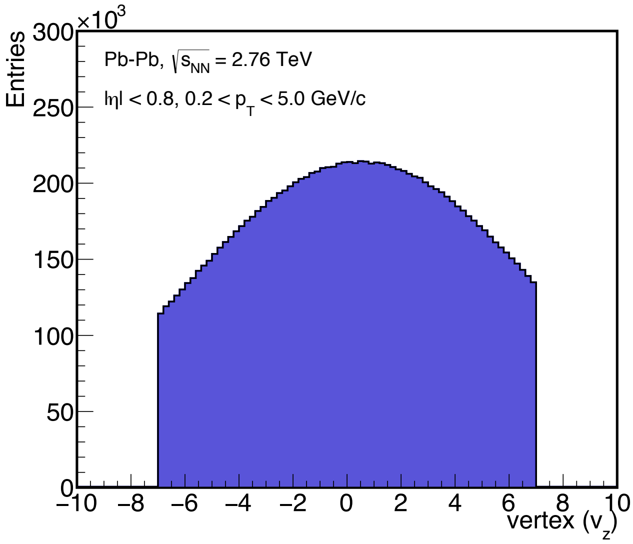

Figure 5.2: Z-vertex distribution in Pb-Pb collisions at $\sqrt{s}_{\rm NN}$ = 2.76 TeV.

The AOD (version 160) data file of LHC10h pass2 is used for the analysis. As explained in Chapter 3, AOD files in ALICE are input data files those are meant for the faster analysis as it includes only object relevant for the data analysis. In total, around 15M events those qualified standard physics selection criteria are flagged as good events and are used for the analysis.

5.2.2 Event Selection

The minimum bias (MB) collision events are analyzed using MB trigger. The MB trigger rejects the events produced by beam-gas interactions or from other possible backgrounds. The vertex cut of $7cm$ at longitudinal vertex position from the nominal interaction point is further applied to MB selected events. The cut ensures a uniform acceptance region in central part of the ALICE detector which is used for the analysis. The vertex cut distribution (v_z) is shown in figure 5.2.

Events and Track Cuts	Value
Physics selection	AliVEvent::kMB
Vertex (| V_{xy} |)	< 3.0 cm
Vertex (| V_z |)	< 7.0 cm
Transverse momentum (p_T)	$0.2 < p_T < 5.0$ GeV/c
Pseudorapidity (η)	$-0.8 < \eta < 0.8$
Azimuthal angle (ϕ)	$0 - 360^{\circ}$
χ^2/ndf	< 4
$\mid DCA_{xy} \mid$	< 3.0 cm
$\mid DCA_z \mid$	< 3.0 cm
Number of TPC clusters	> 80

Table 5.1: Event and track selection cuts used in the analysis.

5.2.3 Track Selection

The track selection criteria rejects the tracks that fails during track reconstruction which may be produced from secondary interactions. These tracks are known as fake tracks. In this analysis, the tracks reconstructed in the ALICE TPC detector are used. As mentioned earlier that AOD allows to make track selection based on its filterbit features. The different definition of filterbit numbers for different set of standard track cuts is available in ALICE framework and in this thesis, filterbit 128 is used. The filterbit 128 selects the tracks reconstructed from TPC detector only and also ensures that the tracks are coming from the primary Pb-Pb collision.

5.3 Quality Assurance

The quality assurance checks have been performed before doing the analysis to make sure that only good quality data is being used. For example, the distributions of track parameters, such as transverse momentum (p_T), azimuthal angle (ϕ), and the number of TPC clusters (N_{TPC}), are studied and are displayed in figure 5.3 run-by-run. It can be seen that run-by-run deviations are small.

The collision centrality is determined using the multiplicity distribution from the V0 detector. The correlation between centrality percentile measured using the V0 multiplicity and the TPC multiplicity is shown in figure 5.4 (left). In order to get

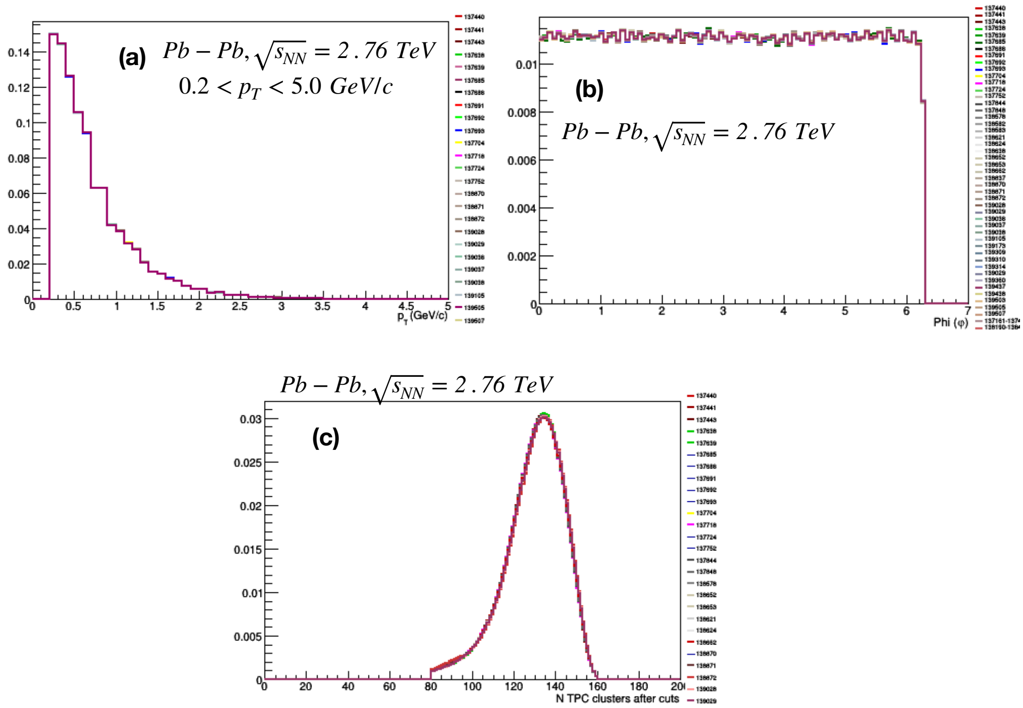

Figure 5.3: QA plots for tracks parameters; (a) p_T distributions, (b) ϕ distributions, and (c) number of TPC clusters for different run numbers as mentioned.

more uniform centrality, the outliers are removed using a cut ($\mid V0M - TPC \mid < 7.5$) based on the centralities determined by TPC and V0 detectors [18]. The centrality correlations after applying cut is linear as shown in figure 5.4 (right).

After applying the cut on centrality distributions, the multiplicity distributions for negative and positive charged particles are studied and are presented in figure 5.5 indicating the similar behaviour for both positive and negative charged particle multiplicities.

5.4 Error Estimation

The measured value of an observable for any physics analysis is different from the true value and the deviation is known as “error”. The experimental error can be

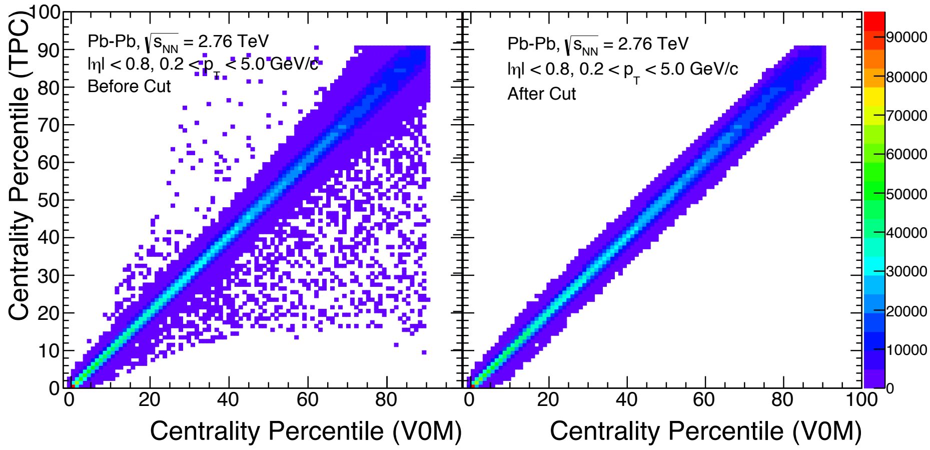

Figure 5.4: Centrality correlations between centrality estimators TPC multiplicity and V0 multiplicity before the centrality cut (left) and after the centrality cut (right).

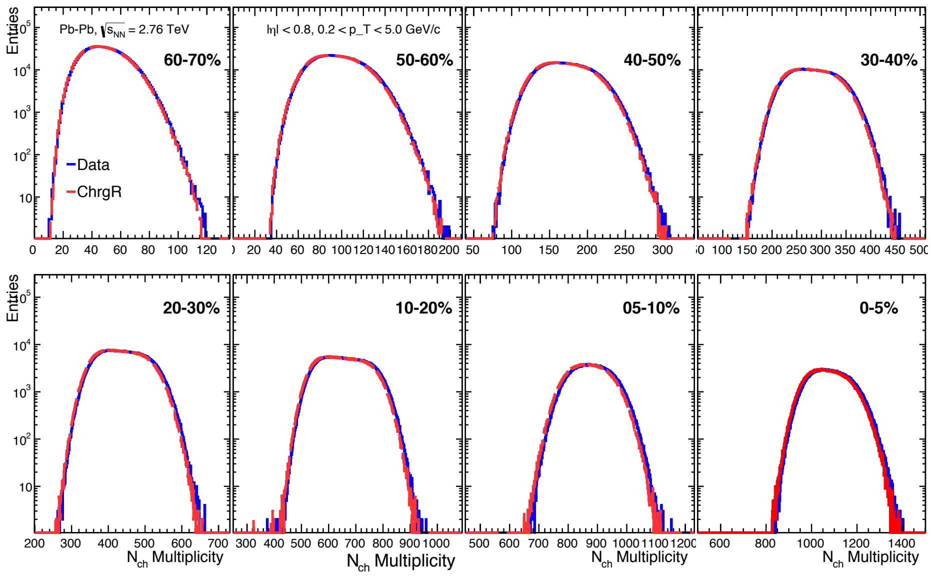

Figure 5.5: Multiplicity distributions of positive and negative charged particles for different centrality intervals.

classified into two, viz., (1) statistical error, and (2) systematic error. In this section, the error estimation for both types of errors are discussed.

5.4.1 Statistical Error

The **sub-sampling** technique is used to determine the statistical error as discussed in Chapter 3.

5.4.2 Systematic Error

To determine the affect of various event and track cuts on the observed quantities, the systematic uncertainties are estimated by varying the standard (default) cuts used in the analysis. The maximum deviation of varied cut from the standard cut in an observable is attributed to the systematic uncertainty. The systematic errors estimated from each varied cut are added in quadrature to obtain the final systematic uncertainty. The standard cuts used for the analysis are listed in Table 5.1.

Event cuts: The events selected using the V0M centrality estimator are analyzed for the current study whereas the centrality estimated via multiplicity of TPC tracks (TRK) and SPD layers (CL1) is used for systematic error estimation. The events within the vertex range of $v_z = \pm 7\ cm$ are analyzed for the analysis and for the systematic study, the vertex cut is varied for $v_z = \pm 10\ cm$ and $\pm 8\ cm$. The Pb-Pb events were recorded with positive magnetic field polarity and negative magnetic field polarity. The magnetic field configuration of each run is taken from the RCT and the difference of positive (B_+) and negative (B_-) magnetic field polarity is considered as systematic uncertainty. The like sign charged particle correlator consists of ++ and - - charge combinations. The difference between like sign charged pairs is assigned as the systematic uncertainty. The systematic uncertainty from the elliptic flow (v_2) is taken as the half of the difference between $v_2\{2\}$ and $v_2\{4\}$.

Track cuts: The track cuts varied for the systematic studies are, distance of closest approach (DCA) and number of TPC clusters. The standard cuts applied to the analysis select the primary tracks and reject the particles originate from the secondary interactions. The values for standard cuts and varied systematic cuts

Sources of uncertainty	Standard cuts	Varied cuts
Vertex ($\mid V_z \mid$)	$< 7\ cm$	$< 8\ cm$ and $< 10\ cm$
Mag Field (B)	B_+ and B_-	Difference of B_+ and B_-
Centrality Estimator	V0M	TPC and SPD
DCA_{xy}	3.0 cm	$< 2.0\ cm$ and $< 4.0\ cm$
Number of TPC clusters	< 80	< 70 and < 90
Charge combinations (SS)	++ and - -	Difference of ++ and - -
v_2	$0.5 * (v_2\{2\} + v_2\{4\})$	$0.5 * (v_2\{2\} - v_2\{4\})$

Table 5.2: Various standard cuts and varied systematic cuts to obtain the systematic uncertainties for the analysis.

from the event and track cuts are listed in Table 5.2. The systematic sources listed in Table 5.2 are studied for two particle and three particle azimuthal correlators.

The Barlow [19] test is performed to check if the variations of systematic cuts are statistically significant.

$$Barlow\ test, \qquad \sigma_B = \frac{X_{def} - X_{syst}}{\sqrt{\mid \sigma^2_{def} - \sigma^2_{syst} \mid}} \tag{5.3}$$

where σ_{def} and σ_{syst} are the statistical errors on the observed quantity obtained for default and varied systematic cuts, respectively. The X_{def} and X_{syst} are the values calculated for default and different systematic cut, respectively. If the Barlow test has value > 1, then the maximum deviation of varied cut from the default value is accounted as a systematic uncertainty corresponding to that particular systematic source. Finally the contributions from all the systematic sources are added in quadrature to obtain the total systematic uncertainty.

5.5 Background Estimation

The study of event-by-event charge separation includes large part of background correlations which can produce the similar effect of charge separation. The major background contributions are from transverse momentum conservation, elliptic flow, resonance decays etc. To suppress such background correlations the two different techniques named as *"Charge Reshuffle (ChrgR)"* and *"Random"* are used. In the first technique, the charges of the particles are reshuffled randomly over the full azimuthal plane keeping the polar angle (θ) and azimuthal angle (ϕ) same. Thus, a new sample of reshuffled charge events is obtained. The second technique includes the randomization of azimuthal angle (ϕ) of charged particles over the azimuthal plane in an event. Results from the data are compared with those reshuffled charges event sample and randomized azimuthal angle event sample.

5.6 Analysis Results

5.6.1 Sliding Dumbbell Method

As explained in Chapter 4, the Sliding Dumbbell Method (SDM) is used for the analysis and the observable $Db_{\pm}$ is measured which is defined as,

$$Db_{\pm} = \frac{N_{+}^{forw}}{(N_{+}^{forw} + N_{-}^{forw})} + \frac{N_{-}^{back}}{(N_{+}^{back} + N_{-}^{back})} \tag{5.4}$$

where N_{+}^{forw} and N_{-}^{forw} are the number of positively and negatively charged particles in the forward side of the dumbbell, respectively, whereas N_{+}^{back} and N_{-}^{back} are the number of positively and negatively charged particles in the backward side of the dumbbell, respectively. As discussed in chapter 4, after calculating the $Db_{\pm}$ every time, the Db_{asy} cut is calculated which rejects the events with large asymmetry in the positive and negative charge excess on either side of the dumbbell. Thus the maximum value for $Db_{\pm}$ is obtained in each event by sliding the dumbbell of 60° in steps of 1° in whole azimuthal plane. The $Db_{\pm}^{max}$ distributions obtained for different centralities are displayed in figure 5.6.

The $Db_{\pm}^{max}$ distributions shift towards higher $Db_{\pm}^{max}$ values as one moves from

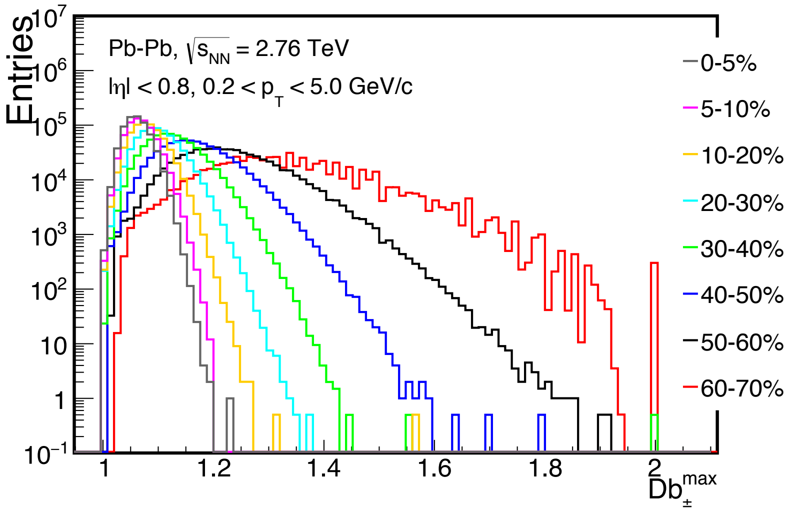

Figure 5.6: Centrality dependence of $Db_{\pm}^{max}$ distributions obtained using the sliding dumbbell method.

more central to semi-central collisions indicating the presence of events exhibiting the charge separation effect. The maximum value for the $Db_{\pm}^{max}$ is 2 which implies that the oppositely charged particles are completely separated from each other.

5.6.2 Comparison of $Db_{\pm}^{max}$ distributions from Data, ChrgR, and Random

In order to estimate the background contributions, the following two methods are used;

- Reshuffling the charges of the particles in an event keeping θ and ϕ same. It is named as ChrgR.
- Particles are randomly distributed on the azimuthal plane keeping the same number of positive and negative charged particles as in the data event. It is named as Random.

The $Db_{\pm}^{max}$ distributions obtained from charge reshuffle (ChrgR) and random-

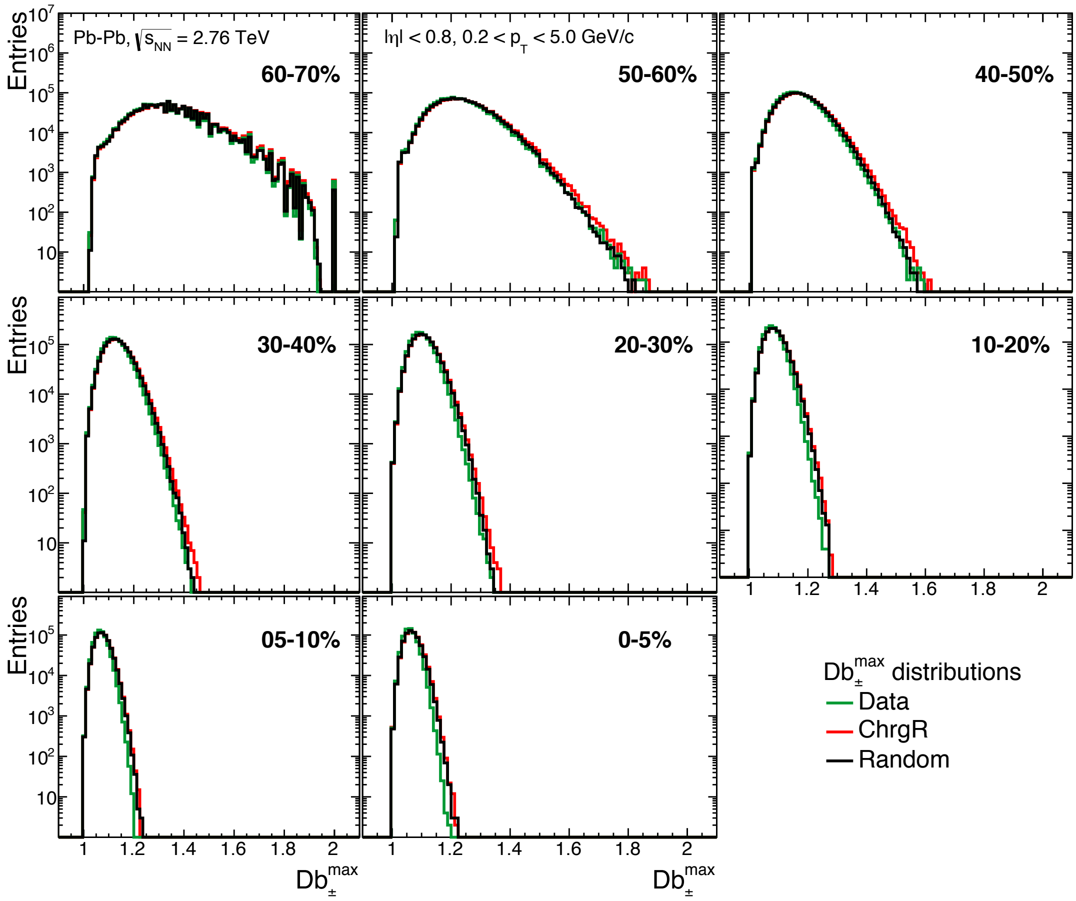

Figure 5.7: $Db_{\pm}^{max}$ distributions obtained using the sliding dumbbell method for data, charge reshuffled and random events in different centrality intervals.

ization of azimuthal angles (Random) are compared with the data in figure 5.7. The three distributions are shown by different colours and each canvas represents different centrality interval. The $Db_{\pm}^{max}$ distributions exhibit similar behaviour for data, charge reshuffle and randomized azimuthal angles in each centrality. The distributions shift towards higher $Db_{\pm}^{max}$ values as one moves from more central to peripheral collisions.

5.6.3 Multi-Particle Azimuthal Correlations

In earlier measurements, the multi-particle azimuthal correlations are studied by averaging over events in a sample for each centrality and reported the results on CME signal. It is believed that the signal may get diluted by averaging over the events. Thus, we have measured the multi-particle azimuthal correlations by slicing the $Db_{\pm}^{max}$ distributions of each centrality into 10 bins where the lowest bin of 0-10% corresponds to higher $Db_{\pm}^{max}$ values and the highest bin (90-100%) corresponds to lower $Db_{\pm}^{max}$ values. Further, the centrality dependence of two- and three- particle correlators has been studied in terms of $Db_{\pm}^{max}$ bins.

5.6.3.1 Two Particle Azimuthal Correlations

The two particle correlator (δ_{ab}) is studied for different charge combinations (++, - -, + -) as a function of collision centrality and is defined as,

$$\delta_{ab} = \langle cos(\phi_a - \phi_b) \rangle \tag{5.5}$$

where ϕ_a and ϕ_b are the azimuthal angles of particles a and b, respectively. The indices a and b represent the charges of the particles.

The centrality dependence of two particle correlator ($\delta_{a,b}$) for the SS and OS charge pairs are shown in figure 5.8. The two particle correlator for SS and OS charge pairs exhibits positive correlation and the values increases with decreasing

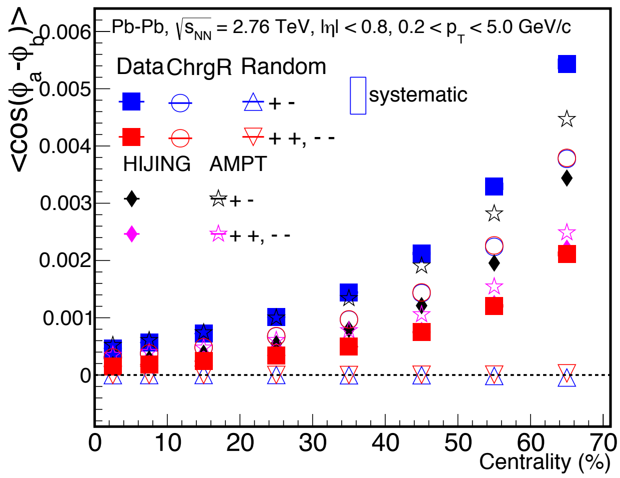

Figure 5.8: Centrality dependence of two particle correlator for the opposite sign and same sign charge pairs for data, ChrgR, and Random. The HIJING and AMPT results are also displayed.

centrality. The same sign pairs are shown with red markers and the opposite sign pairs are represented by blue coloured markers. The magnitude of correlation values is more for OS charge pairs than those of SS charge pairs. The open circles and triangles present the correlation values for charge reshuffle (ChrgR) and random (Random), respectively. The points obtained from ChrgR exhibit positive values, whereas the random points have zero values for both SS and OS charge pairs in each centrality. Also the ChrgR and Random do not differentiate between the OS and SS charge pairs as expected. The HIJING and AMPT results for the two-particle measurement are also displayed in figure 5.8. Both exhibit positive values for OS and SS charge pairs whereas the magnitude of the correlation values are smaller than in data.

5.6.3.2 $Db_{\pm}^{max}$ bin dependence of Two Particle Correlator

The measurement of two particle correlator in different bins of $Db_{\pm}^{max}$ is investigated for all charge combinations. The statistical uncertainties are represented by vertical lines and the systematic uncertainty is shown with boxes.

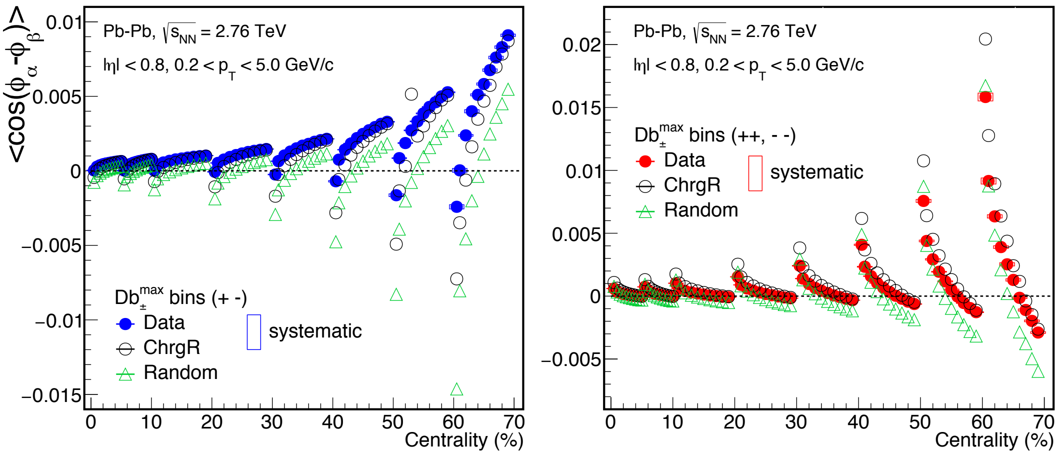

Figure 5.9: Centrality dependence of two particle correlator for pairs of particles with opposite charge (left) and same charge (right) for different $Db_{\pm}^{max}$ bins for data, ChrgR and Random.

- **Opposite Sign:** The centrality dependence of two particle correlator $\langle cos(\phi_a - \phi_b)\rangle$ for OS charge pairs is shown for all $Db_{\pm}^{max}$ bins in figure 5.9 (left). The average correlation values shown in figure 5.8 are always positive for two-particle correlator for SS and OS charge pairs, whereas it is not the case when studied in terms of $Db_{\pm}^{max}$ bins. This can be seen in Figure 5.9 (left), the higher $Db_{\pm}^{max}$ bins (top 10%) show negative correlation values while the $Db_{\pm}^{max}$ bins from 20-100% show positive correlation. The statistical error bars are smaller than the symbol size and the rectangular boxes represent systematic uncertainty. The ChrgR and Random data points exhibit similar trend and the correlation values are more negative than those of data for higher $Db_{\pm}^{max}$ bins.

- **Same Sign:** Figure 5.9 (right) presents the variation of $\langle cos(\phi_a - \phi_b)\rangle$ for SS charge pairs in each $Db_{\pm}^{max}$ bin. The higher $Db_{\pm}^{max}$ bins have positive correlation whereas the values become negative as one moves toward lower $Db_{\pm}^{max}$ bins in each centrality interval. The positive values in higher $Db_{\pm}^{max}$ bins follow the similar pattern as expected for CME.

5.6.3.3 Two Particle Correlator w.r.t top 30% $Db_{\pm}^{max}$

We have also grouped $Db_{\pm}^{max}$ into two parts; where first part consists of top 30% $Db_{\pm}^{max}$ values and the second part corresponds to 30-100% $Db_{\pm}^{max}$.

- **Opposite Sign:** The centrality dependence of $\langle cos(\phi_a - \phi_b)\rangle$ for opposite sign (left) and same sign (right) charge pairs is displayed in figure 5.10. The two particle correlator values for OS (δ_{opp}) are mildly positive for top 30% $Db_{\pm}^{max}$, whereas the higher magnitude for correlation values is observed in 30-100% $Db_{\pm}^{max}$ bins. The average values for data are close to the values in 30-100% $Db_{\pm}^{max}$ bins. The ChrgR and Random points exhibit negative correlation for 0-30% and becomes positive for rest of the events. All the $Db_{\pm}^{max}$ bins in data exhibit positive values which qualitatively describes the predictions of the CME.
- **Same Sign:** For the same sign two particle correlator (δ_{same}), top 30% $Db_{\pm}^{max}$ bins of data exhibit more positive values as predicted for CME than those of the rest of sample events.

5.6.3.4 Systematic uncertainty in $\langle cos(\phi_a - \phi_b)\rangle$ for Same Charge

The $\langle cos(\phi_a - \phi_b)\rangle$ systematics for SS charge pairs are obtained from different systematic sources viz., centrality estimators, vertex cut (v_z) in the longitudinal direction, magnetic field polarity (B_+ and B_-), elliptic flow (v_2), same sign charge pairs, number of TPC clusters, and distance of closest approach (DCA_{xy}). Each figure contains eleven plots for a particular systematic source and each plot corresponds to different $Db_{\pm}^{max}$ bin. The variation of different systematic sources are presented in figures 5.11, 5.12, 5.13, 5.15, 5.16 and 5.14.

The sources of systematic errors and their corresponding fraction values for different collision centralities are summarized in Table 5.4.

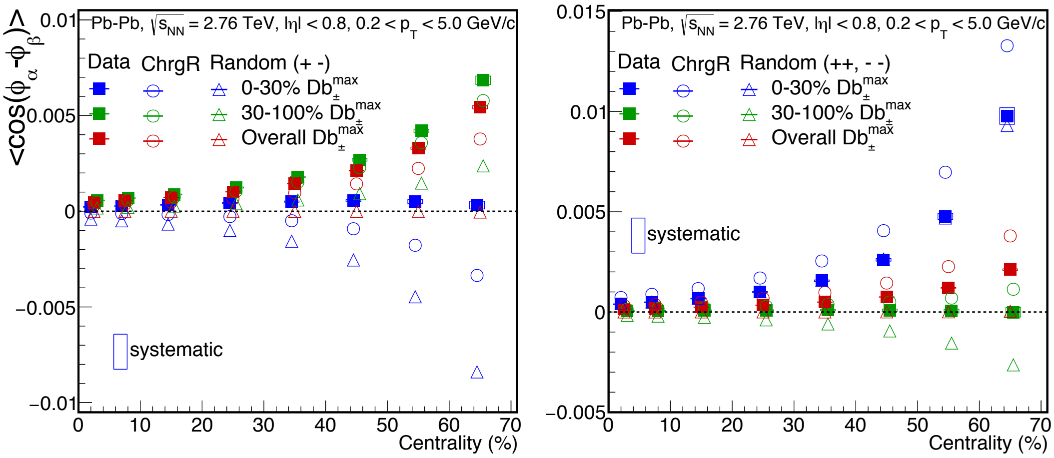

Figure 5.10: Comparison of centrality dependence of two particle correlator for the opposite sign (left) and same sign (right) charge pairs for top 30% $Db_{\pm}^{max}$ bins and for the rest of the sample events. The average values are also shown.

Cent → Sources ↓	0-5%	5-10%	10-20%	20-30%	30-40%	40-50%	50-60%	60-70%
Vertex ($\mid V_z \mid$)	0.0014	0.0039	0.0011	0.0042	0.0032	0.0024	0.0074	0.0049
Mag Field	0.0058	0.023	0.0081	0.0028	0.0112	0.0126	0.00026	0.0232
Cent. Est.	0.0068	0.0098	0.0034	0.00505	0.0068	0.0099	0.0152	0.0127
DCA_{xy}	0.0134	0.0137	0.0132	0.0106	0.01005	0.0089	0.0083	0.0035
Nclust.	0.0087	0.0116	0.0035	0.0017	0.0052	0.0064	0.0019	0.0096
Charge Comb.	0.024	0.0048	0.0186	0.014	0.0094	0.0087	0.029	0.0031

Table 5.3: Fractional systematic uncertainty values for two particle correlator for $\langle cos(\phi_a - \phi_b)\rangle$ same sign charge pairs.

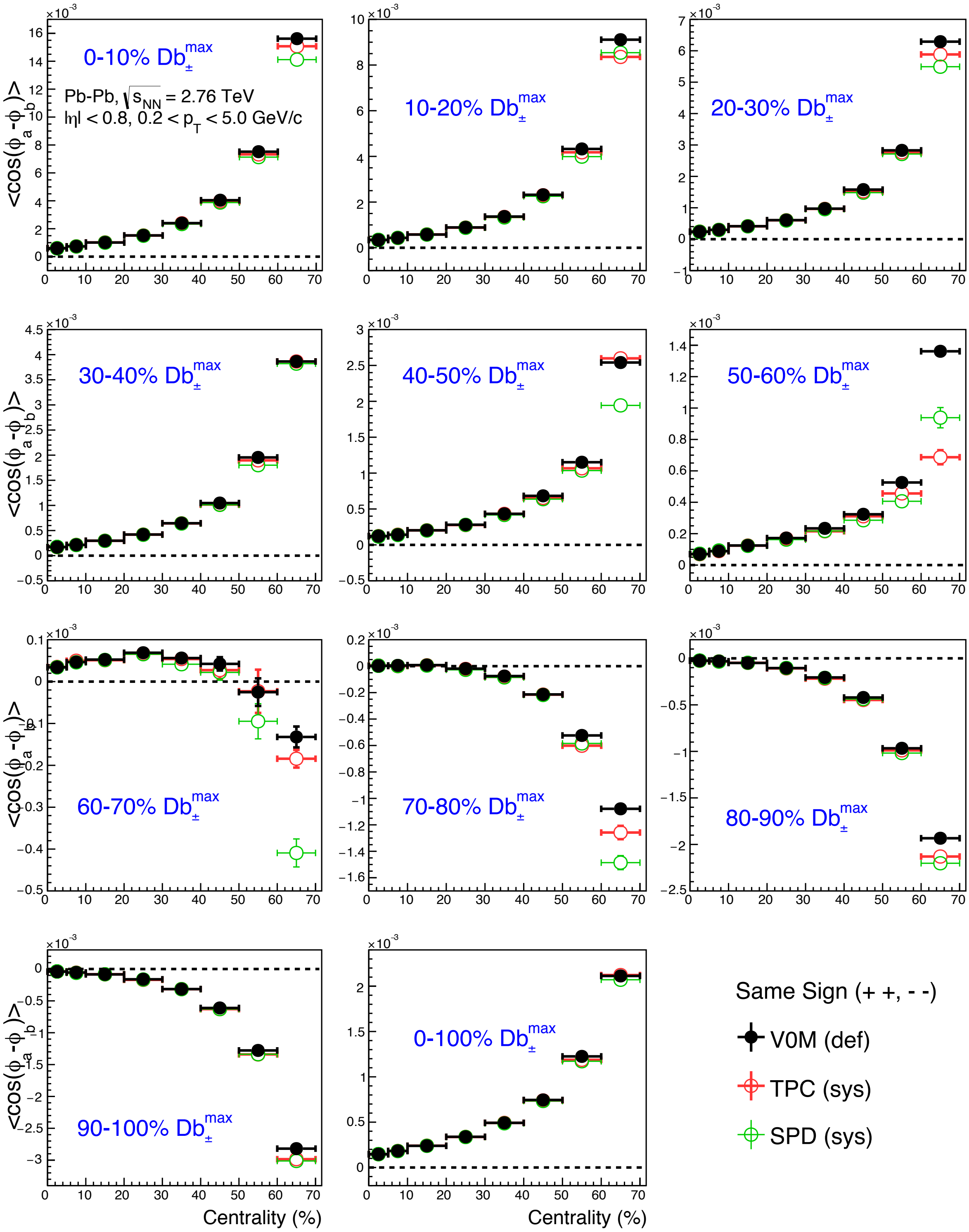

Figure 5.11: Centrality dependence of $\langle cos(\phi_a - \phi_b)\rangle$ for same charge pairs for different centrality definitions for different $Db_{\pm}^{max}$ bins as indicated.

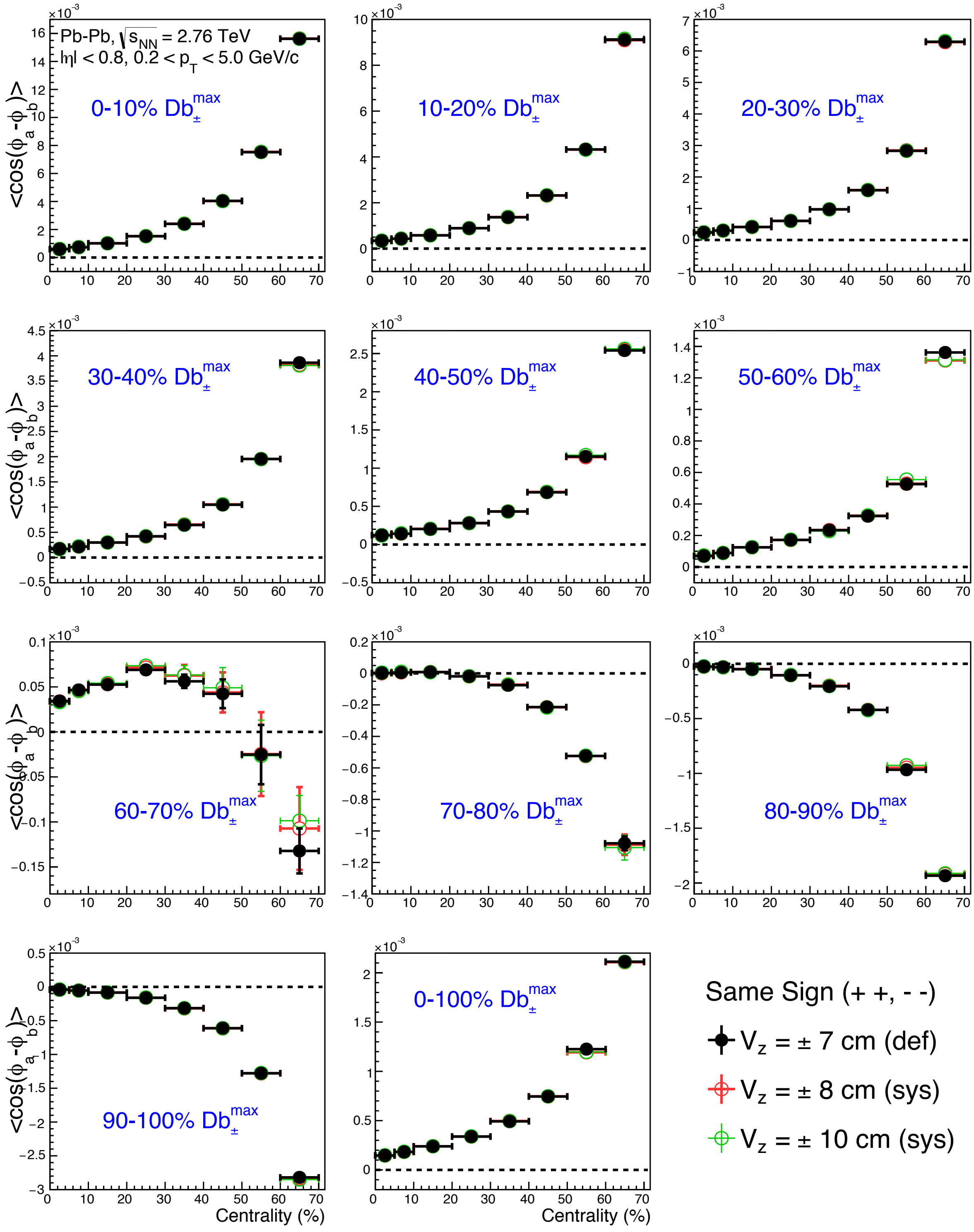

Figure 5.12: Centrality dependence of $\langle cos(\phi_a - \phi_b)\rangle$ for same charge pairs for different vertex cuts for different $Db_{\pm}^{max}$ bins as indicated.

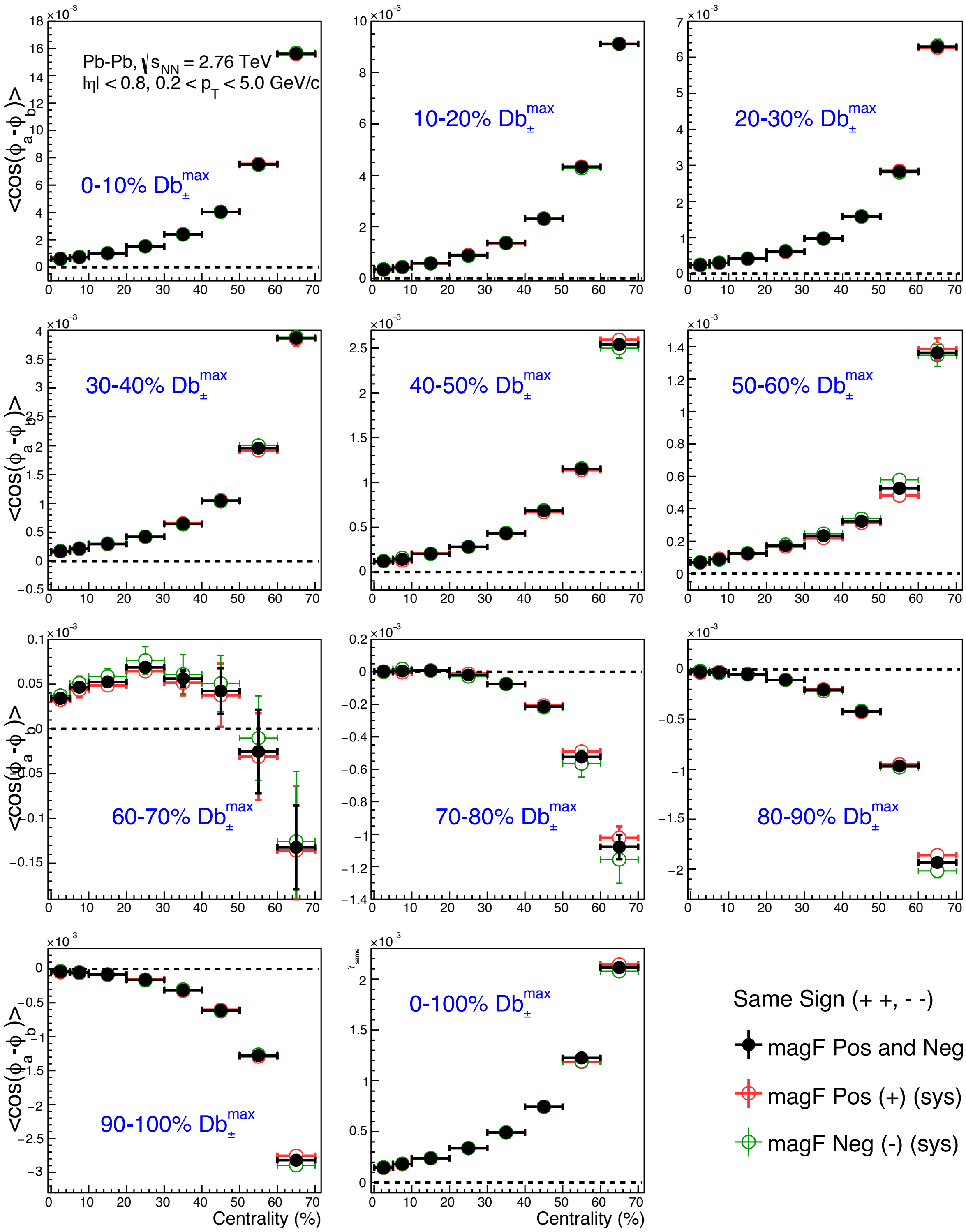

Figure 5.13: Centrality dependence of $\langle cos(\phi_a - \phi_b) \rangle$ for same charge pairs for different magnetic field polarity for different $Db_{\pm}^{max}$ bins as indicated.

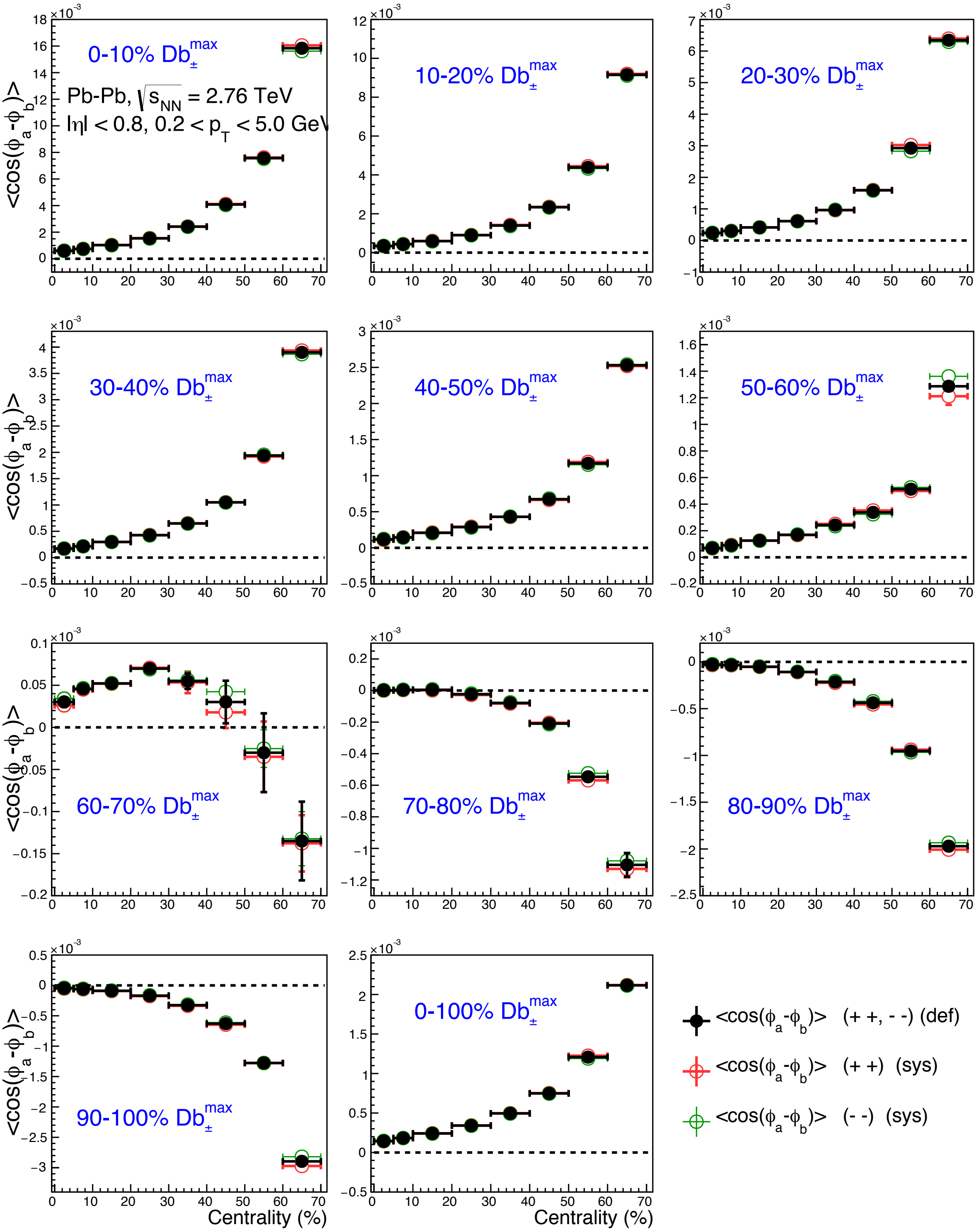

Figure 5.14: Centrality dependence of $\langle cos(\phi_a - \phi_b) \rangle$ for same charge pairs for different charge combinations (++, - -) for different $Db_{\pm}^{max}$ bins as indicated.

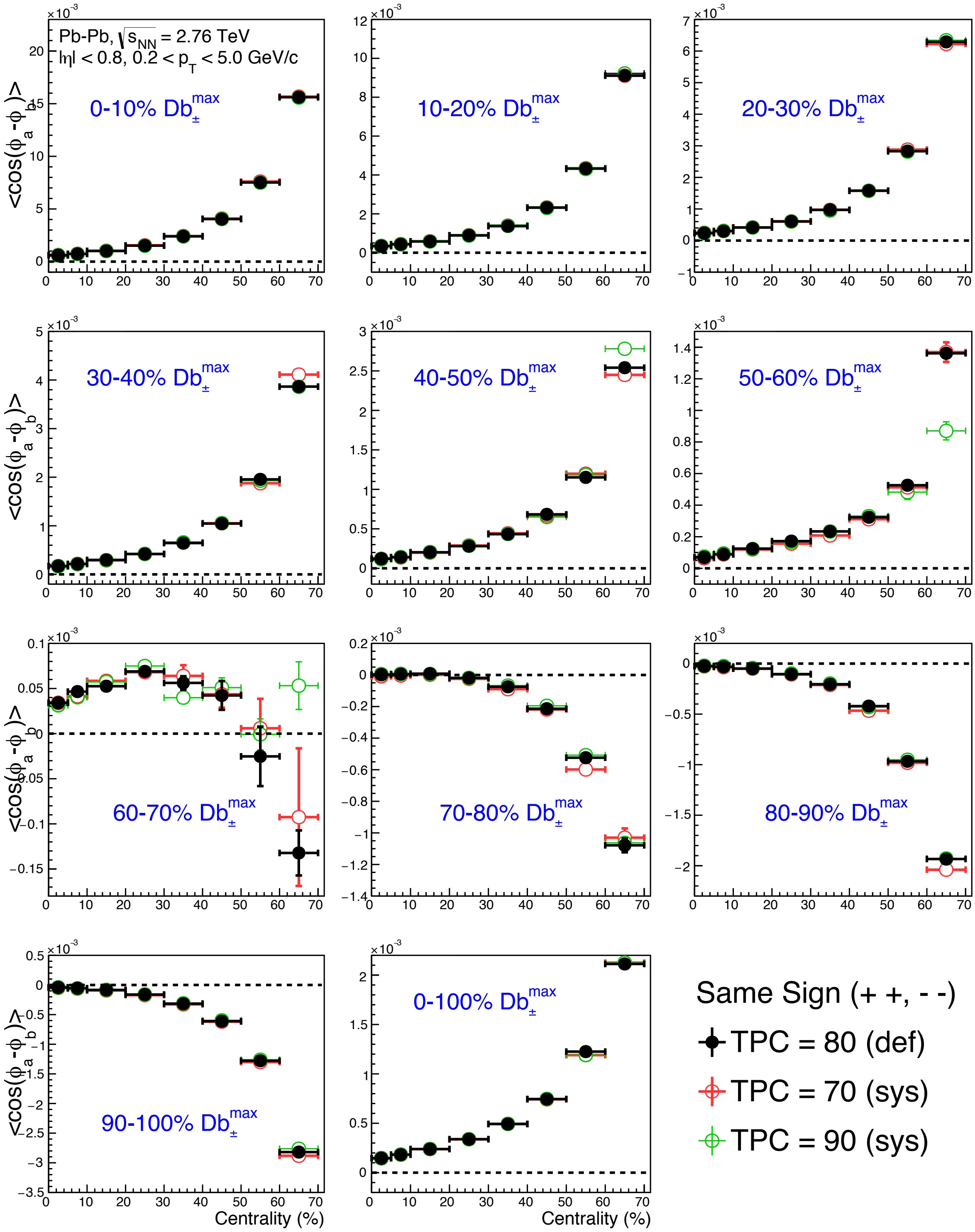

Figure 5.15: Centrality dependence of $\langle cos(\phi_a - \phi_b)\rangle$ for same charge pairs for different cuts on the number of TPC clusters for different $Db_{\pm}^{max}$ bins as indicated.

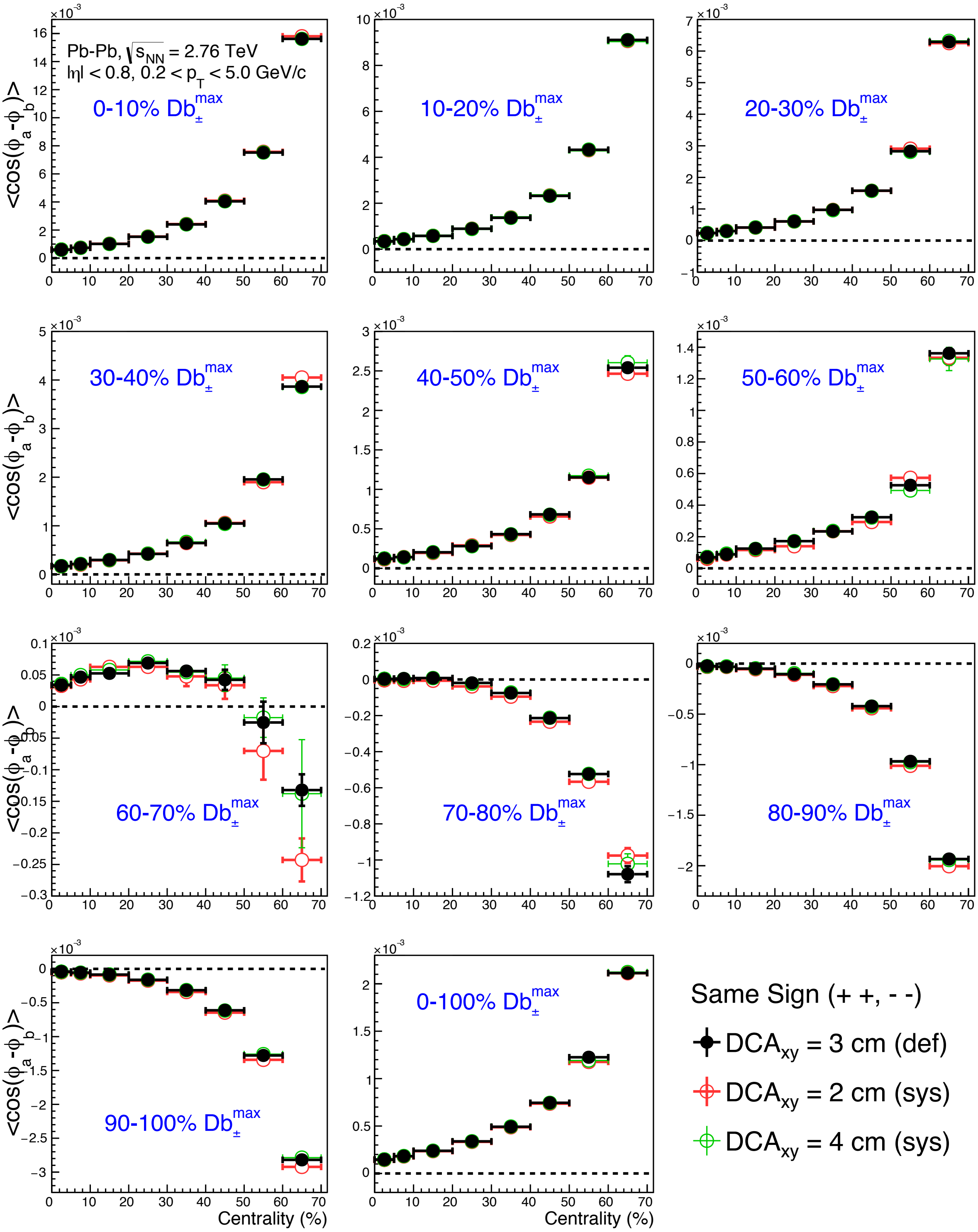

Figure 5.16: Centrality dependence of $\langle cos(\phi_a - \phi_b)\rangle$ for same charge pairs for different DCA_{xy} cuts for different $Db_{\pm}^{max}$ bins as indicated.

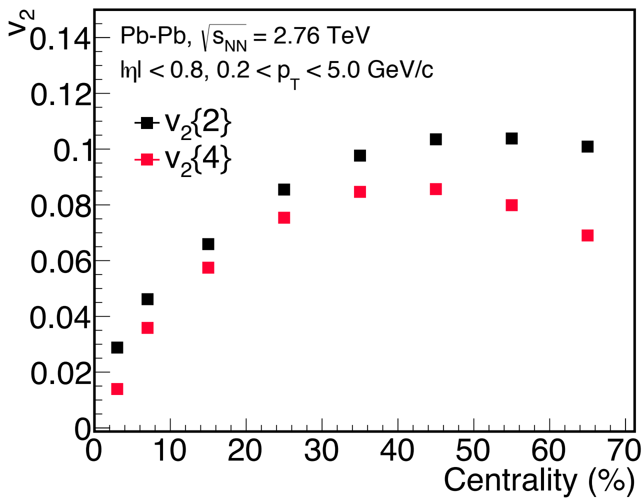

Figure 5.17: Centrality dependence of elliptic flow in Pb-Pb collisions at $\sqrt{s}_{\rm NN}$ = 2.76 TeV.

The systematic errors for OS charge pairs are also estimated in a similar manner. The variation of OS two particle correlator for various systematic sources in each $Db^{max}_{\pm}$ bin is shown in figures in Appendix A. The table listing fractional uncertainties are also added in Appendix A.

5.6.4 Centrality dependence of Elliptic Flow

The charge dependent azimuthal particle correlations contain large contribution from flow-induced correlations along with the flow-independent correlations. The elliptic flow (v_2) is measured using Q-cumulant method and the centrality dependence is shown in figure 5.17. The $v_2\{2\}$ increases as one goes from more central collisions towards semi-central collisions and saturates after 40-50% centrality. Similarly, the $v_2\{4\}$ follows qualitatively similar trend but the values are lower than the $v_2\{2\}$ which is expected as $v_2\{4\}$ does not include non-flow effects. The v_2 is taken as the mean of $v_2\{2\}$ and $v_2\{4\}$ for computing the three particle correlator. The half of the difference between $v_2\{2\}$ and $v_2\{4\}$ is taken as systematic uncertainty.

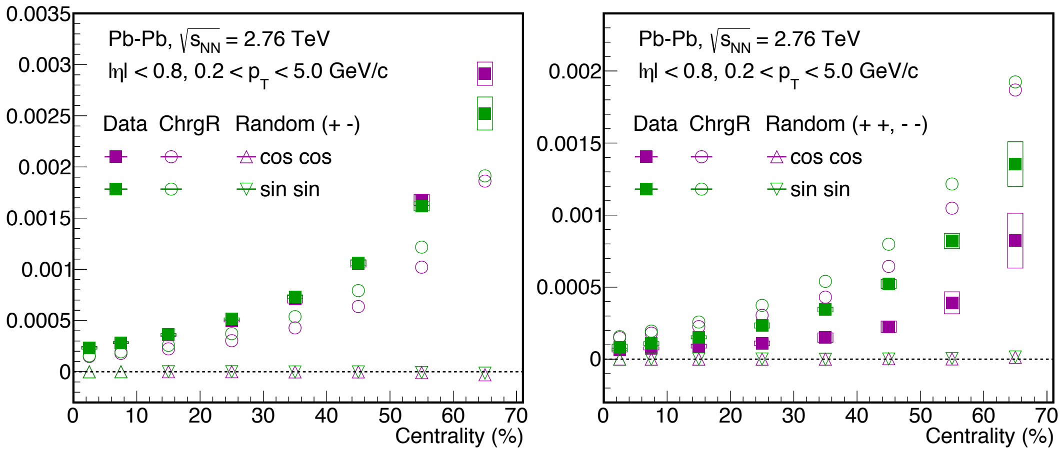

Figure 5.18: Centrality dependence of in-plane and out-of-plane correlations for opposite sign (left) and same sign (right) charge pairs for data, ChrgR, and Random.

5.6.5 In-plane and Out-of-plane Correlations

The separation of oppositely charged particles along the system's orbital angular momentum direction may arise from statistical fluctuations or from the specific dynamical effect such as the CME. The separation of charged hadrons in the out-of-plane direction is the prediction for CME signal. The three particle azimuthal correlation function can be decomposed into two terms and is expressed as,

$$\gamma_{a,b} = \langle cos(\phi_a + \phi_b - 2\phi_c)\rangle / v_{2,c} = \langle cos\Delta\phi_a \; cos\Delta\phi_b\rangle - \langle sin\Delta\phi_a \; sin\Delta\phi_b\rangle \qquad (5.6)$$

where a, b and c indices refer to the charges of the particles. $\Delta\phi_a = \phi_a - \Psi_{RP}$ is the azimuthal angle (ϕ_a) of particle a with respect to the reaction plane angle (Ψ_{RP}). The $v_{2,c}$ denotes the elliptic flow of third particle c. The first term in Eq. 5.6 corresponds to in-plane correlation whereas the second term corresponds to out-of-plane correlation which is sensitive to the charge-dependent correlations. The subtraction of these two terms suppresses the correlations which are not related to the orientation of reaction plane known as non-flow effects and helps to constrain the signal contribution.

Figure 5.18 shows the decomposition of $\gamma_{a,b}$ into the in-plane and out-of-plane correlation terms for OS (left) and SS charge pairs (right). For OS charge pairs, both the in-plane and out-of-plane components have same values except for the peripheral collisions, implying there is no preferred emission. This could be due to the resonance decays or other possible background correlations. In case of SS charged pairs, the out-of-plane component exhibits larger values than those in-plane correlations. This is exactly what has been predicted for charge separation effect due to the CME. The ChrgR exhibits positive correlation for both opposite and same sign pairs, whereas the randomized azimuthal angle events are compatible with zero for both in-plane and out-of-plane correlations and are independent of charges of the particles.

5.6.5.1 $Db_{\pm}^{max}$ bin dependence of In-plane and Out-of-plane Correlations

The overall values for correlation functions exhibit positive values for both OS and SS charge pairs. For further investigation, the correlation functions are studied in different $Db_{\pm}^{max}$ bins for OS and SS charge pairs.

- **Opposite Sign:** The in-plane and out-of-plane correlations in terms of $Db_{\pm}^{max}$ bins for OS charge pairs are displayed in figure 5.19 (left). Data exhibit positive values for the in-plane correlation term in all $Db_{\pm}^{max}$ bins whereas the out-of-plane term has negative values for top 20% $Db_{\pm}^{max}$ bins and is positive in rest of the bins. The ChrgR and Random have negative correlation in higher $Db_{\pm}^{max}$ bins for OS pairs whereas the lower $Db_{\pm}^{max}$ bins have positive values in each centrality.

- **Same Sign:** For the SS charge pairs, the data exhibit positive values in higher $Db_{\pm}^{max}$ bins for both correlation terms. The more positive values are observed for out-of-plane correlations than those of in-plane term as expected for the CME. The ChrgR and Random have the similar patterns as data and the values for Random azimuthal angles matches with the data in higher $Db_{\pm}^{max}$

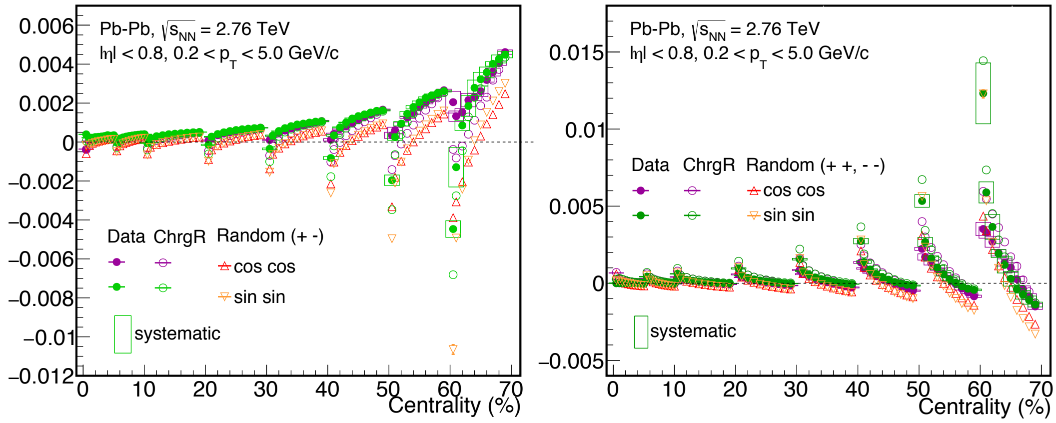

Figure 5.19: Centrality dependence of in-plane and out-of-plane correlations for the opposite sign (left) and same sign (right) charge pairs for different $Db_{\pm}^{max}$ bins.

bins within statistical uncertainties.

5.6.6 Three Particle Correlations

The three particle azimuthal correlations are obtained for same sign (++, - -) and opposite sign (+ -) charge pairs as a function of collision centrality in Pb-Pb collision events at $\sqrt{s}_{\rm NN} = 2.76$ TeV. The three particle correlator can be obtained using,

$$\gamma_{a,b} = \langle cos(\phi_a + \phi_b - 2\Psi_{RP})\rangle = \frac{\langle cos(\phi_a + \phi_b - 2\phi_c)\rangle}{v_{2,c}} \tag{5.7}$$

where the symbols have their usual meanings. Since the determination of reaction plane is not possible experimentally, one has to determine the event plane angle or can use the expression written on right side of the Eq. 5.7 which is basically the three particle correlator divided by the elliptic flow ($v_{2,c}$) of third particle c. We have measured the three particle correlator and elliptic flow using the Q-cumulant method as explained in chapter 4.

The CME predicts that the OS charged particles move away from each other along y-axis and pairs of SS charge pairs move preferentially along the negative

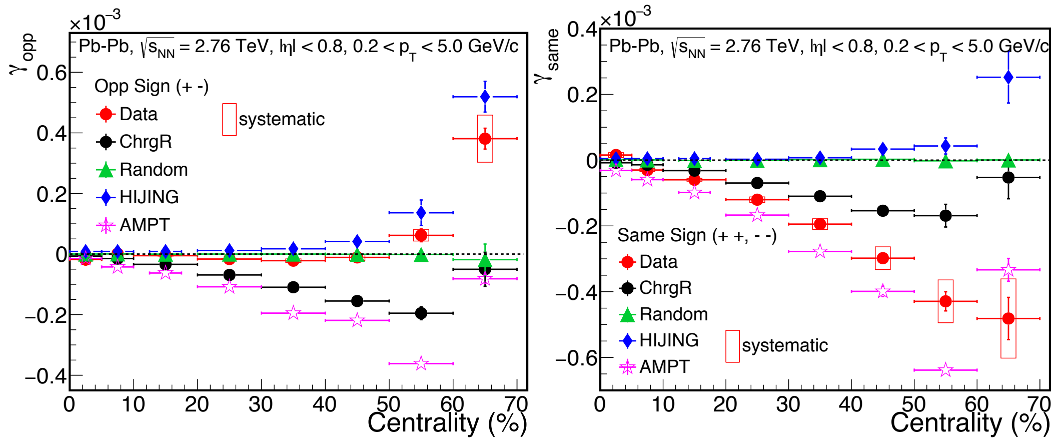

Figure 5.20: Centrality dependence of three particle correlator for pairs of particles of opposite charge (left) and same charge (right). The ChrgR and Random points are also displayed for comparison.

or positive y-axis. Figure 5.20 shows the three particle correlator as a function of collision centrality. The correlation between OS charge pairs is positive (left) in all centralities whereas the SS charge pairs have negative values (right) as expected for the CME, represented by red markers. It is predicted that the pairs of opposite charges move away from each other and exhibit weak correlation as they traverse the entire fireball. The centrality dependence of three particle correlator is also measured for ChrgR and Random. The correlations exhibit similar values for OS and SS charge pairs and do not differentiate between different charge combinations. The ChrgR has negative values in all centralities for both types of charge pairs while the random events are compatible with zero showing no significant correlations of any type. Results from HIJING and AMPT event generators are also displayed in figure 5.20 (left) for OS and (right) SS charge pairs. The HIJING shows positive values for OS and SS charge pairs, whereas AMPT exhibits negative values for both. Thus it is clear that neither HIJING nor AMPT follows the patterns as predicted for CME.

The difference between opposite sign and same sign charge pairs ($\Delta\gamma$) is also studied for three particle correlator. Figure 5.21 shows the centrality dependence

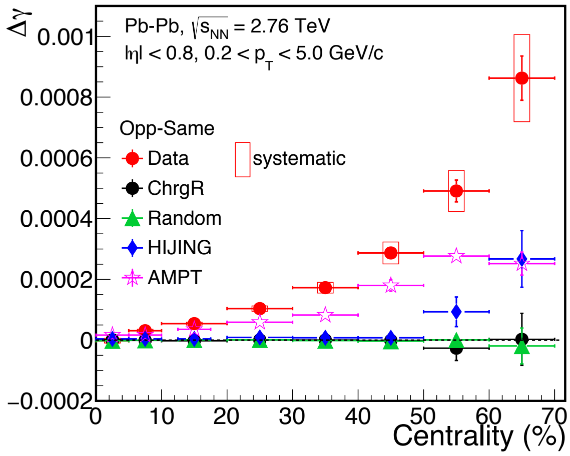

Figure 5.21: Centrality dependence of $\Delta\gamma(= \gamma_{opp} - \gamma_{same})$ for data, ChrgR and Random events. The HIJING and AMPT results are also displayed.

of $\Delta\gamma$ exhibiting positive values in all centrality classes whereas the ChrgR and Random are compatible with zero. The correlation values for HIJING and AMPT are also displayed in figure 5.21 indicating the enhanced signal strength in data compared to Monte Carlo event generators.

5.6.6.1 $Db_{\pm}^{max}$ bin dependence of Three Particle Correlations

For further understanding the behaviour of charge-dependent correlations, the three particle azimuthal correlations relative to reaction plane are obtained in each $Db_{\pm}^{max}$ bin as a function of collision centrality for all charge combinations.

- **Opposite Sign:** Figure 5.22 (left) shows the centrality dependence of three particle correlator for OS charge pairs (γ_{opp}) in all $Db_{\pm}^{max}$ bins. The first point in each centrality class corresponds to top 10% $Db_{\pm}^{max}$ bin and the last one is for 90-100% $Db_{\pm}^{max}$. The three particle correlator measured for data, ChrgR, and Random are shown with different coloured markers in figure 5.22 (left). The data points are slightly more positive than ChrgR and Random in higher $Db_{\pm}^{max}$ bins whereas the correlation values are negligible for lower $Db_{\pm}^{max}$ bins.

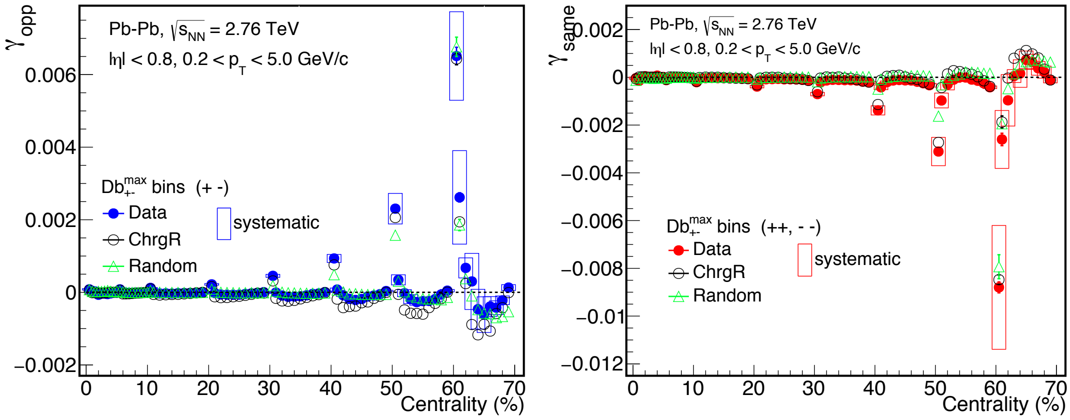

Figure 5.22: Centrality dependence of three particle correlator for opposite sign (left) and same sign (right) charge pairs for different $Db_{\pm}^{max}$ bins for data, ChrgR, and Random.

- **Same Sign:** Similarly, the three particle correlator is obtained for the pairs of particles of same charge (γ_{same}) as a function of centrality in each $Db_{\pm}^{max}$ bin. In figure 5.22 (right), the higher $Db_{\pm}^{max}$ bins in each centrality exhibit negative values showing strong correlation, whereas the correlation decreases for lower $Db_{\pm}^{max}$ bins. The ChrgR and Random have same sign and slightly small values for γ_{same}. The number of $Db_{\pm}^{max}$ bins exhibiting large negative values are different in different centralities.

- **Opposite-Same sign:** In figure 5.23, the higher $Db_{\pm}^{max}$ bins exhibit positive values for $\Delta\gamma(= \gamma_{opp} - \gamma_{same})$ in each centrality. The ChrgR and Random data points are also displayed as a function of $Db_{\pm}^{max}$ bins and observed the similar dependence but the correlation values are slightly smaller in magnitude than those of data. The strong correlation is seen for higher $Db_{\pm}^{max}$ bins indicating the presence of CME-type enriched events corresponding to these $Db_{\pm}^{max}$ bins.

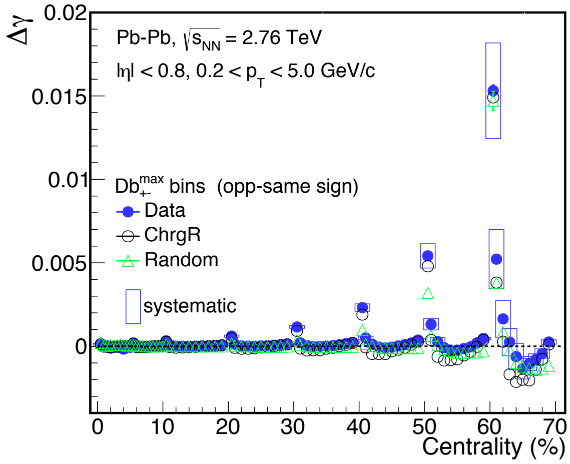

Figure 5.23: Centrality dependence of three particle correlator for opposite and same sign charge pairs for different $Db^{max}_{\pm}$ bins for data, ChrgR, and Random.

5.6.6.2 Three Particle Correlations w.r.t top 30% $Db^{max}_{\pm}$

In figure 5.23, the top 30% $Db^{max}_{\pm}$ bins exhibit strong correlations so the three particle correlator is further studied for 0-30% and 30-100% $Db^{max}_{\pm}$ bins for each collision centrality.

- **Opposite Sign:** Figure 5.24 (left) displays the three particle azimuthal correlation for OS charge pairs as a function of collision centrality. For top 30% $Db^{max}_{\pm}$, the data points exhibit positive and relatively larger correlation values than those of 30-100% $Db^{max}_{\pm}$. The overall values are also displayed in figure 5.24 (left). The correlation values are smaller in each $Db^{max}_{\pm}$ bin for ChrgR and Random events as compared to data. The ChrgR and Random data points agree well with each other within the statistical uncertainties.

- **Same Sign:** The centrality dependence of three particle correlator for the particles of SS charge pairs are presented in figure 5.24 (right) for $Db^{max}_{\pm}$ bins of 0-30% and 30-100%. The correlation exhibit negative values in each centrality for top 30% $Db^{max}_{\pm}$ whereas the rest of the events have nearly zero

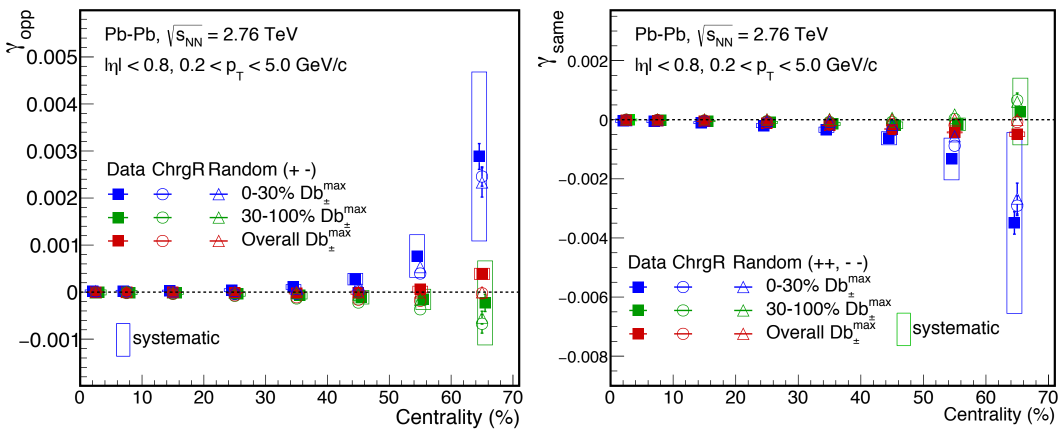

Figure 5.24: Comparison of three particle correlator for opposite sign (left) and same sign (right) charge pairs for top 30% $Db_{\pm}^{max}$ bins and the rest of the sample events. The average values are also displayed.

values and agree with the overall values except for 60-70% centrality. The ChrgR and Random have similar correlation values in each centrality but the magnitude is smaller than those of data.

- **Opposite-Same sign:** Figure 5.25 shows the centrality dependence of $\Delta\gamma$ ($=\gamma_{opp} - \gamma_{same}$) in different $Db_{\pm}^{max}$ bins. The top 30% $Db_{\pm}^{max}$ exhibits positive correlation whereas it is negative for 30-100% $Db_{\pm}^{max}$. The ChrgR points agree with those of the Random data points within the statistical uncertainties and exhibit similar trend as of data. The larger correlation values in each centrality for higher $Db_{\pm}^{max}$ bins indicate that the CME signal is confined to higher $Db_{\pm}^{max}$ bins only.

5.6.6.3 Systematic uncertainty in $\langle cos(\phi_a+\phi_b-2\Psi_{RP})\rangle$ for Same Charge

The systematic uncertainties in three particle correlator (same charge) obtained by varying event and track cuts are added in quadrature to obtain the final systematic uncertainty. The $\langle cos(\phi_a + \phi_b - 2\Psi_{RP})\rangle$ systematic errors from centrality estimators, vertex cuts, magnetic field polarities, and same sign pairs are displayed in

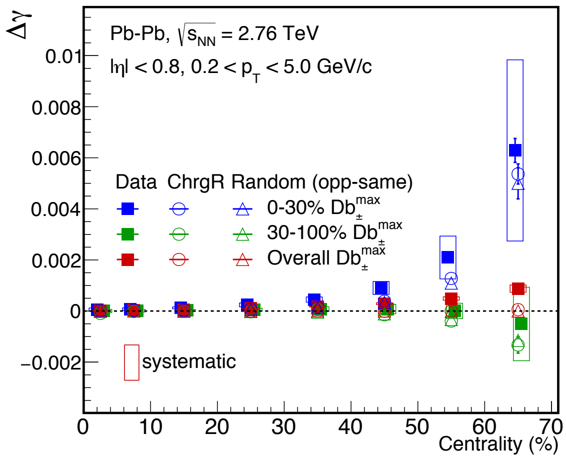

Figure 5.25: Comparison of three particle correlator for opposite and same sign charge pairs for top 30% $Db_{\pm}^{max}$ bins and the rest of the sample events. The average values are also displayed.

figures 5.26, 5.27, 5.28 and 5.29, respectively. Also the same charge systematics from number of TPC clusters and DCA_{xy} cuts are shown in figures 5.30 and 5.31, respectively.

Each figure contains eleven plots correspond to different $Db_{\pm}^{max}$ bins for one particular systematic source. It is observed that the variation in three particle correlator by varying different cuts is more in peripheral events and decreases as one moves toward increasing centrality. The obtained fraction for uncertainty values from different event and track cuts for SS charge pairs in each centrality interval are listed in table 5.4. The systematic uncertainty from the elliptic flow is ∼18% of the measured correlation value in the peripheral collisions.

Similarly, the systematic errors obtained for OS charge pairs and the difference of opposite sign and same sign charge pairs are given in Appendix B. The fractional systematic uncertainty values for OS and OS-SS charge pairs for different centrality classes are given in Appendix B.

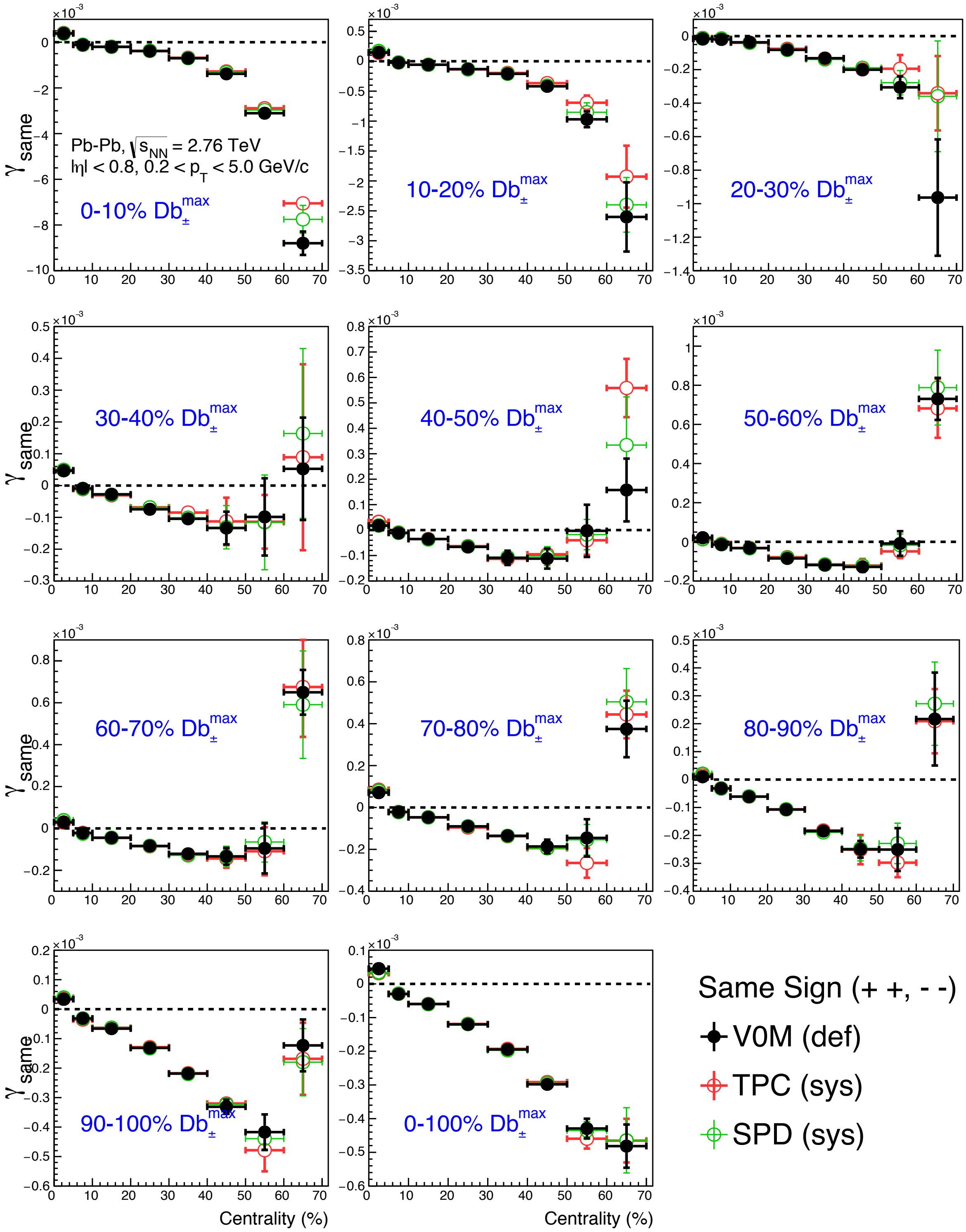

Figure 5.26: Centrality dependence of $\langle cos(\phi_a + \phi_b - \Psi_{RP})\rangle$ for same charge pairs for different centrality definitions for different $Db_{\pm}^{max}$ bins as indicated.

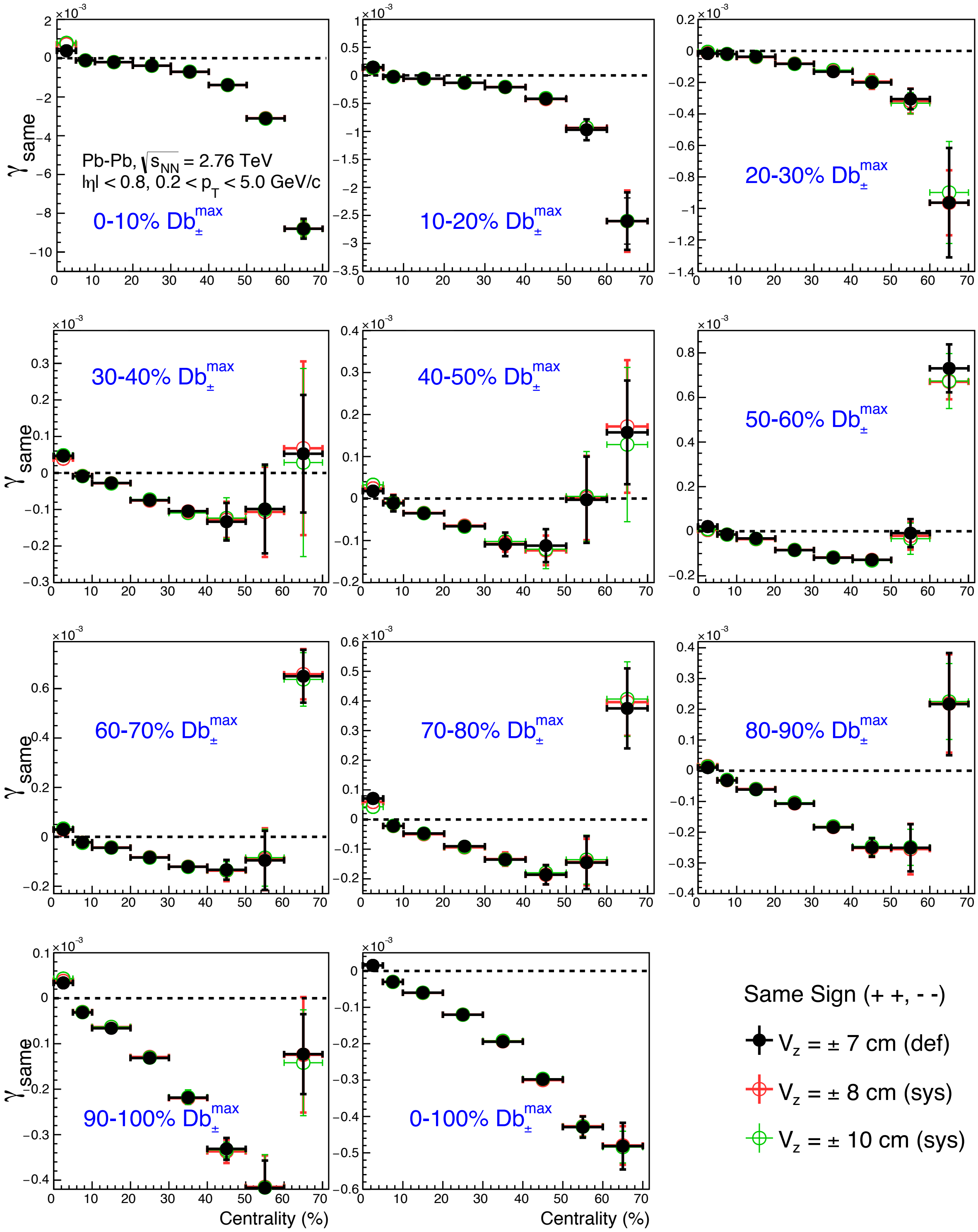

Figure 5.27: Centrality dependence of $\langle cos(\phi_a + \phi_b - \Psi_{RP}) \rangle$ for same charge pairs for different vertex cuts for different $Db_{\pm}^{max}$ bins as indicated.

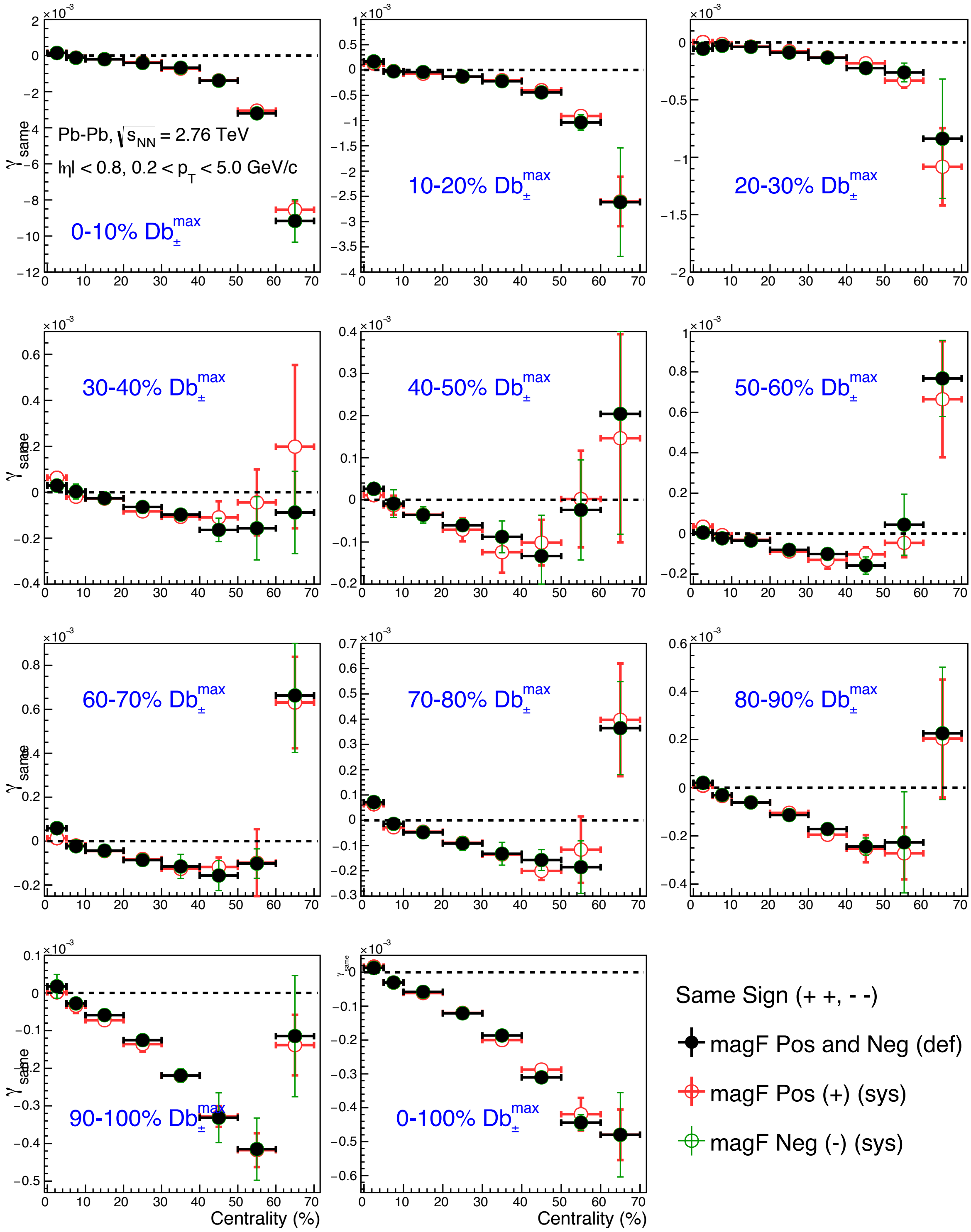

Figure 5.28: Centrality dependence of $\langle cos(\phi_a + \phi_b - \Psi_{RP}) \rangle$ for same charge pairs for different magnetic field polarity for different $Db_{\pm}^{max}$ bins as indicated.

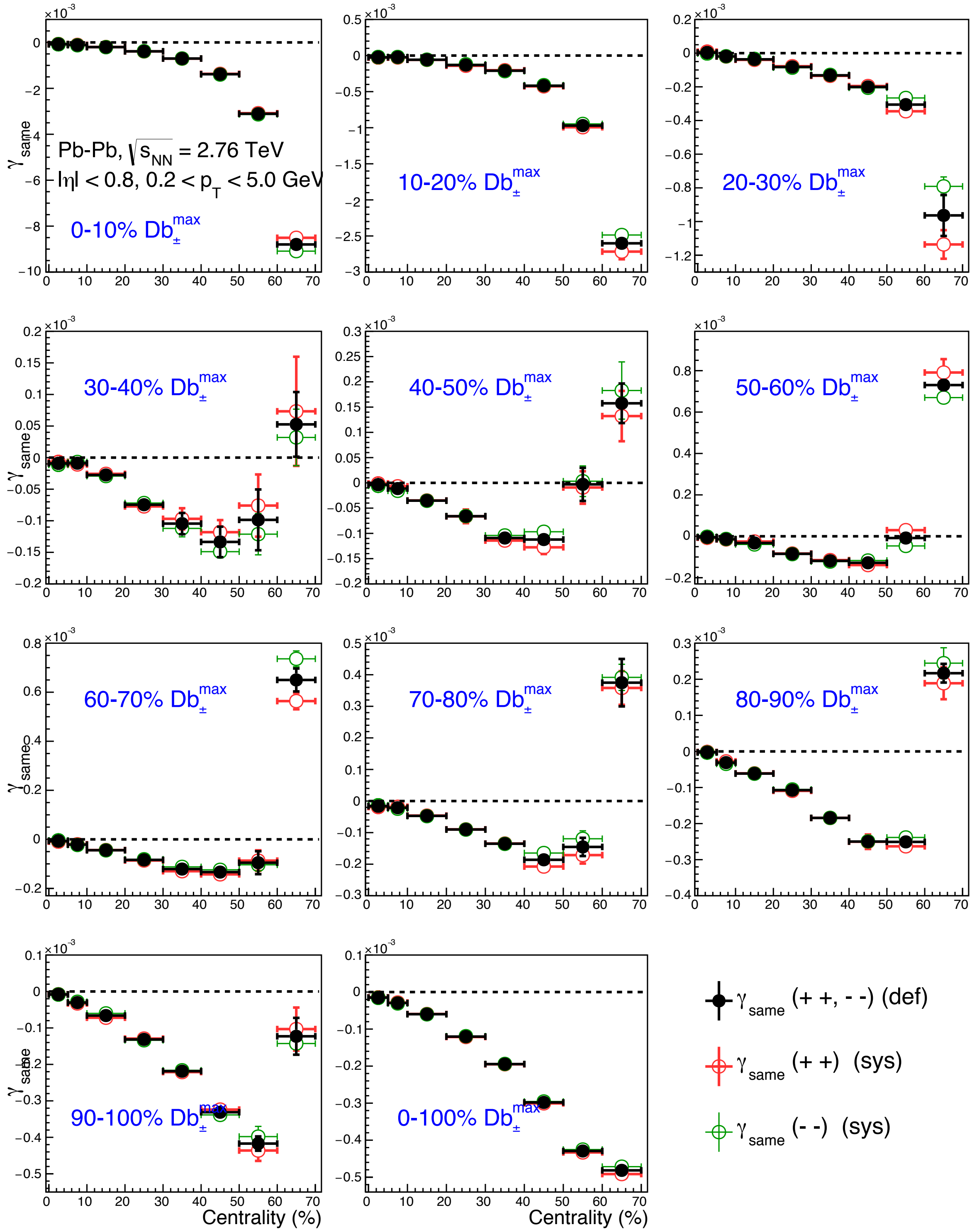

Figure 5.29: Centrality dependence of $\langle cos(\phi_a + \phi_b - \Psi_{RP})\rangle$ for same charge pairs for different charge combinations (++, - -) for different $Db^{max}_{\pm}$ bins as indicated.

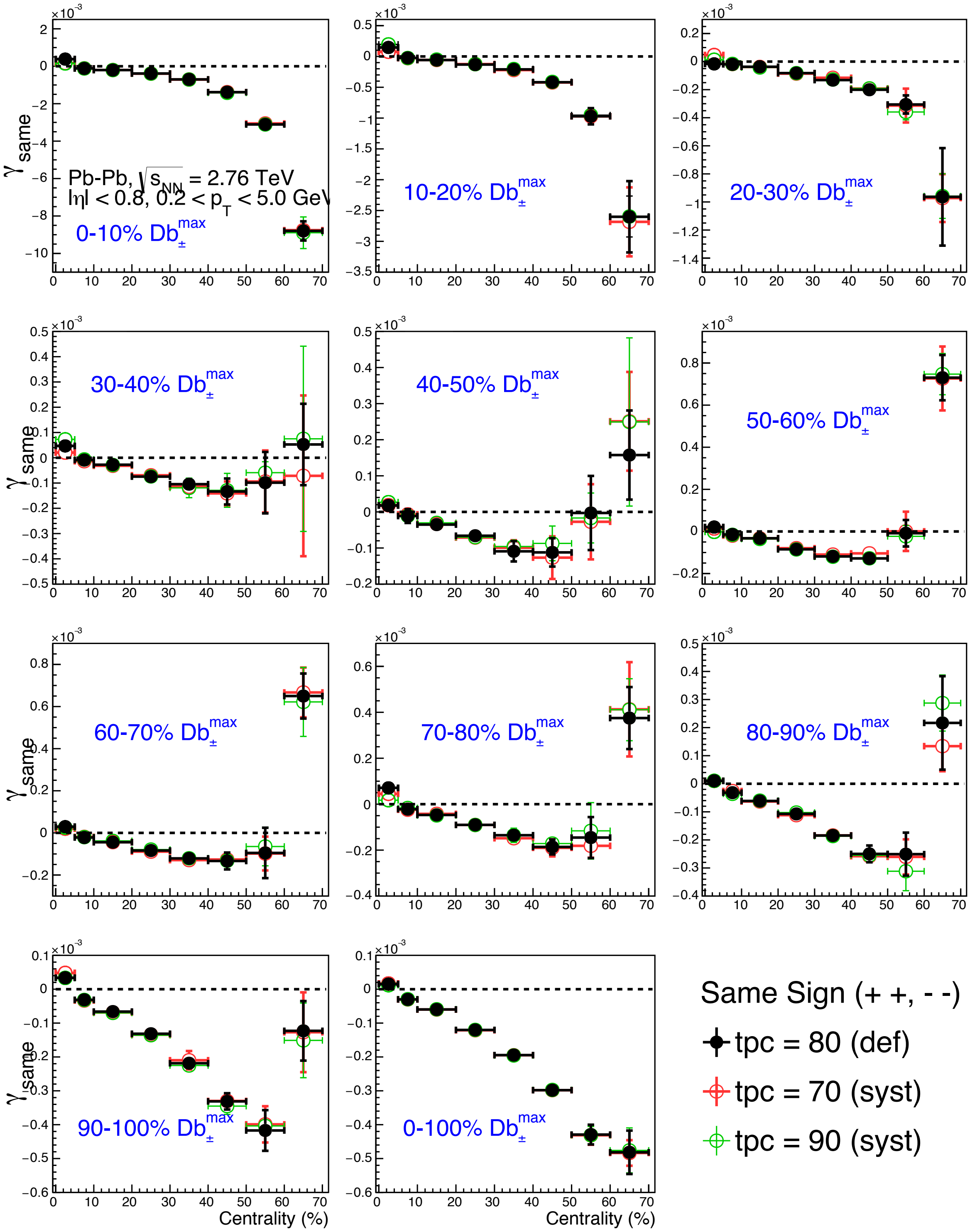

Figure 5.30: Centrality dependence of $\langle cos(\phi_a + \phi_b - \Psi_{RP}) \rangle$ for same charge pairs for different cuts on number of TPC clusters for different $Db_{\pm}^{max}$ bins as indicated.

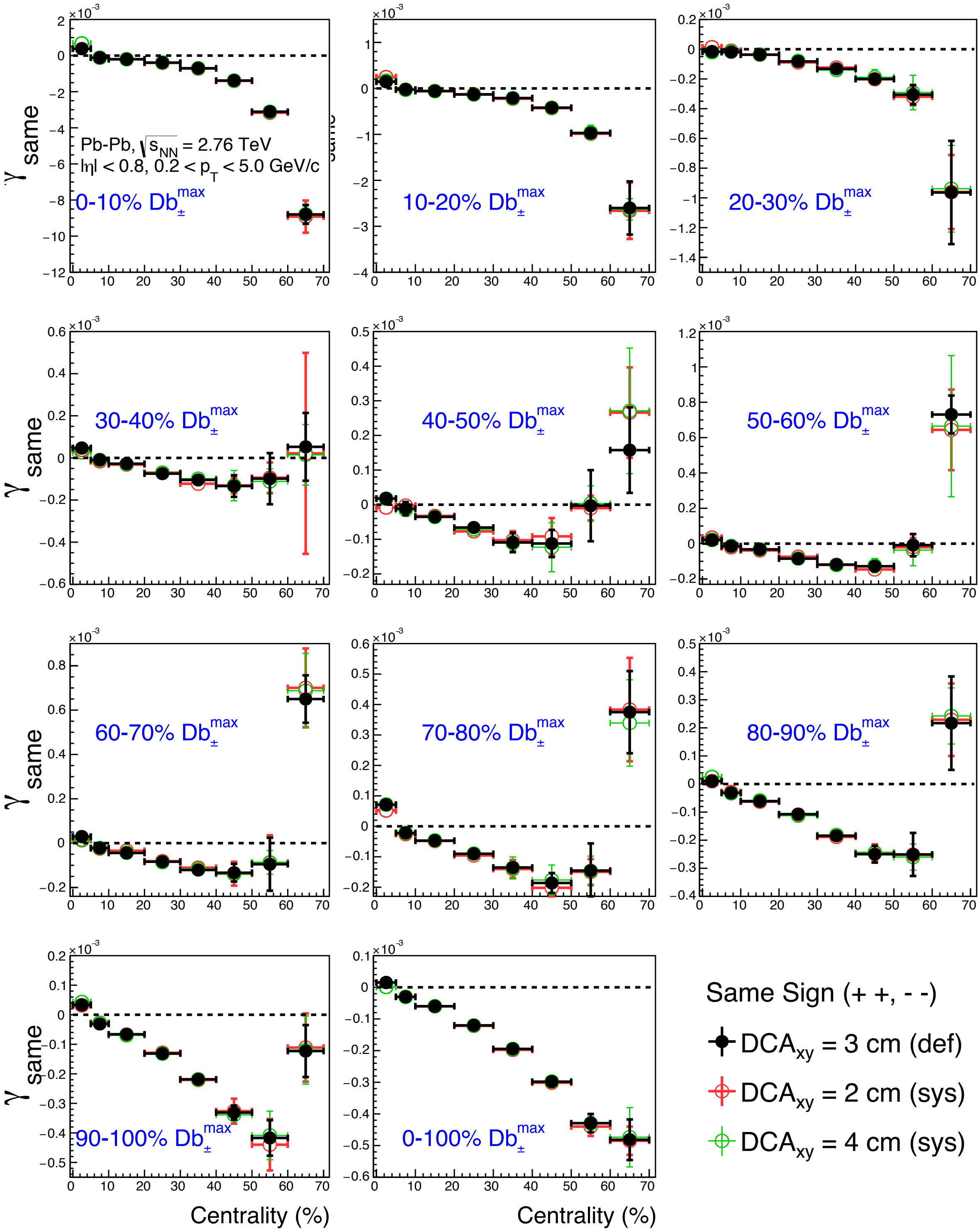

Figure 5.31: Centrality dependence of $\langle cos(\phi_a + \phi_b - \Psi_{RP})\rangle$ for same charge pairs for different DCA_{xy} cuts for different $Db_{\pm}^{max}$ bins as indicated.

Cent → Sources ↓	0-5%	5-10%	10-20%	20-30%	30-40%	40-50%	50-60%	60-70%
Vertex ($\mid V_z \mid$)	0.049	0.023	0.0074	0.0033	0.0105	0.0054	0.0083	0.0074
Mag Field	0.052	0.0076	0.0082	0.0068	0.034	0.042	0.024	0.0052
Cent. Est.	0.0867	0.0166	0.011	0.017	0.014	0.0204	0.015	0.0061
DCA_{xy}	0.080	0.010	0.0080	0.0077	0.0098	0.019	0.012	0.0162
Nclust.	0.068	0.0094	0.011	0.0098	0.0045	0.0025	0.0034	0.0090
Charge Comb.	0.0135	0.028	0.004	0.011	0.0006	0.022	0.015	0.079
v_2	0.34	0.12	0.068	0.062	0.071	0.094	0.131	0.186

Table 5.4: Fractional systematic uncertainty values for $\langle cos(\phi_a + \phi_b - \Psi_{RP})\rangle$ for same sign charge pairs.

5.6.7 Fraction Estimation

It is predicted that the charged particle azimuthal correlations are sensitive to the CME signal but it contains large background correlations which can also produce similar type of charge separation effect. In figure 5.23, it is observed that the top $Db_{\pm}^{max}$ bins in each centrality interval have larger $\Delta\gamma$ values than the rest of the events, indicating the presence of events with large charge separation. Number of $Db_{\pm}^{max}$ bins showing larger correlation are different in different centralities. The charge separation fraction (f_{CME}) is estimated by selecting the top $Db_{\pm}^{max}$ bins in each centrality interval and is defined as,

$$f_{CME} = \frac{(\Delta\gamma_{data} - \Delta\gamma_{bkg})}{\Delta\gamma_{data}} \tag{5.8}$$

where $\Delta\gamma_{data}$ and $\Delta\gamma_{bkg}$ are the difference of opposite sign and same sign charge pair γ correlator for data and background, respectively. The correlations from ChrgR and Random are considered as background in calculating the charge separation fraction. For different centralities, different number of $Db_{\pm}^{max}$ bins contribute to the estimation of fraction (f_{CME}). For 0-30% collision centrality, only top 10% $Db_{\pm}^{max}$ bin, for 30-50% collision centrality top 20% $Db_{\pm}^{max}$ bins and for 50-70% centrality the top 30% $Db_{\pm}^{max}$ bins are used for calculating f_{CME}. Figure 5.32 displays the estimated f_{CME} fraction as a function of centrality. The f_{CME} is more

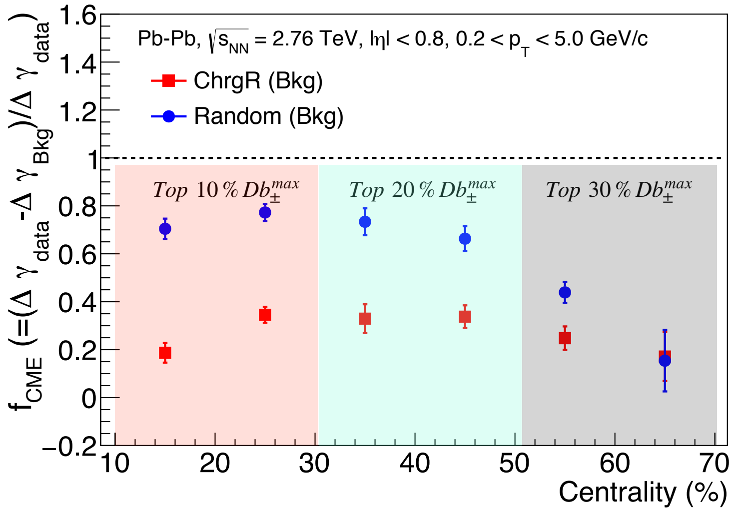

Figure 5.32: Centrality dependence of f_{CME} obtained for the different $Db_{\pm}^{max}$ bins in different centralities. Different colour represent the fraction of events contributing to the CME signal.

if Random is taken as background for 20-50% collision centralities. In Random, particle correlations are completely destroyed which is not true for charge reshuffle. One needs to check Random introducing flow in each event to see if flow give rise to charge separation effect. Further, it is noticed that the CME signal is enhanced many times in top $Db_{\pm}^{max}$ bins, whereas in lower $Db_{\pm}^{max}$ bins, if signal is there it remains within the statistical fluctuations. It is observed that it is possible to get CME enriched sample corresponding to top 10%, 20%, and 30% $Db_{\pm}^{max}$ for 20-30%, 30-50%, and 50-70% collision centralities, respectively. The CME fraction (f_{CME}) is ∼35% in top 10%, 20%, and 30% $Db_{\pm}^{max}$ values in these centralities which corresponds to CME signal ∼ 5-10% in these collision centralities.

5.7 Summary

The study of event-by-event fluctuations plays an important role in observing the presence of any kinds of non-statistical fluctuations which would have been diluted by averaging over the events in an ensemble. In exploring the origin of such dynamical fluctuations one can get important information about the properties of hot-dense matter created in heavy-ion collisions. A detailed study of event-by-event charge separation effect is performed on the TPC reconstructed charged tracks in the pseudorapidity interval $|\eta| < 0.8$ in Pb-Pb collisions at $\sqrt{s_{\rm NN}} = 2.76$ TeV. For the analysis, the observable $Db_{\pm}$ is measured in each event using the Sliding Dumbbell Method (SDM) and the $Db_{\pm}^{max}$ distributions of obtained maxima are studied as a function of collision centrality. A shift towards higher $Db_{\pm}^{max}$ values is observed indicating the presence of events with large charge separation. Further, the $Db_{\pm}^{max}$ distributions are sliced into 10 $Db_{\pm}^{max}$ bins where the 0-10% $Db_{\pm}^{max}$ bin corresponds to top $Db_{\pm}^{max}$ values and the 90-100% $Db_{\pm}^{max}$ bin corresponds to lower $Db_{\pm}^{max}$ values. The multi-particle azimuthal correlators are predicted to be sensitive to the CME study.

The particle azimuthal correlations are also estimated in terms of $Db_{\pm}^{max}$ bins. Results on three particle correlator exhibit positive values for OS charge pairs in higher $Db_{\pm}^{max}$ bins, whereas the values are negative in lower $Db_{\pm}^{max}$ bins. For SS charge pairs, the negative values for γ_{same} are observed indicating strong correlation between the particles of same sign. The centrality dependence of $\Delta\gamma$ is also studied in different $Db_{\pm}^{max}$ bins and large correlation values are observed for higher $Db_{\pm}^{max}$ bins. Thus, the SDM isolates the events exhibiting large charge separation from a given sample of events. For the estimation of background, the two techniques of charge reshuffle and randomization of azimuthal angles of particles over the whole azimuthal plane are used.

The simulation studies are also performed for the charge-dependent correlations using HIJING and AMPT event generators. The observed particle azimuthal correlations agree with those of ChrgR and Random which is expected, as no CME signal is present in HIJING and AMPT events. While analyzing the experimental data an excess in correlation values is observed when compared to ChrgR and Random. The CME signal contribution to the three particle correlator is estimated for different number of $Db_{\pm}^{max}$ bins in different centrality intervals. The observed CME signal is confined to only 10 or 20% of the events in each centrality. The three particle correlator $\Delta\gamma$ ($\gamma_{opp} - \gamma_{same}$) is found to be positive and decreases with increasing collision centrality, whereas charge reshuffle and Random show some correlation or nearly zero correlation. Sliding Dumbbell Method is found to give better insight in to the charge separation effect. It is possible to get sample of events contributing significantly to $\Delta\gamma$ i.e., exhibiting CME type behaviour. It is observed that we can have the CME enriched sample corresponding to top 10%, 20%, and 30% $Db_{\pm}^{max}$ values for 20-30%, 30-50%, and 50-70% collision centralities, respectively. The CME fraction (f_{CME}) extracted is ∼35% in the top 10%, 20%, and 30% $Db_{\pm}^{max}$ values in these centralities which corresponds to CME signal ∼ 5-10% in these collision centralities.

Bibliography

[1] K. Fukushima *et al.*, “The Chiral Magnetic Effect”, Phys. Rev. D **78**, 074033 (2006).

[2] D.E. Kharzeev, “Parity violation in hot QCD: Why it can happen, and how to look for it”, Phys. Lett. B **633**, 260 (2006).

[3] D.E. Kharzeev, and A. Zhitnitsky, “Charge separation induced by P-odd bubbles in QCD matter”, Nucl. Phys. A **797**, 67 (2007).

[4] S.A. Voloshin, “Estimate of the CME signal in heavy-ion collisions from measurements relative to the participant and spectator flow planes”, arXiv:1805.05300v1 [nucl-ex] (2018).

[5] D. Kharzeev *et al.*, “Possibility of spontaneous parity violation in hot QCD”, Phys. Rev. Lett. **81**, 512 (1998).

[6] D. Kharzeev, L.D. McLerran, and H.J. Warringa, “The effects of topological charge change in heavy ion collisions: “Event by event P and CP ciolation”, Nucl. Phys. A **803**, 227 (2008).

[7] A. Bzdak, V. Koch, and J. Liao, “Charge-Dependent Correlations in Relativistic Heavy Ion Collisions and the Chiral Magnetic Effect”, arXiv:1207.7327v1 [nucl-th] (2012).

[8] S.A. Voloshin, “Parity violation in hot QCD: How to detect it,”, Phys. Rev. C **70**, 057901 (2004).

[9] D.E. Kharzeev, “Chiral Magnetic and Vortical Effects in High-Energy Nuclear Collisions - A Status Report”, arXiv:1511.04050v2 [hep-ph] (2016).

[10] STAR collaboration, L. Adamczyk *et al.*, “Fluctuations of charge separation perpendicular to the event plane and local parity violation in $\sqrt{s_{NN}} = 200$ GeV Au+Au collisions at the BNL Relativistic Heavy Ion Collider”, Phys. Rev. C **88**, 064911 (2013).

[11] STAR collaboration, B.I. Abelev *et al.*, “Observation of charge-dependent correlations and possible local strong parity violation in heavy-ion collisions”, Phys. Rev. C **81**, 054908 (2010)

[12] ALICE Collaboration, B. Abelev *et al.*, “Charge separation relative to the reaction plane in Pb-Pb collisions at $\sqrt{s_{\rm NN}} = 2.76$ TeV”, Phys. Rev. Lett. **110**, 012301 (2013).

[13] STAR Collaboration, L. Adamczyk *et al.*, “Beam-Energy Dependence of Charge Separation along the Magnetic Field in Au + Au Collisions at RHIC”, Phys. Rev. Lett. **113**, 052302 (2014).

[14] CMS Collaboration, V. Khachatryan *et al.*, “Observation of charge dependent azimuthal correlations in pPb collisions and its implication for the search for the chiral magnetic effect”, Phys. Rev. Lett. **118**, 122301 (2017).

[15] ALICE Collaboration, S. Acharya *et al.*, “Constraining the magnitude of the Chiral Magnetic Effect with Event Shape Engineering in Pb-Pb collisions at $\sqrt{s_{\rm NN}} = 2.76$ TeV”, Phys. Lett. B **777**, 151 (2018).

[16] A. Bilandzic, R. Snellings, and S. Voloshin, “Flow analysis with cumulants: direct calculations”, Phys. Rev. C **83**, 044913 (2011).

[17] Monalisa Repository for ALICE, https://alimonitor.cern.ch/configuration/.

[18] ALICE Collaboration, A. Dobrin, “Charge-dependent azimuthal correlations and v_n with event shape engineering technique”, ALICE-ANA-2016 (2016).

[19] R. Barlow talk at “SLUO lectures on statistics and Numerical Methods in HEP”, (2000).

Appendix A

The study of charge separation effect is performed via multi-particle azimuthal correlations in terms of different event categories as a function of centrality. The two particle azimuthal correlations for different charge combinations viz, same sign (+ +, - -) and opposite sign (+ -) are studied in different centrality bins and $Db_{\pm}^{max}$ bins. For the systematic study, the different event cuts and track cuts are varied and the maximum deviation from the standard cut is taken as systematic uncertainty for that particular source. The total systematic error is obtained by adding all of them in quadrature. The different cuts varied for the systematic error estimation are, different centrality definitions, vertex cut, magnetic field polarity, cuts on number of TPC clusters, and different DCA_{xy} cuts. The centrality dependence of two particle correlations for different $Db_{\pm}^{max}$ bins for different systematic sources is shown in figures 5.33, 5.34, 5.35, 5.36, and 5.37.

Cent → / Sources ↓	0-5%	5-10%	10-20%	20-30%	30-40%	40-50%	50-60%	60-70%
Vertex ($\mid V_z \mid$)	0.0020	0.0029	0.00091	0.0012	0.0010	0.00094	0.00094	0.0001
Mag Field	0.0056	0.0125	0.0076	0.0010	0.0049	0.0017	0.0042	0.0044
Cent. Est.	0.0027	0.0043	0.0021	0.0063	0.0095	0.0096	0.017	0.0155
DCA_{xy}	0.00058	0.00071	0.0005	0.0010	0.0007	0.00081	0.00086	0.0017
Nclust.	0.0028	0.0080	0.0047	0.00007	0.0031	0.0027	0.0025	0.0025

Table 5.5: Fraction systematic uncertainty values for two particle correlator for $\langle cos(\phi_a - \phi_b)\rangle$ same sign charge pairs.

The fractional uncertainty values for $\langle cos(\phi_a - \phi_b)\rangle$ for same sign charge pairs are listed in Table 5.6.

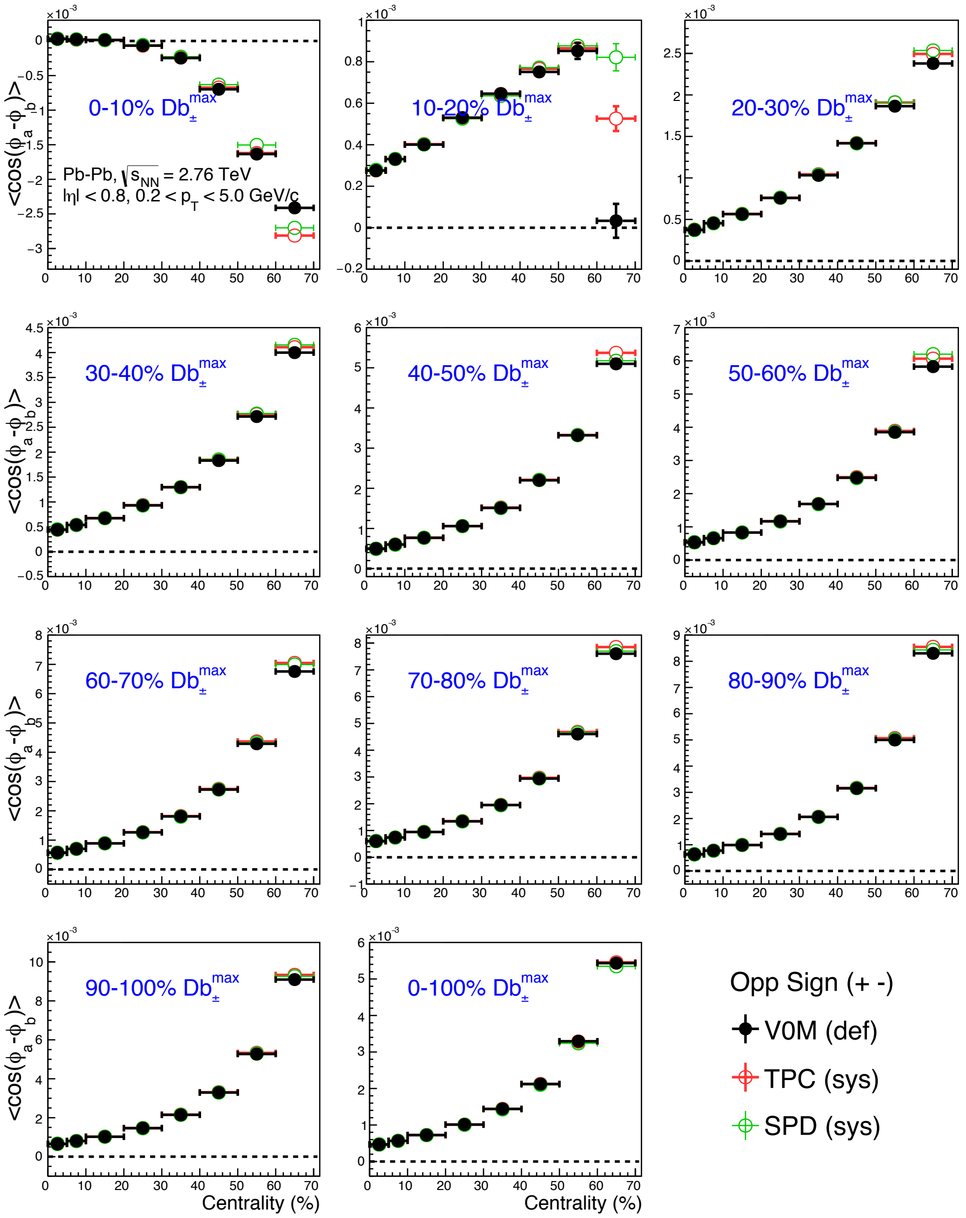

Figure 5.33: Centrality dependence of $\langle cos(\phi_a - \phi_b)\rangle$ for same charge pairs for different centrality definitions for different $Db_{\pm}^{max}$ bins as indicated.

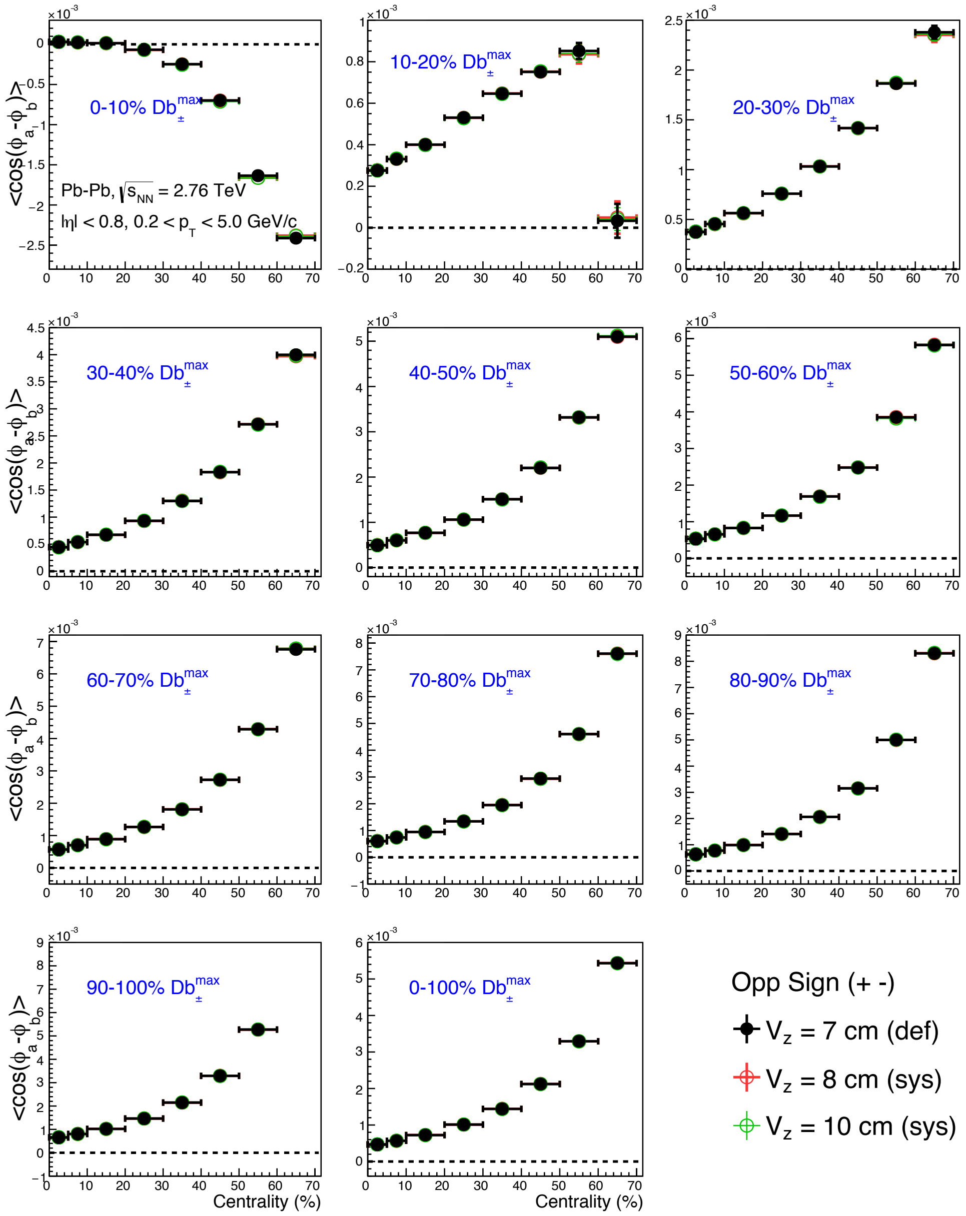

Figure 5.34: Centrality dependence of $\langle cos(\phi_a - \phi_b)\rangle$ for same charge pairs for different vertex cuts for $Db^{max}_{\pm}$ bins as indicated.

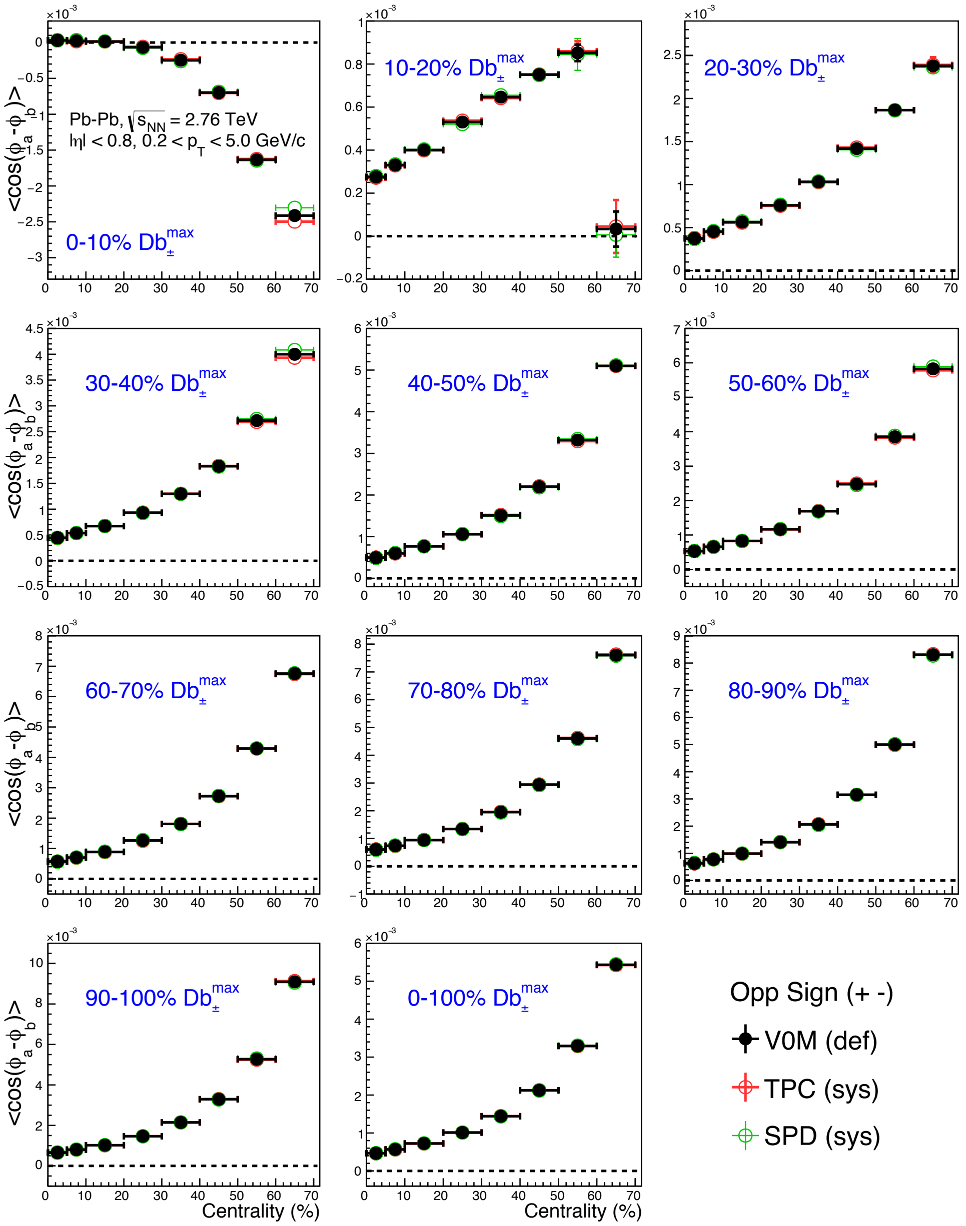

Figure 5.35: Centrality dependence of $\langle cos(\phi_a - \phi_b) \rangle$ for same charge pairs for different magnetic field polarity for different $Db_{\pm}^{max}$ bins as indicated.

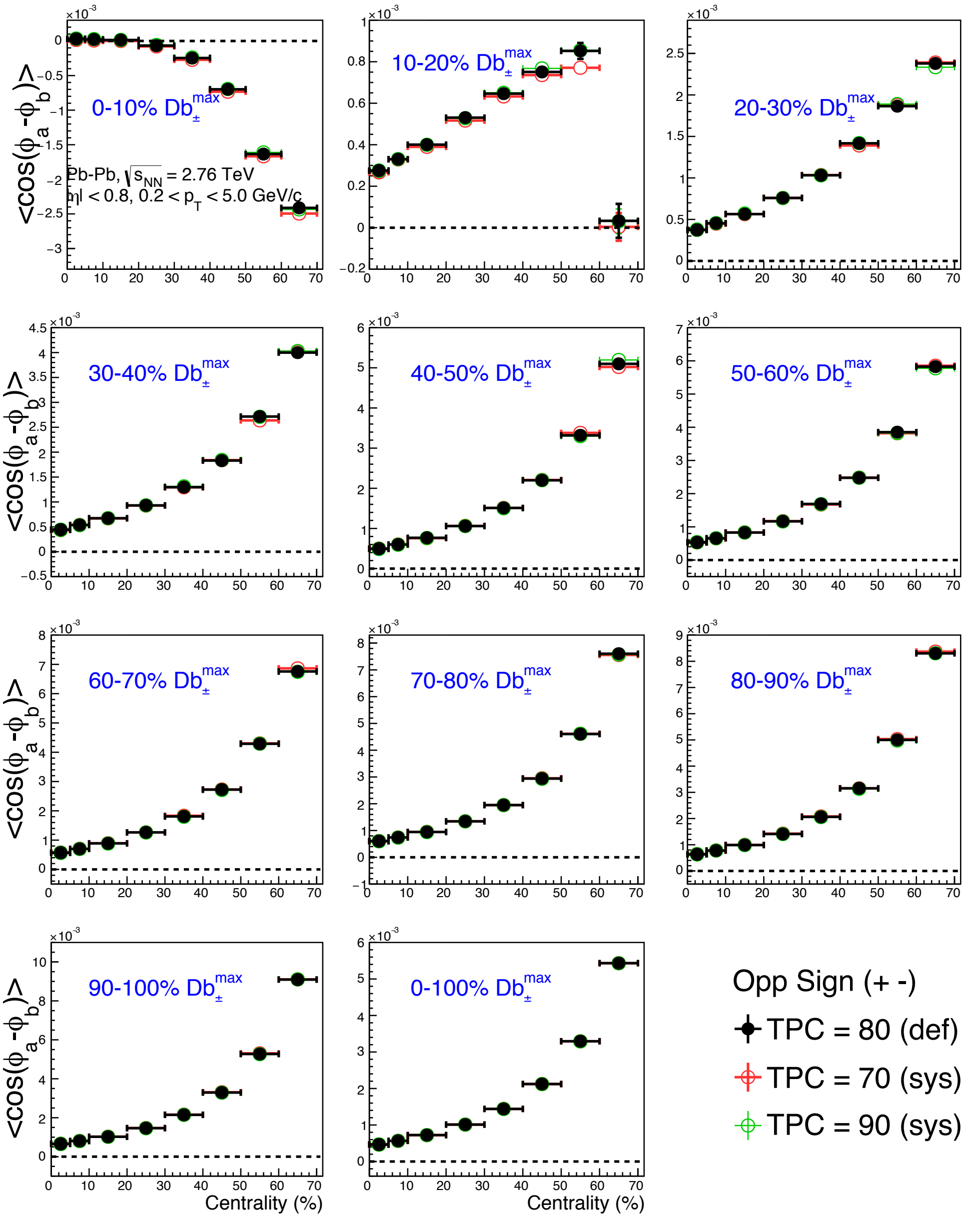

Figure 5.36: Centrality dependence of $\langle cos(\phi_a - \phi_b)\rangle$ for same charge pairs for different cuts on number of TPC clusters for different $Db_{\pm}^{max}$ bins as indicated.

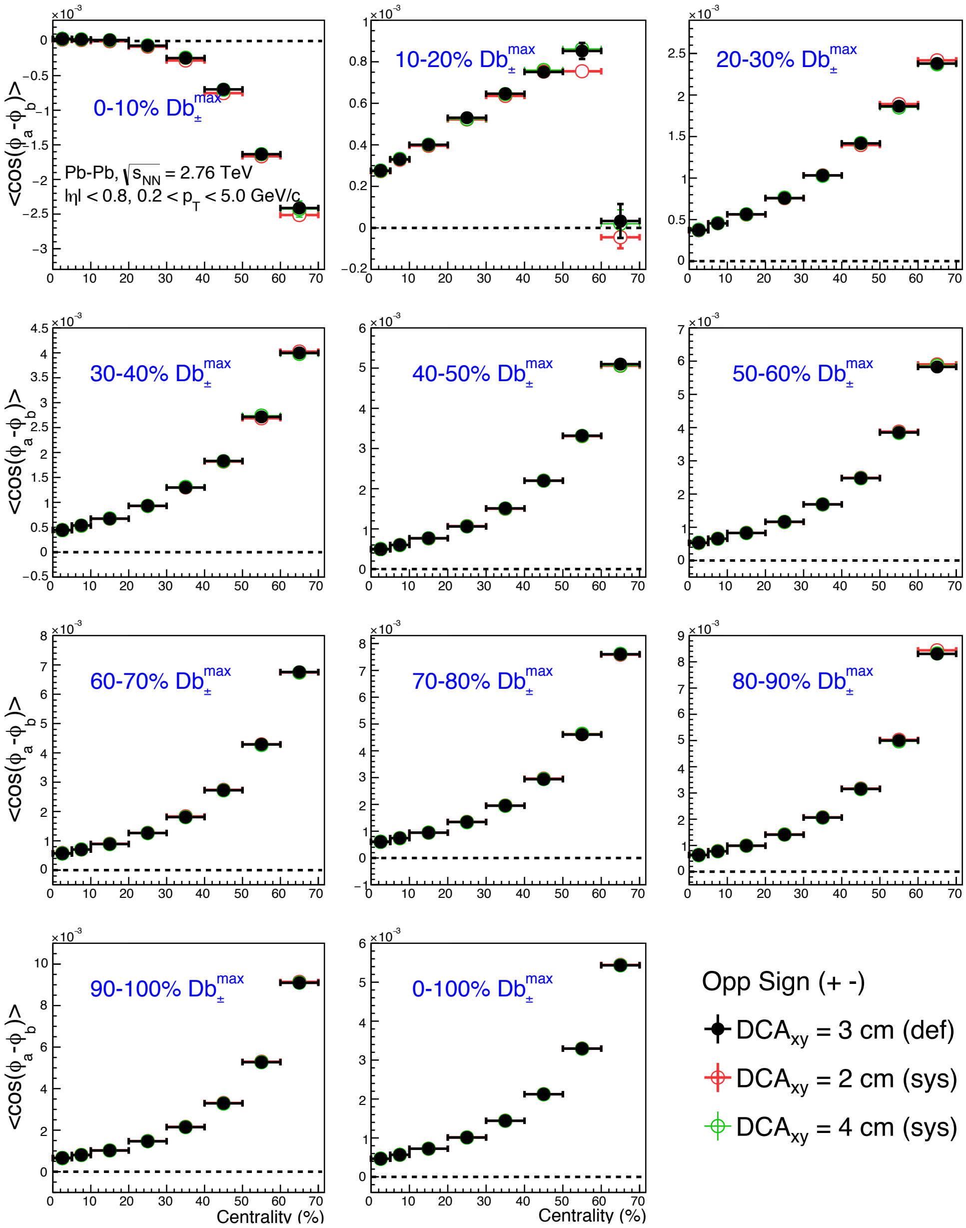

Figure 5.37: Centrality dependence of $\langle cos(\phi_a - \phi_b)\rangle$ for same charge pairs for different DCA_{xy} cuts for different $Db_{\pm}^{max}$ bins as indicated.

Appendix B

The systematic uncertainties estimated for the three particle correlator for opposite sign charge pairs are obtained by varying different event and track cuts, such as different centrality definitions, vertex cut, magnetic field polarity, cuts on number of TPC clusters, and different DCA_{xy} cuts. The centrality dependence of the varied cuts is presented in figures 5.38, 5.39, 5.40, 5.41, and 5.42,respectively. The fractional systematic uncertainty values are summarized in Table 5.6.

For the $\Delta\gamma$ ($=\gamma_{opp} - \gamma_{same}$) charge pairs, the centrality dependence of three particle correlations for different $Db_{\pm}^{max}$ bins for different systematic sources is shown in figures 5.43, 5.44, 5.45, 5.46, and 5.47, respectively. The fractional systematic uncertainty values are listed in Table 5.7.

Cent → Sources ↓	0-5%	5-10%	10-20%	20-30%	30-40%	40-50%	50-60%	60-70%
Vertex ($\mid V_z \mid$)	0.060	0.015	0.010	0.022	0.051	0.0214	0.094	0.039
Mag Field	0.021	0.029	0.060	0.0014	0.043	0.031	0.015	0.012
Cent. Est.	0.042	0.065	0.031	0.057	0.010	0.058	0.045	0.030
DCA_{xy}	0.047	0.035	0.0083	0.0053	0.0036	0.062	0.058	0.017
Nclust.	0.020	0.094	0.010	0.051	0.081	0.055	0.0084	0.0074
v_2	0.34	0.12	0.068	0.062	0.071	0.094	0.131	0.186

Table 5.6: Fractional systematic uncertainty values for $\langle cos(\phi_a + \phi_b - \Psi_{RP}) \rangle$ for opp sign charge pairs.

Cent → Sources ↓	0-5%	5-10%	10-20%	20-30%	30-40%	40-50%	50-60%	60-70%
Vertex ($\mid V_z \mid$)	0.07	0.027	0.012	0.022	0.052	0.022	0.094	0.039
Mag Field	0.056	0.029	0.06	0.0069	0.054	0.052	0.025	0.013
Cent. Est.	0.09	0.06	0.033	0.059	0.017	0.061	0.047	0.030
DCA_{xy}	0.056	0.03	0.011	0.009	0.010	0.065	0.05	0.023
Nclust.	0.07	0.09	0.015	0.051	0.081	0.055	0.009	0.011
v_2	0.34	0.12	0.068	0.062	0.071	0.094	0.131	0.186

Table 5.7: Fractional systematic uncertainty values for $\langle cos(\phi_a + \phi_b - \Psi_{RP}) \rangle$ for $\Delta\gamma$.

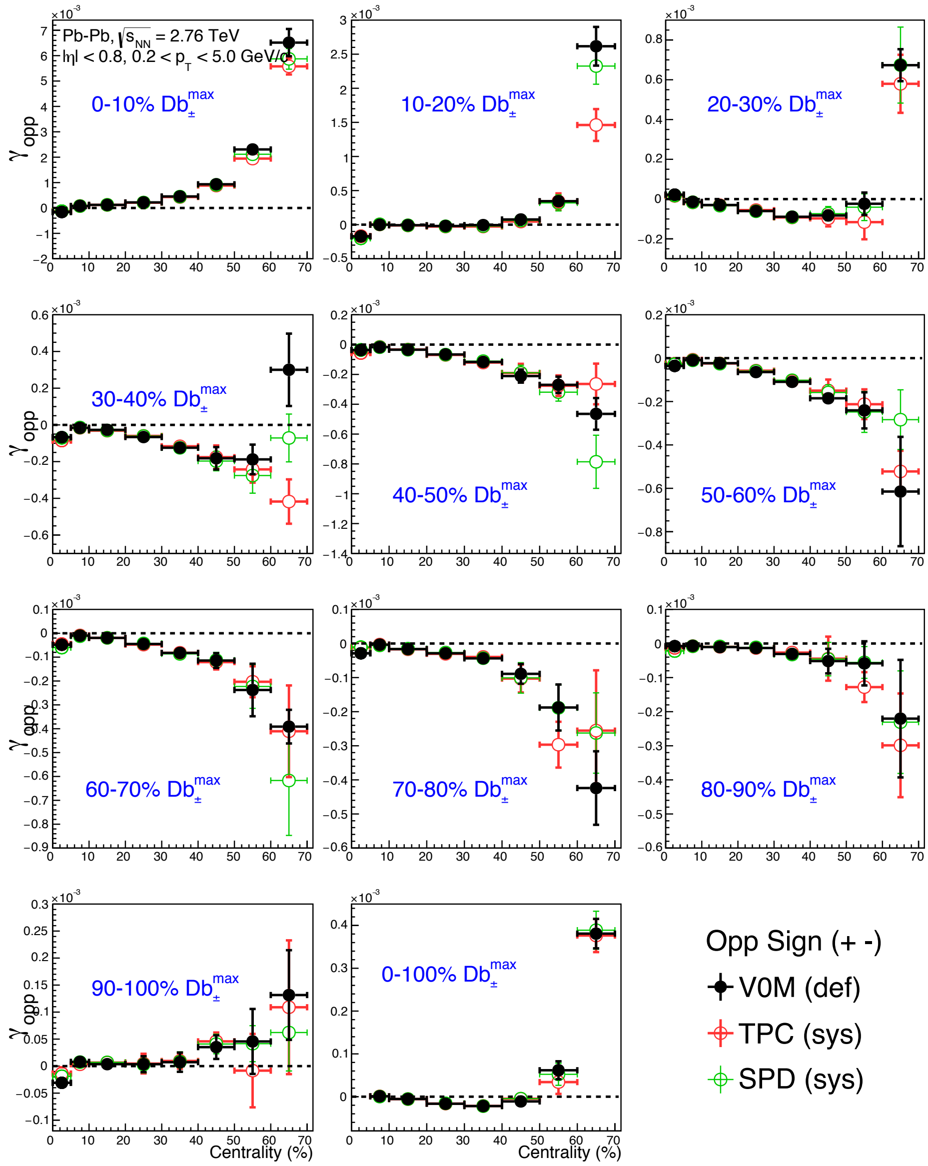

Figure 5.38: Centrality dependence $\langle cos(\phi_a - \phi_b)\rangle$ for opposite sign charge pairs for different centrality definitions for different $Db_{\pm}^{max}$ bins as indicated.

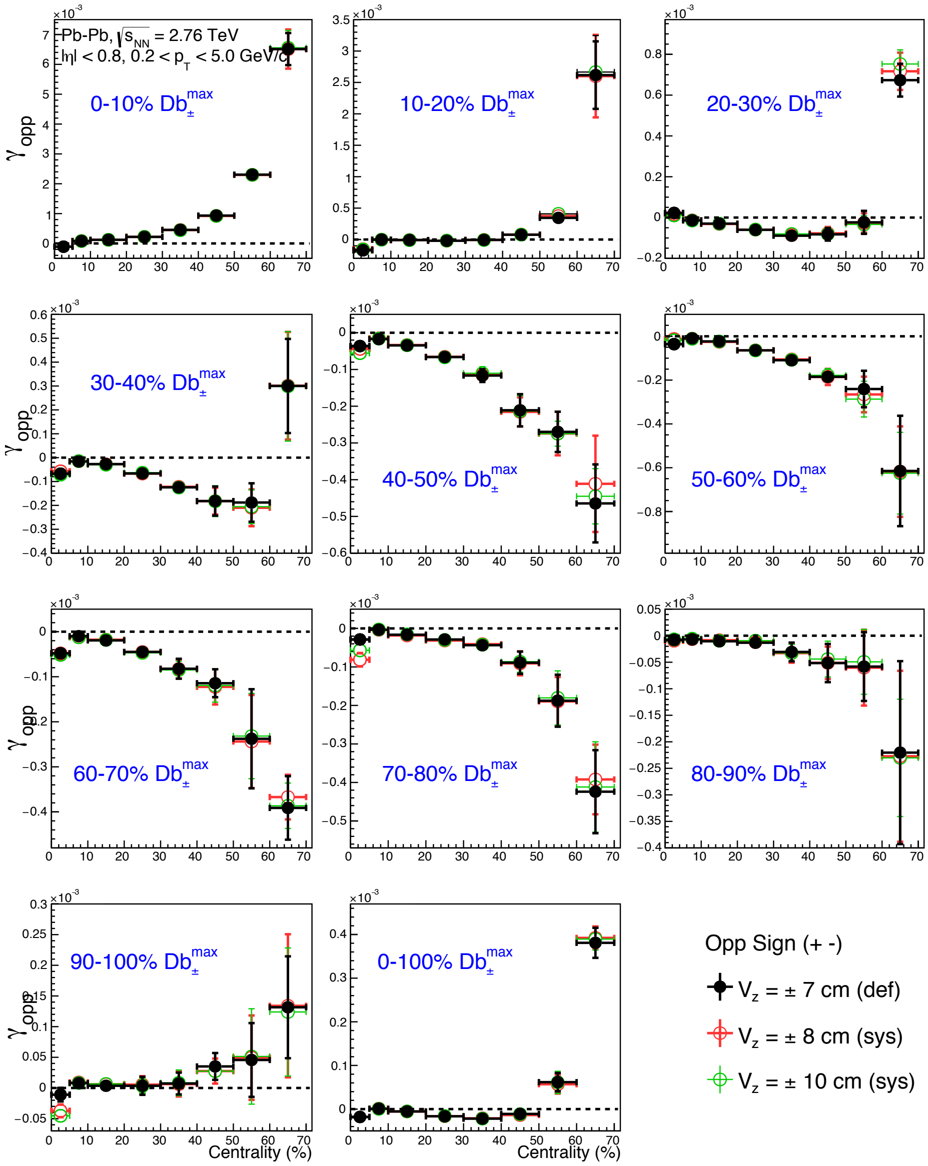

Figure 5.39: Centrality dependence $\langle cos(\phi_a - \phi_b)\rangle$ for opposite sign charge pairs for different vertex cuts for different $Db_{\pm}^{max}$ bins as indicated.

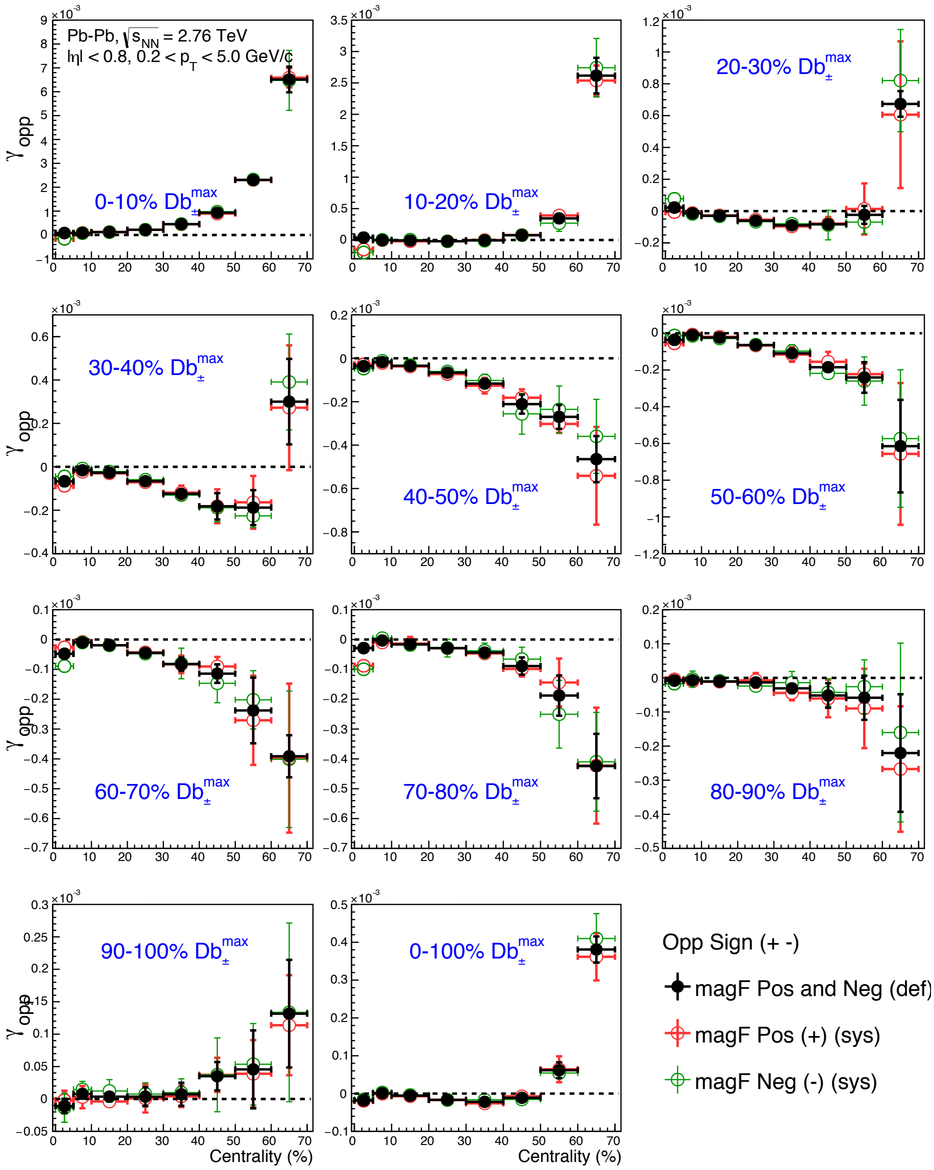

Figure 5.40: Centrality dependence $\langle cos(\phi_a - \phi_b)\rangle$ for opposite sign charge pairs for different magnetic field polarity for different $Db_{\pm}^{max}$ bins as indicated.

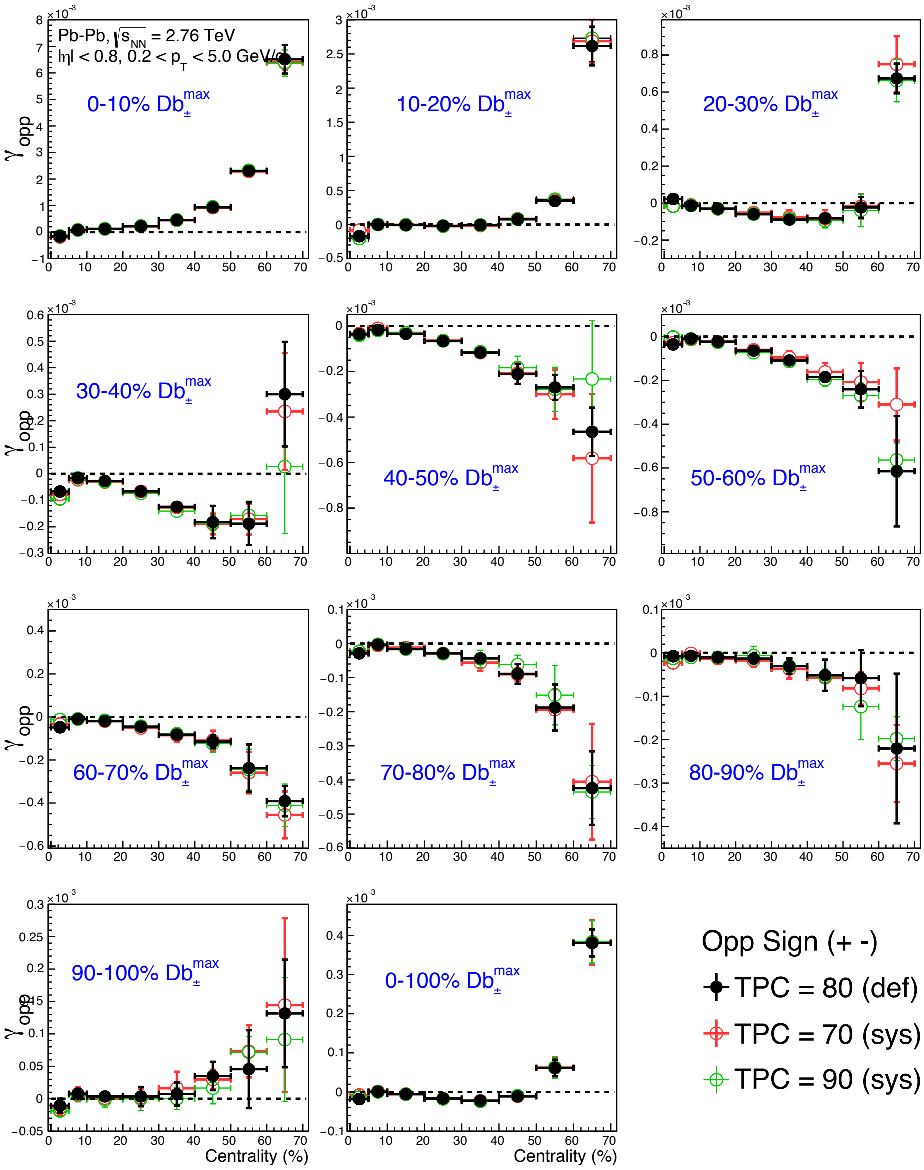

Figure 5.41: Centrality dependence $\langle cos(\phi_a - \phi_b) \rangle$ for opposite sign charge pairs for different cuts on number of TPC clusters for different $Db_{\pm}^{max}$ bins as indicated.

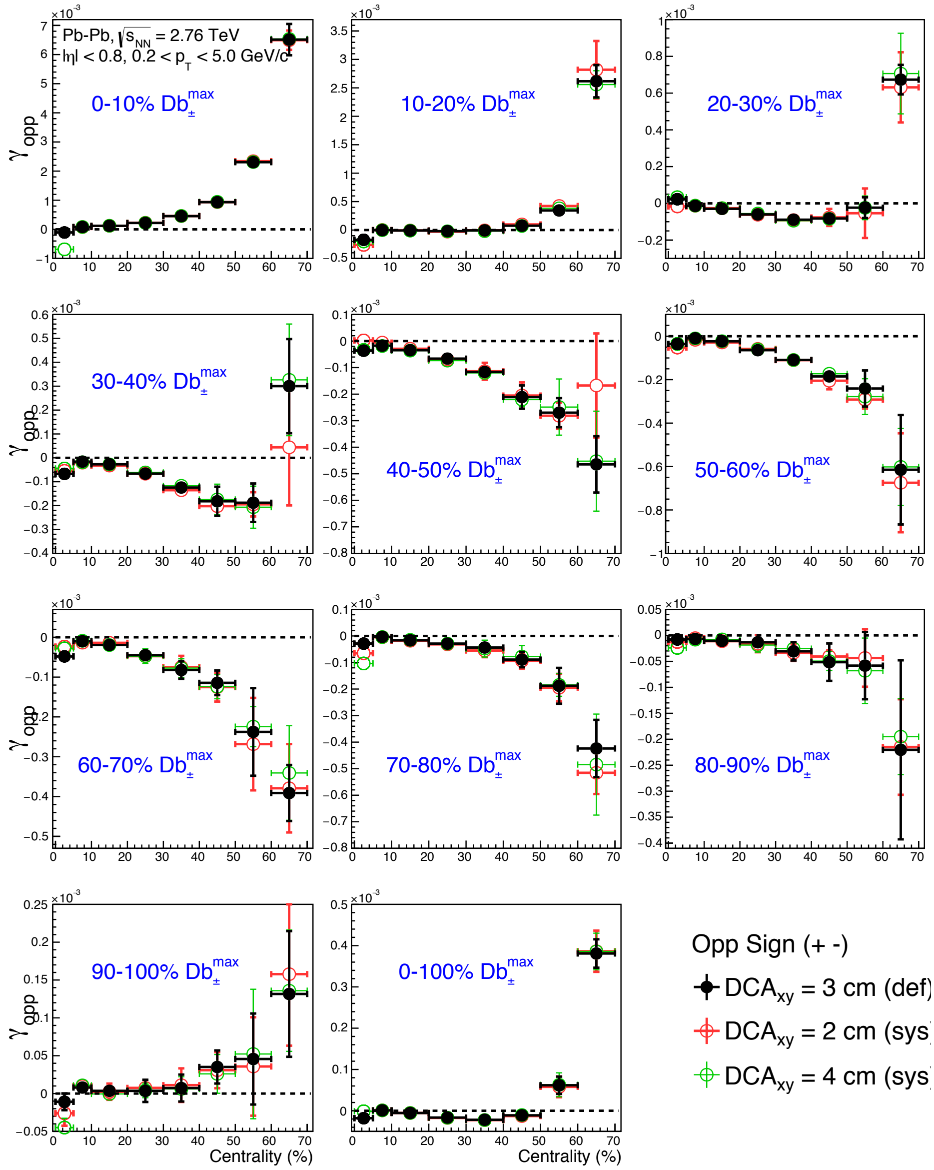

Figure 5.42: Centrality dependence $\langle cos(\phi_a - \phi_b)\rangle$ for opposite sign charge pairs for different DCA_{xy} cuts for different $Db_{\pm}^{max}$ bins as indicated.

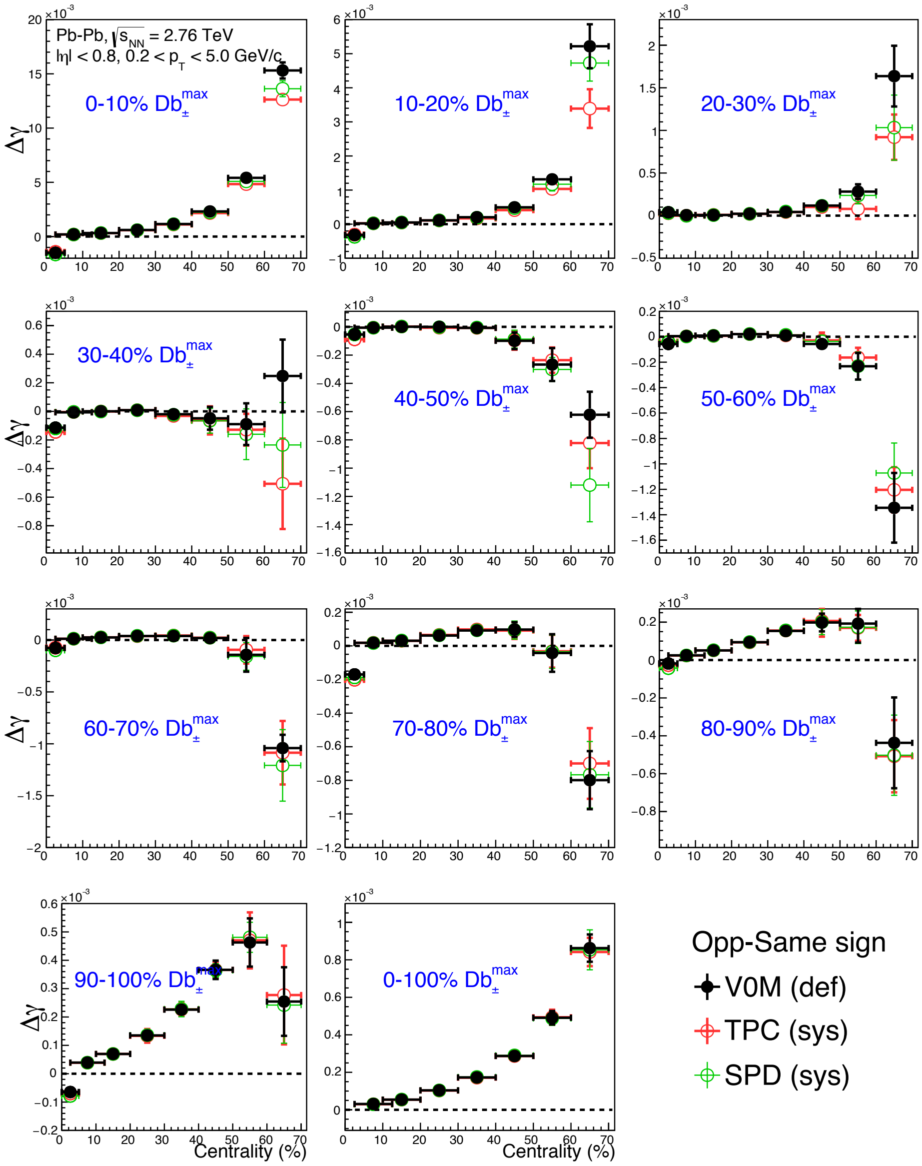

Figure 5.43: Centrality dependence $\langle cos(\phi_a - \phi_b)\rangle$ for $\Delta\gamma$ for different centrality definitions for different $Db_{\pm}^{max}$ bins as indicated.

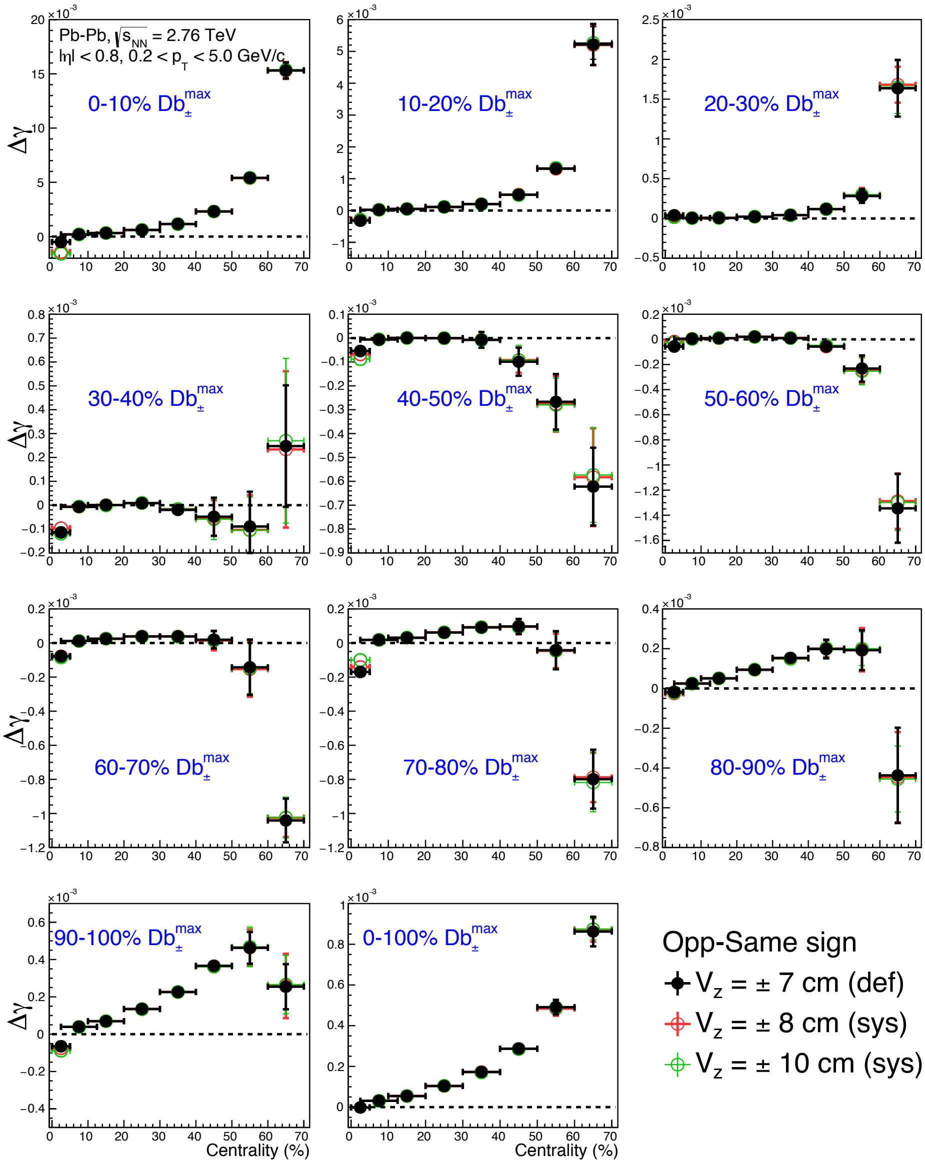

Figure 5.44: Centrality dependence $\langle cos(\phi_a - \phi_b)\rangle$ for $\Delta\gamma$ for different vertex cuts for different $Db_{\pm}^{max}$ bins as indicated.

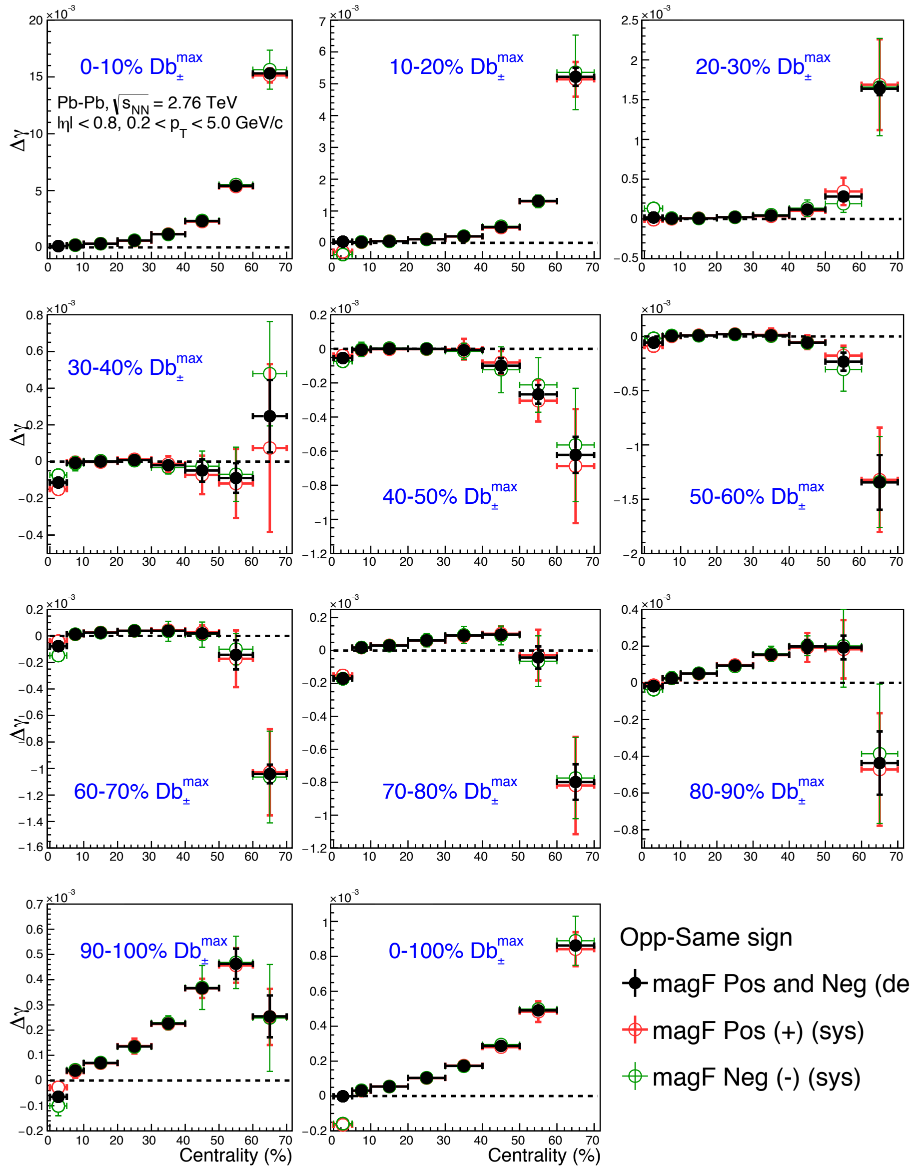

Figure 5.45: Centrality dependence $\langle cos(\phi_a - \phi_b)\rangle$ for $\Delta\gamma$ for different magnetic field polarity for different $Db_{\pm}^{max}$ bins as indicated.

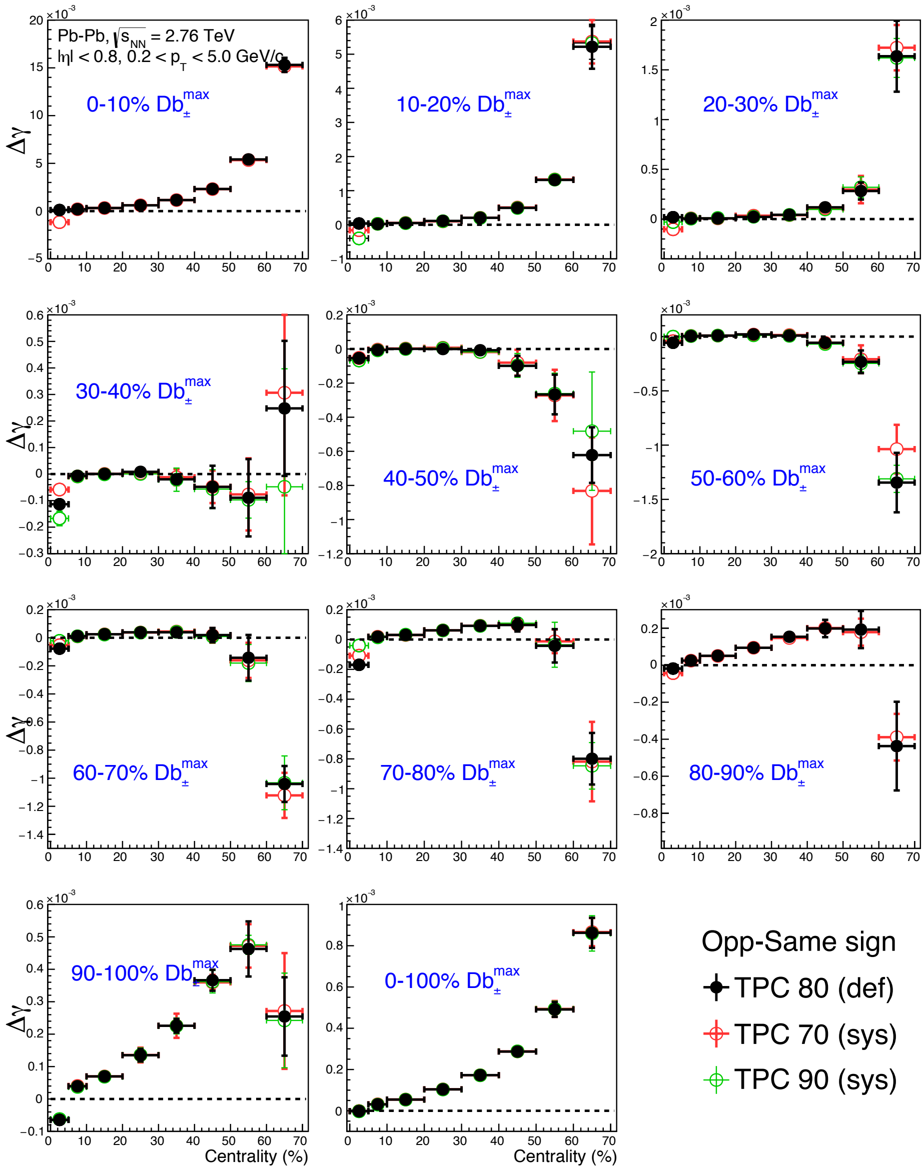

Figure 5.46: Centrality dependence $\langle cos(\phi_a - \phi_b)\rangle$ for $\Delta\gamma$ for different cuts on number of TPC clusters for different $Db_{\pm}^{max}$ bins as indicated.

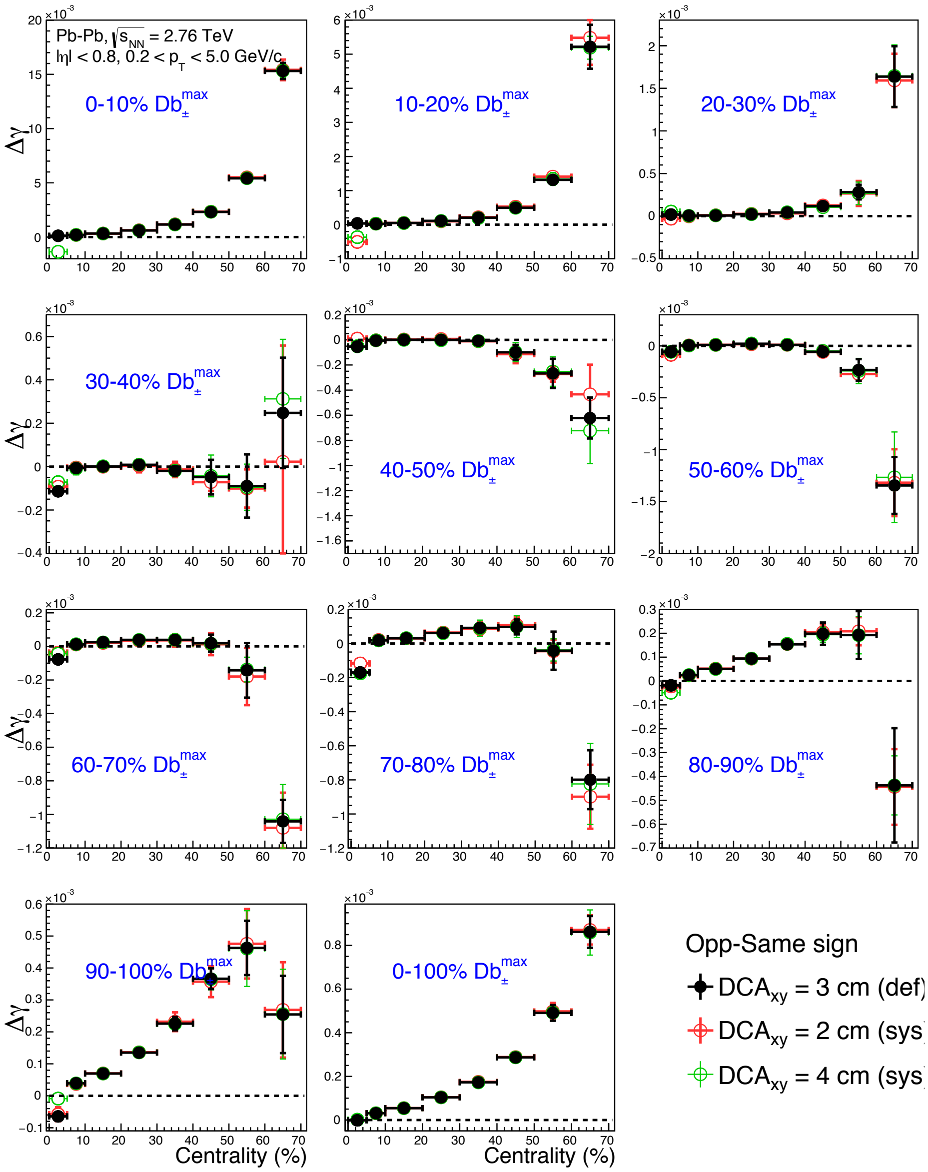

Figure 5.47: Centrality dependence $\langle cos(\phi_a - \phi_b) \rangle$ for $\Delta\gamma$ for different DCA_{xy} cuts for different $Db^{max}_{\pm}$ bins as indicated.

Publications/Conferences

Papers presented in Conferences, Workshops, Symposiums

1. Sonia Parmar et al., *"Constraining the Chiral Magnetic Effect in heavy ion collisions using AMPT model", **DAE International Symposium on Nuclear Physics**, December 10-14, 2018.*

2. Sonia Parmar et al., *"Simulation study of charged-neutral fluctuations in Pb-Pb collisions at $\sqrt{s_{NN}}$ = 2.76 TeV"*, **DAE International Symposium on Nuclear Physics**, December 10-14, 2018.

3. Sonia Parmar et.al., *"Study of charge separation effect in Pb-Pb collisions using AMPT"*, **DAE-BRNS High Energy Physics Symposium**, December 10-14, 2018.

4. Sonia Parmar, *"Event-by-event charge separation in Pb-Pb collisions at $\sqrt{s_{NN}}$ = 2.76 TeV using AMPT"*, **ASIA-EUROPE-PACIFIC SCHOOL OF HIGH ENERGY (AEPSHEP2018)**, September 12-25, 2018, Quy Nhon, Vietnam.

5. Sonia Parmar et al., *"Simulation study of event-by-event localized charge separation in Pb-Pb collisions at $\sqrt{s_{NN}}$ = 2.76 TeV"*, **10^{th} Chandigarh Science Congress (CHASCON 2017)**, March 9-11, 2017, Panjab University Chandigarh.

6. Sonia Parmar, *"Event-by-event study of charge separation effect in Pb-Pb collisions at $\sqrt{s_{NN}}$ = 2.76 TeV with the ALICE experiment"*, **Quark Matter (QM 2017)**, February 5-11, 2017, Chicago Illinois, USA.

7. Sonia Parmar et al., *"Event-by-event charge separation in Pb-Pb collisions at 2.76 TeV with ALICE"*, **DAE Symposium on Nuclear Physics**, December 5-9, 2016.

8. Sonia Parmar et al., *"Event-by-event charge separation in Pb-Pb collisions at 2.76 TeV with ALICE at the LHC"*, **DAE-BRNS High Energy Physics Symposium**, December 12-16, 2016.

Publications

1. "Multiplicity dependence of (anti-)deutron production in pp collisions at $\sqrt{s}$ = 7 TeV", ALICE Collaboration, Phys. Lett. B **794**, 50 (2019).

2. "Relative particle yield fluctuations in Pb-Pb collisions at $\sqrt{s_{\rm NN}} = 2.76$ TeV", ALICE Collaboration, Eur. Phys. J. C **79**, 236 (2019).

3. "Charged-particle pseudorapidity density at mid-rapidity in p-Pb collisions at $\sqrt{s_{\rm NN}} = 8.16$ TeV", ALICE Collaboration, Eur. Phys. J. C **79**, 307 (2019).

4. "Jet fragmentation transverse momentum measurements from di-hadron correlations in $\sqrt{s} = 7$ TeV pp and $\sqrt{s_{\rm NN}} = 5.02$ TeV p-Pb collisions", ALICE Collaboration, JHEP **2019**, 169 (2019).

5. "Centrality and pseudorapidity dependence of the charged-particle multiplicity density in Xe-Xe collisions at $\sqrt{s_{\rm NN}}$ =5.44 TeV", Phys. Lett. B **790**, 35-48 (2019).

6. "Event-shape engineering for the D-meson elliptic flow in mid-central Pb-Pb collisions at $\sqrt{s_{\rm NN}}$ =5.02 TeV", ALICE Collaboration, JHEP **1902**, 150 (2019).

7. "Azimuthal Anisotropy of Heavy-Flavour Decay Electrons in p-Pb Collisions at $\sqrt{s_{\rm NN}}$ =5.02 TeV", ALICE Collaboration, Phys. Rev. Lett. **122**, 072301 (2019).

8. "Constraining the magnitude of the Chiral Magnetic Effect with Event Shape Engineering in Pb-Pb collisions at $\sqrt{s_{\mathrm{NN}}}$ =2.76 TeV", ALICE Collaboration, Phys. Lett. B **777**, 151 (2018).

9. "Measurement of dielectron production in central Pb-Pb collisions at $\sqrt{s_{\mathrm{NN}}}$ =2.76 TeV", ALICE Collaboration, Phys. Rev. C **99**, 024002 (2019).

10. "p-p, p-Λ and $\Lambda-\Lambda$ correlations studied via femtoscopy in pp reactions at $\sqrt{s}$ = 7 TeV", ALICE Collaboration, Phys. Rev. C **99**, 024001 (2019).

11. "Multiplicity dependence of light-flavor hadron production in pp collisions at $\sqrt{s}$ =7 TeV, Phys. Rev. C **99**, 024906 (2019).

12. "Suppression of lambda(1520) resonance production in central Pb-Pb collisions at $\sqrt{s_{\mathrm{NN}}}$ =2.76 TeV", Phys. Rev. C **99**, 024905 (2019).

13. "Dielectron and heavy-quark production in inelastic and high-multiplicity proton-proton collisions at $\sqrt{s}$ =13 TeV", ALICE Collaboration, Phys. Lett. B **788**, 505 (2019).

14. "Direct photon production at low transverse momentum in proton-proton collisions at $\sqrt{s_{\mathrm{NN}}}$ =2.76 TeV", ALICE Collaboration, Phys. Rev. C **99**, 024912 (2019).

15. "Charged jet cross section and fragmentation in proton-proton collisions at $\sqrt{s}$ =7 TeV", ALICE Collaboration, Phys. Rev. D **99**, 012016 (2019).

16. "Direct photon elliptic flow in Pb-Pb collisions at $\sqrt{s_{\mathrm{NN}}}$ =2.76 TeV", ALICE Collaboration, Phys. Lett. B **789**, 308 (2019).

17. " suppression at forward rapidity in Pb-Pb collisions at $\sqrt{s_{\mathrm{NN}}}$ =5.02 TeV", ALICE Collaboration, Phys. Lett. B **790**, 89 (2019).

18. "Measuring K_S^0 $K^{\pm}$ interctions using pp collisions at $\sqrt{s}$ =7 TeV", ALICE Collaboration, Phys. Lett. B **790**, 22 (2019).

19. "Transverse momentum spectra and nuclear modification factors of charged particles in Xe-Xe collisions at $\sqrt{s_{\mathrm{NN}}}$ = 5.44 TeV", ALICE Collaboration, Phys. Lett. B **788** 166-179 (2019).

20. "Transverse momentum spectra and nuclear modification factors of charged particles in pp, p-Pb and Pb-Pb collisions at LHC", ALICE Collaboration, JHEP **1811**, 013 (2018).

21. "Medium modification of the shape of small-radius jets in central Pb-Pb collisions at $\sqrt{s_{\mathrm{NN}}}$ =2.76 TeV", ALICE Collaboration, JHEP **10**, 139 (2018).

22. "Neutral pion and η meson production at mid-rapidity in Pb-Pb collisions at $\sqrt{s_{\mathrm{NN}}}$ =2.76 TeV", ALICE Collaboration, Phys. Rev. C **98**, 044901 (2018).

23. "Dielectron production in proton-proton collisions at $\sqrt{s}$ =7 TeV", ALICE Collaboration, JHEP **1809**, 064 (2018).

24. "Azimuthally-differential pion femtoscopy relative to the third harmonic event plane in Pb-Pb collisions at $\sqrt{s_{\mathrm{NN}}}$ =2.76 TeV", ALICE Collaboration, Phys. Lett. B **785**, 320 (2018).

25. "Anisotropic flow of identified particles in Pb-Pb collisions at $\sqrt{s_{\mathrm{NN}}}$ =5.02 TeV", ALICE Collaboration, JHEP **09**, 006 (2018).

26. "Inclusive J/Ψ production in Xe-Xe collisions at $\sqrt{s_{\mathrm{NN}}}$ =5.44 TeV", ALICE Collaboration, Phys. Lett. B **785**, 419 (2018).

27. "Neutral pion and η meson production at mid-rapidity in Pb-Pb collisions at $\sqrt{s_{\mathrm{NN}}}$ =5.02 TeV", ALICE Collaboration, Eur. Phys .J. **C78**, 624 (2018).

28. "Anisotropic flow in Xe-Xe collisions at $\sqrt{s_{\rm NN}}$ =5.44 TeV", ALICE Collaboration, Phys. Lett. B **784**, 82 (2018).

29. "Inclusive J/Ψ production at forward and backward rapidity in p-Pb collisions at $\sqrt{s_{\rm NN}}$ =8.16 TeV", ALICE Collaboration, JHEP **07**, 160 (2018).

30. "Energy dependence and fluctuations of anisotropic flow in Pb-Pb collisions at $\sqrt{s_{\rm NN}}$ =5.02 and 2.76 TeV", ALICE Collaboration, JHEP **07**, 103 (2018).

31. "ϕ meson production at forward rapidity in Pb-Pb collisions at $\sqrt{s_{\rm NN}}$ =2.76 TeV", ALICE Collaboration, Eur. Phys. J. C **78**, 559 (2018).

32. "Measurement of the inclusive J/Ψ polarization at forward rapidity in pp collisions at $\sqrt{s}$ =8 TeV", ALICE Collaboration, Eur. Phys. J. C **78**, 562 (2018).

33. "Constraints on jet quenching in p-Pb collisions at $\sqrt{s_{\rm NN}}$ =5.02 TeV measured by the event-activity dependence of semi-inclusive hadron-jet distributions", ALICE Collaboration, Phys. Lett. B **783**, 95-113 (2018).

34. "Prompt and non-prompt J/Ψ production and nuclear modification at mid-rapidity in p-Pb collisions at $\sqrt{s_{\rm NN}}$ =5.02 TeV", ALICE Collaboration, Eur. Phys. J. C **78**, 466 (2018).

35. "Λ_c^+ production in pp collisions at $\sqrt{s}$ =7 TeV and in p-Pb collisions at $\sqrt{s_{\rm NN}}$ =5.02 TeV", ALICE Collaboration, JHEP **04**, 108 (2018).

36. "First measurement of $psic$ production in pp collisions at $\sqrt{s}$ =7 TeV", ALICE Collaboration, Phys. Lett. B **781**, 8 (2018).

37. "Longitudinal asymmetry and its effect on pseudorapidity distributions in Pb-Pb collisions at $\sqrt{s_{\rm NN}}$ =2.76 TeV", ALICE Collaboration, Phys. Lett. B **781**, 20 (2018).

38. "π^0 and η meson production in proton-proton collisions at $\sqrt{s}$ =8 TeV", ALICE Collaboration, Eur. Phys. J. C **78**, 263 (2018).

39. "Measurement of Z^0 -boson production at large rapidities in Pb-Pb collisions at $\sqrt{s_{\rm NN}}$ =5.02 TeV", ALICE Collaboration, Phys. Lett. B **780**, 372 (2018).

40. "D-meson azimuthal anisotropy in mid-central Pb-Pb collisions at $\sqrt{s_{\rm NN}}$ =5.02 TeV", ALICE Collaboration, Phys. Rev. Lett. **120**, 102301 (2018).

41. "Search for collectivity with azimuthal J/Ψ-hadron correlations in high multiplicity p-Pb collisions at $\sqrt{s_{\rm NN}}$ =5.02 and 8.16 TeV", ALICE Collaboration, Phys. Lett. B **780**, 7 (2018).

42. "Production of deuterons, tritons, He nuclei and their anti-nuclei in pp collisions at $\sqrt{s}$ =0.9, 2.76 and 7 TeV", ALICE Collaboration, Phys. Rev. C **97**, 024615 (2018).

43. "Systematic studies of correlations between different order flow harmonics in Pb-Pb collisions at =2.76 TeV", ALICE Collaboration, Phys. Rev. C **97**, 024906 (2018).

44. "Production of He and He in Pb-Pb collisions at $\sqrt{s_{\rm NN}}$ =2.76 TeV at the LHC", ALICE Collaboration, Nucl. Phys. A **971**, 1 (2018).;

45. "Kaon femtoscopy in Pb-Pb collisions at $\sqrt{s_{\rm NN}}$ =2.76 TeV", ALICE Collaboration, Phys. Rev. C **96**, 064613 (2017).

46. "J/Ψ elliptic flow in Pb-Pb collisions at $\sqrt{s_{\rm NN}}$ =5.02 TeV", ALICE Collaboration, Phys. Rev. Lett. **119**, 242301 (2017).

47. "Charged-particle multiplicity distributions over a wide pseudorapidity range in proton-proton collisions at $\sqrt{s}$ = 0.9, 7 and 8 TeV", ALICE Collaboration, Eur. Phys. J. C **77**, 852 (2017).

48. "The ALICE Transition Radiation Detector: construction, operation, and performance", ALICE Collaboration, Nucl. Instr. Meth. A **881**, 88 (2018).

49. "First measurement of jet mass in Pb-Pb and p-Pb collisions at the LHC", ALICE Collaboration, Phys. Lett. B **776**, 249 (2018).

50. "J/Ψ production as a function of charged-particle pseudorapidity density in p-Pb collisions at $\sqrt{s_{\rm NN}}$ =5.02 TeV", ALICE Collaboration, Phys. Lett. B **776**, 91 (2018).

51. "Measurement of $D^0, D^+, D^{*+} and D_s^+$ production in p-Pb collisions at $\sqrt{s_{\rm NN}}$ =5.02 TeV", ALICE Collaboration, JHEP **1810**, 174 (2018).

52. "Measurement of deuteron spectra and elliptic flow in Pb-Pb collisions at $\sqrt{s_{\rm NN}}$ =2.76 TeV at the LHC", ALICE Collaboration, Eur. Phys. J. C **77**, 658 (2017).

53. "Searches for transverse momentum dependent flow vector fluctuations in Pb-Pb and p-Pb collisions at the LHC", ALICE Collaboration, JHEP **09**, 032 (2017).

54. "Measuring $K_S^0, K^{\pm}$ interactions using Pb-Pb collisions at $\sqrt{s_{\rm NN}}$ =2.76 TeV at the LHC", ALICE Collaboration, Phys. Lett. B **774**, 64 (2017).

55. "Anomalous broadening of the near-side jet peak in Pb-Pb collisions at $\sqrt{s_{\rm NN}}$ =2.76 TeV", ALICE Collaboration, Phys. Rev. Lett. **119**, 102301 (2017).

56. "Evolution of the longitudinal and azimuthal structure of the near-side jet peak in Pb-Pb collisions at $\sqrt{s_{\rm NN}}$ =2.76 TeV", ALICE Collaboration, Phys. Rev. C **96**, 034904 (2017).

57. "Insight into particle production mechanisms via angular correlations of identified particles in pp collisions at $\sqrt{s}$ =7 TeV", ALICE Collaboration,

Eur.Phys.J. C **77**, 569 (2017).

58. "Measurement of D-meson production at mid-rapidity in pp collisions at $\sqrt{s}$ =7 TeV", ALICE Collaboration, Eur. Phys. J. C **77**, 550 (2017).

59. "Linear and non-linear flow modes in Pb-Pb collisions at $\sqrt{s_{\rm NN}}$ =2.76 TeV", ALICE Collaboration, Phys. Lett. B **773**, 68 (2017).

60. "Measurement of electrons from beauty-hadron decays in p-Pb collisions at $\sqrt{s_{\rm NN}}$ =5.02 TeV and Pb-Pb collisions at $\sqrt{s_{\rm NN}}$ = 2.76 TeV.

61. "Centrality dependence of the pseudorapidity density distribution for charged particles in Pb-Pb collisions at $\sqrt{s_{\rm NN}}$ = 5.02 TeV", ALICE Collaboration, Phys.Lett. B **772**, 567 (2017).

62. "Measurements of low-p_T electrons from semileptonic heavy-flavour hadron decays at mid-rapidity in pp and Pb-Pb collisions at $\sqrt{s_{\rm NN}}$ =2.76 TeV", ALICE Collaboration, JHEP **10**, 061 (2018).

63. "Energy dependence of forward-rapidity J/Ψ and $\Psi(2S)$ production in pp collisions at the LHC", ALICE Collaboration, Eur. Phys. J. C **77**, 392 (2017).

64. "Production of muons from heavy-flavour hadron decays in p-Pb collisions at $\sqrt{s_{\rm NN}}$ =5.02 TeV", ALICE Collaboration, Phys. Lett. B **770**, 459-472 (2017).

65. "Production of $\Sigma(1385)^{\pm}$ and $si(1530)^0$ in p-Pb collisions = 5.02 TeV", ALICE Collaboration, Eur. Phys. J. C **77**, 389 (2017).

66. "$K^*(892)^0$ and $\phi(1020)$ meson production at high transverse momentum in pp and Pb-Pb collisions at $\sqrt{s_{\rm NN}}$ =2.76 TeV", ALICE Collaboration, Phys. Rev. C **95**, 064606 (2017).

67. "Azimuthally differential pion femtoscopy in Pb-Pb collisions at $\sqrt{s_{\rm NN}}$ =2.76 TeV", ALICE Collaboration, Phys. Rev. Lett. **118**, 222301 (2017).

68. "Measurement of the production of high-p_T electrons from heavy-flavour hadron decays in Pb-Pb collisions at $\sqrt{s_{\rm NN}}$ = 2.76 TeV", ALICE Collaboration, Phys. Lett. B **771**, 467 (2017).

69. "Production of π^0 and η mesons up to high transverse momentum in pp collisions at 2.76 TeV", ALICE Collaboration, Eur. Phys. J. C **77**, 339 (2017).

70. "Enhanced production of multi-strange hadrons in high-multiplicity proton-proton collisions", ALICE Collaboration, Nature Physics **13**, 535 (2017).

71. "Flow dominance and factorization of transverse momentum correlations in Pb-Pb collisions at the LHC", ALICE Collaboration, PRL **118**, 162302 (2017).

72. "Measurement of azimuthal correlations of D mesons and charged particles in pp collisions at $\sqrt{s}$ =7 TeV and p-Pb collisions at $\sqrt{s_{\rm NN}}$ =5.02 TeV", ALICE Collaboration, Eur. Phys. J. C **77**, 245 (2017).

73. "J/Ψ suppression at forward rapidity in Pb-Pb collisions at $\sqrt{s_{\rm NN}}$ =5.02 TeV", ALICE Collaboration, Phys. Lett. B 766, 212 (2017).

74. "Determination of the event collision time with the ALICE detector at the LHC", ALICE Collaboration, Eur. Phys. J. Plus **132**, 99 (2017).

75. "ϕ-meson production at forward rapidity in p-Pb collisions at $\sqrt{s_{\rm NN}}$ =5.02 TeV and in pp collisions at $\sqrt{s_{\rm NN}}$ = 2.76 TeV", ALICE Collaboration, Phys. Lett. B **768**, 203-217 (2017).

76. "W and Z boson production in p-Pb collisions at $\sqrt{s_{\rm NN}}$ = 5.02 TeV", ALICE Collaboration, JHEP **02**, 077 (2017).

77. "Charged-particle multiplicities in proton-proton collisions at $\sqrt{s}$ = 0.9 to 8 TeV", ALICE Collaboration, Eur. Phys. J. C **77**, 33 (2017).

78. "Correlated event-by-event fluctuations of flow harmonics in Pb-Pb collisions at $\sqrt{s_{\rm NN}}$ =2.76 TeV", ALICE Collaboration, Phys. Rev. Lett. **117**, 182301 (2016).

79. "Jet-like correlations with neutral pion triggers in pp and central Pb-Pb collisions at 2.76 TeV", ALICE Collaboration, PLB **763**, 238 (2016).

80. "Higher harmonic flow coefficients of identified hadrons in Pb-Pb collisions at $\sqrt{s_{\rm NN}}$ =2.76 TeV", ALICE Collaboration, JHEP **1609**, 164 (2016).

81. "Measurement of transverse energy at midrapidity in Pb-Pb collisions at $\sqrt{s_{\rm NN}}$ =2.76 TeV", ALICE Collaboration, Phys. Rev. C **94**, 034903 (2016).

82. "Elliptic flow of electrons from heavy-flavour hadron decays at mid-rapidity in Pb-Pb collisions at $\sqrt{s_{\rm NN}}$ =2.76 TeV", ALICE Collaboration, JHEP **09**, 028 (2016).

83. "Measurement of D-meson production versus multiplicity in p-Pb collisions at $\sqrt{s_{\rm NN}}$ =5.02 TeV", ALICE Collaboration, JHEP **8**, 1 (2016).

84. "Multiplicity dependence of charged pion, kaon, and (anti)proton production at large transverse momentum in p-Pb collisions at $\sqrt{s_{\rm NN}} = 5.02$ TeV", ALICE Collaboration, Phys. Lett. B **760**, 720 (2016).

85. "Pseudorapidity dependence of the anisotropic flow of charged particles in Pb-Pb collisions at $\sqrt{s_{\rm NN}}$ =2.76 TeV", ALICE Collaboration, Phys. Lett. B **762**, 376 (2016).

86. "Centrality dependence of $\Psi(2S)$ suppression in p-Pb collisions at $\sqrt{s_{\rm NN}}$ =5.02 TeV", ALICE Collaboration, JHEP **06**, 50 (2016).

87. "Centrality dependence of the charged-particle multiplicity density at mid-rapidity in Pb-Pb collisions at $\sqrt{s_{\rm NN}} = 5.02$ TeV", ALICE Collaboration,

Phys. Rev. Lett. **116**, 222302 (2016).

88. "Measurement of an excess in the yield of J/Ψ at very low p_T in Pb-Pb collisions at $\sqrt{s_{\mathrm{NN}}} = 2.76$ TeV", ALICE Collaboration, Phys. Rev. Lett. **116**, 222301 (2016).

89. "Differential studies of inclusive J/Ψ and $\Psi(2S)$ production at forward rapidity in Pb-Pb collisions at $\sqrt{s_{\mathrm{NN}}} = 2.76$ TeV", ALICE Collaboration, JHEP **05**, 179 (2016).

90. "Particle identification in ALICE: a Bayesian approach", ALICE Collaboration, Eur. Phys. J. Plus **131**, 168 (2016).

91. "Centrality dependence of charged jet production in p-Pb collisions at $\sqrt{s_{\mathrm{NN}}}$ =5.02 TeV", ALICE Collaboration, Eur. Phys. J. C **76**, 271 (2016).

92. "Multi-strange baryon production in p-Pb collisions at $\sqrt{s_{\mathrm{NN}}}$ =5.02 TeV", ALICE Collaboration, Phys. Lett. B **758**, 389 (2016).

93. "Production of $K^*(892)^0$ and $\phi(1020)$ in p-Pb collisions at $\sqrt{s_{\mathrm{NN}}}$ =5.02 TeV", ALICE Collaboration, Eur. Phys. J. C **76**, 245 (2016).

94. "Charge-dependent flow and the search for the Chiral Magnetic Wave in Pb-Pb collisions at $\sqrt{s_{\mathrm{NN}}}$ =2.76 TeV", ALICE Collaboration, Phys. Rev. C **93**, 044903 (2016).

95. "Inclusive quarkonium production at forward rapidity in pp collisions at $\sqrt{s}$ =8 TeV", ALICE Collaboration, Eur. Phys. J. C **76**, 184 (2016).

96. "Anisotropic flow of charged particles in Pb-Pb collisions at $\sqrt{s_{\mathrm{NN}}}$ =5.02 TeV", ALICE Collaboration, Phys. Rev. Lett. **116**, 132302 (2016).

97. "Event shape engineering for inclusive spectra and elliptic flow in Pb-Pb collisions at $\sqrt{s_{\rm NN}} = 2.76$ TeV", ALICE Collaboration, Phys. Rev. C **93**, 034916 (2016).

98. "Centrality dependence of the nuclear modification factor of charged pions, kaons, and protons in Pb-Pb collisions at $\sqrt{s_{\rm NN}} = 2.76$ TeV", ALICE Collaboration, Phys. Rev. C **93**, 034913 (2016).

99. "Transverse momentum dependence of D-meson production in Pb-Pb collisions at $\sqrt{s_{\rm NN}}$ =2.76 TeV", ALICE Collaboration, JHEP **03**, 081 (2016).

100. "Measurement of D_S^+ production and nuclear modification factor in Pb-Pb collisions at JHEP **03**, 082 (2016).

101. "Multipion Bose-Einstein correlations in pp, p-Pb, and Pb-Pb collisions at the LHC", ALICE Collaboration, Phys. Rev. C **93**, 054908 (2016).

102. "Production of light nuclei and anti-nuclei in pp and Pb-Pb collisions at LHC energies", ALICE Collaboration, Phys. Rev. C **93**, 024917 (2015).

103. "Multiplicity and transverse momentum evolution of charge-dependent correlations in pp, p-Pb, and Pb-Pb collisions at the LHC", ALICE Collaboration, Eur. Phys. J. C **76**, 86 (2016).

104. "Centrality dependence of pion freeze-out radii in Pb-Pb collisions at $\sqrt{s_{\rm NN}}$ =2.76 TeV", ALICE Collaboration, Phys. Rev. C **93**, 024905 (2016).

105. "Direct photon production in Pb-Pb collisions at $\sqrt{s_{\rm NN}}$ =2.76 TeV", ALICE Collaboration, Phys. Lett. B **754**, 235 (2016).

106. "Centrality evolution of the charged-particle pseudorapidity density over a broad pseudorapidity range in Pb-Pb collisions at $\sqrt{s_{\rm NN}} = 2.76$ TeV", ALICE Collaboration, Phys. Lett. B **754**, 373 (2016).

107. "Forward-central two-particle correlations in p-Pb collisions at $\sqrt{s_{\rm NN}} = 5.02$ TeV", ALICE Collaboration, Phys. Lett. B **753**, 126 (2016).

108. "H and $\bar{H}$ production in Pb-Pb collisions at $\sqrt{s_{\rm NN}}$ =2.76 TeV", ALICE Collaboration, Phys. Lett. B **754**, 360 (2016).

109. "Study of cosmic ray events with high muon multiplicity using the ALICE detector at the CERN Large Hadron Collider", ALICE Collaboration, JCAP **01**, 032 (2016).

110. "Search for weakly decaying $\bar{\Lambda}$n and $\Lambda\ \Lambda$ exotic bound states in central Pb-Pb collisions at $\sqrt{s_{\rm NN}} = 2.76$ TeV", ALICE Collaboration, Phys. Lett. B **752**, 267 (2016).

111. "Measurement of electrons from heavy-flavour hadron decays in p-Pb collisions at $\sqrt{s_{\rm NN}} = 5.02$ TeV", ALICE Collaboration, Phys. Lett. B **754**, 81 (2016).

112. "Azimuthal anisotropy of charged jet production in $\sqrt{s_{\rm NN}}$ =2.76 TeV Pb-Pb collisions", ALICE Collaboration, Phys.Lett. B **753**, 511 (2016).

113. "Pseudorapidity and transverse-momentum distributions of charged particles in proton-proton collisions at $\sqrt{s}$ =13 TeV", ALICE Collaboration, Phys. Lett. B **753**, 319 (2016).

114. "Elliptic flow of muons from heavy-flavour hadron decays at forward rapidity in Pb-Pb collisions at $\sqrt{s_{\rm NN}}$ =2.76 TeV", ALICE Collaboration, Phys. Lett. B **753**, 41 (2016).

115. "Centrality dependence of high-p_T D meson suppression in Pb-Pb collisions at $\sqrt{s_{\rm NN}}$ =2.76 TeV", ALICE Collaboration, JHEP **11**, 205 (2015).

116. "One-dimensional pion, kaon, and proton femtoscopy in Pb-Pb collisions at $\sqrt{s_{\rm NN}}$ =2.76 TeV", ALICE Collaboration, Phys. Rev. C **92**, 054908 (2015).

117. "Centrality dependence of inclusive J/Ψ production in p-Pb collisions at $\sqrt{s_{\rm NN}}$ =5.02 TeV", ALICE Collaboration, JHEP **11**, 127 (2015).

118. "Coherent Ψ(2S) photo-production in ultra-peripheral Pb-Pb collisions at $\sqrt{s_{\rm NN}}$ =2.76 TeV", ALICE Collaboration, Phys. Lett. B **751**, 358 (2015).

119. "Measurement of jet quenching with semi-inclusive hadron-jet distributions in central Pb-Pb collisions at $\sqrt{s_{\rm NN}}$ =2.76 TeV", ALICE Collaboration, JHEP **09**, 170 (2015).

120. "Measurement of charm and beauty production at central rapidity versus charged-particle multiplicity in proton-proton collisions at $\sqrt{s}$ = 7TeV", ALICE Collaboration, JHEP **09**, 148 (2015).

121. "Coherent ρ photoproduction in ultra-peripheral Pb-Pb collisions at $\sqrt{s_{\rm NN}}$ =2.76 TeV", ALICE Collaboration, JHEP **09**, 095 (2015).

122. "Precision measurement of the mass difference between light nuclei and antinuclei", ALICE Collaboration, Nature Physics 11 811 (2015).

123. "Measurement of charged jet production cross sections and nuclear modification in p-Pb collisions at $\sqrt{s_{\rm NN}}$ =5.02 TeV", ALICE Collaboration, Phys. Lett. B **749**, 68 (2015).

124. "Inclusive, prompt and non-prompt J/Ψ production at mid-rapidity in Pb-Pb collisions at $\sqrt{s_{\rm NN}}$ =2.76 TeV", ALICE Collaboration, JHEP **07**, 051 (2015).

125. "Elliptic flow of identified hadrons in Pb-Pb collisions at $\sqrt{s_{\rm NN}}$ =2.76 TeV", ALICE Collaboration, JHEP **06**, 190 (2015).

126. "Charged jet cross sections and properties in proton-proton collisions at $\sqrt{s}$ = 7 TeV", ALICE Collaboration, Phys. Rev. D **91**, 112012 (2015).

127. "Rapidity and transverse-momentum dependence of the inclusive J/Ψ nuclear modification factor in p-Pb collisions at $\sqrt{s_{\rm NN}}$ =5.02 TeV", ALICE Collaboration, JHEP **06**, 55 (2015).

128. "Centrality dependence of particle production in p-Pb collisions at $\sqrt{s_{\rm NN}}$ =5.02 TeV", ALICE Collaboration, Phys. Rev. C **91**, 064905 (2015).

129. "D-meson production in p-Pb collisions at $\sqrt{s_{\rm NN}}$ =5.02 TeV and in pp collisions at $\sqrt{s}$ = 7 TeV", ALICE Collaboration, Phys. Rev. C **94**, 054908 (2016).

130. "Measurement of pion, kaon and proton production in proton-proton collisions at $\sqrt{s}$ = 7 TeV", ALICE Collaboration, EPJC **75**, 226 (2015).

131. "Forward-backward multiplicity correlations in pp collisions at $\sqrt{s}$ = 0.9, 2.76 and 7 TeV", ALICE Collaboration, JHEP **05**, 097 (2015).

132. "Measurement of dijet k_T in p-Pb collisions at $\sqrt{s_{\rm NN}}$ =5.02 TeV", ALICE Collaboration, Phys. Lett. B **746**, 385 (2015).

133. "Measurement of jet suppression in central Pb-Pb collisions at $\sqrt{s_{\rm NN}}$ =2.76 TeV", ALICE Collaboration, Phys. Lett. B **746**, 1 (2015).

134. "Inclusive photon production at forward rapidities in proton-proton collisions at $\sqrt{s}$ = 0.9, 2.76 and 7 TeV", ALICE Collaboration, EPJC **75**, 146 (2015).

135. "Two-pion femtoscopy in p-Pb collisions at $\sqrt{s_{\rm NN}}$ =5.02 TeV", ALICE Collaboration, Phys. Rev. C **91**, 034906 (2015).

136. "$K^*(892)^0$ and $\Phi(1020)$ production in Pb-Pb collisions at $\sqrt{s_{\rm NN}}$ =2.76 TeV", ALICE Collaboration, Phys. Rev. C **91**, 024609 (2015).

137. "Production of $\Sigma(1385)^{\pm}$ and $(1530)^0$ in proton-proton collisions at $\sqrt{s}$ = 7 TeV", ALICE Collaboration, Eur. Phys. J. C **75**, 1 (2015).

138. "Measurement of electrons from semileptonic heavy-flavor hadron decays in pp collisions at $\sqrt{s_{\rm NN}}$ =2.76 TeV", ALICE Collaboration, Phys. Rev. D **91**, 012001 (2015).

139. "Multiplicity dependence of jet-like two-particle correlations in p-Pb collisions at $\sqrt{s_{\rm NN}}$ =5.02 TeV", ALICE Collaboration, Phys. Lett. B **741**, 38 (2015).

140. "Suppression of Ψ(2S) production in p-Pb collisions at $\sqrt{s_{\rm NN}}$ =5.02 TeV", ALICE Collaboration, JHEP **12**, 073 (2014).

141. "Exclusive J/Ψ photoproduction off protons in ultra-peripheral p-Pb collisions at $\sqrt{s_{\rm NN}}$ =5.02 TeV", ALICE Collaboration, Phys. Rev. Lett. **113**, 232504 (2014).

142. "Production of inclusive $\Xi(1S)$ and $\Xi(2S)$ in p-Pb collisions at $\sqrt{s_{\rm NN}}$ =5.02 TeV", ALICE Collaboration, Phys. Lett. B **740**, 105 (2015).

143. "Measurement of visible cross sections in proton-lead collisions at $\sqrt{s_{\rm NN}} = 5.02$ TeV in van der Meer scans with the ALICE detector", ALICE Collaboration, JINST **9**, 1100 (2014).

144. "Multi-particle azimuthal correlations in p-Pb and Pb-Pb collisions at the CERN Large Hadron Collider", ALICE Collaboration, Phys. Rev. C **90**, 054901 (2014).

145. "Event-by-event mean p_T fluctuations in pp and Pb-Pb collisions at the LHC", ALICE Collaboration, Eur. Phys. J. C **74**, 3077 (2014).

146. "Freeze-out radii extracted from three-pion cumulants in pp, p-Pb and Pb-Pb collisions at the LHC", ALICE Collaboration, Phys. Lett. B **739**, 139 (2014).

147. "Neutral pion production at midrapidity in pp and Pb-Pb collisions at $\sqrt{s_{\rm NN}}$ =2.76 TeV", ALICE Collaboration, Eur. Phys. J. C **74**, 3108 (2014).

148. "Suppression of $\Xi(1S)$ at forward rapidity in Pb-Pb collisions at $\sqrt{s_{\rm NN}}$ =2.76 TeV", ALICE Collaboration, Phys. Lett. B **738**, 361 (2014).

149. "Performance of the ALICE Experiment at the CERN LHC", ALICE Collaboration, Int. J. Mod. Phys. A **29**, 1430044 (2014).

150. "Beauty production in pp collisions at $\sqrt{s_{\rm NN}} = 2.76$ TeV measured via semi-electronic decays", ALICE Collaboration, Phys. Lett. B 738 (2014) 97, Phys. Lett. B **763**, 507 (2016).

151. "Transverse momentum dependence of inclusive primary charged-particle production in p-Pb collisions at $\sqrt{s_{\rm NN}} = 5.02$ TeV", ALICE Collaboration, Eur. Phys. J. C **74**, 3054 (2014).

152. "Azimuthal anisotropy of D meson production in Pb-Pb collisions at $\sqrt{s_{\rm NN}}$ =2.76 TeV", ALICE Collaboration, Phys. Rev. C **90**, 034904 (2014).

153. "Measurement of quarkonium production at forward rapidity in pp collisions at $\sqrt{s} = 7$ TeV", ALICE Collaboration, Eur. Phys. J. C **74**, 2974 (2014).

154. "Production of charged pions, kaons and protons at large transverse momenta in pp and Pb-Pb collisions at $\sqrt{s_{\rm NN}}$ =2.76 TeV", ALICE Collaboration, Phys. Lett. B **736**, 196 (2014).

155. "Centrality, rapidity and transverse momentum dependence of J/Ψ suppression in Pb-Pb collisions at $\sqrt{s_{\rm NN}}$ =2.76 TeV", ALICE Collaboration, Phys. Lett. B **734**, 314 (2014).

156. "Measurement of charged jet suppression in Pb-Pb collisions at $\sqrt{s_{\rm NN}}$ =2.76 TeV", ALICE Collaboration, JHEP **03**, 073 (2014).

157. "J/Ψ production and nuclear effects in p-Pb collisions at $\sqrt{s_{\rm NN}}$ =5.02 TeV", ALICE Collaboration, JHEP **02**, 073 (2014).

158. "Two and Three-Pion Quantum Statistics Correlations in Pb-Pb Collisions at $\sqrt{s_{\rm NN}}$ =2.76 TeV at the LHC", ALICE Collaboration, Phys. Rev. C **89**, 024911 (2014).

159. "Directed flow of charged particles at mid-rapidity relative to the spectator plane in Pb-Pb collisions at $\sqrt{s_{\rm NN}}$ =2.76 TeV", ALICE Collaboration, Phys. Rev. Lett. **111**, 232302 (2013).

160. "Energy Dependence of the Transverse Momentum Distributions of Charged Particles in pp Collisions Measured by ALICE", ALICE Collaboration, Eur. Phys. J. C **73**, 2662 (2013).

Conferences, Schools, Symposiums, Workshops attended

1. 10-14 Dec, 2018 **DAE International Symposium on Nuclear Physics**, BARC Mumbai, India.
2. 10-14 Dec, 2018 **XXIII DAE-BRNS High Energy Physics Symposium**, IIT Madras, India.
3. 12-25 Sept, 2018 **AEPSHEP 2018: ASIA-EUROPE-PACIFIC SCHOOL OF HIGH ENERGY**, Quy Nhon, Vietnam.
4. 09-11 March, 2017 **CHASCON 2017: 10th Chandigarh Science Congress**, Department of Physics, Panjab University Chandigarh, India.
5. 05-11 Feb, 2017 **QM 2017: International conference of Quark Matter**, Chicago, Illinois, USA.
6. 12-16 Dec, 2016 **XXII st DAE-BRNS High Energy Symposium**, University of Delhi, India.

7. 05-09 Dec, 2016 **61st DAE-BRNS Symposium on Nuclear Physics**, SINP Kolkata, India.

8. 15-18 March, 2016 **National School cum Workshop in Accelerator Physics**, Department of Physics, Panjab University Chandigarh, India.

9. 15-19 Feb, 2016 **ATHIC 2016: 6th Asian Triangle Heavy-Ion Conference**, Delhi, India.

10. 19-21 Oct, 2015 **Workshop on Research Methodology** at Dr. S. S. Bhatnagar UICET under TEQIP- II, Department of Physics, Panjab University Chandigarh, India.

11. 25-27 Feb, 2015 **CHASCON 2015: 9th Chandigarh Science Congress**, Panjab University Chandigarh, India.

12. April, 2014 **Workshop on Contemporary Trends in High Energy Physics and Experimentation**, Panjab University Chandigarh, India.

13. 29 March - 07 April, 2014 **Winter School on Accelerator Nuclear and Particle Physics**, BHU Varanasi, India.

14. 02-21 Dec, 2013 **IX SERC School on Experimental High Energy Physics**, Indian Institute of Technology (IIT) - Madras, Chennai, India.